



City Research Online

City, University of London Institutional Repository

Citation: Kajan, K. (2009). Finite Element Modelling and Investigation of High Speed, Large Force and Long Lifetime Electromagnetic Actuators. (Unpublished Doctoral thesis, City University)

This is the accepted version of the paper.

This version of the publication may differ from the final published version.

Permanent repository link: <http://openaccess.city.ac.uk/19571/>

Link to published version:

Copyright and reuse: City Research Online aims to make research outputs of City, University of London available to a wider audience. Copyright and Moral Rights remain with the author(s) and/or copyright holders. URLs from City Research Online may be freely distributed and linked to.

City Research Online:

<http://openaccess.city.ac.uk/>

publications@city.ac.uk



School of Engineering
and Mathematical Sciences
CITY UNIVERSITY LONDON

Electrical, Electronic and Information
Engineering

**Finite Element Modelling and Investigation
of High Speed, Large Force and Long
Lifetime Electromagnetic Actuators**

Kamalanathan Kajan

Thesis submitted for the fulfilment of the requirements for the degree
of Doctor of Philosophy of the City University of London

July 2009

I hereby declare that the presented work in this thesis is my own or was developed in a joint effort with other members of the research group as it is stated and referenced in the text accordingly!

London, _____

(Kamalanathan Kajan)

ABSTRACT

The prime topic of research presented in this report is the development and use of computer-based modelling methodologies for design and performance modelling of an industrial component in the food sorting industry, exemplified in actuators used in bulk food sorting machines.

Electromagnetic (EM) solenoid actuators are widely used in many applications such as the automobile, aerospace, printing and food industries where repetitive, often high-speed linear or rotating motions are required. In some of these applications they are used as high-speed 'switching' valves for switching pneumatic channels.

The complex nature of electromagnetic, motional and thermal problems is discussed. The methodologies for FE modelling of such high-performance actuators are developed and discussed. These are used for modelling, design, performance evaluation and prediction of the above high-speed actuators. Modelling results showing some of the key design features of the actuators are presented in terms of force produced as a function of various design parameters.

Optimization calculations for the dynamic behaviour are executed at the design process of electromagnetic actuators. Finite element method used for modelling the electromagnetic actuator model. The models are implemented in the design software Opera-2d/3d and were tested at different tasks. The capability is shown at a magnetic actuator.

Magnetically controlled shape memory materials are a new way to produce motion and force. The material changes shape in a magnetic field. Usual applications of the material are actuators that produce linear motion. MSM actuator type is designed and initial investigation presented in this thesis.

Finite element modelling methodologies have been developed for the design and investigation of electromagnetic and thermal behaviours of high-speed, large-force and long-lifetime solenoid actuators used as pneumatic ejector valves in optical sorting machines for bulk food sorting. Operating at frequencies between 150-300 Hz, these actuators are unique in terms of the large force they produced (8-19 N) with very long lifetime (2-5 billion cycles).

ACKNOWLEDGEMENTS

All the work described in this report has been conducted in the Computer Aided Modelling and Design (CAMAD) Group, School of Engineering and Mathematical Sciences of City University. I would like to take the opportunity and thank the following for their help during the course of this work.

First and foremost, I would like to thank my supervisor, Professor S. H. Khan. His guidance and advice were irreplaceable during this trying journey. Always ready to make sure that I remained focused on the important details instead of the future problem. He helped me not only in my studies, but provided support in life as well. I sincerely thank him for all the help he provided.

To my Group members, I would like to express my genuine appreciation for your help and support. Professor K. T. V. Grattan is an invaluable resource with knowledge to spare and kindness enough to share it.

I would also like to thank my family members who are always there for me.

Finally, I would like to acknowledge the ESPRC and Sortex Limited for supporting the work presented in this report.

TABLE OF CONTENTS

ABSTRACT 3

ACKNOWLEDGEMENTS 5

TABLE OF CONTENTS 6

LIST OF FIGS 10

LIST OF TABLES 16

NOMENCLATURE 19

CHAPTER 1 INTRODUCTION..... 22

 1.1 Motivation for this Study..... 22

 1.2 Project Objectives 24

 1.3 Aims And Objectives Of The Work..... 27

 1.4 Outline of the Thesis 28

CHAPTER 2 MAGNETIC SYSTEM AND EQUIVALENT CIRCUIT..... 31

 2.1 Introduction 31

 2.2 Magnetomotive Force (MMF) and Kirchoff's Voltage Law for Magnetic
 Circuits 32

 2.3 Flux and Kirchhoff's Current Law for Magnetic Circuits..... 35

 2.4 Material Characteristics and Ohm's Law for Magnetic Circuits 36

 2.4.1 Linear Materials 38

 2.5 Translation of Magnetic Circuits to Electric Circuits 40

 2.5.1 Flux Linkage 40

 2.5.2 Inductance 41

 2.5.3 Faraday's Law 43

 2.6 The Construction of Magnetic Equivalent Circuit 44

 2.6.1 Electric Circuit Equivalent of Magnetic Circuit of C-core Actuators .. 46

 2.6.2 Selection of Nodes 47

 2.6.3 The Mean Path Approximation 48

 2.6.4 MMF Sources 49

 2.6.5 Voltage Equation and Winding Resistance of C-core Actuators 50

 2.7 Magnetic Equivalent Circuit of E-core Actuators 51

 2.7.1 Nodes Selection and Equivalent Circuit..... 53

2.8 Force in an Electromagnetic Actuator	55
2.8.1 Magnetic Force Due to Air Gap	56
2.8.2 Simplification of the Force Equation	58
2.9 Summary.....	60
CHAPTER 3 ELECTROMAGNETICALLY AND THERMALLY COUPLED FIELD ANALYSIS .	61
3.1 Introduction	61
3.2 Electromechanical Model of a Solenoid Actuator.....	63
3.3 Electrical Circuit of a Solenoid Actuator	64
3.4 Induced EMF in the excitation coil for a linear actuator.....	66
3.5 Mechanical Circuit of a Solenoid Actuator	69
3.5.1 Force Calculation from Energy and Co-Energy	69
3.6 Three State Variables For Simulating an Actuator	73
3.7 Electromagnetic Heating.....	75
3.7.1 Fundamental Equations.....	76
3.7.2 Convection	77
3.7.3 Radiation	77
3.7.4 One dimensional Heat Conduction Equation.....	78
3.7.5 Boundary Conditions	81
3.8 Summary.....	84
CHAPTER 4 MAGNETIC MATERIALS USED IN ELECTROMAGNETIC ACTUATORS	86
4.1 Introduction	86
4.2 Magnetic Properties	86
4.2.1 Permeability.....	88
4.2.2 Coercivity.....	88
4.2.3 Saturation Magnetization.....	89
4.2.4 Hysteresis Loss	89
4.2.5 Energy Dissipation and Power Losses	89
4.3 Prerequisites to Obtain Soft Magnetic Materials	90
4.4 Typical Requirements	92
4.5 Materials	92
4.6 Material Properties.....	93
4.6.1 Nickel – Iron Alloys	93
4.6.2 Cobalt-Iron Alloys	94
4.6.3 Silicon-iron crystalline alloy	94

4.7 Material List.....	96
4.8 Materials for the Actuator Design.....	97
4.9 Summary.....	99
CHAPTER 5 FINITE ELEMENT MODELLING OF ELECTROMAGNETIC ACTUATORS	100
5.1 Introduction	100
5.2 Mathematical Modelling of Electromagnetic Actuators.....	101
5.3 General Procedures.....	104
5.4 Discretisation of the Field Region	105
5.5 Finite Element Computer Program – Opera -2d.....	106
5.5.1 Convergence Factor and Some Aspects of Convergence.....	110
5.5.2 Post-Processing	110
5.5.3 Boundary Conditions	113
5.5.4 Estimation of Errors in Finite Element Modelling	113
5.5.5 The Data Command Input File	115
5.6 Mathematical Modelling and Design of High-Speed Actuators	115
5.6.1 Practical Elements of an Electromagnetic Actuator.....	122
5.7 Design Variables of C-core and E-core Actuators and Their Optimisation	123
5.8 Investigation of C-core-I Actuator Design.....	131
5.8.1 Investigation OF C-Core-II Actuator Design	136
5.8.2 Investigation Of C-core- III Model Design.....	138
5.9 E-Core Solenoid Valve.....	140
5.9.1 Investigation of E-Core-I Model Design	140
5.9.2 Investigation of E-core-II Model Design.....	143
5.10 Analyzing C-core-II and E-core-II Electromagnetic Actuator	146
5.10.1 C-Core-II Analysis	147
5.10.2 E-core-II Analysis	151
5.11 Computation of 3D Magnetic Field Distribution in Electromagnetic Actuator	153
5.12 Summary.....	159
CHAPTER 6 INVESTIGATION OF ELECTROMAGNETIC ACTUATOR DESIGN CONCEPT .	161
6.1 INTRODUCTION	161
6.2 C-core Electromagnetic Actuator	162
6.2.1 Force, Current Analysis for Different Air gap.....	163

6.2.2 Variation of Force with different Air Gap Values	167
6.2.3 Force, Air gap Analysis for Different Materials	170
6.3 E-core Electromagnetic Actuator	171
6.3.1 Force, Current Analysis for Different Air gap	172
6.3.2 Force air Gap Analysis	176
6.4 Summary.....	178
CHAPTER 7 DESIGN OF PROTOTYPES AND EXPERIMENTAL VALIDATION OF FINITE ELEMENT RESULTS.....	179
7.1 Introduction	179
7.2 Air Flow Rate Test	181
7.3 Experimental Validation of Inductance Modelling Results.....	185
7.3.1 C-core-II Model Radiometal - 4550 Valve Response Test.....	186
7.3.2 C-core-II Model Armco Valve Response Test	191
7.4 Experimental Valve Response Characteristics Test	200
7.5 Experimental Validation of Thermal Modelling Results	209
7.6 Summary.....	212
CHAPTER 8 DEVELOPMENT OF ADVANCED ACTUATORS USING MAGNETIC SHAPE MEMORY MATERIAL	214
8.1 Introduction	214
8.2 Magnetic Shape Memory Materials.....	215
8.3 MSM Actuators	217
8.4 Modelling and Investigation of MSM Actuator.....	219
8.5 Summary.....	224
CHAPTER 9 CONCLUSIONS	225
9.1 Work Done	225
9.2 Future Work	227
REFERENCES	228
APPENDICES	242
Appendix A	242
Maxwell Stress Tensor Law	242

LIST OF FIGS

Fig. 2.2-1. Amperean loop 33

Fig. 2.2-2. Magnetic field around the core 34

Fig. 2.5-1. Flux linkage 41

Fig. 2.6-1. C-core actuator..... 46

Fig. 2.6-2. C-core nodes..... 47

Fig. 2.6-3. Equivalent magnetic circuit..... 48

Fig. 2.7-1. E-core actuator..... 53

Fig. 2.7-2. E-core nodes 53

Fig. 2.7-3. E-core equivalent magnetic circuit..... 54

Fig. 2.8-1. Illustration of an actuator 55

Fig. 3.1-1. Concept map of electromechanical system modelling..... 62

Fig. 3.2-1. The interaction of subsystems of an actuator 63

Fig. 3.3-1. Equivalent magnetic circuit of a solenoid actuator..... 64

Fig. 3.4-1. Linear actuator 66

Fig. 3.4-2. Equivalent diagram of the electrical circuit of an actuator..... 67

Fig. 3.6-1. Equivalent diagram of the mechanical part of an actuator..... 73

Fig. 3.7-1 Electromagnetic thermal interaction 75

Fig. 3.7-2. Heat flow conduction 76

Fig. 3.7-3. Schematic of radiation between a body and an enclosure 78

Fig. 3.7-4. One dimensional conduction 79

Fig. 3.7-5. Boundary conditions for general heat conduction..... 82

Fig. 4.2-1. Hysteresis loop [57]..... 87

Fig. 4.3-1. Round hysteresis loop..... 91

Fig. 4.3-2. Square/ Rectangular hysteresis loop..... 91

Fig. 4.3-3. Flat hysteresis loop 91

Fig. 4.8-1. B-H curve for Radiometal-4550 97

Fig. 4.8-2. B-H curve for Armco 97

Fig. 4.8-3. B-H curve for Hypermco-50..... 98

Fig. 4.8-4. B-H curve for Hyperm-0..... 98

Fig. 5.4-1. Map of the mesh..... 105

Fig. 5.5-1. FE model showing the boundary condition.....	113
Fig. 5.6-1. Schematic diagram of an optical sorting machine showing	116
Fig. 5.6-2. Simplified schematic showing the main constructive features	117
Fig. 5.7-1. Schematic of the EM actuator, showing the lines ab,	125
Fig. 5.7-2. Variation of force with valve plate thickness for c-core actuator, ..	125
Fig. 5.7-3. Field distribution along the lines ab (yoke) and ef (valve plate); TV =	126
Fig. 5.7-4. Field distribution along the lines ab and ef; TV = 2.5 mm,.....	126
Fig. 5.7-5. Variation of electromagnetic force, F with height of the yoke (HY) 127	
Fig. 5.7-6. Variation of electromagnetic force, F for different.....	128
Fig. 5.7-7. Variation of electromagnetic force, F with the width W_{co} of.....	128
Fig. 5.7-8. Variation of electromagnetic force, F with the width W_{co} of.....	129
Fig. 5.7-9. Variation of electromagnetic force, F with the valve pole width W_p for various models	130
Fig. 5.8-1. Simplified schematic showing C-core-I actuator.....	131
Fig. 5.8-2. C-core- I Opera-2d model.....	133
Fig. 5.8-3. C-core-I model field lines.....	134
Fig. 5.8-4. C-core-I contour plot.....	135
Fig. 5.8-5. C-core-II model.....	136
Fig. 5.8-7. C-core-II model contour plot	138
Fig. 5.8-8. C-core-III model contour plot.....	139
Fig. 5.8-9. Equipotential line contours of vector potential	139
Fig. 5.9-1. E-core solenoid valve	140
Fig. 5.9-2. E-core-I Opera-2d model.....	141
Fig. 5.9-3. E-core-I model filled zone contours of magnetic flux density	143
Fig. 5.9-4. E-core-II Opera-2d model.....	145
Fig. 5.9-5. E-core-II contour plot of flux density	146
Fig. 5.10-1. C-core-II actuator model mesh	147
Fig. 5.10-2. C-core-II equipotential line contours of vector potential-1.....	149
Fig. 5.10-3. C-core-II Equipotential line contours of vector potential-2	150
Fig. 5.10-4 C-core-II magnetic field distribution	150
Fig. 5.10-5. The E-core-II model mesh.....	151
Fig. 5.10-6. E-core-II equipotential line contours of vector potential.....	152
Fig. 5.10-7. E-core-II equipotential line contours of vector potential in the	153

Fig. 5.11-1. Main constructive features of a long lifetime C- 154

Fig. 5.11-2. Typical 3D finite element (FE) model of the EM actuator shown in
..... 155

Fig. 5.11-3. FE discretization of the 3D problem domain showing the distribution
of 155

Fig. 5.11-4. FE modelling results: variation of EM force with 156

Fig. 5.11-5. FE modelling results: variation of EM force with 157

Fig. 5.11-6. Schematic of the EM actuator showing lines ab, cd and ef along
..... 157

Fig. 5.11-7. Effects of the valve plate thickness TV on magnetic field
distributions in 158

Fig. 5.11-8. Typical 3D finite element model of the newly designed 'C-core-II
..... 158

Fig. 5.11-9. Current rise in the excitation coil for the 'C-core-II 159

Fig. 6.2-1. C-core-II electromagnetic Opera-2d model 162

Fig. 6.2-2. C-core-II model variation of electromagnetic force for 163

Fig. 6.2-3. C-core-II model variation of electromagnetic force for different 164

Fig. 6.2-4. C-core-II model variation of electromagnetic force for different 164

Fig. 6.2-5. C-core-II model variation of electromagnetic force for different 165

Fig. 6.2-6. C-core-II model variation of electromagnetic force for different 165

Fig. 6.2-7. C-core-II model variation of electromagnetic force for 166

Fig. 6.2-8. C-core-II model variation of electromagnetic force for different 166

Fig. 6.2-9. C-core-II model variation of electromagnetic force for different 167

Fig. 6.2-10. C-core-II model variation of electromagnetic force for different .. 168

Fig. 6.2-11. C-core-II model variation of electromagnetic force for different .. 168

Fig. 6.2-12. C-core-II model variation of electromagnetic force for different .. 169

Fig. 6.2-13. C-core-II model variation of electromagnetic force for different .. 169

Fig. 6.2-14. C-core-II model variation of electromagnetic force for 170

Fig. 6.3-1. E-core-II model electromagnetic actuator 171

Fig. 6.3-2. E-core-II model variation of electromagnetic force for different 172

Fig. 6.3-3. E-core-II model variation of electromagnetic force for different 172

Fig. 6.3-4. E-core-II model variation of electromagnetic force 173

Fig. 6.3-5. E-core-II model variation of electromagnetic force for 173

Fig. 6.3-6. E-core-II model variation of electromagnetic force for 174

Fig. 6.3-7. E-core-II model variation of electromagnetic force for 174

Fig. 6.3-8. E-core-II model variation of electromagnetic force for different 175

Fig. 6.3-9. E-core-II model variation of electromagnetic force for different 176

Fig. 6.3-10. E-core-II model variation of electromagnetic force for different .. 176

Fig. 6.3-11. E-core-II model variation of electromagnetic force for different .. 177

Fig. 6.3-12. E-core-II model variation of electromagnetic force for different .. 177

Fig. 7.1-1. Prototype design of the C-core actuator 180

Fig. 7.2-1. Exploded drawing of the valve 181

Fig. 7.2-2. C-core-II prototype ejector valve 182

Fig. 7.2-3. Flexible driving circuit board for the valve 182

Fig. 7.2-4. Equipment setup for flow rate test 183

Fig. 7.3-1. C-core model-II valve response for 0.5 A current with 0.1 mm air gap
..... 186

Fig. 7.3-2. C-core model-II valve response for 1.0 A current with 0.1 mm air gap
..... 187

Fig. 7.3-3. C-core model-II valve response for 2.0 A current with 0.1 mm air gap
..... 187

Fig. 7.3-4. C-core model-II valve response for 0.5 A current with 0.05 mm air
gap 188

Fig. 7.3-5. C-core model-II valve response for 1.0 A current with 0.05mm air
gap 188

Fig. 7.3-6. C-core model-II valve response for 2.0 A current with 0.05 mm air
gap 189

Fig. 7.3-7. C-core model-II valve response for 0.5 A current with 0.03 mm air
gap 189

Fig. 7.3-8. C-core model-II valve response for 1.0 A current with 0.03 mm air
gap 190

Fig. 7.3-9. C-core model-II valve response for 2.0 A current with 0.03 mm air
gap 190

Fig. 7.3-10. C-core model-II valve response for 0.5 A current with 0.1 mm air
gap 191

Fig. 7.3-11. C-core model-II valve response for 1.0 A current with 0.1 mm air
gap 191

Fig. 7.3-12. C-core model-II valve response for 2.0 A current with 0.1 mm air gap 192

Fig. 7.3-13. C-core model-II valve response for 0.5 A current with 0.05 mm air gap 192

Fig. 7.3-14. C-core model-II valve response for 1.0 A current with 0.05 mm air gap 193

Fig. 7.3-15. C-core model-II valve response for 2.0 A current with 0.05 mm air gap 193

Fig. 7.3-16. C-core model-II valve response for 0.5 A current with 0.03 mm air gap 194

Fig. 7.3-17. C-core model-II valve response for 1.0 A current with 0.03 mm air gap 194

Fig. 7.3-18. C-core model-II valve response for 2.0 A current with 0.03 mm air gap 195

Fig. 7.3-19. C-Core-II model Radiometal-4550 inductance comparison graph for 0.5 A..... 196

Fig. 7.3-20. C-core-II model Radiometal-4550 inductance comparison graph for 1.0 A current..... 197

Fig. 7.3-21. C-core-II model Armco inductance comparison graph for 0.5 A current..... 198

Fig. 7.3-22. C-core-II model Armco inductance comparison graph for 1.0 A current..... 199

Fig. 7.4-1. C-core-II model Radiometal-4550 valve, I=1.0 A, current characteristic curve 202

Fig. 7.4-2. C-core-II model Radiometal-4550 valve, I=1.0 A current pressure 202

Fig. 7.4-3. C-core-II model Radiometal-4550 valve, I= 2.0 A, current characteristic 203

Fig. 7.4-4. C-core-II model Radiometal-4550 valve, I=2.0 A current pressure 204

Fig. 7.4-5. C-core-II model Radiometal-4550 valve, I= 2.5 A, current characteristic 205

Fig. 7.4-6. C-core model-II Radiometal-4550 valve, I=2.5 A current, pressure 205

Fig. 7.4-7. C-core model-II Armco valve, $I=1.7$ A, current characteristic curve	206
Fig. 7.4-8. C-core model-II Armco valve, $I=1.7$ A current, pressure.....	207
Fig. 7.4-9. C-core model-II Armco valve, $I= 2.0$ A, current characteristic curve	208
Fig. 7.4-10. C-core model-II Armco valve, $I=2.0$ A current pressure characteristic	208
Fig. 7.5-1. Comparison of the thermal modelling results with the corresponding	210
Fig. 7.5-2. Variation of temperature with time corresponding to results.....	212
Fig. 8.2-1. MSM material B-H curve	216
Fig. 8.3-1. Schematic view of the structure of MSM actuator	218
Fig. 8.4-1. MSM actuator model	219
Fig. 8.4-2. MSM actuator Opera-2d model	220
Fig. 8.4-3. Field plot for $MMF=8304$ A-turn model, with its core and MSM material in.....	221
Fig. 8.4-4. Contour plot for $MMF=8304$ A-turn model, with its core and MSM material in.....	222
Fig. 8.4-5. Contour plot for $MMF=8000$ A-turn model , with its core and MSM material	223

LIST OF TABLES

Table 4.7-1 Material list 96

Table 5.7-1 Geometric variables used for FE simulation results shown in Fig.
5.7-9..... 130

Table 5.8-1 C-core model-I dimensions..... 132

Table 5.8-2 C-core-I force 134

Table 5.8-3 C-core-II model dimensions..... 136

Table 5.8-4 C-core-II force 137

Table 5.8-5 C-core-III model dimensions..... 139

Table 5.9-1 E-core- I model dimensions..... 141

Table 5.9-2 E-core-I force..... 142

Table 5.9-3 E-core-II dimensions..... 144

Table 5.9-4 E-core-II force..... 145

Table 5.10-1 C-core-II force 148

Table 5.10-2 E-core-II model force..... 151

Table 7.1-1 Coil winding technical data for C-core-II valve..... 180

Table 7.3-1 C-core model-II valve response data for 0.5 A current with 0.1 mm
air gap 186

Table 7.3-2 C-core model-II valve response data for 1.0 A current with 0.1 mm
air gap 187

Table 7.3-3 C-core model-II valve response data for 0.5 A current with 0.1 mm
air gap 187

Table 7.3-4 C-core model-II valve response data for 0.5 A current with 0.05 mm
air gap 188

Table 7.3-5 C-core model-II valve response data for 1.0 A current with 0.05 mm
air 188

Table 7.3-6 C-core model-II valve response data for 2.0 A current with 0.05 mm
air 189

Table 7.3-7 C-core model-II valve response data for 0.5 A current with 0.03 mm
air gap 189

Table 7.3-8 C-core model-II valve response data for 1.0 A current with 0.03 mm
air gap 190

Table 7.3-9 C-core model-II valve response data for 2.0 A current with 0.03 mm
air 190

Table 7.3-10 C-core model-II valve response data for 0.5 A current with 0.1 mm
air gap 191

Table 7.3-11 C-core model-II valve response data for 1.0 A current with 0.1 mm
air gap 191

Table 7.3-12 C-core model-II valve response data for 0.5 A current with 0.01
mm air 192

Table 7.3-13 C-core model-II valve response data for 0.5 A current with 0.05
mm air 192

Table 7.3-14 C-core model-II valve response data for 1.0 A current with 0.05
mm air 193

Table 7.3-15 C-core model-II valve response data for 2.0 A current with 0.05 mm
air gap 193

Table 7.3-16 C-core model-II valve response data for 0.5 A current with 0.03
mm air 194

Table 7.3-17 C-core model-II valve response / data for 1.0 A current with 0.03
mm air 194

Table 7.3-18 C-core model-II valve response / data for 2.0 A current with 0.03
mm air 195

Table 7.4-1 C-Core-II model Radiometal-4550 valve, I=1.7 A current test 201

Table 7.4-2 C-core-II model Radiometal-4550 valve, I= 1.7 A current test results
..... 203

Table 7.4-3 C-core-II model Radiometal-4550 valve, I= 2.0 A current test 203

Table 7.4-4 C-core-II model Radiometal-4550 valve, I= 2.0 A current test results
..... 204

Table 7.4-5 C-core-II model Radiometal-4550 valve, I= 2.5 A current test
specification 205

Table 7.4-6 C-core-II model Radiometal-4550 valve, I=2.5 A current test results
..... 206

Table 7.4-7 C-core model-II Armco valve, I= 1.7 A current test specification . 206

Table 7.4-8 C-core model-II Armco valve, I=1.7 A current test results 207

Table 7.4-9 C-core model-II Armco valve, I= 2.0 A current test specification . 207

Table 7.4-10 C-core model-II Armco valve, I= 2.0 A current test results 209

Table 7.5-1 Experimental data for the thermal test of one of the prototype
valves. 211

Table 8.4-1 MSM model -I dimensions 219

Table 8.4-2 MSM model- I modelling results 221

Table 8.4-3 MSM model-II dimensions 222

Table 8.4-4 MSM model- II modelling results 223

NOMENCLATURE

Abbreviations

2d	Two dimensions
3d	Three dimensions
AG	Actual air gap between MSM material and pole
AHP	Actual height of the pole
A_p	Area of Pole
CAD	Computer aided design
EM	Electro magnetic
EMC	Electromagnetic circuit
EMSL	Extended MSM material length
FDM	Finite difference method
FE	Finite element
FEA	Finite element analysis
FEM	Finite element method
GMM	Giant magnetostrictive materials
HC	Height of the coil
HCL	Height of coil
HCO	Total Height of core
HP	Height of pole
HPM	Height of the extended pole
HY	Height of yoke
KCL	Kirchhoff's current law
KVL	Kirchhoff's voltage Law
MSM	Magnetic shape memory
MMF	Magneto-motive force
RHS	Right hand side
TCH	Height of the core
TCO	Thickness of core

TCW	Width of the core
TV	Thickness of valve plate
WCL	Width of coil
WCO	Total Width of the core
WMS	Width of the MSM material
WPL	Width of left pole
WPM	Width of middle pole
WPR	Width of right pole
WV	Width of the valve plate

Equation’s Symbols

Symbol	Description	units
α	Absorption coefficient	m^{-1}
a	Acceleration	ms^{-2}
g	Air gap	mm
δ	Air gap length	mm
A	Area	mm^2
r	Resistance	Ω
i	Current	A
B_x	Damping co-efficient	Nsm^{-1}
ρ	Density	Kgm^{-3}
d_c	Diameter of conductor	mm^2
ρ_r	Electrical Resistivity	Ωm
E	Energy	J
H	Field intensity	Am^{-1}
λ	Flux linkage	Wb-turn
F,F _e	Force	N
q	Heat flow	W
L	Inductance	H
l	length	m
ϕ	Magnetic flux	Wb

B	Magnetic Flux density	T
MMF, F_T	Magnetomotive force	A-turn
M	Mass	Kg
M_g	Gravitational force	N
N	Number of turns	
p_f	Packing factor	
μ	Permeability	Hm ⁻¹
μ_0	Permeability in vacuum	Hm ⁻¹
μ_m	Permeability of core material	Hm ⁻¹
P	Power	W
μ_r	Relative permeability	
R	Reluctance	H ⁻¹
c	Specific heat capacity	Jkg ⁻¹ K ⁻¹
K_s	Spring Constant	Nm ⁻¹
σ	Stefan-Boltzmann constant	Wm ⁻² K ⁻⁴
T	Temperature	K
k	Thermal conductivity	Wm ⁻¹ K ⁻¹
D	Thermal diffusivity of the medium	m ² s ⁻¹
t	Time	s
V	Voltage	V

Chapter 1

INTRODUCTION

1.1 MOTIVATION FOR THIS STUDY

The present highly competitive international economy demands that companies should search for new methods to increase efficiency, improve productivity and streamline operations. In the manufacturing sector, the reduction of costly prototype development and production represents a significant competitive advantage. Magnetic field analysis for optimum design is now entering the mainstream of Computer-Aided Engineering. Field simulation permits electrical engineers to vastly improve both their visualization and manipulation of the electrical and magnetic fields which underlie all electrical products [1]. The purpose of field simulation is to create reliable and accurate prototypes using a computer. A computer graphics interface allows the engineer to draw a geometric model, specify the material properties of objects and to identify the source of electromagnetic fields [2]. The simulator then computes the fields that exist throughout the structure and allows the solution to be both quantitatively manipulated and displayed on the screen.

Technologies for developing electromagnetic actuators have been advanced significantly in the past two decades. Their applications range from low force actuators such as optical mirrors or magnetic printing systems, to large force actuators, such as motors, relays, and valves. High speed sorting machines based on optical properties are in the forefront of bulk sorting of many food products (rice, peanuts, coffee, peas, beans, etc.) [3-9]. An EM ejector is essentially an EM valve actuator whose active components comprise an excitation coil wound around a magnetic core that attracts or releases a movable valve plate depending on the excitation state of the coil. Very tight design and rigorous performance specifications make the EM ejectors which are needed for high-speed sorting applications to be unique in terms of their design, manufacture and reliable exploitation.

Electromagnetic (EM) solenoid actuators of wide variety of sizes, shapes, power outputs and technological realizations are used in many applications where discrete cyclic motions are required. Compared to other actuating mechanisms based on, for example, piezoelectric and hydraulic principles EM actuators are simpler, cheaper, repairable, robust, and easier to manufacture. Although the analysis and design of such actuators are well covered in the literature [10-13], there are, however, very few situations which involve commercial EM actuators that normally operate under continuous duty cycles at frequencies between 150-300 Hz, producing a relatively large force (8-10 N). These are combined with a stroke length of 0.05-0.1 mm, 'fully open' and 'fully closed' at times of 0.2 ms and 0.46 ms respectively becomes a requirement for a multibillion cycle operation (in excess of 5 billion cycles) without maintenance. These actuators operate at the limit of what can be achieved by solenoid-based EM actuator technology.

We have investigated different designs of actuators of this type, which are used as pneumatic ejector valves in high-speed optical food sorting machines [14]. The whole area of systematic research into high frequency EM valve-based ejector technology is new. To our knowledge, apart from previous 'trial and error' methods used in this industry, no comprehensive research has been done so far. Given the demanding fast duty cycle, high frequency of operation, high reliability and robustness needed for the ejector technology, the EM ejector valve being developed should be unique, meeting very tight design and rigorous performance specifications. Some of the novel aspects of the design being pursued include the minimisation of the overall size of the valve, and meeting the constraints of the particular geometric and material parameters of the magnetic circuit and the dedicated control circuitry used.

The design methodologies developed for this research are based upon the modelling and computation of 2D/3D nonlinear magnetic field distribution in the ejector valve using the finite element (FE) technique. This involves the steady-state and transient solutions of nonlinear Poisson's equation for which there are no analytical solutions. The results are used for design optimisation and

investigation of the effects of geometry, material, EM and mechanical parameters on the output performance of the valve [15-28].

The work carried out here is built upon a previous brief study carried out at City University in collaboration with Sortex Limited UK, to investigate the viability of a successful approach which has been put forward towards the design, development and implementation of an ultimate ejector sub-system. The resulting EM ejector currently lasts between 500 million to 1 billion cycles before failure.

The newly developed ejector sub-system that would be ultra compact and have a long lifetime cycles. While an ideal ejector would be a valve that never fails, this work focused on the development of methodologies and software design tools for both modelling and CAD of novel concepts for the design, development, fabrication and testing of key industrial components in the bulk food sorting industry, exemplified in the EM actuator-based ejector sub-systems used in optical sorting machines.

1.2 PROJECT OBJECTIVES

Although conventional actuators are well covered in literature [29-34]. A very few studies have been carried out so far that concern high speed and large force magnetic actuators [5-36]. The published literature in this area concerns analytical and experimental studies of high speed electromagnetic actuators with very small force

Linear actuation systems typically include electrical, mechanical, and hydraulic components as well as control systems. The solenoid plays the role of an interfacing component between the electrical domain and mechanical loads [37-40]. It is very challenging to model the solenoid accurately because its operation is based on complex electromagnetic principles. It is a multi-domain component in itself comprising the electrical driver circuit and the mechanical plunger behaviour.

Numerical and analytical studies are carried out to investigate and understand the mechanisms of electrical, mechanical and thermal effects of the high speed and large force electromagnetic actuators [21], [41]. The analytical techniques used are unsuitable for tackling the complicated non-linear problems involved.

Despite the fact that the actuators described above are generally simple and robust electromechanical devices. They rely on complex nonlinear electromagnetic, thermal and electromechanical processes that underlie their efficient, reliable and safe operation. These usually interrelated processes need to be understood and quantified in order to optimise their design and ensure long-term safe and reliable performances.

In order to understand the basic electromagnetic processes and other effects on the design and performance of an electromagnetic actuator a detailed study of its magnetic field distribution is needed. FE technique is used for the development of appropriate methodologies for mathematical modelling and computation of the 2D/3D nonlinear magnetic field distribution in actuators [17-26]. This would involve the steady-state and nonlinear Poisson's equation in the complex geometry of such actuators for which there are no analytical solutions.

Accuracy in the calculation of field distributions and device parameters remains the foremost consideration in the choice of the appropriate tools, followed by speed of solution and cost. Over the last few decades numerical methods have gained in accuracy and applicability. The growing power of the computer has put the final touch on the appeal of the computer-aided approach.

The 2D/3D models and the software design tools that have been developed would be used to investigate the magnetic field distribution in and around the core and plunger taking into account saturation and eddy-current effect for various design parameters (e.g. geometric, material and electrical) [42-44]. In addition, the results would be essential in the investigation of the nature and magnitude of the magnetic force acting on the valve plate for various air gap distances, thicknesses of the valve plates and various excitation currents.

In the absence of any existing methodologies for mathematical modelling and CAD of electromagnetic actuator that tackle the problems discussed above, the academic and industrial context of the research undertaken in this study is clear.

The modelling methodologies that need to be developed should give a fundamental insight into the physical nature and extent of these problems and solve for CAD, performance evaluation and the prediction of actuators. The CAD techniques to be developed should lead to significant improvements to the design and performance of actuators. By their generic nature, the methodologies would be applicable to tackle similar problems in many other related areas.

Mathematical model for the component is developed representing its basic functionality. This model will allow us to predict the value of the force.

The FE model can be easily generated using Opera. Opera is ideal for FEA modelling software since it allows an easy and fast model implementation [45-46]. However, the actual properties of the solenoid typically determined by a variety of physical effects that cannot be easily included in analytical calculations. Most of these effects are non-linear and are primarily due to the magnetic saturation of the iron within the solenoid.

Two distinct approaches which exist as the solutions for field problems are: domain-type and boundary-type. Domain type formulation is the direct solution of the differential equation governing the field. The finite difference (FDM) and finite element (FEM) methods are the two most commonly used domain-type methods. In our solutions we have used finite element method.

1.3 AIMS AND OBJECTIVES OF THE WORK

The above discussion set out the academic and industrial context and establishes the scope of the work that needs to be undertaken for investigation of electromagnetic actuator by mathematical modelling. This also leads to the following aims of the work:

- (a) To develop methodologies and finite element (FE) software design tools for 2D/3D electromagnetic and thermal modelling of electromagnetic (EM) valve-based ejector sub-systems for their full computer aided design (CAD), functional modelling and performance prediction.
- (b) To design and build appropriate prototypes of ejector valves using methodologies developed in (a).
- (c) To laboratory and life test the prototypes in industrial test conditions in order to validate and refine the above modelling methodologies and thus to evaluate their performance in terms of EM, mechanical, thermal, pneumatic and dynamic characteristics.
- (d) To investigate and research into the feasibility of conceptually new ejector technology for the next generation of sorting machines using the validated modelling and software design tools.

The above aims will be met by fulfilling the following objectives:

- (i) Investigation and research into a range of potentially viable ejector technologies (e.g. EM valves, ultra high pressure valves, multiple power and/or angles of ejection, etc.) in order to identify a number of most appropriate technologies to be developed that will meet the requirement specifications for the present and the next generation of sorting machines.
- (ii) Development of methodologies and design tools for CAD and optimisation of EM valve-based ejector sub-system by solving coupled or decoupled electric circuit, magnetic field and mechanical equations.

- (iii) Development of methodologies and design tools for 2D thermal modelling of both individual and banks of ejector valves by direct or indirect coupling of magnetic field and thermal equations.
- (iv) Design and building of appropriate prototypes of ejector valves using methodologies developed in (ii) and (iii). Design and building of matching control circuitry for these prototypes.
- (v) Laboratory and life testing of the prototypes in industry (Sortex) to validate and refine the above modelling methodologies and to evaluate their performance in terms of EM, mechanical, thermal, pneumatic and dynamic characteristics.
- (vi) Investigation and research into conceptually new ejector technology for the next generation of sorting machines.
- (vii) Dissemination of results via patents and publications for their generic applicability in diversified industrial applications.

Based on the above aims and objectives, the primary aim of the project is to develop software design tools and use these tools to design, build, test and implement an ejector technology to the specification agreed by industry. The design tools and technology will have specific application in present and next generation sorting machines, and generic application in other areas such as automobile, aerospace and printing industries.

1.4 OUTLINE OF THE THESIS

The research work presented was carried out with the aim of obtaining a model of a solenoid actuator which consists of part of a greater complete model for food sorting technology. This report presents operational principle methodologies and the results of performance modelling of actuators. This is done by finite element modelling and computation of 2D/3D magnetic field distribution in actuators used as bulk food sorting machines. The present thesis

consists of nine chapters including the introductory Chapter 1, where the motivation and present contribution of this research work is outlined.

The purpose of Chapter 2 and Chapter 3 is to provide the information necessary to understand the basic theory and capabilities of magnetism and electromagnetic actuators to enable us to select or design an actuator for a specific application and set of design constraints.

The purpose of Chapter 4 is to provide information on the electromechanical and thermal systems with the specific perspective of an actuator development. Also this chapter explains the coupled nature of electromagnetic and mechanical forces in an actuator system which necessitates the simultaneous solution of the governing electromagnetic and mechanical equations to predict the system performance characteristics.

This describes the important categories of magnetic material properties. For each category the various properties of prime interest are discussed, how these differ from one class to another, and how these properties can be controlled.

The purpose of Chapter 5 is to analyze the C-core and E-core actuator computational finite element modelling. An interactive method of solution with well-known successive technique has been adopted and described the important design for this type of actuators is the variables of geometry, e.g. size, shape number of turns of the coil, shape and dimension of the valve plate. For electromagnetic actuators the dimensions of the magnetic circuit and their magnetic material properties are the design variables. By the use of these mathematical models a new design can be generated or an existing design can be modified for optimum performance. Some useful techniques, e.g. dimensional analysis, input current analysis, have been used to optimise a design to meet specified design criteria.

The purpose of Chapter 6 concerns the application of the finite element method in the analysis of electromagnetic actuators. The effect of the air gap and excitation current for different material and different shapes of the actuators has

been investigated. In electromagnetic actuators the main objective is to maximise the flux density in the air gap. The mathematical models developed can be used for such design optimisation without costly and time consuming experimentation.

In chapter 7 the results of the computations are presented and they are validated with experimental results.

Chapter 8 presents the general background on the MSM actuator and the study of preliminary modelling which have been carried out in this chapter with a simple design of MSM actuator.

The purpose of Chapter 9 is to discuss the conclusions arrived at as a result of the work done and presents suggestions for ways in which further research would enhance the utility and versatility of the work to continue.

Chapter 2

MAGNETIC SYSTEM AND EQUIVALENT CIRCUIT

2.1 INTRODUCTION

The purpose of this chapter is to set forth the basic background needed to analyze electromagnetic and electromechanical systems. The circuit is an ingenious abstraction for representing in a simple integrated form of what is in fact a highly complex electromagnetic system which is associated with a conducting path. Many simple linear or vibratory machines (such as relays and actuators) can be represented by a single magnetic path linked with a coil whose inductance is a function of the relative position of the fixed and movable parts. Each component electric circuit has a behaviour expressed as a differential equation and the whole device being represented by as many equations as there are recognizably separate circuits. The parameters must be known in an appropriate form, based on field analysis, design estimate or experiment.

Electromagnetic actuators can be described by mathematical models. These mathematical models help to understand their behaviour and the effect of various features of their construction. The performance characteristics can also be evaluated from the geometry and material properties of the device. The mathematical model can be used for a systematic overall design process, firstly to select a design concept. When a concept is chosen, the design can be formulated to give the form and structure, dimension and the materials to achieve satisfactory and /or optimal performance characteristics [47-52].

For some practical problems this may be enough, but a complete analysis requires the construction in sequence of the electric circuit equations, the energy conversion relation and the equation of motion. The full process may present analytical difficulty, not because the approach is faulty (in, fact, only the circuit approach enables us to get so far) but because a linked

electromagnetic/mechanical system is complex. Analytical solution may have to be obtained with the help of simplifying assumptions, but numerical solutions can always be computed [47-52].

2.2 MAGNETOMOTIVE FORCE (MMF) AND KIRCHHOFF'S VOLTAGE LAW FOR MAGNETIC CIRCUITS

Despite the fact that electromagnetic actuators are generally simple and robust electrical devices, that rely on complex nonlinear electromagnetic, electromechanical and thermal processes and also that underlie their efficient, reliable and safe operation. These usually interrelated processes need to be understood and quantified in order to optimise their design and ensure long-term safe and reliable performance.

In order to understand the basic electromagnetic processes and other effects on the design and performance of an electromagnetic actuator a detailed study of its magnetic field distribution is needed. To develop appropriate methodologies we need to know the analytical method and computation of the 2D linear solutions in electromagnetic actuators using the FE technique.

An important aspect of modelling work is creating the right model. This has been checked by comparing the 2D linear modelling solutions and analytical solutions calculated by us. However the analytical solution is only applicable where,

- (a) Magnetic circuit is linear
- (b) There is no leakage flux
- (c) There is no fringing of flux

The agreement between analytical solutions and 2D linear modelling solutions will establish confidence in the modelling methodologies already developed and it leads us to do the modelling and computation of the 2D nonlinear magnetic field distribution in electromagnetic actuators using the FE technique. The 2D nonlinear modelling techniques to be developed should lead to significant improvements to the design and performance of electromagnetic actuators.

We begin our analysis of magnetic systems by developing the concept of Kirchhoff's voltage law for magnetic systems. In particular the idea that the sum of the magneto-motive force drops around any closed loop is equal to the sum of the magneto-motive force sources.

To formalize this idea, we begin with Ampere's law, which states that the line integral of the field intensity is equal to the current enclosed by that path.

This is illustrated in Fig. 2.2-1 and may be stated mathematically as

$$\oint_x \mathbf{H} \cdot d\mathbf{l} = Ni_{enc} \quad (2.2-1)$$

Where N is the number of turns

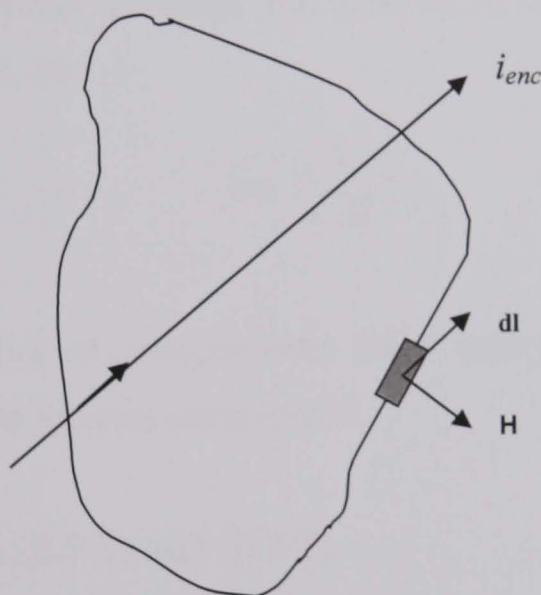


Fig. 2.2-1. Amperian loop

In the equation (2.2-1), \mathbf{H} is the field intensity (a vector field), $d\mathbf{l}$ is an incremental segment in the path (again a vector), and total i_{enc} current enclosed by that path, where the sign is determined in accordance with the curled-straight right-hand rule.

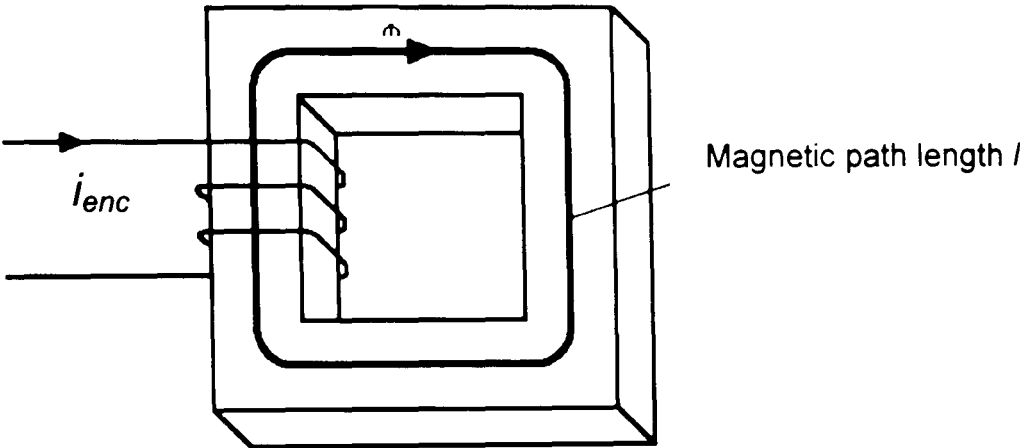


Fig. 2.2-2. Magnetic field around the core

The total enclosed current for the path is the total magneto-motive force (MMF) source F_T for the path, i.e.

$$F_T = N \cdot i_{enc} \tag{2.2-2}$$

It will often be convenient to break the total enclosed current into a number of separate components, i.e.

$$i_{enc} = \sum_{j=1}^J i_{T,j} \tag{2.2-3}$$

Where J is the number of components; each component can be viewed as a magneto- motive force source component

Combining equations (2.2-2) and (2.2-3)

$$F_T = N \cdot \sum_{j=1}^J i_{T,j} \tag{2.2-4}$$

It will be also be convenient to break the path integral in equation (2.2-1) into a number of sub line-integrals. If the path integral is broken into K segments we have

$$\sum_{k=1}^{K-1} \int_{l_k}^{l_{k+1}} \mathbf{H} \cdot d\mathbf{l} + \int_{l_K}^{l_1} \mathbf{H} \cdot d\mathbf{l} = F_T \tag{2.2-5}$$

Where at this point it is convenient to define a magneto-motive force drop as

$$F_{a,b} = \int_{l_a}^{l_b} \mathbf{H} \cdot d\mathbf{l} \quad (2.2-6)$$

Combining equations (2.2-5) and (2.2-6), we have that

$$\sum_{k=1}^{K-1} F_{k,k+1} + F_{K,1} = \sum_{j=1}^J F_{T,j} \quad (2.2-7)$$

This result is Kirchhoff's law for magnetic circuits, which may be stated as: The sum of the MMF drops around a closed loop is equal to the sum of the MMF sources for that loop.

2.3 FLUX AND KIRCHHOFF'S CURRENT LAW FOR MAGNETIC CIRCUITS

For electric circuits, Kirchhoff's current law states that the sum of the current into a node of an electric circuit is equal to zero. As it turns out, the same can be said of flux in a magnetic circuit. To see this, we must first define a node of the magnetic circuit, which will be taken to be a closed volume which is small enough that the MMF drop between any two points is negligible.

To derive Kirchhoff's current law for magnetic circuits, we begin with Gauss's Law which states that the surface integral of flux density over a closed volume is zero. In particular,

$$\oint \mathbf{B} \cdot d\mathbf{S} = 0 \quad (2.3-1)$$

Where, \mathbf{B} is flux density and $d\mathbf{S}$ is an incremental surface area in equation (2.3-1). It is convenient to break the surface integral equation (2.3-1) into M regions where S_m denotes the m^{th} region of the set. These yields,

$$\sum_{m=1}^M \int_{S_m} \mathbf{B} \cdot d\mathbf{S} = 0 \quad (2.3-2)$$

Flux is defined as the integral of the normal component of a field over a surface. Stated mathematically, the flux through surface region m may be expressed,

$$\phi_m = \int_{S_m} \mathbf{B} \cdot d\mathbf{S} \quad (2.3-3)$$

Substitution of equation (2.3-3) into equation (2.3-2) yields,

$$\sum_{m=1}^M \phi_m = 0 \quad (2.3-4)$$

This relationship establishes Kirchhoff's current law for magnetic circuits, which can be stated as: The sum of the flux leaving a node of a magnetic circuit is zero.

2.4 MATERIAL CHARACTERISTICS AND OHM'S LAW FOR MAGNETIC CIRCUITS

In both magnetic and electric circuits, Kirchhoff's laws are in fact physical laws they stem directly from Maxwell's equations. However, in electric circuits, a third commonly quoted physical law; in particular Ohm's law is not a physical law at all but is instead a property of some types of conducting materials. The same can be said of Ohm's law for magnetic circuits; it is not a physical law, merely a property that some materials possess.

The interaction of materials with magnetic fields stems from two principal effects, the first of which arises because of the magnetic moment of the electron as it moves through its shell (crudely viewed as the moment of the electron moving through an orbit), and the second effect is due to the magnetic moment that arises because of electron spin. The interaction of these two effects produces six different types of material-diamagnetic, paramagnetic, ferromagnetic, anti-ferromagnetic, ferrimagnetic, and super paramagnetic [55-56].

The diamagnetic effect is present in all materials, and has a net effect of acting against an applied magnetic field. Consider an electron moment caused by the

electron moving within its shell. An applied magnetic field will create an outward force on the electron. However, the Coulomb force on the electron is unaffected. Since the effective radius of the electron's orbit (as viewed in crude terms) is fixed by the shell, the electron must slow, thereby reducing the moment of the electron moving in its shell. Diamagnetic materials are those materials in which the diamagnetic effect dominates other mechanisms so that the material's field tends to act against the applied field. In these materials, the net magnetic moment of the material is either zero or very small. Diamagnetic materials include hydrogen, helium, copper, gold, and silicon.

Let us next consider paramagnetic materials. In these materials there is a small net magnetic moment. The moments due to electron spin do not quite cancel the moments of electrons within their shells. In this case, the moments will align with an applied field. Materials in which the tendency to aid the field overcoming the diamagnetic effect are called paramagnetic. Paramagnetic materials include oxygen and tungsten.

In ferromagnetic, anti-ferromagnetic, ferrimagnetic, and super paramagnetic materials, the individual atoms possess a strong net moment. In ferromagnetic materials the atoms possess a large net moment, and inter atomic forces are such as to cause these moments to line up over large regions called domains. In the absence of an external field, the net effect of the net moments of the domains is to cancel out; however in the presence of an external field the domain walls will move in such a way and the domains which are aligned with the applied field will grow; and also domains which are not aligned will shrink. This class of materials has a very strong interaction with external fields and are very important in engineering applications. Materials which possess this property at room temperature are iron, nickel, and cobalt [56].

Anti-ferromagnetic materials possess the properties that inter atomic forces cause the magnetic moments of adjacent atoms to be aligned in an anti-parallel fashion. The net magnetic moment of a group of atoms is therefore zero. These materials are not greatly affected by the presence of an external field.

Ferromagnetic materials are similar to anti-ferromagnetic materials in that the magnetic moments of adjacent atoms are aligned in an anti-parallel fashion; however in this case the moments between directions are unequal. These materials exhibit a significant response to an external field. While their response is, in generally, less than that of ferromagnetic materials, one class of ferrimagnetic materials (ferrites) have a conductivity which is much lower than ferromagnetic materials, making them very well suited for high-frequency applications. Examples of ferrites include iron oxide magnetite (Fe_3O_4), Nickel-Zinc-Ferrite ($\text{Ni}_2\text{Zn}_2\text{Fe}_2\text{O}_4$), and Nickel-Ferrite (NiFe_2O_4) [34].

A final class of materials which is useful in magnetic tape is super paramagnetic materials which consist of ferromagnetic materials in a non ferromagnetic matrix, which blocks domain wall movement.

For a more extensive discussion of the different types of materials, the reader is referred to [57]. However, our interest will primarily be in ferromagnetic and ferrimagnetic materials and other materials we will simply consider have the same response to a magnetic material as a vacuum. The detail discussion about the magnetic material will be present in chapter 4.

2.4.1 Linear Materials

In some magnetic materials, saturation is reached when there is an increase in applied external magnetizing. If the field H cannot increase the magnetization of the material further, the total magnetic field B levels off.

Although the relationship between flux density and field intensity can be quite complex, the relationship between flux density B and field intensity H may be expressed,

$$B = \mu H \tag{2.4-1}$$

Where μ is the permeability. In electromagnetism, permeability is the degree of magnetization of a material that responds linearly to an applied magnetic field.

Let us now consider a segment of material of length l and cross sectional area A in which the \mathbf{B} and \mathbf{H} fields are uniform and directed in the same direction. Since the direction of the field has been defined, we can treat both B and H as scalar variables where upon equation (2.4-1) reduces to,

$$B = \mu H \quad (2.4-2)$$

In this segment of material, noting that the field is uniform, from equation (2.2-6) we have that,

$$F_{a,b} = lH \quad (2.4-3)$$

Solving for the field intensity,

$$H = \frac{F_{a,b}}{l} \quad (2.4-4)$$

Combining equation (2.4-2) with equation (2.4-4),

$$B = \frac{\mu}{l} F_{a,b} \quad (2.4-5)$$

Again noting that the field and flux density are uniform, the flux from node a to node b may be expressed,

$$\phi_a = \frac{A\mu}{l} F_{a,b} \quad (1.3-6)$$

This can also be written as;

$$\phi_a = P_{a,b} F_{a,b} \quad (2.4-7)$$

Where the permeance $P_{a,b}$ defined as,

$$P_{a,b} = \frac{A\mu}{l} \quad (2.4-8)$$

Dividing equation (2.4-7) by the permeance yields Ohm's law for the magnetic circuits,

$$F_{a,b} = R_{a,b} \phi_a \quad (2.4-9)$$

Where $R_{a,b}$ is the reluctance from node a to node b. From equation (2.4-7) and equation (2.4-9) this reluctance is given by [35],

$$R_{a,b} = \frac{l}{A\mu} \quad (2.4-10)$$

2.5 TRANSLATION OF MAGNETIC CIRCUITS TO ELECTRIC CIRCUITS

The magnetic equivalent circuit is a tool that we can use to relate flux Φ to a MMF source Ni . Often, however, it is our desire to develop an electrical circuit model that will represent an electromechanical device. In this section, we will consider the relationship between the magnetic equivalent circuit and the electric equivalent circuit.

2.5.1 Flux Linkage

The basic concept of flux as the integral of flux density over a finite surface was set forth in equation (2.3-3). The concept of flux linkage is closely related to the concept of flux. In particular, let us assume that a winding is wound around the periphery of a surface 'x', and that the flux linking of this surface in the winding is denoted λ_x and is related to the flux by,

$$\lambda_x = N_x \phi_x \quad (2.5-1)$$

N_x is number of turns in the system. It should be observed that for this to be true the direction of the winding, that is the defined direction for positive current, must be counter clockwise around the surface as viewed from a vantage wherein the defined direction of positive flux is toward the observer [26]. Alternately, stated in terms of the 'right hand rule,' if the fingers of one's right hand wrap around the periphery of a surface in the defined direction for positive current, then one's right thumb (extended away from one's hand) will be pointing in the defined direction for positive flux. If this convention is not followed, then a '-' sign is introduced into equation (2.5-1).

2.5.2 Inductance

Let us consider a single winding in a system. Neglecting hysteresis, the relationship between flux linkage through winding and the current into winding is depicted in Fig. 2.5-1. We will use this Fig. 2.5-1 to introduce the concept of inductance.

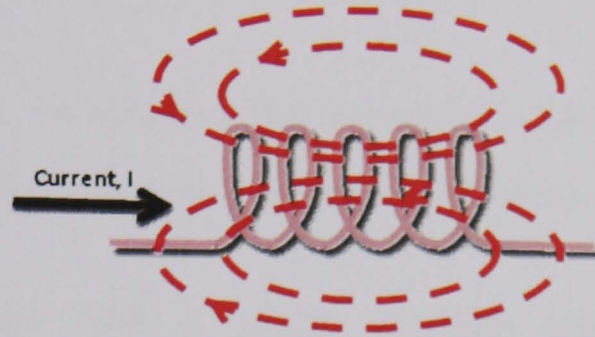


Fig. 2.5-1. Flux linkage

The absolute inductance at an operating point i_{x1}, λ_{x1} is defined as,

$$L_{abs,x} = \left. \frac{\lambda_x}{i_x} \right|_{i_{x1}, \lambda_{x1}} \quad (2.5-2)$$

Also of interest is the incremental inductance, which is defined as the slope of the flux linkage versus current characteristic at a given operating point. In particular,

$$L_{inc,x} = \left. \frac{\partial \lambda_x}{\partial i_x} \right|_{i_{x1}, \lambda_{x1}} \quad (2.5-3)$$

Several observations are in order. First, the incremental inductance is generally lower than the absolute inductance. Secondly, in a magnetically linear system, the absolute and incremental inductances are the same.

In order to understand how inductance is related to our EMC, the Fig. 2.5-1 is connected to MMF. Therein flux in winding would be proportional to the

MMF as,

$$\phi_x = \frac{N_x i_x}{R_x} \quad (2.5-4)$$

From equation (2.5-1),

$$\lambda_x = \frac{N_x^2 i_x}{R_x} \quad (2.5-5)$$

We can obtain the following equation,

$$\frac{\lambda_x}{i_x} = L_x = \frac{N_x^2}{R_x} \quad (2.5-6)$$

The flux in winding ϕ_x is constant, the system is magnetically linear and there is no reason to distinguish between absolute and incremental inductance.

In a magnetic system with a single winding, the inductance is a self inductance. In other words, the inductance relates how much flux links a winding due to the amount of current in that winding. In systems with multiple windings, self inductance is still of interest. However, in addition, there is also the concept of mutual inductance which relates how much flux will appear in a given winding to a current in a different winding.

Let us consider a system with several windings. In linear magnetic systems, or when discussing incremental inductance, the mutual inductance $L_{x,y}$ between winding 'x' and winding 'y' describes how much the flux linking winding 'x' changes due to a change in the current in winding 'y'. In particular,

$$L_{x,y} = \frac{\partial \lambda_x}{\partial i_y} \quad (2.5-7)$$

Ordinarily, the concept of absolute self and mutual inductances is not terribly useful in multi-winding nonlinear magnetic systems. Instead, it is more common to define flux linkages in terms of a leakage component and magnetizing component; and then relates the magnetizing flux to a magnetizing current in a way where it can essentially be treated as a single-winding problem.

2.5.3 Faraday's Law

Consider a winding 'x' on an electromechanical device. Denoting the voltage across the winding as v_x , Faraday's law states the voltage across the winding is equal to the time rate of change of the flux linkages.

If we allow for an Ohmic drop $r_x i_x$ where r_x is the resistance of the winding, we thus have the following equation.

$$v_x = r_x i_x + \frac{d\lambda_x}{dt} \quad (2.5-8)$$

Equation (2.5-8) is extremely important; it will form the basic voltage equation for nearly every device considered throughout this work.

Before concluding this section, let us briefly return to the system shown in Fig. 2.5-1 from equation (2.5-6), we have that,

$$\lambda_x = L_x i_x \quad (2.5-9)$$

Substitution of equation (2.5-9) into equation (2.5-8) yields,

$$v_x = r_x i_x + L_x \frac{di_x}{dt} \quad (2.5-10)$$

Note that this simple form is only possible if L_x is constant; otherwise there will be additional terms. Before concluding this discussion, let us briefly consider the energy stored in an inductor. The electrical power flowing into the winding is given by,

$$P_x = v_x i_x \quad (2.5-11)$$

Upon ignoring losses (i.e. setting $r_x = 0$), equations (2.5-10) and (2.5-11),

$$P_x = L_x i_x \frac{di_x}{dt} \quad (2.5-12)$$

Let us suppose that at time $t = 0$ the inductor current, and stored energy, are zero. Let us further suppose that at time $t = t_1$, the inductor current is $i_x = i_{x1}$.

The energy flowing into the inductor (and hence stored in the inductor) may be expressed,

$$E_x = \int_{t=0}^{t_1} P_x dt \quad (2.5-13)$$

Substituting of equation (2.5-12) into equation (2.5-13) yields,

$$E_x = \int_0^{i_{x1}} L_x i_x di_x \quad (2.5-14)$$

This reduces to,

$$E_x = \frac{1}{2} L_x i_{x1}^2 \quad (2.5-15)$$

Since this expression is valid for any value of familiar expression i_{x1} , we may more simply write the familiar expression,

$$E_x = \frac{1}{2} L_x i_x^2 \quad (2.5-16)$$

This well known result will prove valuable in the next chapter when we wish to defined the coupled equations.

2.6 THE CONSTRUCTION OF MAGNETIC EQUIVALENT CIRCUIT

A mathematical model may be defined as a set of equations relating the input and output variables of a device in terms of the characteristics of the components and the manner of interconnection. The adequacy of a mathematical model depends on its ability to predict the behaviour and performance characteristics with the desired degree of accuracy. There are various other factors that also determine the usefulness and applicability of a mathematical model for any engineering application in the analysis or design of a system, a device or an element. The most important ones are:

- (1) Complexity – Complex mathematical models are difficult to implement. They are also costly and generally time consuming.
- (2) Flexibility – The models should be sufficiently flexible to be used efficiently to generate a design or to improve the existing differing designs.

Until very recently the design of magnetic circuits remained an "obscure art", requiring a vast experience on part of the designer, and the use of extensive prototyping during the development stage. This approach to magnetic circuit design was poor in terms of time and cost effectiveness, due to the inherent "trial and error" procedure involved in the approach.

Two main factors have however changed this state of affairs, namely the increasing power and availability of fast digital computers and the application of numerical techniques to the solution of the magnetic circuit problem. The end result is the practical feasibility of the development of highly efficient mathematical models in the form of computer orientated algorithms, suitable for interactive design.

In this section a review of the different modelling techniques available is presented. A systematic modelling technique based on a flux path reluctance approach is proposed for the development of fast algorithms and for the design of axis-symmetrical magnetic circuits.

We translate a geometrical description of C-core and E-core actuators into magnetic equivalent circuits. The analysis presented herein is crude it is certainly not sufficiently accurate to perform a design. However, it will be useful in illustrating the procedure for obtaining the magnetic equivalent circuit. It will also be useful in the next section wherein the translation of magnetic circuits to electric circuits is considered. Of course, the ultimate goal of this analysis is to provide an analysis which is sufficiently accurate to facilitate design.

Analogous to electrical circuit analysis, the approach models the iron elements as essentially for the magnetic fields are established by the actuator coils. As such, the analysis tends to miss some effects – especially that part of the magnetic field which lies outside of the iron of the actuator. It also assumes field uniformity within large elements of the actuator. By making the assumptions that give rise to these errors, the analysis becomes very simple and quick, making it suitable for analytic evaluation and rapid design iteration.

In the end, predictions made with a magnetic circuit analysis should be checked using a more detailed approach like finite element analysis. Such tools are more cumbersome to use, but allow examination in detail of issues in the design of the actuator which cannot be revealed by the circuit analysis. Finite element analysis can also accurately account for the magnetic field which lies outside of the iron and thereby properly account for its effect on the actuator forces and electrical properties.

2.6.1 Electric Circuit Equivalent of Magnetic Circuit of C-core Actuators

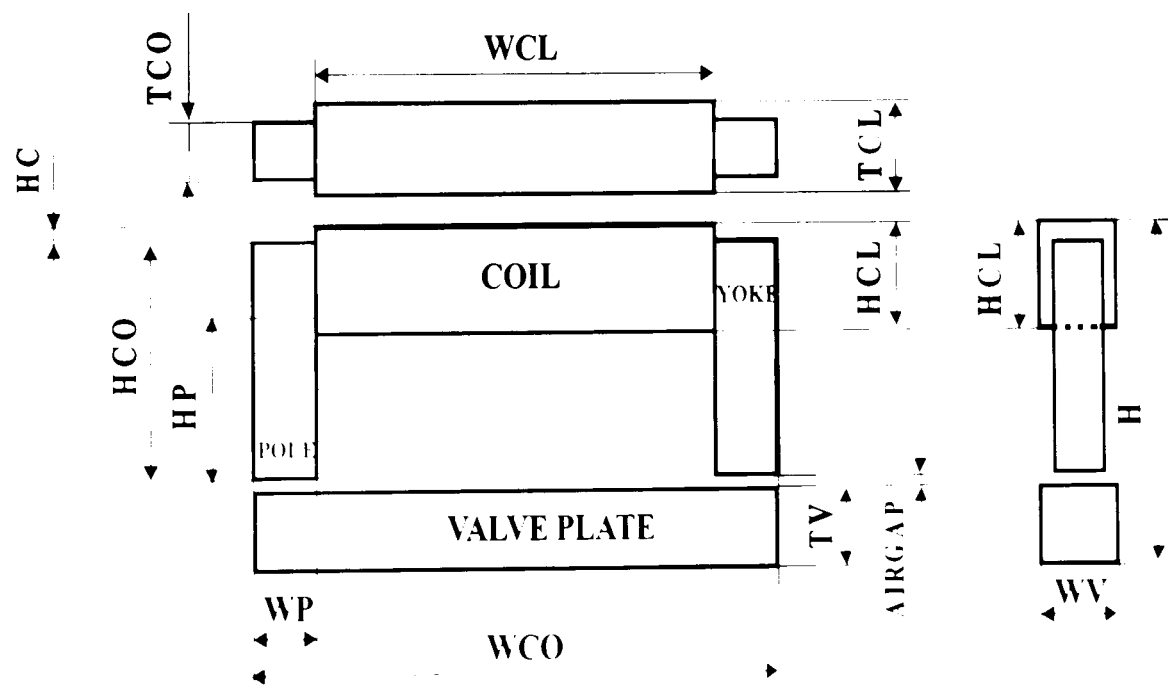


Fig. 2.6-1. C-core actuator

The common type of the C-core electromagnetic actuator has a coil wound around the yoke as shown in the Fig. 2.6-1. It consists of a ‘C’ and ‘I’ shaped pieces of ferromagnetic material separated by an air gap. All dimensions are

indicated in the Fig. 2.6-1; note that the core extends to a depth TCO into the page.

2.6.2 Selection of Nodes

The first step in the analysis is to select node locations for the magnetic equivalent circuit. In doing this, it is important to realize that there is no unique choice. In essence, the role of the nodes is to break the circuit into regions which may be treated as a simple reluctance; either linear or nonlinear. These nodes should have the property that there is negligible (preferably zero) MMF drop across them, because they will be treated as equipotential points in the equivalent circuits. In general, there is a trade-off between accuracy and the number of nodes. Another factor in selecting nodes is that they usually mark the endpoints of regions that can be treated by simple, lumped, magnetic circuit elements.

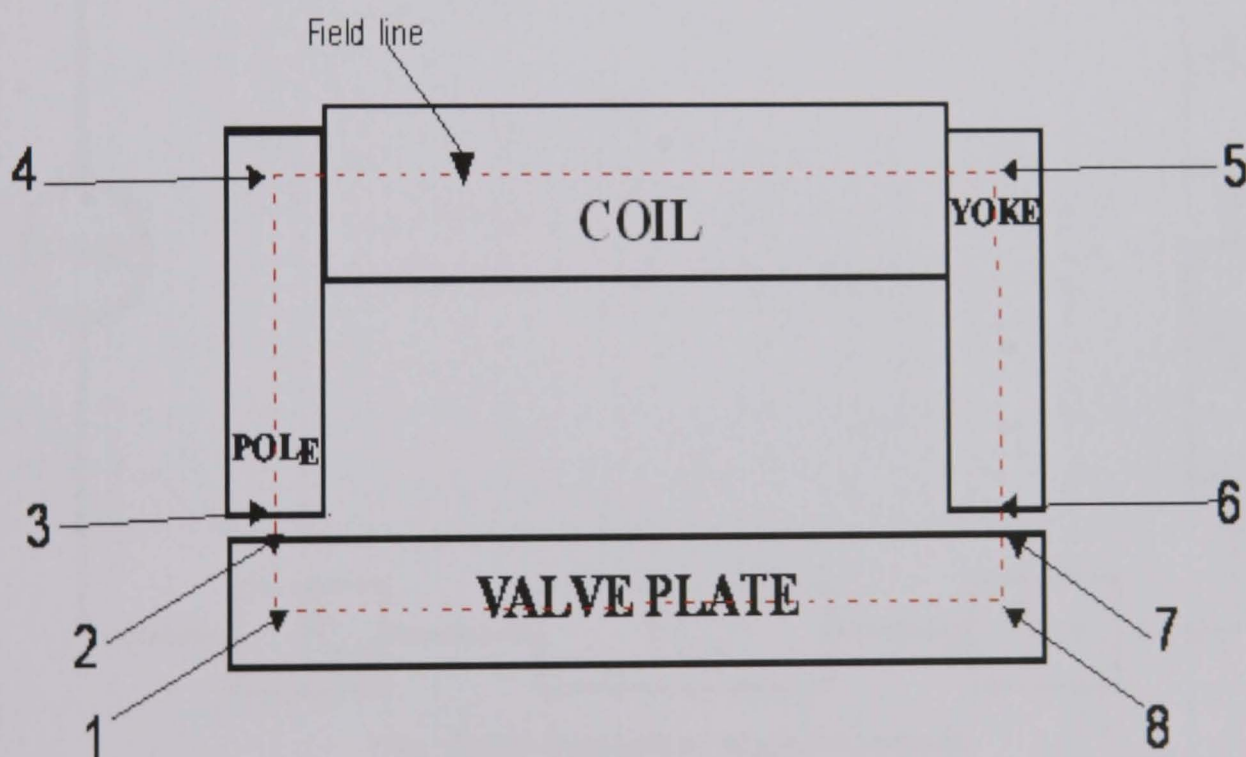


Fig. 2.6-2. C-core nodes

One possible selection of nodes is illustrated in Fig. 2.6-2. Therein, the nodes are number 1 to 8. The flux enters in one direction, and is assumed to make a right angle turn into another direction. Since flux does not make right angle turns, it is somewhat surprising that this technique will yield acceptable results.

2.6.3 The Mean Path Approximation

The next step in developing the magnetic equivalent circuit is to connect the nodes with circuit elements representing the reluctance between nodes, and to represent the MMF sources. In connecting these nodes, we will often estimate the reluctance between nodes by representing the distance between nodes as a rectangular section of material (such as in Fig. 2.6-2) wherein the length of the rectangular section is given by the mean distance between nodes.

This procedure is known as the mean path approximation, and results in the equivalent circuit shown in Fig. 2.6-3.

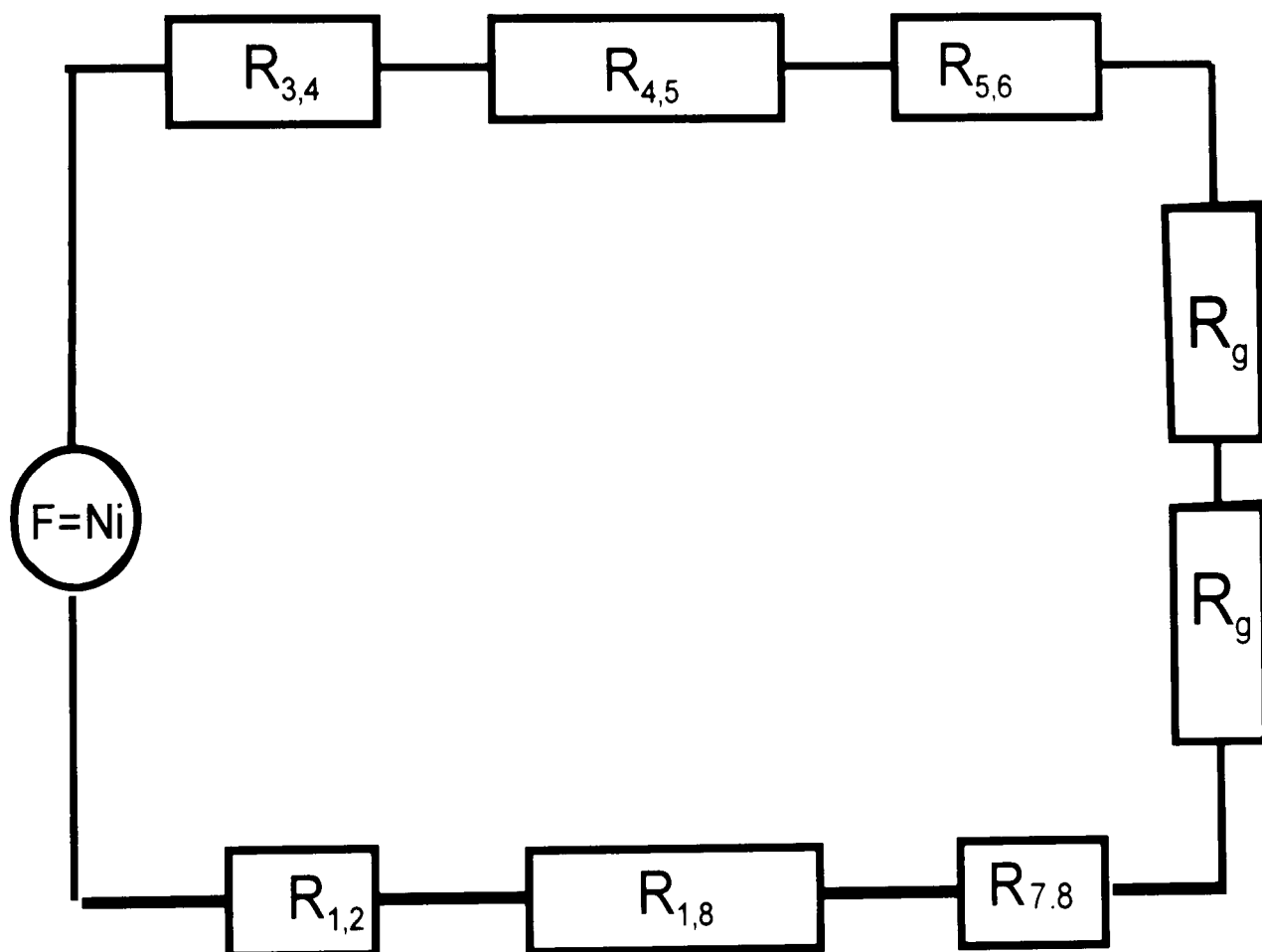


Fig. 2.6-3. Equivalent magnetic circuit

Therein, the reluctance has been expressed as functions of the flux going through them, and so the permeability function has been taken to be a function of flux density. From geometrical constraints, we have that,

$$R_{3,4} = R_{5,6} = \frac{HCO - (HCO - HP) \cdot 2}{\mu_M \times A_p} \quad (2.6-1)$$

We can calculate the value of A_p as,

$$A_p = WP \times TCO \quad (2.6-2)$$

$$R_{3,4} = R_{5,6} = \frac{(HCO + HP)/2}{\mu_M \times (WP \times TCO)} \quad (2.6-3)$$

$$R_{4,5} = \frac{(WCO - WP)}{\mu_M \times (HCO - HP) \times TCO} \quad (2.6-4)$$

$$R_{6,7} = R_{3,2} = \frac{\delta}{\mu_0 (WP \times TCO)} \quad (2.6-5)$$

$$R_{7,8} = R_{2,1} = \frac{TV_l^2}{\mu_M (WT \times TV)} \quad (2.6-7)$$

$$R_{1,8} = \frac{WCO - WP}{\mu_M (WT \times TV)} \quad (2.6-8)$$

At this point, the nodes and majority of the circuit elements values associated with the C-core example have been discussed. However, one important point remains, that is the MMF source in Fig. 2.6-3. Treatment of the MMF sources will be considered in the following section.

2.6.4 MMF Sources

From Kirchhoff's MMF law, the sum of the MMF drops around a closed loop is equal to the sum of the MMF sources for that loop. Thus, traversing the nodes in the order 1, 2... 7, 8, 1 in Fig. 2.6-3, the sum of the voltage drops must be equal to the enclosed current which, by the right-hand rule, is Ni . Placing the current source as shown, we see that this requirement is satisfied, i.e.

$$Ni = (R_{3,4} + R_{4,5} + R_{5,6} + R_{6,7} + R_{3,2} + R_{7,8} + R_{1,8} + R_{1,2})\phi \quad (2.6-9)$$

The placement in this example, and in many examples, is highly arbitrary since the MMF source could have been placed between any two nodes and (equation (2.6-9)) would be satisfied. However, some restrictions do apply. These arise because the MMF sources must satisfy Kirchhoff's MMF law for all current loops. If we traversed the loop in the opposite direction, i. e. 8, 7... 2, 1 then the enclosed current would have been $-Ni$.

2.6.5 Voltage Equation and Winding Resistance of C-core Actuators

Although the prediction of the $\lambda - i$ characteristic is critical to the electrical model, we must also consider the voltage equation which involves a winding resistance. From equation (2.5-8), the voltage equation for our system will be [59],

$$v = ri + \frac{d\lambda}{dt}$$

However, we do not know the resistance. To calculate the resistance we can use the following method.

The cross-sectional area of the conductor (single turn) must be equal to:

$$A_c = \frac{\pi d_c^2}{4} \quad (2.6-10)$$

Cross Sectional area of the coil window:

$$A = HC \times WCL \quad (2.6-11)$$

Effective cross-sectional area of the coil window:

$$A_e = A \times P_f \quad (2.6-12)$$

Number of turns in the coil:

$$N = \frac{A_e}{A_c} \quad (2.6-13)$$

Length of one turn:

$$l_t = 2(l_1 + l_2) \quad (2.6-14)$$

Where,

$$l_1 = HCO - HP + HC \quad (2.6-15)$$

$$l_2 = \frac{1}{2}(TCL + TCO) \quad (2.6-16)$$

Total length of the coil:

$$l_{\Sigma} = N \times l_t \quad (2.6-17)$$

Resistance of the coil:

$$R = \frac{\rho_r l_{\Sigma}}{A_c} \quad (2.6-18)$$

At this point, we know how to calculate the resistance of the coil. The methods of calculation of the field quantities by using simpler methods of assuming the probable flux paths of various magnetic circuits and evaluating the reluctance of these paths has been used here for the analysis and design of magnetic circuits for actuators.

The main sources of errors in this type of model can be listed as follows

- (a) Assumption of the flux path.
- (b) Nonlinearity of magnetic materials used for the magnetic circuit.
- (c) Non-uniformity of magnetic flux distribution in the iron.
- (d) Variation in the shape of flux lines in the actuator with the displacement of the valve plate.
- (e) Calculation of reluctance for the equivalent section by assuming its mean length flux path.

For better accuracy in these types of model needs to take the assumption with sufficient care and best justification.

2.7 MAGNETIC EQUIVALENT CIRCUIT OF E-CORE ACTUATORS

Most electromagnetic applications required a lamination pattern (or patterns) that would form a closed magnetic loop when assembled together. These patterns included rings for toroids, "L" shapes, "U" shapes, "E" shapes and "I" shapes (used with the "E" and the "U"). Patterns were sought that were easy to

assemble, could be interleaved to minimize gap effects, and would minimize waste. “E” shapes used in “E-E” and “E-I” combinations became popular choices. For our industrial partners (Sortex Ltd) specification and needs the “E-I” pattern are also suitable.

In the typical E-core, the center leg (one of three legs) is twice the width of either outer leg. In theory, magnetic flux flowing out of the center leg divides equally and flows into the outer two “E” core legs. Since the outer legs handle half the flux they only need to have half the cross-section that the center leg has. An “E” core structure occupies two coils. In the E-core the winding window area became two and the windings to be placed across the yoke. Also placing the coils in the yoke, which allows the ease of winding.

In contrast, C-core structure (which has two legs) only occupies one coil placed over its yoke. Since “E” cores have two open coil sides, they provide substantial room to bring high current lead wires out from the coil. E-core also permits good heat dissipation.

In this section, we will consider the detailed analysis of an E-core actuator using magnetic equivalent circuit modelling. The detailed investigation can be started with geometrical description of the core and its material properties and end with an electrical description in terms of the $\lambda - i$ characteristic of the device. The Fig. 2.7-1 shows the geometry of an E-core actuator.

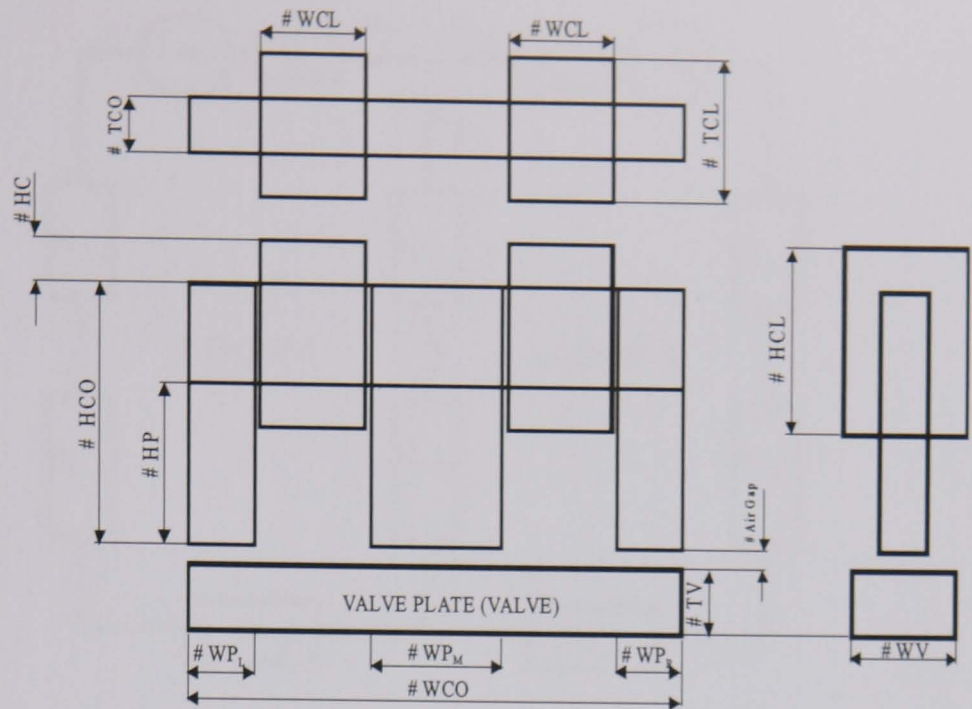


Fig. 2.7-1. E-core actuator

As we discussed earlier in this chapter we defined the possible selection of nodes as illustrated in Fig. 2.7-2.

2.7.1 Nodes Selection and Equivalent Circuit

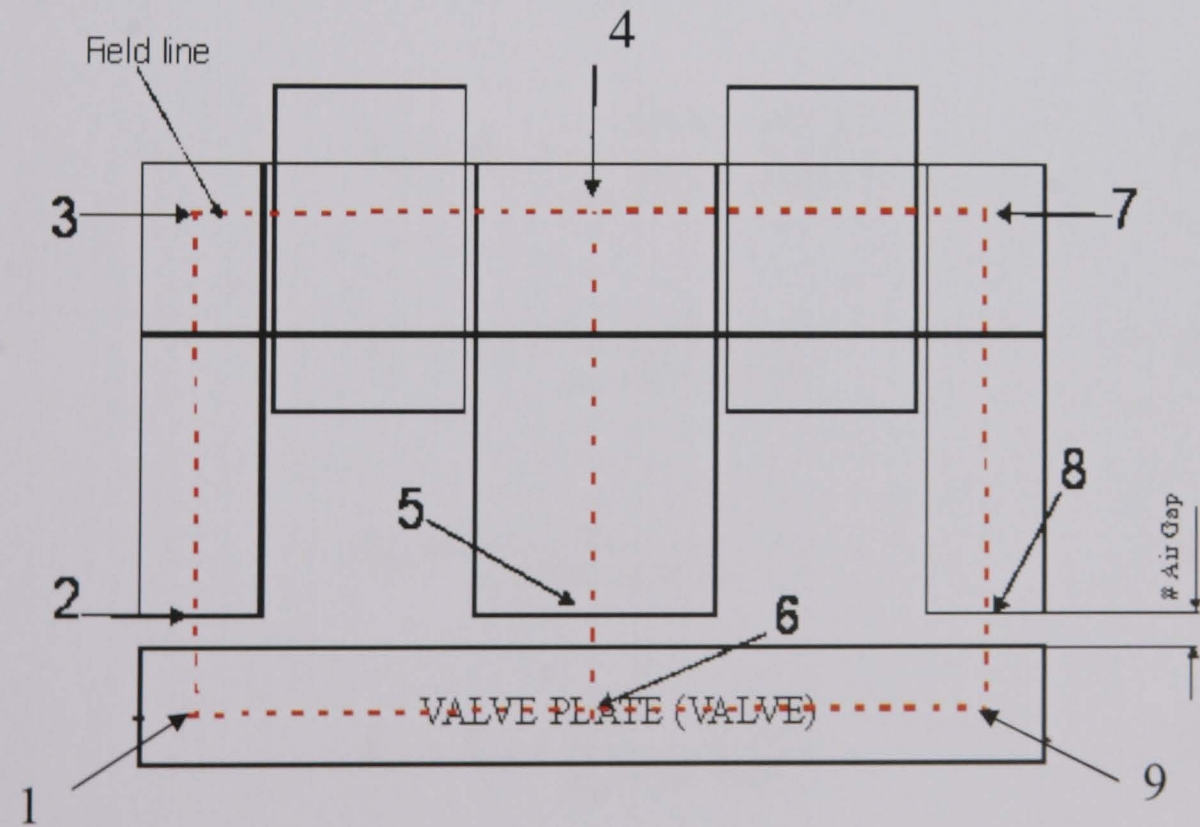


Fig. 2.7-2. E-core nodes

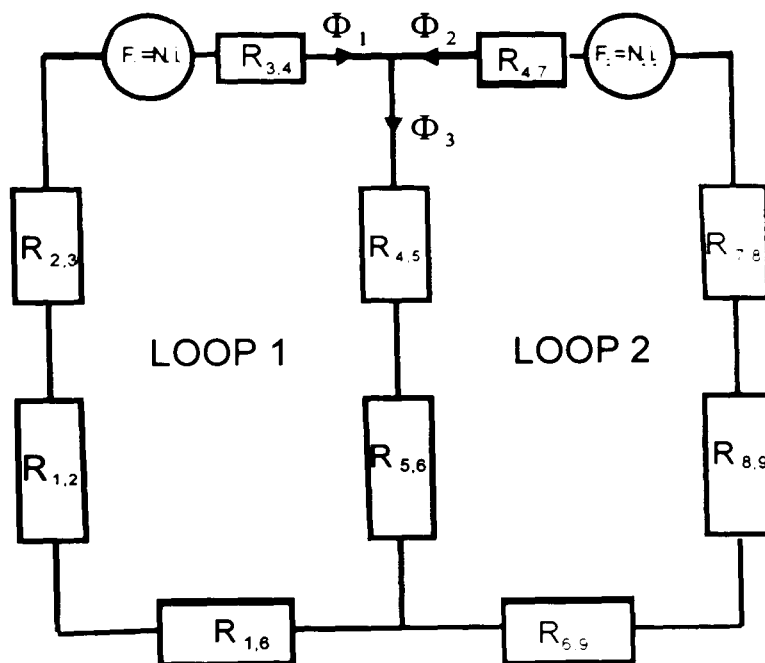


Fig. 2.7-3. E-core equivalent magnetic circuit

$$R_{2,3} = R_{7,8} = \frac{(HCO + HP) 2}{\mu_M \times WP_L \times TCO} \quad (2.7-1)$$

$$R_{4,5} = \frac{(HCO + HP)/2}{\mu_M \times WP_M \times TCO} \quad (2.7-2)$$

$$R_{3,4} = R_{4,7} = \frac{(WCO - WP_L) 2}{\mu_M (HCO - HP) \times TCO} \quad (2.7-3)$$

$$R_{1,2} = R_{8,9} = \frac{\delta}{\mu_0 \times WP \times TCO} \quad (2.7-4)$$

$$R_{5,6} = \frac{\delta}{\mu_0 \times WP_M \times TCO} \quad (2.7-5)$$

$$R_{1,6} = R_{6,9} = \frac{(WCO - WP) 2}{\mu_M \times TV \times WV} \quad (2.7-6)$$

Where, $WP = WP_L = WP_R$

From Kirchhoff's MMF law, the sum of the MMF drops around a closed loop is equal to the sum of the MMF sources for that loop.

Using Kirchhoff's MMF law, for loop 1 in clock wise direction gives

$$N_1 i_1 = \phi_1 R_{3,4} + \phi_3 (R_{4,5} + R_{5,6}) + \phi_1 (R_{1,6} + R_{1,2} + R_{2,3}) \quad (2.7-7)$$

Using Kirchhoff's MMF law, in loop 2 in anti-clock wise gives

$$N_2 i_2 = \phi_2 R_{4,7} + \phi_3 (R_{4,5} + R_{5,6}) + \phi_2 (R_{6,9} + R_{8,9} + R_{7,8}) \quad (2.7-8)$$

But we know,

$$\phi_3 = \phi_1 + \phi_2 \quad (2.7-9)$$

We have three unknowns, also we have three equations. From these equations we can calculate the ϕ_1, ϕ_2, ϕ_3 .

2.8 FORCE IN AN ELECTROMAGNETIC ACTUATOR

The force equation governing a magnetic actuator can be derived completely from the first principles. Magnetic circuit theory is employed to develop the basic equations that are extended to describe the magnetic actuator. A device of simple geometry is assumed so as to keep the equations of reasonable length. The device is a simple C-I core actuator of material that has a rectangular cross-section, A , as shown in Fig. 2.8-1.

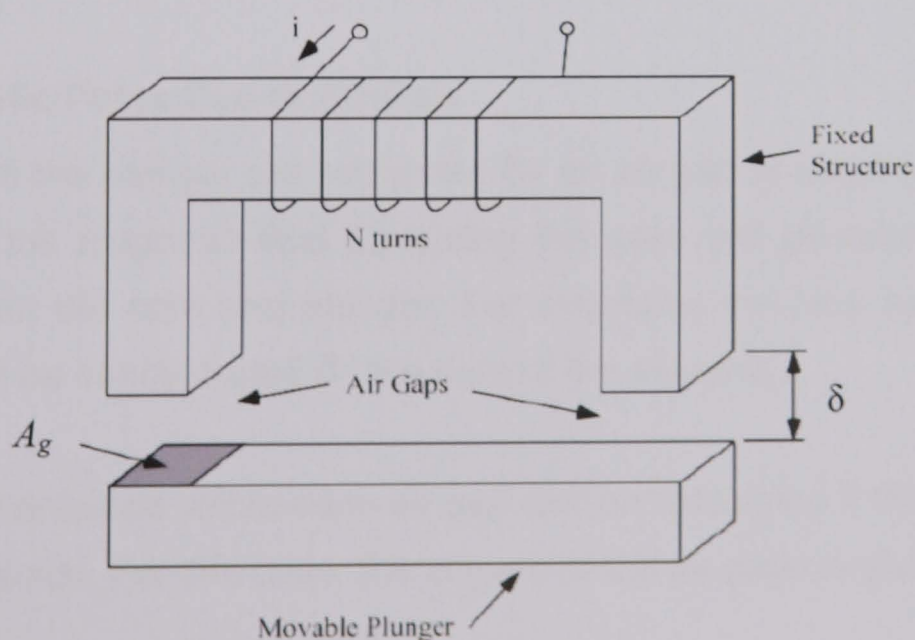


Fig. 2.8-1. Illustration of an actuator

If copper wire of length l is wrapped with N turns that carry a current, I , equation (2.8-1) governs the magnetic field strength, H , that is generated.

$$H = \frac{Ni}{l} \quad (2.8-1)$$

This simple relationship is valid because the magnetic field and cross-sectional area are uniform. If they were not, an integral relationship would have to be solved to find the proper relationship. The relationship between magnetic field strength, H , and flux density, B , is given by equation (2.4-2):

$$B = \mu H = \frac{\mu Ni}{l}$$

The magnetic flux, ϕ , in the circuit is given by [47], [51],

$$\phi = \iint B \cdot d\mathbf{a} = B \cdot A \quad (2.8-2)$$

If the area of the magnetic circuit is constant, the energy density, w , contained in the system of volume V_w is given by [47],

$$w = \frac{W}{V_w} = \int_0^B H dB = \int_0^B H \mu dH = \frac{\mu H^2}{2} \quad (2.8-3)$$

Where, W , is the total energy.

2.8.1 Magnetic Force Due to Air Gap

The core and the plunger are separated by an air gap of length δ as shown in Fig. 2.8-1, the magnetic field traversing the gaps will generate an attractive force between the core and plunger. For simplicity, the total number of Amp-turns, NI , will be concentrated on the core of the assembly.

The energy contained within each air gap can be calculated if the volume of the air gaps is known. For this case, the volume of the air gaps is given by,

$$v_g = A_g \cdot \delta \quad (2.8-4)$$

and the energy within it is defined as,

$$W_g = \frac{\mu H^2 v_g}{2} = \frac{\mu H^2 A_g \delta}{2} \quad (2.8-5)$$

If the core and plunger are pulled apart by an incremental amount, Δx , the energy required is ΔW , and given by equation (2.8-6) if the flux is assumed to be held constant. This incremental work is the difference between the two energy states.

The factor of two in the equation is because there are two air gaps in the magnetic circuit, and each is increased by Δx .

$$\Delta W = 2 \left(\frac{\mu H^2 A_g (\delta + \Delta x)}{2} - \frac{\mu H^2 A_g \delta}{2} \right) = \mu H^2 A \Delta x \quad (2.8-6)$$

The magnetic force required to move an object over a distance x is defined as the energy expended in the move divided by the distance of the move.

By substituting the known quantities into this relationship, equation (2.8-7) is found.

$$F = \left. \frac{-\partial W}{\partial x} \right|_{\phi=\text{const}} \approx \frac{-\Delta W}{\Delta x} = \frac{-\mu H^2 A \Delta x}{\Delta x} = -\mu H^2 A \quad (2.8-7)$$

If equations (2.4-2) and (2.8-2) are substituted into the above relationship, the magnetic force can be expressed in terms of different quantities. The negative sign can be dropped since only the magnitude of the force is of interest.

$$F = \mu H^2 A = \frac{B^2 A}{\mu} \quad (2.8-8)$$

But we know,

$$\phi = B.A$$

$$F = \frac{\phi^2}{\mu A} = \frac{\mu A (Ni)^2}{l^2} \quad (2.8-9)$$

In the above equation, l is the total length of the magnetic circuit. These expressions give the exact force between the core and plunger assembly if the exact values of the parameters are known. The difficult parameter to define is μ , since it is the permeability of the entire magnetic path, which includes the magnetic material and air in the gaps. However, a simplification can be made that will allow the magnetic force to be expressed in terms of the air gap length only and eliminate this complication.

2.8.2 Simplification of the Force Equation

The path of the magnetic flux through the system assembly can be separated into four separate sections. Section 1 is the core of the system, section 2 is one air gap, section 3 is the plunger of the system, and section 4 is the second air gap. The definition of magneto-motive force is given by equation (2.8-10). If the closed loop integral is broken into the four segments described above, it can be rewritten as equation (2.8-11) [section 2.6.4],

$$MMF = Ni = \oint H dl \quad (2.8-10)$$

$$NI = \int_1 H_1 dl_1 + \int_2 H_2 dl_2 + \int_3 H_3 dl_3 + \int_4 H_4 dl_4 \quad (2.8-11)$$

If the magnetic field strength is assumed constant across each section of the magnetic circuit, this equation can be rewritten as:

$$NI = H_1 l_1 + H_2 l_2 + H_3 l_3 + H_4 l_4 \quad (2.8-12)$$

The magnetic field strength, H , can be expressed in terms of flux density, B , according to equation (2.4-2). If the actual permeability in this equation is replaced with relative permeability as defined in equation (2.8-13), then equation (2.8-12) can be expressed as equation (2.8-14).

$$H = \frac{B}{\mu}$$

$$\mu = \mu_0 \mu_r \quad (2.8-13)$$

$$NI = \frac{B_1 l_1}{\mu_0 \mu_1} + \frac{B_2 l_2}{\mu_0 \mu_2} + \frac{B_3 l_3}{\mu_0 \mu_3} + \frac{B_4 l_4}{\mu_0 \mu_4} \quad (2.8-14)$$

The relative permeability of a ferromagnetic material and air are drastically different. Most magnetic materials have a relative permeability on the order of 3000, where air is very close to unity. Because of the large difference in these values, the terms where the flux is travelling through magnetic material (section 1 (core) and section 3 (valve plate)) can be neglected, and only the air gaps can be considered. If the lengths of the air gaps and the flux density in them are assumed equal, then equation (2.8-14) becomes,

$$Ni = \frac{2B_g \delta}{\mu_0} \quad (2.8-15)$$

Where δ is the length of the air gaps and μ_0 is the magnetic permeability of vacuum, rearranging this equation to define the flux density B , and substituting into equation (2.8-8) gives the relationship governing the magnetic force between core and plunger of the system in terms of the Amp-turns of the circuit, the pole-face area, and the air gap width.

$$F = \frac{\mu_0 A (Ni)^2}{4\delta^2} \quad (2.8-16)$$

Equation (2.8-16) shows the force equation for a magnetic actuator when using current measurements. In addition to a current measurement, an accurate measurement of the air gap is required. The air gap measurement typically being very small and being squared in the denominator of equation (2.8-16) means that small position measurement errors that can lead to large force errors.

Using equation (2.8-9) only, the magnetic flux measurement and the pole face area are required to predict the actuator force. Another benefit is that by measuring the flux directly, non-linearity such as saturation (in magnetic material) can be avoided.

2.9 SUMMARY

In order to model and design real device, it is very often necessary to understand the basic field problems. In this chapter we analysed some practical problems. For these problems analytical solution have been obtained with the help of simplifying assumptions. We can use these analytical solutions to compare the linear numerical modelling results. This will establish confidence in the modelling methodologies and in the 2D FE models methodologies for further simulation studies.

Chapter 3

ELECTROMAGNETICALLY AND THERMALLY COUPLED FIELD ANALYSIS

3.1 INTRODUCTION

Modern applications use faster acting and low energy actuators which are manufactured in high quantities. Most of them are electromagnetic actuators that are applied up to the limits of their capacity.

The analysis of dynamical behaviours presents a great importance in the design and control of electro mechanical systems. It consists of finding the electric current and mechanical motion responses of the system for a given electric voltage or mechanical force excitation. This study requires a solution of the electric circuit equation, the magnetic field equation and the mechanical motion equation [60-69]. In addition to these matters we considered the electromagnetic heating effects also [70-77].

For energy conversion between electrical and mechanical forms, electromechanical devices are developed. In general, electromechanical energy conversion devices can be divided into three categories:

- (1) Transducers (for measurement and control) these devices transform the signals of different forms. Examples are microphones, pickups, and speakers.
- (2) Force producing devices (linear motion devices) These type of devices produce forces mostly for linear motion drives, such as relays, solenoids (linear actuators), and electromagnets.
- (3) Continuous energy conversion equipment these devices operate in rotating mode. A device would be known as a generator if it converts

mechanical energy into electrical energy, or as a motor if it does the other way around (from electrical to mechanical).

Since the permeability of ferromagnetic materials is much larger than the permittivity of dielectric materials, it is more advantageous to use magnetic field as the medium for electromechanical energy conversion. As illustrated in the following diagram, an electromechanical system consists of an electrical subsystem (electric circuits such as windings), a magnetic subsystem (magnetic field in the magnetic cores and air gaps), and a mechanical subsystem (mechanically movable parts such as a plunger in a linear actuator and a rotor in a rotating electrical machine). Voltages and currents are used to describe the state of the electrical subsystem and they are governed by the basic circuit laws: Ohm's law, Kirchhoff's current law and Kirchhoff's voltage law [47-52].

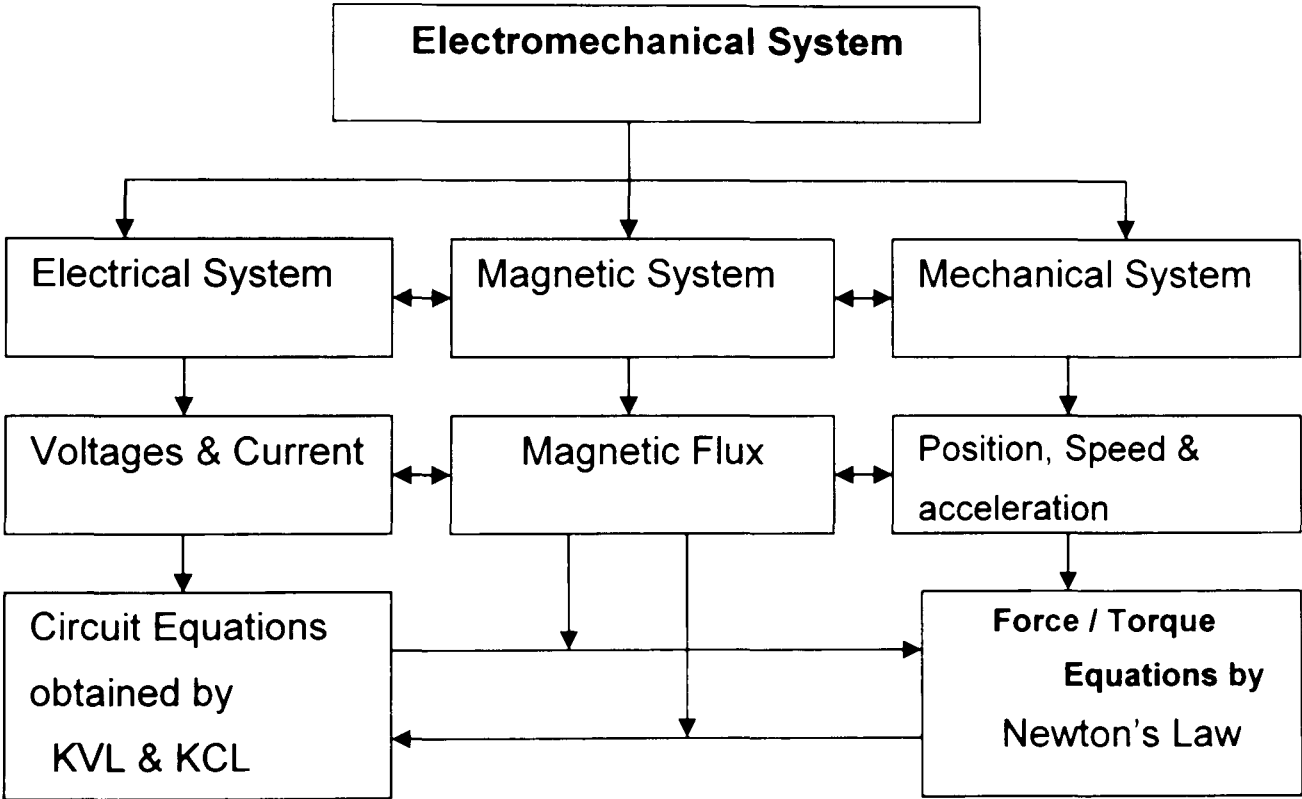


Fig. 3.1-1. Concept map of electromechanical system modelling

The state of the mechanical subsystem can be described in terms of positions, velocities, and accelerations, and is governed by Newton's laws. The magnetic subsystem or magnetic field fits between the electrical and mechanical subsystems and acts as a "ferry" in energy transform and conversion. The field quantities such as magnetic flux, flux density, and field strength, are governed

by Maxwell's equations. When coupled with an electric circuit, the magnetic flux interacting with the current in the circuit would produce a force or torque on a mechanically movable part. On the other hand, the movement of the moving part could change the magnetic flux linking and induces an electromotive force (emf) in the circuit. The product of the torque and speed (the mechanical power) equal the product of the emf and current. Therefore, the electrical energy and the mechanical energy are inter-converted via the magnetic field [41], [60], [67].

3.2 ELECTROMECHANICAL MODEL OF A SOLENOID ACTUATOR

The calculation method is coupled with a magnetic circuit, an electric circuit and motion analysis using finite element method.

Analyzing the subsystems respectively, we got the relationships between them. In order to achieve fast response, it is necessary to find the limitations of performance, and to do this numerical analysis is required.

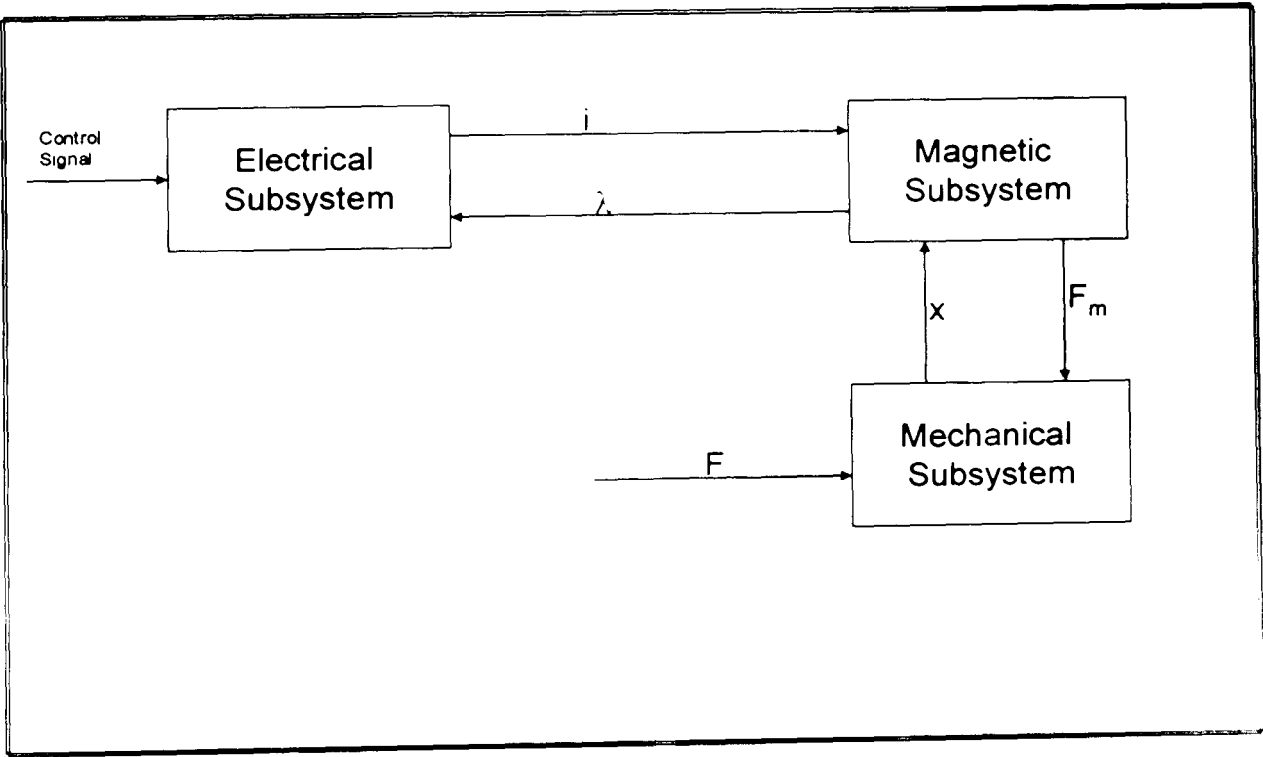


Fig. 3.2-1. The interaction of subsystems of an actuator

The equation for the electrical circuit is then [65],

$$\frac{1}{N} L(x) \frac{di}{dt} = (v_b - i_c r_t) - i c v \quad (3.2-1)$$

$$L(i, x) \frac{di}{dt} = N(v_b - i_c r_t) - i \frac{dL(i, x)}{dt} \quad (3.2-2)$$

The differential equation describing the mechanical subsystem is given by,

$$M \frac{d^2 x}{dt^2} + B_x \frac{dx}{dt} + k_s x = \frac{1}{2} i^2 \frac{dL(i, x)}{dx} \quad (3.2-3)$$

$$M \frac{d^2 x}{dt^2} + B_x \frac{dx}{dt} + k_s x = -\frac{\mu l}{4\delta} (Ni)^2 \quad (3.2-4)$$

3.3 ELECTRICAL CIRCUIT OF A SOLENOID ACTUATOR

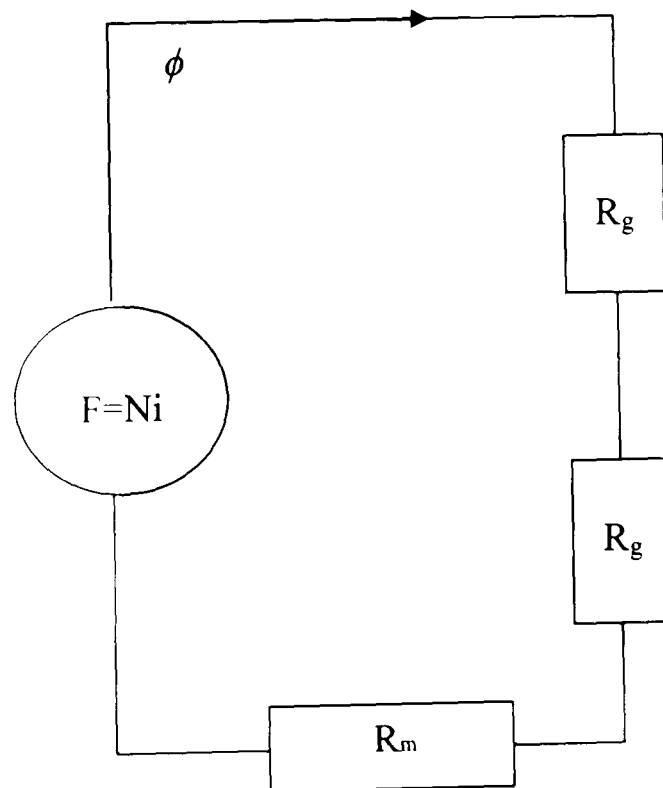


Fig. 3.3-1. Equivalent magnetic circuit of a solenoid actuator

The direction of the EMF can be determined by the "right hand rule" for cross products.

In a coil of N turns, the induced EMF can be calculated by,

$$V = -\frac{d\lambda}{dt} \quad (3.3-1)$$

Where λ the flux linkage of the coil and the minus sign indicates that the induced voltage opposes the variation of the field. It makes no difference whether the variation of the flux linkage is a result of the field variation or coil movement.

In practice, the equation (3.3-1) can be rewritten as,

$$V = \frac{d\lambda}{dt} = L \frac{di}{dt} + i \frac{dL}{dx} \frac{dx}{dt} \quad (3.3-2)$$

But we know from equation (2.5-6),

$$L(x) = \frac{N^2}{R_g(x)} \quad (3.3-3)$$

Equation (2.4-10) can be rewritten for Reluctance of air gap R_g as,

$$R_g = \frac{x}{\mu l} \quad (3.3-4)$$

The total reluctance is broken up as the sum of the reluctances of the air gaps (R_g) and the metallic structure (R_m),

$$R_T = R_g + R_m \quad (3.3-5)$$

Since, in magnetic structures, the reluctance of the metallic structure is usually negligible as compared to that of the air gaps, we replace the total reluctance by

the reluctance of the air gaps only. The reluctance of an air gap varies with the movement of the plunger (x).

Either l or A (or both) is usually a function of the plunger motion x . The exact dependence varies with the geometry of the solenoid. For example, in Fig. 3.4-1, the gap area A is a function of x . Different plunger shapes (for example cylindrical, conical or square) could result in l being a function of x as well. Note here that x is defined such that an increase in x results in an increase in the air gap reluctance.

3.4 INDUCED EMF IN THE EXCITATION COIL FOR A LINEAR ACTUATOR

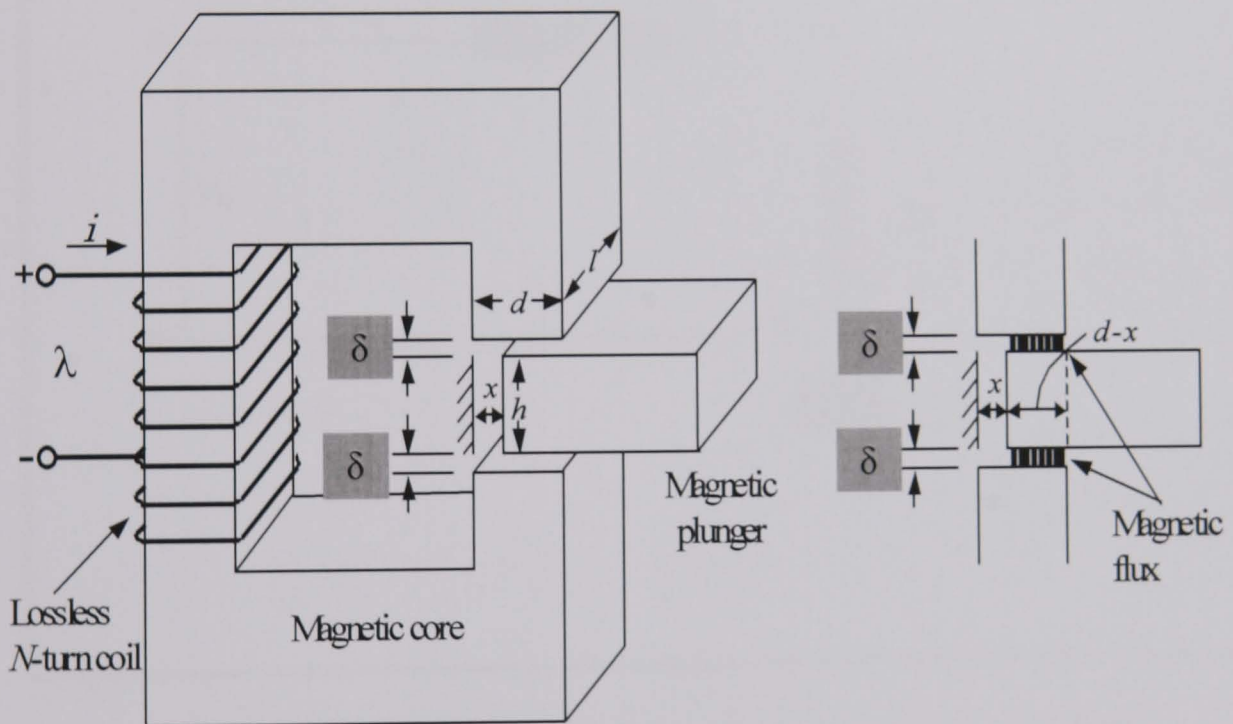


Fig. 3.4-1. Linear actuator

From Equation (2.5-6),

$$L(x) = \frac{N^2}{R_g(x)} \quad (3.4-1)$$

Using equation (3.3-4),

$$R_g(x) = \frac{2\delta}{\mu(d-x)l} \quad (3.4-2)$$

$$L(x) = \frac{\mu N^2 l}{2\delta} (d - x) \quad (3.4-3)$$

$$\frac{dL(x)}{dx} = -\frac{\mu N^2 l}{2\delta} \quad (3.4-4)$$

The diagram below describes the equivalent electrical circuit of the solenoid actuator.

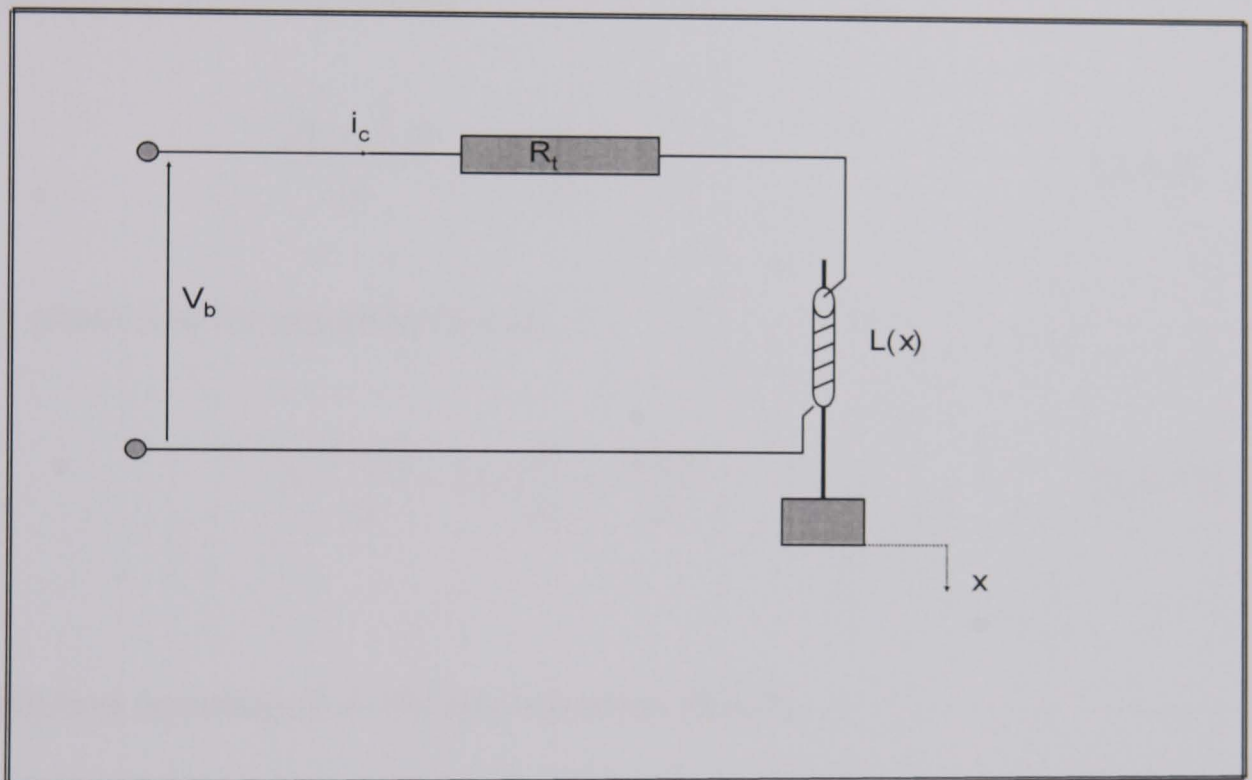


Fig. 3.4-2. Equivalent diagram of the electrical circuit of an actuator

The electric and magnetic models are coupled through the voltage equation,

$$V_b - i_c r_t - \frac{d\lambda_m}{dt} = 0 \quad (3.4-5)$$

But λ is a function of i_c, x ,

$$\lambda_m = \lambda(i_c, x) \quad (3.4-6)$$

substituting equation (3.4-6) into equation (3.4-5),

$$V_b - i_c r_t - \frac{d\lambda(x)}{dt} = 0 \quad (3.4-7)$$

but we know,

$$L = \frac{N\lambda}{i}$$

$$L(x,t) = N \frac{\lambda(x,t)}{i(t)} \quad (3.4-8)$$

Differentiating equation (3.4-8),

$$\frac{d[L(x) \cdot i]}{dt} = N \frac{d\lambda(x)}{dt} \quad (3.4-9)$$

Using chain rule for equation (3.4-9),

$$N \frac{d\lambda(x)}{dt} = L(x) \frac{di}{dt} + i \frac{dL(x)}{dt} \quad (3.4-10)$$

Substituting equation (3.4-10) into equation (3.4-7),

$$V_b - i_c r_t - \left[L(x) \frac{di}{dt} + i \frac{dL(x)}{dt} \right] \frac{1}{N} = 0 \quad (3.4-11)$$

After transformation of equation (3.4-5) we obtain:

$$L(x) \frac{di}{dt} = N(V_b - i_c r_t) - i \frac{dL(x)}{dt}$$

$$L(x) \frac{di}{dt} = N(V_b - i_c r_t) - i \frac{dL(x)}{dx} \frac{dx}{dt}$$

$$L(x) \frac{di}{dt} = N(V_b - i_c r_t) - i \frac{\mu N^2 l}{2\delta} v$$

$$\frac{1}{N} L(x) \frac{di}{dt} = (V_b - i_c R_t) - i \alpha v \quad (3.4-12)$$

Where,

$$\alpha = \frac{\mu N l}{2\delta}$$

3.5 MECHANICAL CIRCUIT OF A SOLENOID ACTUATOR

3.5.1 Force Calculation from Energy and Co-Energy

Consider an excited linear actuator. The winding resistance is r . At a certain time instant t , we record that the terminal voltage applied to the excitation winding is v , the excitation winding current i , the position of the movable plunger x , and the force acting on the plunger F with the reference direction chosen in the positive direction of the x axis, as shown in the diagram. After a time interval dt , we notice that the plunger has moved for a distance dx under the action of the force F . The mechanical work done by the force acting on the plunger during this time interval is thus

$$dW_m = F dx \quad (3.5-1)$$

The amount of electrical energy that has been transferred into the magnetic field and converted into the mechanical work during this time interval can be calculated by subtracting the power loss dissipated in the winding resistance from the total power fed into the excitation winding as

$$dW_e = dW_r + dW_m = v i dt - i^2 r dt \quad (3.5-2)$$

Because,

$$e = \frac{d\lambda}{dt} = v - ir$$

We can write,

$$\begin{aligned} dW_f &= dW_e - dW_m = e idt - F dx \\ &= id\lambda - F dx \end{aligned} \quad (3.5-3)$$

From the above equation, we know that the energy stored in the magnetic field is a function of the flux linkage of the excitation winding and the position of the plunger. Mathematically, we can also write,

$$dW_f(\lambda, x) = \frac{\partial W_f(\lambda, x)}{\partial \lambda} d\lambda + \frac{\partial W_f(\lambda, x)}{\partial x} dx \quad (3.5-4)$$

Therefore, by comparing equations (3.5-3) and (3.5-4), we conclude,

$$i = \frac{\partial W_f(\lambda, x)}{\partial \lambda} \quad \text{and} \quad F = -\frac{\partial W_f(\lambda, x)}{\partial x}$$

From the knowledge of electromagnetic theory, the energy stored in a magnetic field can be expressed as,

$$W_f(\lambda, x) = \int_0^\lambda i(\lambda, x) d\lambda \quad (3.5-5)$$

For a magnetically linear system (with a constant permeability or a straight line magnetization curve where the inductance of the coil is independent of the excitation current), the above expression becomes,

$$W_f(\lambda, x) = \frac{1}{2} \frac{\lambda^2}{L(x)} \quad (3.5-6)$$

and the force acting on the plunger is then,

$$F = -\frac{\partial W_f(\lambda, x)}{\partial x} = \frac{1}{2} \left[\frac{\lambda}{L(x)} \right]^2 \frac{dL(x)}{dx} = \frac{1}{2} i^2 \frac{dL(x)}{dx} \quad (3.5-7)$$

In the diagram below, it is shown that the magnetic energy is equivalent to the area above the magnetization or λ - i curve. Mathematically, if we define the area underneath the magnetization curve as the co-energy (which does not exist physically) i.e.

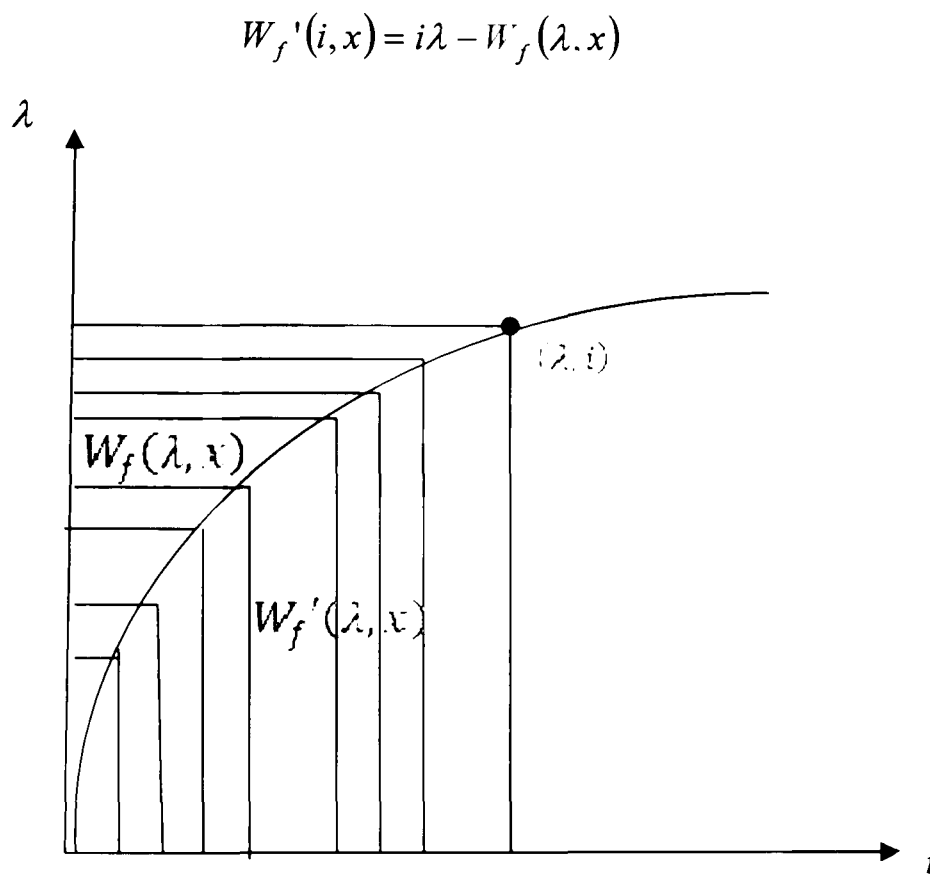


Fig . 3.5-1 Energy and co-energy

We can obtain,

$$\begin{aligned} dW_f'(i, x) &= \lambda di + i d\lambda - dW_f(\lambda, x) \\ &= \lambda di + F dx \\ &= \frac{\partial W_f'(i, x)}{\partial i} di + \frac{\partial W_f'(i, x)}{\partial x} dx \end{aligned}$$

Therefore,

$$\lambda = \frac{\partial W_f'(i, x)}{\partial i} \quad \text{and} \quad F = \frac{\partial W_f'(i, x)}{\partial x}$$

From the Fig. 3.5-1, the co-energy or the area underneath the magnetization curve can be calculated by [67],

$$W_f'(i, x) = \int_0^i \lambda(i, x) di \quad (3.5-8)$$

For a magnetically linear system, the above expression becomes,

$$W_f'(i, x) = \frac{1}{2} i^2 L(x) \quad (3.5-9)$$

and the force acting on the plunger is then,

$$F = \frac{\partial W_f'(i, x)}{\partial x} = \frac{1}{2} i^2 \frac{dL(x)}{dx}$$

$$F = \frac{1}{2} i^2 \frac{dL(x)}{dx} \quad (3.5-10)$$

3.6 THREE STATE VARIABLES FOR SIMULATING AN ACTUATOR

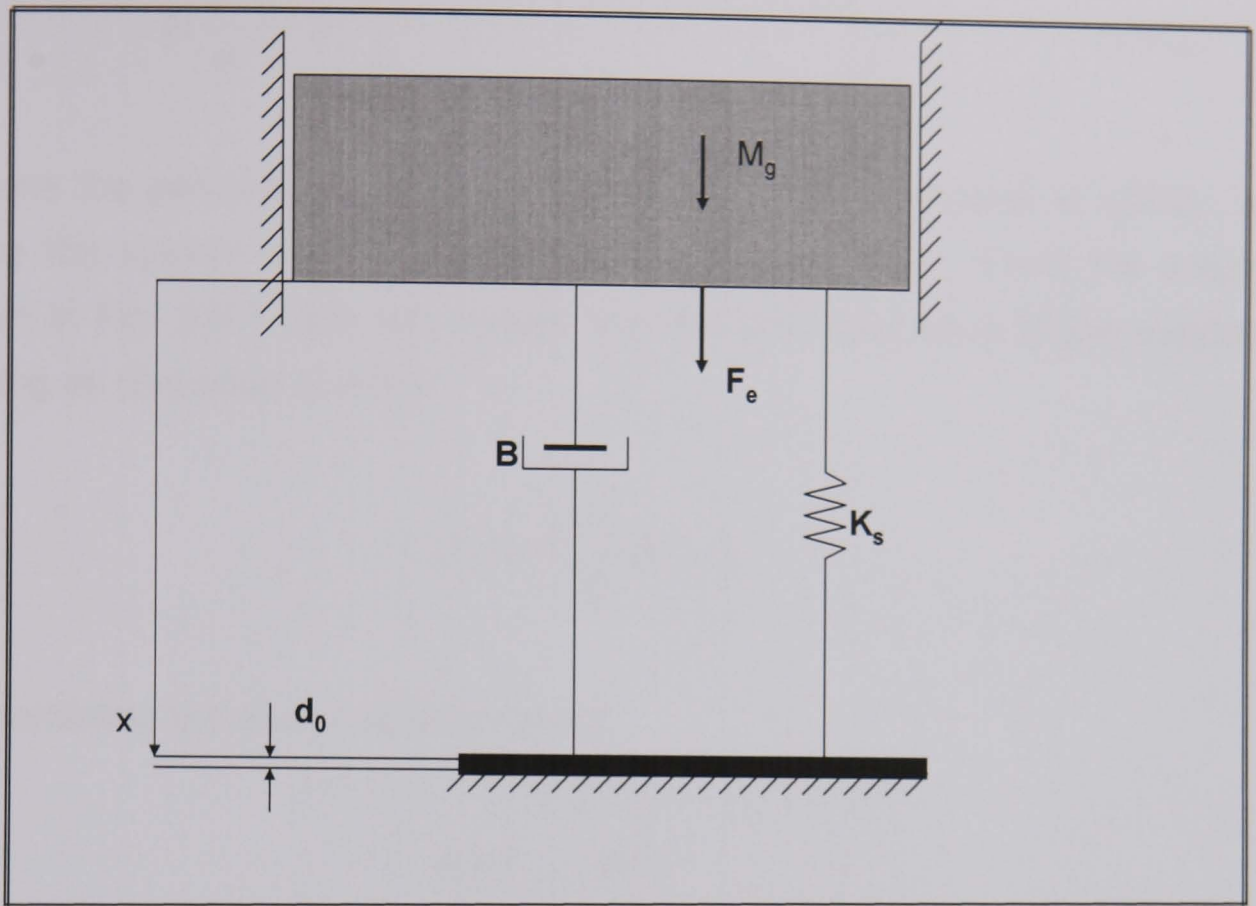


Fig. 3.6-1. Equivalent diagram of the mechanical part of an actuator

The balance equation of forces acting on the actuator [41];

Using Newton's law,

$$F = m \cdot a$$

$$F_e + M_g - B_x \frac{dx}{dt} - K_s(x + x_p) = M \frac{dx^2}{dt^2} \quad (3.6-1)$$

For the current i flowing through the coil, the magnetic force (F) exerted is given by the following form (equation (3.5-11)):

$$F_e = \frac{1}{2} \frac{dL(x)}{dx} i^2$$

Substituting the equation (3.5-10) into equation (3.6-1):

$$M \frac{d^2 x}{dt^2} + B_x \frac{dx}{dt} + K_s (x + x_p) = M_g + \frac{1}{2} i^2 \frac{dL(x)}{dx} \quad (3.6-2)$$

Assume the permeability of the magnetic core of the actuator is infinity, and hence the system can be treated as magnetically linear. From the actuator shown in Fig. 3.4-1, one can readily find the self inductance of the excitation winding as (Equation (3.4-3)),

$$L(x) = \frac{\mu N^2 l}{2g} (d - x)$$

Differentiating the above equation gives,

$$\frac{dL(x)}{dx} = -\frac{\mu N^2 l}{2g}$$

Dynamic equation of motion of an actuator can be written as the following format:

$$M \frac{d^2 x}{dt^2} + B_x \frac{dx}{dt} + K_s x = -\frac{1}{2} i^2 \frac{\mu N^2 l}{2\delta}$$

$$M \frac{d^2 x}{dt^2} + B_x \frac{dx}{dt} + K_s x = -\frac{\mu l}{4\delta} (Ni)^2 \quad (3.6-3)$$

The minus sign of the force indicates that the direction of the force is to reduce the displacement so as to reduce the reluctance of the air gaps. Since this force is caused by the variation of magnetic reluctance of the magnetic circuit, it is known as the reluctance force.

3.7 ELECTROMAGNETIC HEATING

Heat transfer can be defined as the transmission of thermal energy from one region to another as a result of temperature differences between them. When a temperature gradient exists in a solid medium, conduction heat transfer occurs. Thermal energy will transmit from the higher temperature region to the lower temperature one [72-76].

For one dimensional conduction problem, which means that the temperature in the material is a function only of the x coordinate and time ($T = T(x,t)$).

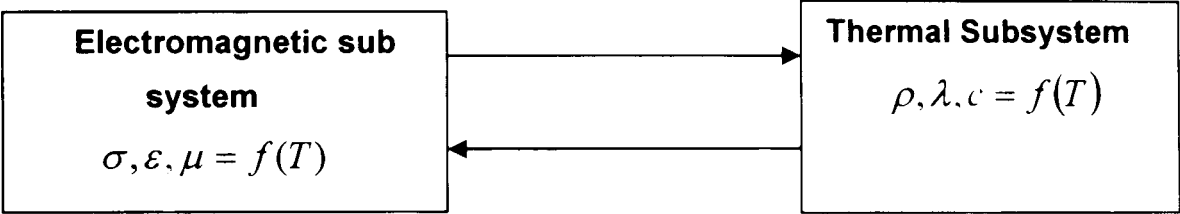


Fig. 3.7-1 Electromagnetic thermal interaction

The rate of heat transfer per unit area is:

$$q = -k \frac{dT}{dx}$$

(3.7-1)

Where

$$\frac{dT}{dx}$$

= is the temperature gradient.

The above equation is also known as the Fourier’s law of heat conduction. The minus sign results from the fact that heat flows from a warmer to a colder region, i.e., the temperature gradient dT/dx is negative in the direction of positive heat flow (Fig. 3.7-2). Therefore a minus sign is placed in equation (3.7-1) to make the heat flow rate positive [72].

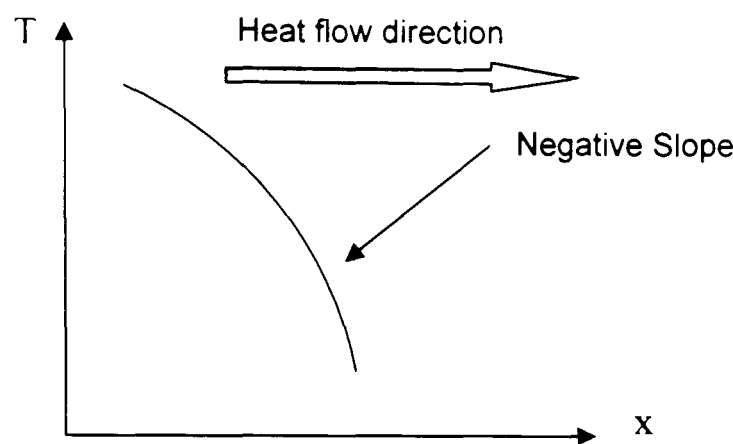


Fig. 3.7-2. Heat flow conduction

3.7.1 Fundamental Equations

In three dimensional heat flow problems, the temperature is a function of all three coordinates and time. Therefore Fourier’s law of heat conduction becomes:

$$q_n = -k_n \frac{\partial T}{\partial n} \tag{3.7-2}$$

Where, n is a spatial coordinate.

In Cartesian coordinates, the heat flow in the three coordinate directions is given by:

$$q_x = -k_x \frac{\partial T}{\partial x}, \quad q_y = -k_y \frac{\partial T}{\partial y}, \quad q_z = -k_z \frac{\partial T}{\partial z}, \tag{3.7-3}$$

If the material is isotropic, the thermal conductivity is constant and the equation (3.7-3) may be written in the following form:

$$k_x = k_y = k_z = k$$

$$\begin{Bmatrix} q_x \\ q_y \\ q_z \end{Bmatrix} = k \begin{Bmatrix} \partial T / \partial x \\ \partial T / \partial y \\ \partial T / \partial z \end{Bmatrix} \tag{3.7-4}$$

3.7.2 Convection

Convection is the transfer of thermal energy through a fluid medium, such as air, caused by the movement of the heated particles of the fluid. As an example, in a building space, warm air rises and cold air settles to create a convection loop and is called *free* or *natural convection*. If the movement of fluid is caused by external means such as a fan or a pump, the transfer of energy is termed forced convection. The rate of heat transfer by both free and forced convection between a surface and a fluid can be calculated from the relation [72].

$$-k_n \frac{\partial T}{\partial n} = q_c = h(T_s - T_f) \quad (3.7-5)$$

3.7.3 Radiation

Radiant heat transfer is concerned with the exchange of thermal energy between two or more bodies by electromagnetic waves. Two important factors that affect radiation heat transfer are emissivity and absorptivity. Emissivity refers to the ability of a material's surface to give off or emit radiant energy. Emissivity values range from zero to one for all materials. The lower the emissivity of a material becomes the lower the heat radiated from its surface. A body having emissivity equals to one is called a perfect radiator or a *black body*. If the surface emissivity of a body is less than 1 and is independent of the radiation wavelength, then the body is called a "*gray*" body. In contrast to emissivity, absorptivity indicates the ability of a material to absorb radiant energy. Assume a gray body of surface temperature T_s , is enclosed by another gray or black enclosure with wall temperature T_c , (Fig. 3.7-3). Then the radiant energy emitted from the surface of body per unit time and area is given by [72]

q_e :

$$q_e = \varepsilon \sigma T_s^4 \quad (3.7-6)$$

The radiant energy absorbed by the surface is given by q_{ab} ,

$$q_{ab} = \alpha \sigma T_c^4 \quad (3.7-7)$$

Where, α is the absorptivity of the surface of the grey body.

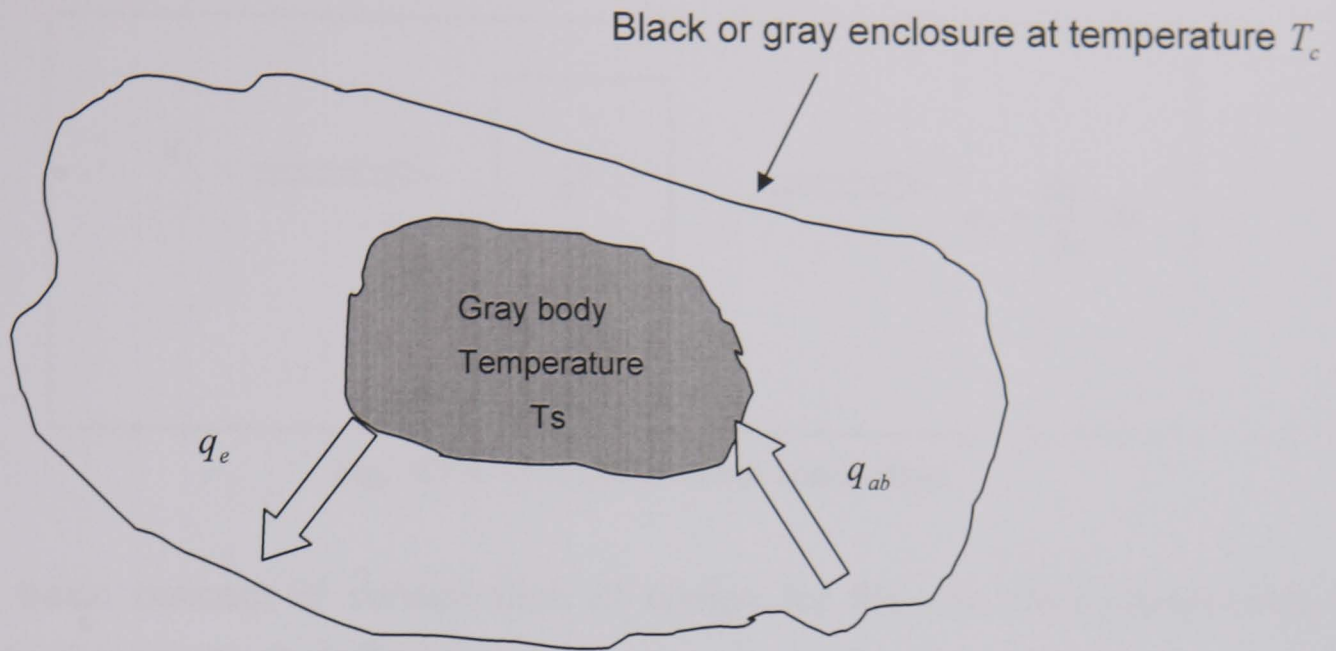


Fig. 3.7-3. Schematic of radiation between a body and an enclosure

Owing to Kirchhoff's law of thermal radiation $\alpha = \varepsilon$ and the net rate of radiant heat flux out of the surface is given by q_{out} :

$$q_{out} = q_e - q_{ab} \quad (3.7-8)$$

$$q_{out} = \varepsilon \sigma [T_s^4 - T_e^4] = -k_n \frac{\partial T}{\partial n} \quad (3.7-9)$$

The ε may be a function of temperature, surface finish and view factor between two bodies. In radiative heat transfer, a view factor is the proportion of all that radiation which leaves from one surface and strikes another surface.

The above equations assumed that the gray body is completely enclosed by an enclosure. Hence, all radiation leaving the body would reach the enclosure and vice versa.

3.7.4 One dimensional Heat Conduction Equation

In this section, we derive the general conduction equation, which is a mathematical expression of the conservation of energy in a solid. Solving the conduction equation with initial and boundary conditions, the temperature distribution of the solid can be obtained. We first consider a one-dimensional problem, i.e. $T = T(x, t)$, in Cartesian coordinate as shown in Fig. 3.7-4.

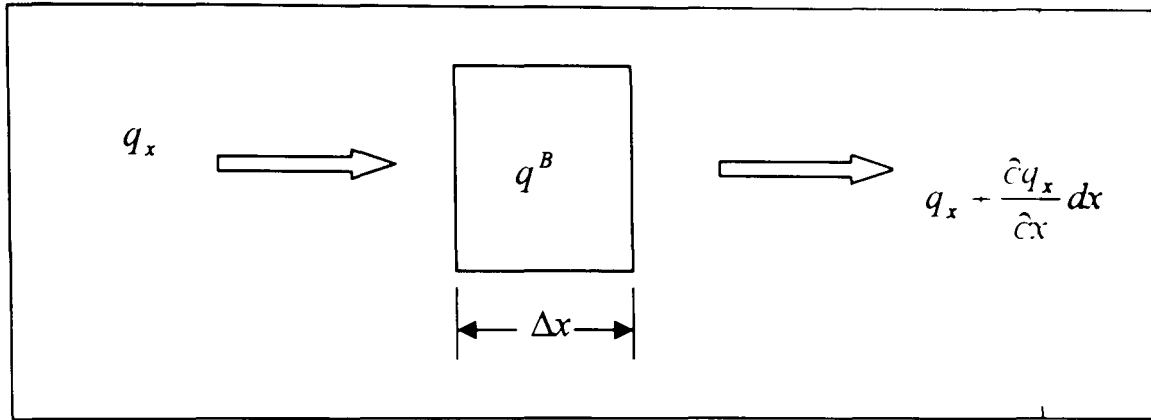


Fig. 3.7-4. One dimensional conduction

The basic concept of conservation of energy for the one dimensional heat conduction can be described as:

$$\left(\begin{array}{l} \text{Rate of Heat} \\ \text{Conduction} \\ \text{into Solid} \end{array} \right) + \left(\begin{array}{l} \text{Rate of Heat} \\ \text{Generation} \\ \text{Inside Solid} \end{array} \right) = \left(\begin{array}{l} \text{Rate of Heat} \\ \text{Conduction} \\ \text{Out of Solid} \end{array} \right) + \left(\begin{array}{l} \text{Rate of Energy} \\ \text{Storage Inside} \\ \text{Solid} \end{array} \right) \quad (3.7-10)$$

Equation (3.7-10) can be expressed as:

$$-k \frac{\partial T}{\partial x} \Big|_x + q^B \Delta x = -k \frac{\partial T}{\partial x} \Big|_{x+\Delta x} + \rho \cdot c \cdot \Delta x \frac{\partial T(x + \Delta x, t)}{\partial t} \quad (3.7-11)$$

Where k is the thermal conductivity, q^B is the internal rate of heat generated per unit volume, t is the time, ρ is the density and c is the specific heat, where no distinction is given between c_p and c_v (specific heat at constant pressure and constant volume for solid).

We can expand the $-k \frac{\partial T}{\partial x} \Big|_{x+\Delta x}$ term as follow,

$$-k \frac{\partial T}{\partial x} \Big|_{x+\Delta x} = -k \left(\frac{\partial T}{\partial x} \Big|_x + \frac{\partial}{\partial x} \left(\frac{\partial T}{\partial x} \right) \Delta x \right) = -k \left(\frac{\partial T}{\partial x} \Big|_x + \frac{\partial^2 T}{\partial x^2} \Delta x \right) \quad (3.7-12)$$

Also we may expand the $\frac{\partial T(x + \Delta x/2, t)}{\partial t}$ term using Taylor series,

$$\frac{\partial T(x + \Delta x/2, t)}{\partial t} = \frac{\partial T}{\partial t} \left[\left(x + \frac{\Delta x}{2} \right), t \right] = \frac{\partial T}{\partial t} \Big|_x + \frac{\partial^2 T}{\partial x \partial t} \Big|_x \frac{\Delta x}{2} + \dots \quad (3.7-13)$$

Considering the terms to the order of Δx (i.e., neglecting second order increments), we can rewrite the equation (3.7-11) in the following format.

$$k \frac{\partial^2 T}{\partial x^2} + q^B = \rho \cdot c \frac{\partial T}{\partial t} \quad (3.7-14)$$

The above equation (3.7-14) is the governing equation for conduction heat transfer in one dimensional solid. The first term on the left side is the net rate of heat conduction into the control volume per unit volume. The second term on the left side represents the rate of heat generation per unit volume inside the solid. The RHS can be considered as the rate of increase in internal energy inside the solid per unit volume.

For three-dimensional conduction problems, temperature is a function of all the x , y and z directions and time.

Therefore, the heat conduction equation becomes:

$$k_x \frac{\partial^2 T}{\partial x^2} + k_y \frac{\partial^2 T}{\partial y^2} + k_z \frac{\partial^2 T}{\partial z^2} + q^B = \rho \cdot c \frac{\partial T}{\partial t} \quad (3.7-15)$$

The equation (3.7-15) is the general equation for conduction heat transfer, which may take one of the following forms for special cases.

For constant conductivity and an isotropic material, the heat conduction equation (3.7-15) can be expressed as the following form,

$$k \left(\frac{\partial^2 T}{\partial x^2} + \frac{\partial^2 T}{\partial y^2} + \frac{\partial^2 T}{\partial z^2} \right) + q^B = \rho \cdot c \frac{\partial T}{\partial t} \quad (3.7-16)$$

$$\nabla^2 T + \frac{q^B}{k} = \beta \frac{\partial T}{\partial t} \quad (3.7-17)$$

Where,

$$\nabla^2 T = \left(\frac{\partial^2 T}{\partial x^2} + \frac{\partial^2 T}{\partial y^2} + \frac{\partial^2 T}{\partial z^2} \right)$$

The thermal diffusivity of the medium $D = \frac{\rho \cdot c}{k}$

Case One: Isotropic material with no heat generation

When $q^B = 0$, the equation (3.7-17) can be written as:

$$\nabla^2 T = \beta \frac{\partial T}{\partial t} \quad (3.7-18)$$

Case Two: Isotropic material and steady state conditions

For steady state heat transfer, the conduction equation is not a function of time,
i.e. $\frac{\partial T}{\partial t} = 0$

Therefore we can state the equation (3.7-17) in the following form,

$$\nabla^2 T + \frac{q^B}{k} = 0 \quad (3.7-19)$$

Case Three: Isotropic material and steady state conditions and no heat generation.

The conduction equation in this conduction reduces to,

$$\nabla^2 T = 0 \quad (3.7-20)$$

3.7.5 Boundary Conditions

The above conduction equations may be solved according to initial and boundary conditions. The initial condition is the temperature of the solid at an initial time. The boundary conditions may take several forms. The most common

conditions, which are summarized schematically in Fig. 3.7-5, include prescribed temperature, prescribed heat flow, no heat flow, convection heat exchange and radiation.

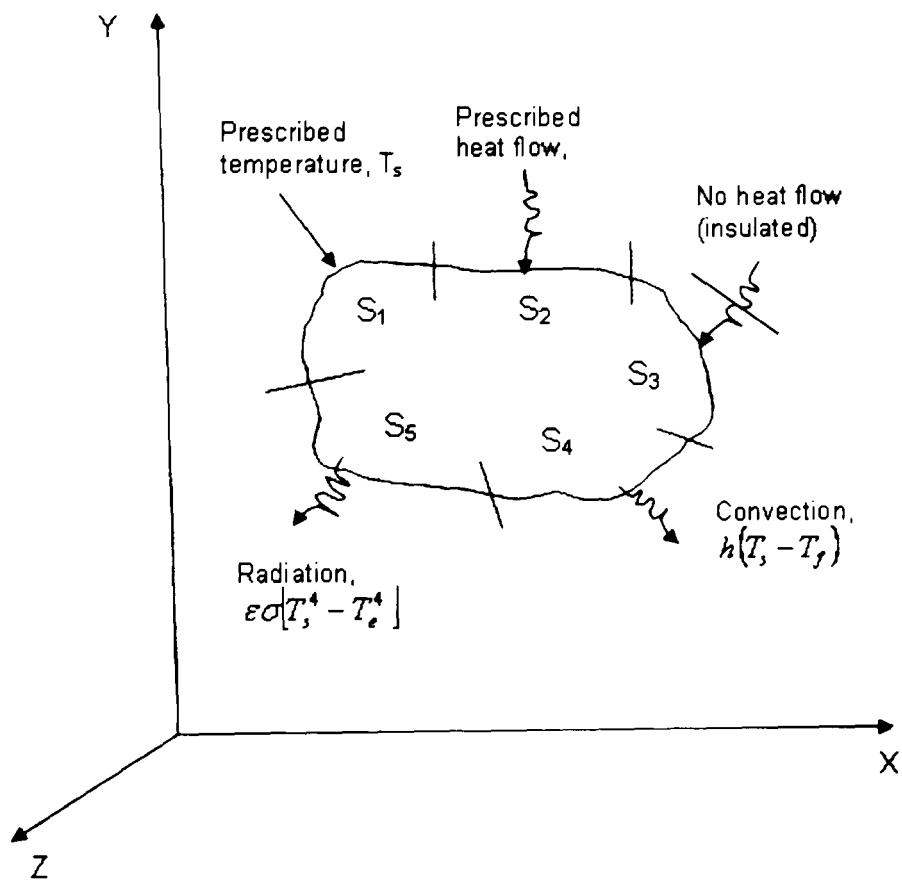


Fig. 3.7-5. Boundary conditions for general heat conduction

Prescribed Temperature:

The temperature may be prescribed on a specific boundary of the body. In Fig. 3.7-5 the surface temperature of boundary S_1 is specified to be T_s .

The prescribed temperature may be constant or a function of boundary coordinate and / or time.

$$T = T_s(x, y, z, t)$$

On S_1

(3.7-21)

Prescribed heat flow:

On surface S_2 the heat flow is specified to be q_n , which may be constant, or a function of boundary coordinate and or time. Recall equation (3.7-19), the heat flux can be expressed as,

$$-k_n \frac{\partial T}{\partial n} = q_s \quad \text{On } S_2 \quad (3.7-22)$$

Where n is the normal to boundary S_2 and q_s is the rate of heat flow per unit area. Prescribed heat flow is an example of Cauchy's or Neumann boundary condition.

No Heat flow (Adiabatic or natural boundary):

On boundary S_3 , the rate of heat flow across the boundary is zero. This boundary condition is called the adiabatic or natural boundary condition, which is a special form of the previous case.

$$\frac{\partial T}{\partial n} = 0 \quad \text{On } S_3 \quad (3.7-23)$$

Convection heat exchange:

When there is a convective heat transfer on a part on the body surface, S_4 in Fig. 3.7-5, due to contact with a fluid medium, we have convective boundary condition. From equation (3.7-2), the governing equation for convective boundary condition can be written as:

$$-k_n \frac{\partial T}{\partial n} = h(T_s - T_f) \quad \text{On } S_4 \quad (3.7-24)$$

Where h is the convection heat transfer coefficient, which may be temperature dependent (non-linear), T_s is the surface temperature on S_4 and T_f is the fluid temperature, which may be constant, or a function of boundary coordinate and or time.

Radiation:

The last boundary condition considered here is radiation boundary condition. Assume that the solid that we are interested in, is a grey body for which the emissive power is independent of the radiation wavelength.

Then from equation (3.7-24), we can write the governing equation for radiation boundary condition as [72],

$$-k_n \frac{\partial T}{\partial n} = \varepsilon \sigma [T_s^4 - T_e^4] \quad \text{On } S_s \quad (3.7-25)$$

Where ε is the emissivity of the surface of the body, σ is the Stefan-Boltzmann constant, T_s is the absolute temperature of surface S_s and T_e is the known temperature of the external source.

3.8 SUMMARY

In the electric and electromechanical devices, the electromagnetic phenomena are at the origin of mechanical phenomena. In the general case, the relative movement of the structure, the deformation of materials as well as magnetic non-linearity make that the studies of the two phenomena cannot be carried out independently. The development of the coupled models is then necessary.

Electrical circuit equation (3.4-5),

$$V_b - i_c r_t - \frac{d\lambda_m}{dt} = 0$$

Mechanical equation (3.6-1),

$$F_c + M_g - B_x \frac{dx}{dt} - K_s (x + x_p) = M \frac{dx^2}{dt^2}$$

Thermal diffusion equation (3.7-17),

$$k \frac{\partial^2 T}{\partial x^2} + q^B = \rho \cdot c \frac{\partial T}{\partial t}$$

The current produced by equation (3.4-5) creates the magnetic field and this magnetic field produces the magnetic force which causes the displacement,

speed and acceleration of the actuator obtained from equation (3.6-1). The current also generates the heat (per unit volume) and the resulting temperature distribution given by equation (3.7-17) [72-74].

To study the dynamic behaviours of electric machines and actuators, we have studied existing models of coupling such as the parametric model and the indirect model, and developed a model of direct coupling 'electric circuit - magnetic field - mechanical movement'.

The parametric model is based on the parameterization of the system using a calculation of the magnetic field. It is a question of determining initially, using the finite element method, the variation of the impedance and the force according to the movement and the current, and of then solving the electric and mechanic equations by taking account of the variation of these parameters. It is a relatively simple model if the eddy currents are neglected in the conductors.

The indirect model is a model of sequential coupling. With each step of calculation in time, one calculates the magnetic force by solving the equation of the magnetic field by associating the equations of the electric circuit (if this is fed by a voltage source lastly), and one solves then the mechanical equation of the movement to obtain displacement. This model requires, if the step of calculation is relatively large, an algorithm known as of prediction - correction in order to obtain a good precision of simulation.

The model of strong coupling developed in our study consists in simultaneously solving various equations. The use of the method of virtual work previously described for calculation of the magnetic force as well as the linearization of the system of equations by the method of Newton-Raphson made it possible to symmetry the final matrix system. This relatively heavy model on the other hand avoids the influence of the time stepping on the precision of simulation.

Chapter 4

MAGNETIC MATERIALS USED IN ELECTROMAGNETIC ACTUATORS

4.1 INTRODUCTION

Magnetic materials have played an important role in the field of electrical engineering for over a century. New materials have given access to new fields of applications and conversely, new applications have lent impetus to the development of special material.

In last few years an attention has been focused on the similarities and differences of the various material groups and on pure material development and processing technology [78-79]. This has resulted in a wide ranging spectrum of soft magnetic materials. The purpose of this chapter in, finding suitable magnetic materials for an actuator that will be used in food sorting machines.

4.2 MAGNETIC PROPERTIES

The magnetic properties of material are measured from certain defined points and derivatives obtained from the variation of magnetization with magnetic field as shown in Fig. 4.2-1. Magnetic materials are broadly classified into two main groups with either hard or soft magnetic characteristics. Soft magnetic materials can be magnetized by relatively low-strength magnetic fields, and when the applied field is removed, they return to a state of relatively low residual magnetism. Soft magnetic materials typically exhibit coercivity [section 4.2.2] values of approximately 400 Am^{-1} to 0.16 Am^{-1} . Soft magnetic materials behaviour is important in any application involving a change in magnetic induction.

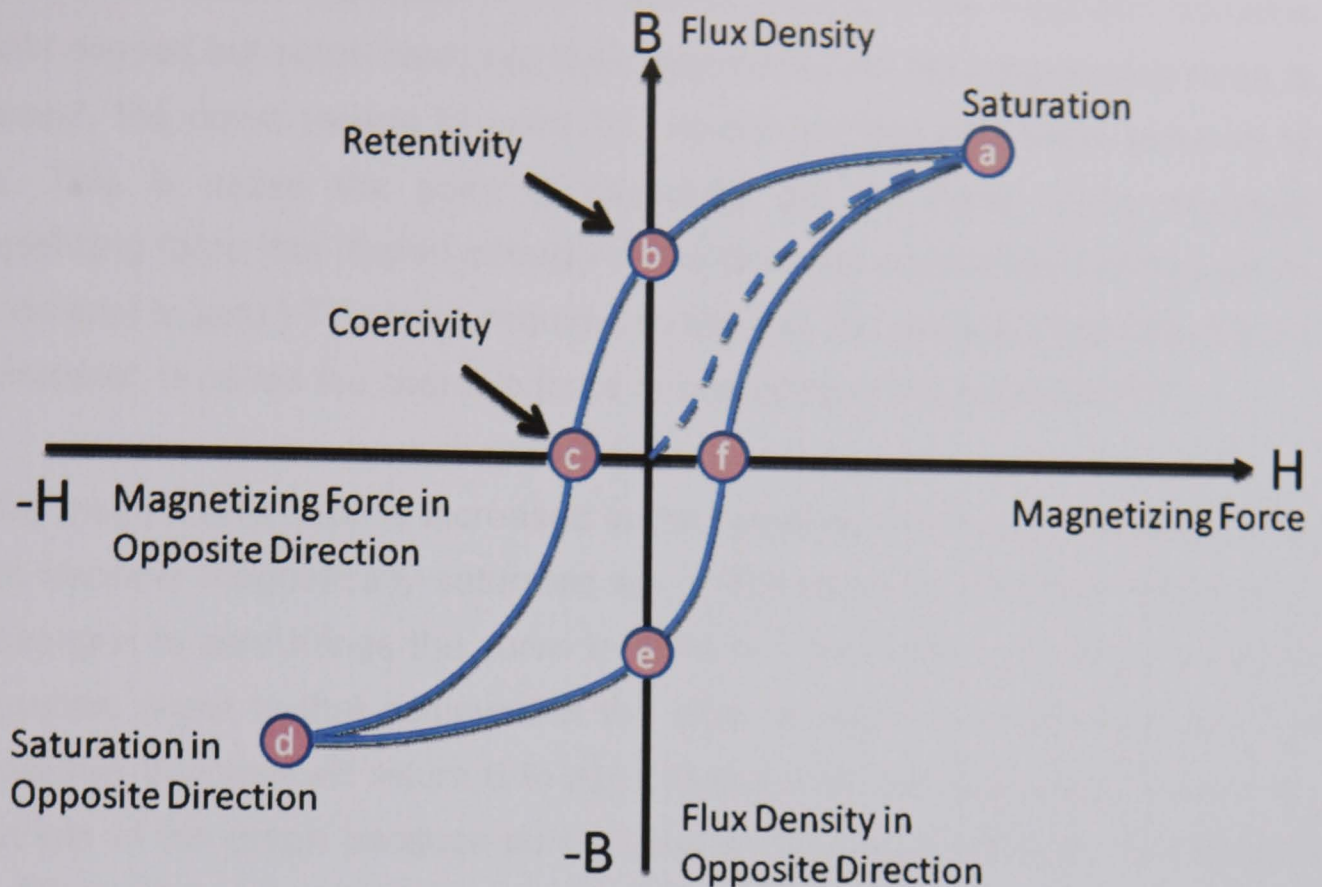


Fig. 4.2-1. Hysteresis loop [57]

Hard magnetic materials retain a large amount of residual magnetism after exposure to a magnetic field. These materials typically have coercivities, H_c , of 10 kA/m to 1 MA/m. The materials at the high coercivity end of this range are known as permanent magnets. These materials are used principally to supply a magnetic field [78].

The loop is generated by measuring the magnetic flux B of a ferromagnetic material while the magnetizing force H is changed. A ferromagnetic material that has never been previously magnetized or has been thoroughly demagnetized, will follow the dashed line when H is increased. As the line demonstrates, the greater the amount of current applied ($H+$) and the stronger the magnetic field in the component ($B+$). At point "a" almost all of the magnetic domains are aligned and an additional increase in the magnetizing force will produce very little increase in magnetic flux. The material has reached the point of magnetic saturation. When H is reduced back down to zero, the curve will move from point "a" to point "b." At this point, it can be seen that some magnetic flux remains in the material even though the magnetizing force is zero. This is referred to as the point of retentivity on the graph and indicates the remanence

or level of residual magnetism in the material. (Some of the magnetic domains remain aligned but some have lost their alignment.) As the magnetizing force is reversed, the curve moves to point "c", where the flux has been reduced to zero. This is called the point of coercivity on the curve. (The reversed magnetizing force has flipped enough of the domains so that the net flux within the material is zero.) The force required to remove the residual magnetism from the material, is called the coercive force or coercivity of the material [78].

As the magnetizing force is increased in the negative direction, the material will again become magnetically saturated but in the opposite direction (point "d"). Reducing H to zero brings the curve to point "e." It will have a level of residual magnetism equal to that achieved in the other direction. Increasing H back in the positive direction will return B to zero. Notice that the curve did not return to the origin of the graph because some force is required to remove the residual magnetism. The curve will take a different path from point "f" back to the saturation point where it completes the loop.

4.2.1 Permeability

Permeability is the most important parameter for soft magnetic materials since it indicates how much magnetic induction B is generated by the material in a given magnetic field strength H . It is known that initial permeability and coercivity have in broad terms a reciprocal relationship, so that materials with high coercivity necessarily have a low initial permeability and vice versa.

4.2.2 Coercivity

Coercivity is the parameter which is used to distinguish hard and soft magnetic materials. Traditionally a material with a coercivity of less than 1000Am^{-1} is considered magnetically 'soft'. A material with a coercivity of greater than $10,000\text{Am}^{-1}$ is considered magnetically 'hard'. Low coercivities are achieved in nickel alloys such as perm alloy in which the coercivity can be as low as 0.4Am^{-1} [78], [80].

4.2.3 Saturation Magnetization

The highest saturation magnetization available in bulk magnetic materials is $B_s = 2.6$ T; which is achieved in an iron-cobalt alloy containing 35% cobalt [81]. The possible values of saturation magnetization then range downward continuously to effectively zero. There has been little progress in improving the range of saturation magnetization of materials for about 100 years [78].

4.2.4 Hysteresis Loss

The hysteresis loss is the area enclosed by the hysteresis loop on the B,H plane. It represents the energy expended per unit volume during one cycle of the hysteresis loop. The hysteresis loss increases as the maximum magnetic field reached during the cycle increases. This loss is closely related to the coercivity so that processing of materials reduces coercivity also reduce the hysteresis loss. Generally low hysteresis loss is a desirable characteristic of soft magnetic materials.

4.2.5 Energy Dissipation and Power Losses

A related property is the power loss which arises when a soft magnetic material is subjected to a time dependent magnetic field. The hysteresis loss is only one component of the power loss, being the power loss obtained when the field is cycled very slowly under quasi-static conditions. The total power loss depends on the frequency of excitation, the amplitude of magnetic induction, the hysteresis loss, the physical dimensions of the material being magnetized and the eddy current dissipation.

In addition there is usually a discrepancy between the measured power loss and the loss expected from the sum of hysteresis and eddy current losses and this is usually referred to as the “anomalous loss”. The total electrical power loss can be expressed as the sum of these various components. Total power losses can be reduced if the conductivity of the material is reduced [78].

4.3 PREREQUISITES TO OBTAIN SOFT MAGNETIC MATERIALS

Selecting the right magnetic alloy for a product application does not have to be intimidating. The designer first needs to find the candidate alloy that best combines the characteristics required, then select the lowest cost alloy that will meet those requirements.

To reverse the process and select an alloy that may or may not do the job, in the interest of saving upfront material costs, may put the job at risk at a potential cost many times more than the initial alloy investment.

Soft magnetic alloys, it should be noted also, that they are made by means of premium melting practice and specialized processing to achieve optimum properties. The performance of these alloys depends not only on how they are made, but often on the knowledge of how they are to be used.

It can be productive, therefore, for the designer to consult with the alloy supplier and explain his/her specialized needs. Mill processing can be tailored to provide certain critical magnetic properties, and chemical compositions can be adjusted to make some alloys more suitable for certain methods of fabrication.

We consider the soft magnetic materials as containing certain magnetic properties, such as high magnetic flux density, high permeability etc. A further subdivision has been made within the different alloy groups according to loop shapes: round (R), rectangular / square (Z), or flat (F) [78].

R: Round loop where the remanence is approximately 50% of the saturation. This loop is normally given in text books on magnetism as the typical hysteresis loop.

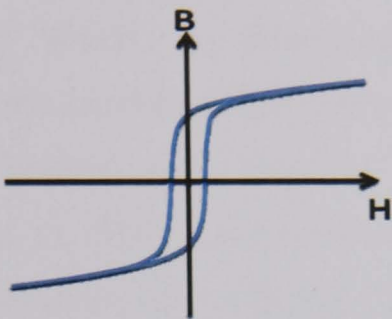


Fig. 4.3-1. Round hysteresis loop

Z: Square or rectangular shaped loop with high remanence which may be over 95% of the saturation. Materials with these loops are called rectangular materials.

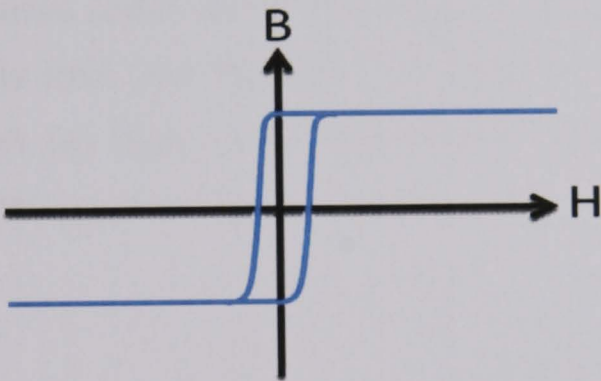


Fig. 4.3-2. Square/ Rectangular hysteresis loop

F: Flat loop with very low remanence, e.g. below 10% of the saturation. The entire ranges of values of the two important characteristic parameters are saturation polarization and coercivity.

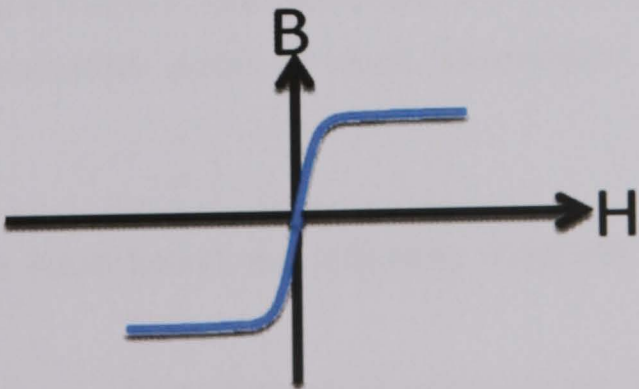


Fig. 4.3-3. Flat hysteresis loop

4.4 TYPICAL REQUIREMENTS

Technical applications place widely varying requirements on material. On the one hand, they involve the saturation polarization and the curie temperature (the temperature above which a ferromagnetic substance loses its ferromagnetism and becomes paramagnetic) which are primarily dependent on the alloy composition and should, as a rule, be high. On the other hand, high permeability, low coercivity, or other terms which affect the magnetic softness are important. The requirements also include certain hysteresis loop shapes and, in particular, dynamic properties like low total losses, minor dependence of permeability on frequency etc.

It is important to find suitable magnetic materials that would meet the design and performance specifications. For this the following search criteria for an 'ideal' magnetic material used were : (a) high saturation flux density, (b) 'thin' hysteresis loop – low loss, low 'sticktion', (c) high electrical resistivity, (d) food safe, chemically inert (e) high Curie temperature, and (f) strong and durable mechanical properties.

4.5 MATERIALS

The available range of magnetic properties of soft magnetic material is continually being expanded. This amounts to reduction in coercivity, increase in permeability and consequently a decrease in hysteresis loss.

We consider the soft magnetic materials classified in the most important alloy groups. In these classifications the materials are directly grouped according to certain magnetic properties such as high saturation, polarization and high permeability [78].

From our search we have found the following magnetic materials are suitable for our design.

Cobalt-iron crystalline alloys (CoFe),
Nickel-iron crystalline alloys (NiFe),
Silicon-iron crystalline alloys (SiFe).

4.6 MATERIAL PROPERTIES

4.6.1 Nickel – Iron Alloys

Soft magnetic NiFe alloys are cubic face centred and have a Ni content of between approximately 30% and 80%. They can be divided into five groups which exhibit widely varying magnetic properties [81-82] :

72-83% Ni (additions of Mo, Cu, Cr)

54-68% Ni (additions of Mo)

45-50% Ni

35-40% Ni

approximately 30% Ni

The NiFe alloy group includes the magnetically softest materials. This becomes clear when the parameters governing the degree of softness are studied.

(a) As with Ni contents of about 80%, the highest permeability and the lowest coercivity are found in the 72-83% NiFe group. The peak values are currently around $H_c \approx 0.5 A/m$ and $\mu_i \approx 2 \times 10^5$. Depending on the composition of the alloy and the annealing treatment, either high initial permeability or special loop shapes (Z and F) can be set. Moreover, the temperature behaviour and the temperature Constant of the permeability can be influenced. The saturation polarization of 72-82% NiFe is between approximately 0.8 and 1 T.

(b) The group of 54-68% NiFe combines relatively high permeability with higher saturation than the group (a). This group reacts especially well to annealing in a magnetic field permitting pronounced Z or F loops. However; High permeability can also be achieved in this group with R-loops.

(c) Maximum saturation of approximately 1.6 T is achieved in NiFe systems in alloys with Ni content between 45-50%. Cubic texture and a rectangular hysteresis loop (Z) or normal round loops (R) with coarse grained structure can be set by selecting appropriate rolling and annealing conditions. Group (c) offers further loop variants attained via crystal orientation and magnetic field

annealing. Optimized melting technology or sintering leads to excellent magnetic properties, especially low coercivities ($H_c \approx 3.1/m$) even in materials of greater thickness.

(d) Alloys with 35–40% Ni previously played a major role as materials for transformer laminations in telecommunications. They have a relatively low and constant permeability, that is, a slight increase in permeability and the highest resistivity in the NiFe system. The permeability is in the range 2000 to 8000, the saturation polarization is between 1.3 T and 1.5 T.

(e) The Curie temperature of 30% NiFe is in the vicinity of room temperature and can be varied between 30° C and 120° C through fine adjustment of the Ni content. This material is thus used primarily for temperature compensation, for example, in permanent systems, electrical circuits etc.

4.6.2 Cobalt-Iron Alloys

The technically significant CoFe alloys have Co-contents between 27% and 50% of all the soft magnetic materials they attain the highest saturation polarization, 2.4 T and the highest Curie temperature, approximately 950°C. A commonly used alloy composition is 49% Co and 2% V. The addition of V reduces the brittleness, improves the rolling behaviour and increase the resistivity. Workability, in particular rolling to thin strips, is far more difficult and complex – for metallurgical reasons – than with NiFe alloys. While pronounced crystal structures cannot be set as in NiFe or SiFe alloys, rectangular hysteresis loops can be produced by magnetic field tempering. Beside the approximately 50% CoFe alloys with 27% Co and 35% Co have gained some importance. Although they are easier to roll, the magnetization curves achieve lower flux density values at medium field strengths (1000 A/m) than 50% CoFe, while at high field strengths almost equivalent values are attained [81-83].

4.6.3 Silicon-iron crystalline alloy

SiFe with 6.5% Si: The Si-addition increases the electrical resistivity of iron and reduces the eddy current loss. Silicon steels with 3% Si manufactured on an

industrial scale are, in fact, not magnetically optimized. The saturation polarization of 6.5 % SiFe is 1.8 T as opposed to 2.03 T for 3% SiFe. It is nevertheless higher than that of 50% NiFe. 6.5% SiFe in a thin strip (<0.1mm) is considered interesting for medium frequency applications [81-83].

4.7 MATERIAL LIST

#	Product or Referen ce	Properties Composition (%)	Magnetic					Electric and Thermal				Mechanic		Manufact ure Company
			Bs	Br	Hc	Permeability		Electrical Resistivity	Core Loss	Tc	Mean Coefficient of Thermal Expension	Density	Hardness	
						Max	Initial							
						T	T							
1	Hiperco Alloy 50A	Carbon 0.004 Silicon 0.05 Vanadium 2.0 Manganese	2.40		31.80			40.01	1.0 (at 1 T of Induction at 60 Hz for 0.35 mm thick	938	11.34	8.11		Carpenter
2	Vacoflux 48	Cobalt 48 Iron Balance	2.35		40.00	15k		44.00	1.0 (at 1 T of Induction at 60 Hz for 0.35	950	9.50	8.12	180	VACUUM SCH - MELZE
3	Vacoflux 50	Cobalt 50 Iron Balance	2.35		80.00	13k		44.00	1.0 (at 1 T of Induction at 60 Hz for 0.35	950	9.50	8.12	190	VACUUM SCH - MELZE
4	Vacodur 50	Cobalt 50 Iron Balance	2.30		160.00	10k		43.00	1.0 (at 1 T of Induction at 60 Hz for 0.35 mm thick strip)	950	10.20	8.12	210	VACUUM SCH - MELZE
5	Vacoflux 17	Cobalt 17 Iron Balance	2.00		200.00	3.5k		39.00	1.0 (at 1 T of Induction at 60 Hz for 0.35 mm thick strip)	920	10.80	7.94	140	VACUUM SCH - MELZE
6	Hyperm 0	Carbon 0.05 Silicon 0.15 Iron Balance	2.20			3.5k ~ 20k	200 ~300	15.00						Telcon
7	Hyperm 36	Nickel 36 Iron Balance	1.55			8k ~ 15k	2k ~3k	70.00						Telcon
8	Hyperm Co50	Co 50 Iron Balance	2.60			12k	1k	60.00						Telcon
9	Radiome tal 4550	Nickel 45 Iron Balance	1.60			40k dc	6000 dc	45.00						Telcon
10	Radiome tal 48	Nickel 48 Iron Balance	1.60			60k dc	8000 dc	40.00						Telcon
11	Super Radiome tal	Nickel 48 Iron Balance	1.60			100 k dc	11k dc	40.00						Telcon
12	Radiome tal 36	Nickel 36 Iron Balance	1.20			30k	5k	80.00						Telcon

Table 4.7-1 Material list

4.8 MATERIALS FOR THE ACTUATOR DESIGN

The Table 4.7-1 give an overview of typical magnetic properties and selected physical properties of the magnetic materials. From the Table 4.7-1; we chose the following materials for our actuator design to be carried out in chapter 5.

Radiometal-4550

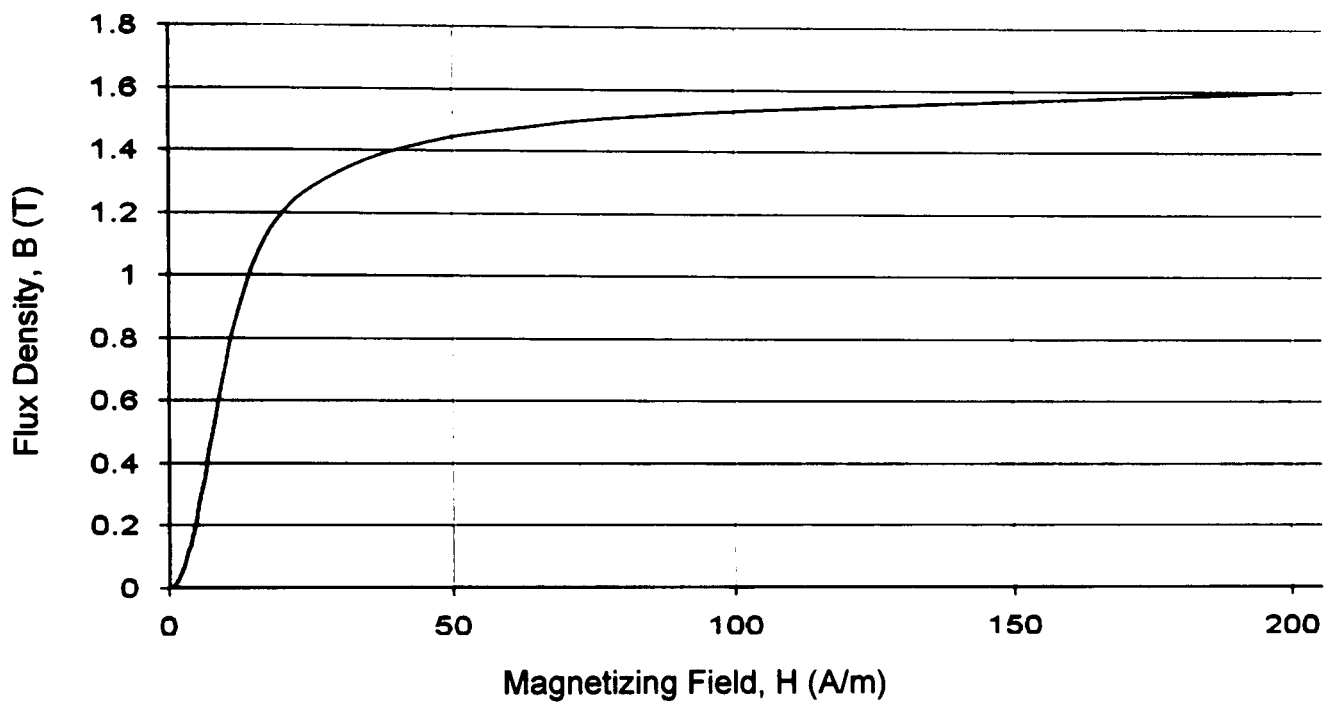


Fig. 4.8-1. B-H curve for Radiometal-4550

Armco

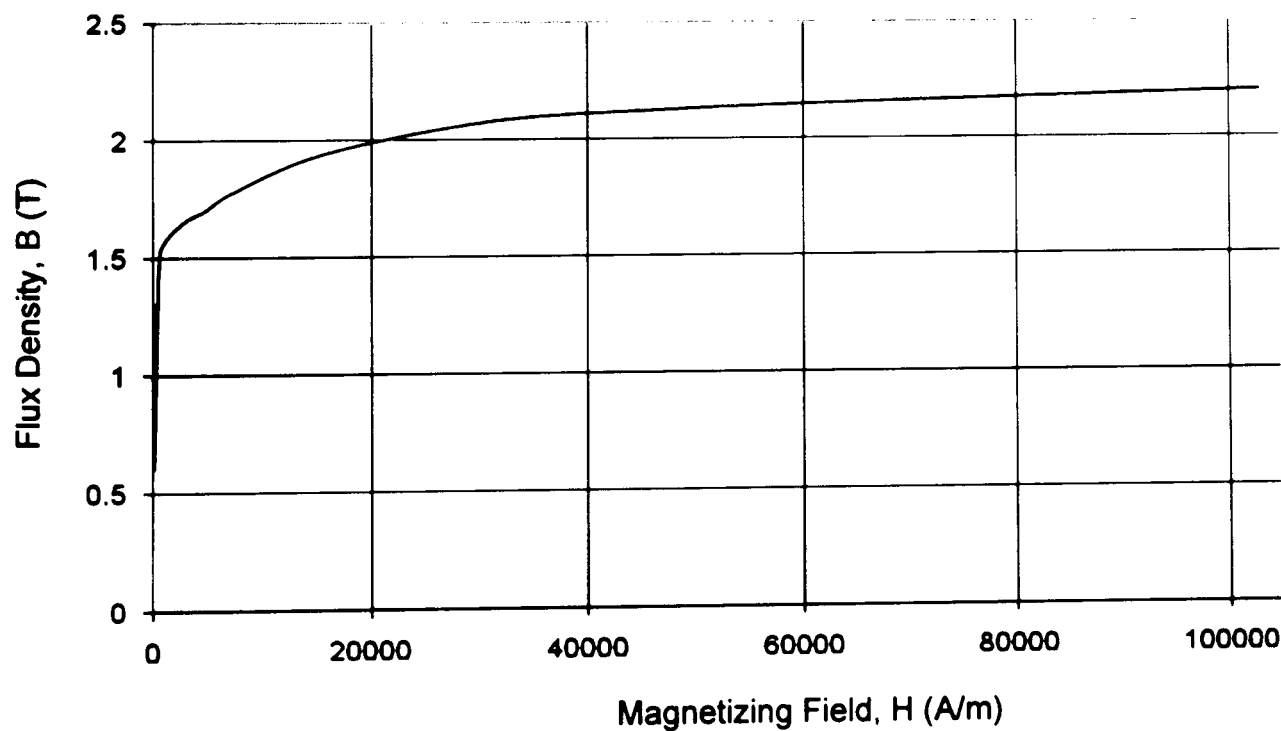


Fig. 4.8-2. B-H curve for Armco

Hypermco 50

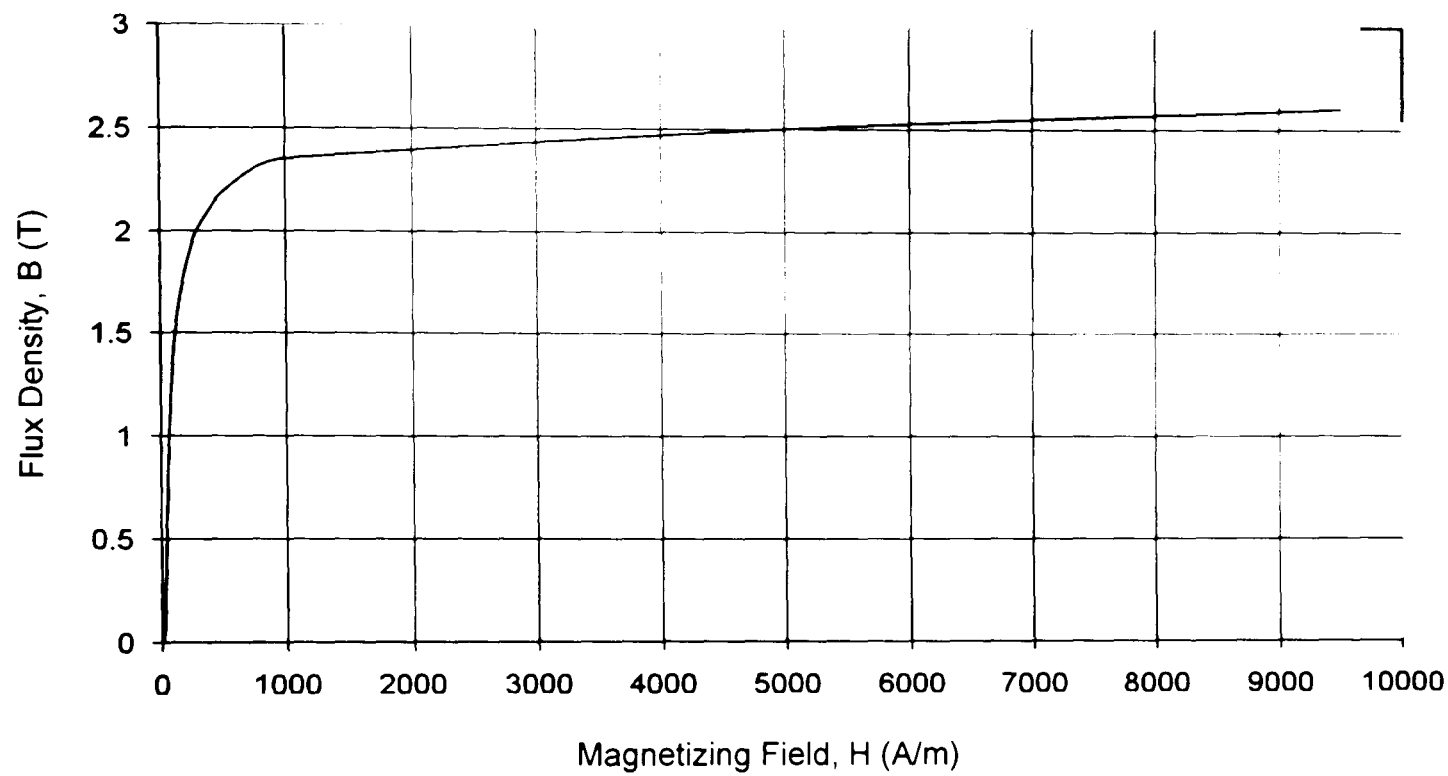


Fig. 4.8-3. B-H curve for Hypermco-50

Hyperm 0

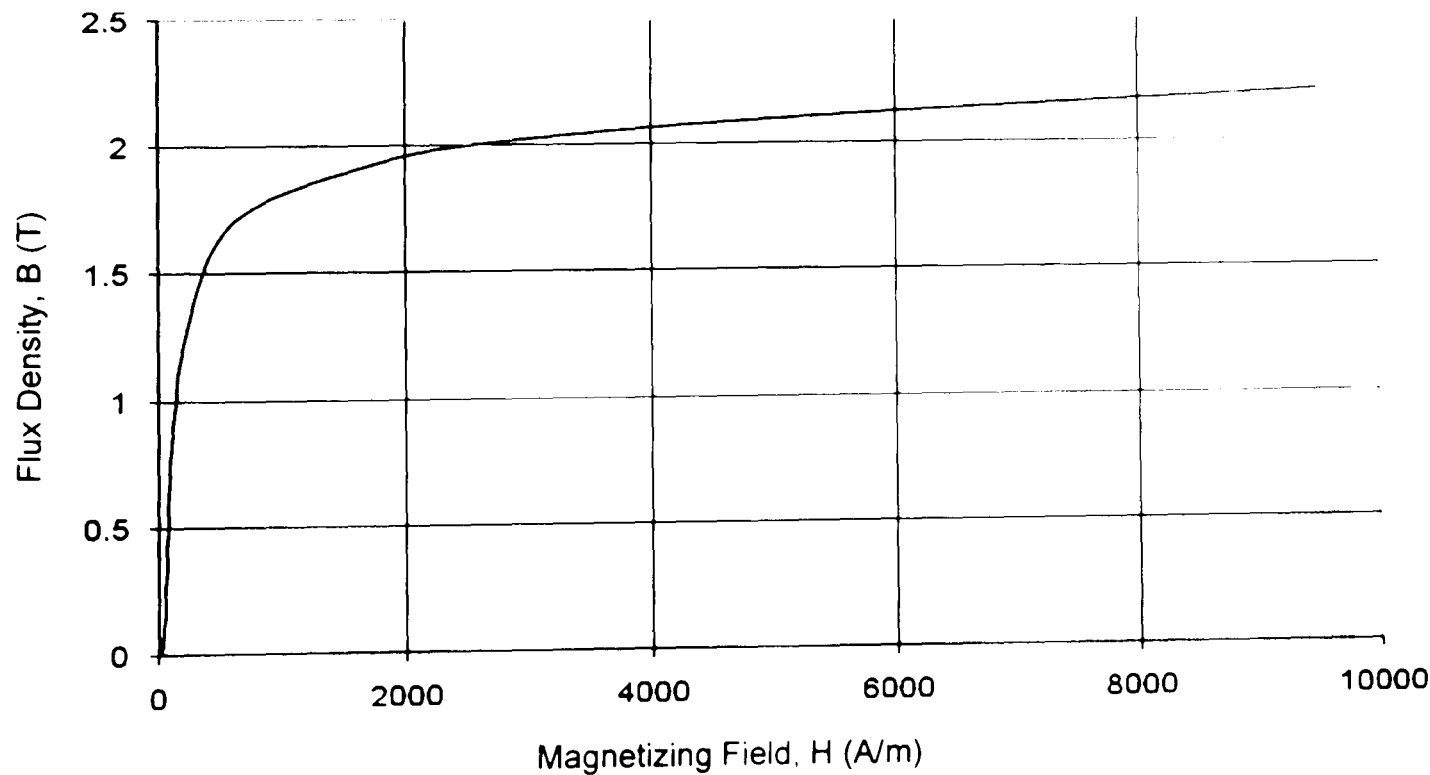


Fig. 4.8-4. B-H curve for Hyperm-0

4.9 SUMMARY

In recent years there has been an explosion of interest in new magnetic materials. These materials provide a fertile subject area for scientific investigations which transcend the boundaries of condensed matter physics, materials science and electrical and computer engineering. They also have current and future technologies applications in diverse areas such as energy conversion devices, field generation, sensors, actuators, data storage and memory devices.

A range of magnetic materials have been reviewed. The identification of new and improved materials, with enhanced properties (such as permeability, saturation polarization) is vital to the future development of many actuators and sensors.

Magnetic materials are classed as 'soft' if they have a low coercivity (the critical field strength H_c required to flip the direction of magnetization). Soft magnetic materials are a central component of electromagnetic devices such as step motors, magnetic sensors, transformers and magnetic recording heads. Miniaturization of these devices requires materials that can develop higher saturation flux density, B_s , so that the necessary flux densities can be preserved on reducing device dimensions, while simultaneously achieving a low coercivity. Common high- B_s soft magnetic films currently in use are electroplated CoFe-based alloys electroplated CoNiFe alloys.

Chapter 5

FINITE ELEMENT MODELLING OF ELECTROMAGNETIC ACTUATORS

5.1 INTRODUCTION

In chapter 2 mathematical formulations for analytical solution for an electromagnetic actuator have been elaborately discussed. In this chapter the finite element method is applied to the electromagnetic actuator for their analysis. The nature of physical phenomena governing electromagnetic system is complex and a complete model should account for magnetic, electric, mechanical and thermal aspects. The corresponding variables are not independent and parameters may vary due to several of these variables. A physical model is more or less coupled due to the importance of the interdependence of the operative phenomena. Because of this complex parameters, we can't solve these models using analytical solution [14], [84-86]. The methodologies for modelling and designing of EM ejector valves are based upon the modelling and computation of the 2D/3D nonlinear magnetic field distribution using the numerical finite element (FE) technique. This involves the steady-state and transient solutions of the nonlinear Poisson's equation for which there are no analytical solutions. The results are used for designing optimisation and for investigating the effects of various geometric, material, EM and mechanical parameters on the output performance of ejectors.

The primary requirement in the analysis of actuator is the evaluation of its output characteristics, i.e. the force output at various valve plate displacements. This is achieved by solving the field once for every position of the valve plate.

As usual with the finite element method, the first step is the discretisation of the field region. In this work the triangular discretisation is used all along. It attempts to summarise the magnetic field computations as used by Opera-2d package.

but it does not claim to present the computing method with full mathematical rigor.

In general the objective of finite element analysis is to approximate with a sufficient degree of accuracy and the values of the unknowns of a governing differential equation at selected points on the domain of a continuous physical system or structure. A mathematical model of the physical system or structure, divided into nodes and finite elements, is created, and the governing equations are applied to it and solved for each node .

The main function of the finite element program is to reduce the differential equation to a set of simultaneous algebraic equations, which can be readily solved by the computer [85]. The solution of these equations yields directly, or by means of minor additional computation, the desired unknown quantities.

The main step involved in a finite element analysis is to create the finite element model. The finite element model is a geometrical representation of the actual physical structure or body being analysed. Dividing the structure into a number of sub regions called “elements” creates the model [86]. The values of the unknown quantities are to be computed at selected points in the elements, usually at the corners. These points are called “nodes”.

It is important to emphasize that the finite element model is a mathematical simulation of the actual physical structure or body that it represents. The physical properties must be specified. If the body is made of an iron, the material properties of iron must be assigned to the elements of the body.

5.2 MATHEMATICAL MODELLING OF ELECTROMAGNETIC ACTUATORS

In analyzing the behaviour of a magnetic actuator, the primary objective is to determine the forces generated by the actuator in response to voltage applied to its coils and motion of the actuated device. Once this analysis is well established, it can be used in the design of actuators both in that it provides insight to the effects of the various design parameters and in that the analysis can be used to evaluate design choices [87-93].

The 2D finite element (FE) modelling of actuators is mainly based on the mathematical modelling and computation of magnetic field distributions in the 2D problem domain $\Omega(r, \theta)$ by solving appropriate field equations. This leads, in general, to the solution of the following non-linear Poisson's equation in terms of magnetic vector potential \mathbf{A} and current density \mathbf{J} . Magneto static problems are problems in which the fields are time-invariant. In this case, the *field intensity* (\mathbf{H}) and *flux density* (\mathbf{B}) must be obeyed [94-98]:

$$\nabla \times \mathbf{H} = \mathbf{J} \quad (5.4-1)$$

\mathbf{B} has zero divergence:

$$\nabla \cdot \mathbf{B} = 0 \quad (5.4-2)$$

Subject to a constitutive relationship between \mathbf{B} and \mathbf{H} for each material:

$$\mathbf{B} = \mu(\mathbf{H} - \mathbf{H}_c) \quad (5.4-3)$$

Where, \mathbf{H}_c is the coercive force of any permanent magnetic material.

$$\mu = \frac{\mathbf{B}}{(\mathbf{H} - \mathbf{H}_c)} \quad (5.4-4)$$

Opera goes about finding a field that satisfies equations (5.4-1) to (5.4-3) via a magnetic vector potential approach. Flux density is written in terms of the vector potential, \mathbf{A} , as:

$$\mathbf{B} = \nabla \times \mathbf{A} \quad (5.4-5)$$

Now, the definition of \mathbf{B} always satisfies equation (5.4-2). Then equation (5.4-1) can be rewritten as:

$$\nabla \times \left(\frac{1}{\mu} \nabla \times \mathbf{A} \right) = \mathbf{J} \quad (5.4-6)$$

Opera retains the form of equation (5.4-6), so that magneto static problems with a nonlinear B - H relationship can be solved. The advantage of using the vector

potential formulation is that all the conditions to be satisfied have been combined into a single equation. If ' \mathbf{A} ' is found, \mathbf{B} and \mathbf{H} can then be deduced by differentiating ' \mathbf{A} '.

If the field is time-varying, eddy currents can be induced in materials with non-zero conductivity. Several other Maxwell's equations related to the electric field distribution must also be accommodated. Denoting the *electric field intensity* as \mathbf{E} and the *current density* as \mathbf{J} , \mathbf{E} and \mathbf{J} obey the constitutive relationship [46]:

$$\mathbf{J} = \sigma \mathbf{E} \quad (5.4-7)$$

The induced electric field then obeys:

$$\nabla \times \mathbf{E} = -\frac{\partial \mathbf{B}}{\partial t} \quad (5.4-8)$$

Substituting the vector potential form of \mathbf{B} into equation (5.4-8) yields:

$$\nabla \times \mathbf{E} = -\nabla \times \mathbf{A} \quad (5.4-9)$$

In the case of 2D problems, equation (5.4-9) can be integrated to yield:

$$\mathbf{E} = -\mathbf{A} - \nabla V \quad (5.4-10)$$

and the constitutive relationship, equation (5.4-7) employed to yield:

$$\mathbf{J} = -\sigma \mathbf{A} - \sigma \nabla V \quad (5.4-11)$$

Substituting into equation (5.4-6) yields the partial differential equation:

$$\nabla \times \left(\frac{1}{\mu} \nabla \times \mathbf{A} \right) = -\sigma \mathbf{A} + -\sigma \nabla V \quad \text{in } \Omega(r, \theta) \quad (5.4-12)$$

The ∇V term is an additional voltage gradient that, in 2D problems, is constant over a conducting body. Opera uses this voltage gradient in some harmonic problems to enforce constraints on the current carried by conductive regions.

The alternative scalar potential form is derived by substituting $\mu \nabla \phi$ in equation (5.4-2) to give

$$\nabla \cdot \mu (\nabla \phi - \mathbf{H}_c) = \rho \quad (5.4-13)$$

The value ρ must be zero for a magnetic scalar potential, however if ϕ is an electric scalar potential then ρ is the charge density. The term involving \mathbf{H}_c represents permanent magnets for magnetic field analysis and electrets for electric field analysis.

Opera-2d/ST solves for the vector or scalar potential are defined by a non-linear Poisson equation. The vector potential form is usually used in magnetic field analysis because the scalar potential solution cannot include current as the source of the fields, however if a model is only excited by boundary conditions or by permanent magnets then either equation (5.4-12) or equation (5.4-13) can be used.

5.3 GENERAL PROCEDURES

In a continuum physical problem the field variable possesses infinite values because it is a function of each point in the body, or region. In the finite element method this problem of infinite number of unknowns is reduced to a problem of finite number of unknowns. The region is divided into sub-regions (called elements) and the approximate solution is represented by a function, over each sub-region with matching conditions on the boundary between them. Regardless of the approach used to formulate a finite element problem, the essential steps of the method can be listed as follows:

- (a) Discretisation of the field region by the selection of a type, or types, of elements. These elements are interconnected at certain nodal points,
- (b) Obtain the system equation for the entire solution region of the system,
- (c) Boundary condition,
- (d) Solution of the resulting set of equation.

5.4 DISCRETISATION OF THE FIELD REGION

The first, and an important, step on the finite element method is to divide continuum into elements. There are many ways of dividing the field region or systems with various element types. We are mainly concerned with two dimensional solutions of magnetic field, so we will limit our description to some of the commonly used plane elements in two dimension.

The most commonly used types of plane elements are general quadrilateral, rectangular and triangular elements.

Although the differential equations that describe \mathbf{A} appear relatively compact, it is very difficult to get closed-form solutions for all but the simplest geometries. That's where finite element analysis comes in.

The idea of finite elements is to break the problem down into large number regions, each with a simple geometry (e.g. triangles). For example, Fig. 5.4-1 shows a map of the mesh broken down into triangles. Over these simple regions, the "true" solution for \mathbf{A} is approximated by a very simple function. If enough small regions are used, the approximate \mathbf{A} closely matches the exact \mathbf{A} .

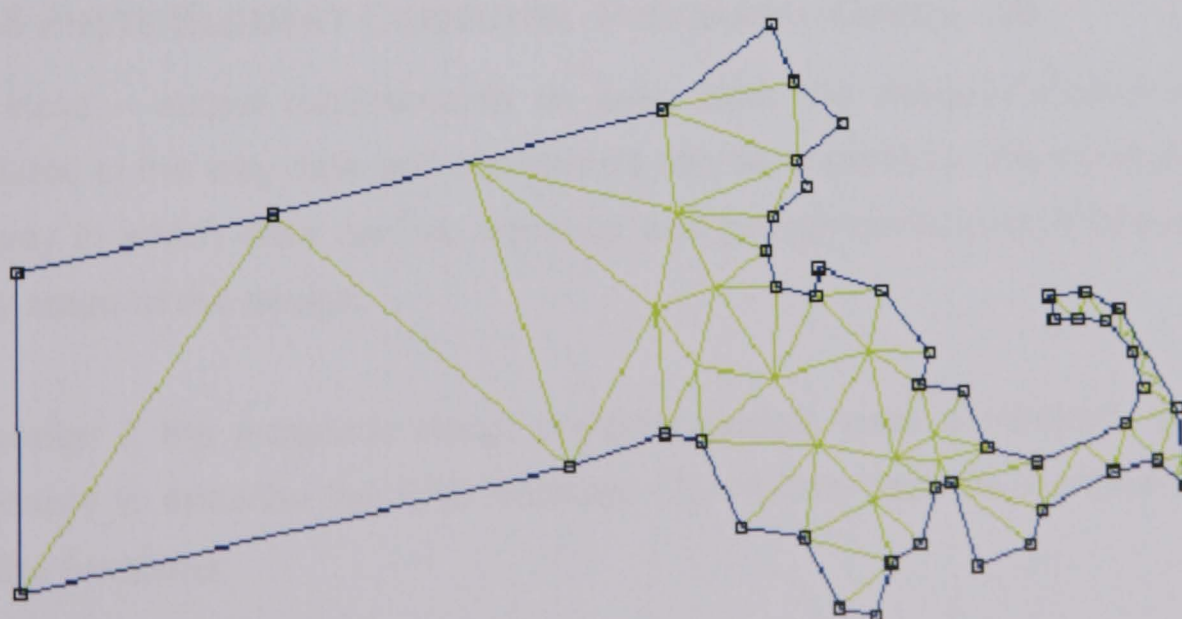


Fig. 5.4-1. Map of the mesh

The advantage of breaking the domain down into a number of small elements is that the magnetic problem becomes transformed from a small but difficult to solve problem into a big but relatively easy to solve problem. Specifically, triangulation of the problem results in a linear algebra problem with perhaps tens of thousands of unknowns. However, techniques exist that allow the computer to solve for all the unknowns very quickly.

Another important step in the process of finite element analysis is the choice of element types for discretising the field region. No general rule or criterion is available for choosing elements for a particular problem to give optimum performance. However, one can sum up the following points which require careful consideration before making a choice of element type,

- (a) Type of problem,
- (b) The number of nodal variables required,
- (c) The accuracy required,
- (d) Available computer time and storage.

In making the choice of element these factors need to be considered since, in the end, they can save time and labour.

5.5 FINITE ELEMENT COMPUTER PROGRAM – OPERA -2D

The input – output requirements as seen from the designer's point of view consisted in the way data and commands can be imparted to the computer, and the way in which data can be retrieved and design performance evaluated at every stage of the design.

In chapter 2 the magnetic circuit physical models were developed. It is now necessary to describe the CAD software Opera-2d's data file interface module and the functions.

The complete problems and solutions provided by the Opera-2d software consisted of three phases are:

- (a) Model set-up or pre processing,

- (b) Analysis,
- (c) Result display or post-processing,

The package allows generation of two dimensional models under its pre-processing stage using the 'DRAW' command, together with various identification parameters. Segmentation of the model creates smaller regions easing computations regarding the finite element analysis. Each region requires assigned parameter values, which are shown, listed below.

	<u>PARAMETER</u>	<u>NOTATION</u>
1.	Shape Code	POLYGON
2.	Material Number	0 (default value for air region)
3.	Permeability	1 (default value, permeability of air)
4.	Density	0 (current density)
5.	Conductivity	0 (default value)
6.	Phase	0 (default, angle in degree)
7.	N	0 (Conductor number)
8.	Symmetry	0 (default, program calculate total current)
9.	Velocity	0 (default, velocity of moving part)

The 'DRAW' command is the first command used for setting up the model. All regions contributing to the model were input in this way. There are five other input commands.

- (a) MODIfy – modifies the region
- (b) ERASe – erase a region
- (c) COPY- copies a region
- (d) BH data- provides data for B-H curve regarding magnetic field analysis
- (e) SYMM - defines co-ordinate system

It was the third command above 'COPY' which greatly assisted in forming the full model. This command allows the regions to be copied to a different position, with rotation and reflection where appropriate. Hence the basic regions

constituting the geometrical data for the model are copied using this command. An angle needs to be specified for either a rotation or reflection, and for a distinction between the two; mirror=yes/no is to be clarified. Replications made in this way do not give rise to new regions. They possess the same material and boundary conditions as the original regions.

Any modification made to region properties reflected or rotated is carried out using the MODIfy command. This command becomes useful when simple alterations are required without causing an increase in complexity of the model itself. The MODIfy command was used in the same way as the copy command for the relevant regions.

Parameters defining boundary conditions are the face values. Concerned with potential, it is necessary to give each of the four faces of the region individual potential values.

Before entering region data, it is essential to select appropriate units for the various geometric and physical variables using the options given by the 'UNITS' COMMAND. The co-ordinate axes for displaying models are set up by using the 'RECO' command. The need to set solution parameters is essential and is most important as results are the direct the 'SET' command which are used to define the type of problem to be solved. There are four parameters to be set:

- (a) SYMM – symmetry type; indicates any symmetry in field distribution
- (b) SOLN – solution type
- (c) ELEM – type of finite elements used. eg: linear, quadratic etc.
- (d) FIELD – it is set to Magnetic

For the model of concern, SYMM was set to XY Cartesian and SOLN to V (scalar potential). The latter two are default set values, ELEM-linear and FREQ=0.

After the solution parameters are set, mesh generation can be initiated using the 'MESH' command. It subdivides the model regions with smaller triangular finite elements and forms the data necessary to solve the field problem in the analysis that depending on the values assigned to N1, N2, N3 and N4 described earlier. For individual region, mesh density can be determined. Care has to be taken not to exceed the maximum number of elements for all regions, which stands at 100000. It is essential to use the mesh command after 'DRAW' in order to check the data is given. The boundary nodes with assigned potential can only be displayed using the RECOstruct command after the mesh has been generated. To ensure satisfactory execution, the program responds by displaying the boundary of the mesh. The boundary consists of all region boundaries. Adjacent regions which do not match are also displayed. The total number of nodes and elements are then listed followed by any inconsistencies in the region data. These are clarified as warnings or errors. The mesh data will only be stored if it is correct. A visual display of the meshed model can be seen before the mesh data is stored.

At this stage, the model definition and meshing are complete. With the 'WRITE' command a file can be created which will hold region and mesh data under the same file name but carrying different extensions, i.e. example.op2 and example.mesh.

The region and mesh data files created, are automatically formatted for input into the analysis program when the 'WRITE' command is executed. There are four main analysis programs available for solution of field problems set up by the pre - processor. They are referred to by two - character names.

- (a) ST- static,
- (b) SS- steady state a.c,
- (c) TR-transient,
- (d) PF-special analysis for static's regarding laminated materials.

They all are read data prepared by the pre- and post-processor and created result files which can then be read by the pre and post processor.

After quitting from the pre-processor stage, the analysis stage commences by selecting the appropriate program. The electromagnetic actuator is an electromagnetic field problem, therefore the option 'ST' was chosen. The name of the file given for the model is promptly requested and calculations carried out by the finite element method.

The mathematical analysis regarding magnetic problems uses formulation based on the low frequency limit Maxwell's equations. In section 5.2 these equations are clearly stated.

5.5.1 Convergence Factor and Some Aspects of Convergence

The convergence criterion can be applied to the permeability itself. If the maximum change of permeability between two successive iteration cycles falls below a certain value, the iteration is stopped.

The problem of convergence is the whole subject of computation of the magnetic field. This is especially so with non-linear permeability. Thus it is important to study the nature of the convergence for a solution.

One of the important factors is, of course the shape and size of the discretised elements. The convergence is also dependent to some extent on B-H characteristics and their form of representation.

5.5.2 Post-Processing

This stage of processing is accessed after the finite element method of analysis has been performed. The computations associated with model in the simulation stage are stored in a results file carrying extension *.res. The results are processed from the Opera-2d analysis program and field investigation of the model can be pursued.

The post - processing commands allow many field components to be viewed at points, along or over the cross - section of the model. Components can be integrated in one or two dimensions.

There is various different post - processing commands, of which the most common are listed below.

- POINT** : Evaluate field components at a point.
- LINE** : Evaluate field components along a line and display as a graph.
- CONTOUR** : Evaluate field components over regions and display as line coloured zone contours.
- VECTOR** : Evaluate field components over a quadrilateral patch and display as vector.
- INTLINE** : Integrate field components along line.
- INTAREA** : Integrate field components over regions.

Most post - processing commands have parameters COMPOnent, or VX or VY, to define scalar and vector field components to be displayed. Expressions can be used to define these output field quantities with the variables being system variables, user CONSTants and user PARAMeters of the commands. The expressions are evaluated for each field point.

The expressions fro COMPOnent, VX and VY used with any command become the default value for all other commands which use these parameters. The initial value for COMPOnent is POT (i.e. potential) and VX and VY are initially set to BX and BY. The CONSTant and PARAMeter commands can be used to perform further calculations on the results of the commands.

The system variable must be correctly used to achieve valid field results. The system variables hold the co-ordinates of the field point, normal and tangential unit vectors to lines, basic field quantities, material properties, the result of the post processing commands and physical constants.

The main system variables are listed,

- POT** : The solution potential at the field point.
MINIMUM : The minimum and maximum quantities for LINES and contours,
MAXIMUM : the maximum length of a field vector.
ERROR : The error in the element containing the field point.
INTEGRAL : The integral of the component from the INTarea and INTline commands.
FLUX : The potential integral from the INTline command.
ENERGY : The potential integral of the INTarea command.
Pi : π
Muo : μ_0
Epsilon 0 : ϵ_0
RMS ERROR: The RMS field error expressed as a percentage.

The initial command in the post-processing stage after 'clearing' from the analysis and selecting 'PP' is the READ command which reads results file from the analysis program.

Hence the file is read into the post-processing program. The mesh data file is also read at this stage. The co-ordinates for the model are given together with the RECOstruct command in order to create the display. At this point the commands listed above can be used. e.g. calculation of contour plots or line integrals.

After performing various field investigations on the model, the behaviour can be determined, and it is here that a redesign process can begin. Using the MODIfy command regions can be altered and properties changed. Also in the case of filed lines, what is usually apparent qualitatively is a more refined mesh needs to be generated from the shape of field lines and their smoothness relative to the model. If a redesign model is required then the alterations made must be re-processed i.e. A re-mesh must be generated and the model saved once again. Following this a re-run of the analysis must take place.

After mesh generation, the model may be viewed to display the meshed structure with its boundary conditions.

5.5.3 Boundary Conditions

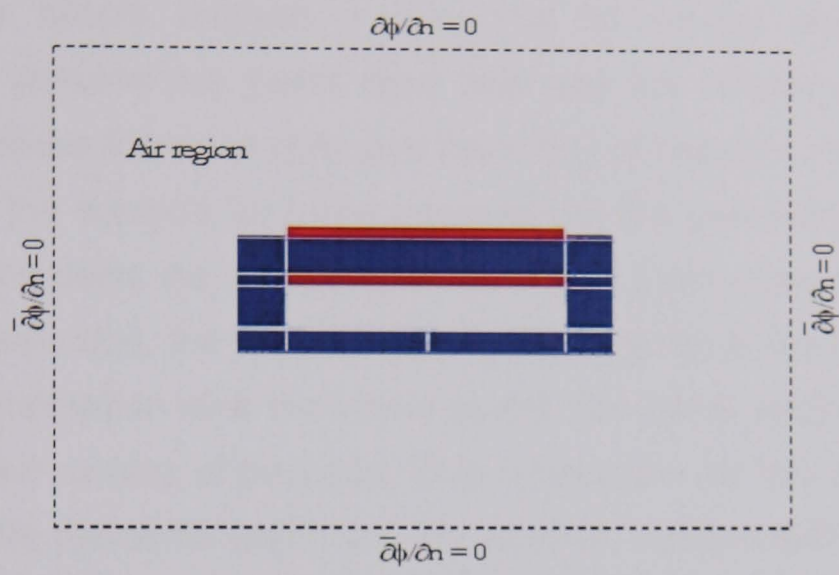


Fig. 5.5-1. FE model showing the boundary condition

In general, the essential boundary conditions are prescribed values of potential or field, valid on the boundary surfaces. In this case the tangential magnetic field (i.e. $\partial\phi/\partial n = 0$) is specified.

This is justified if the outer boundary of the problem domain around the actuator is chosen sufficiently far apart so that any further repositioning of the boundary surfaces away from the does not appreciably changes the FE solution.

5.5.4 Estimation of Errors in Finite Element Modelling

The local error at a point within a finite element model is strongly linked to the size of the elements surrounding the point and weakly linked to the average element size over the whole space, although this second source of error becomes more important and less easily estimated in non-linear solutions. The relationship between the local error in the solution and the surrounding elements' size is given by:

For linear shape functions,

$$E(\Phi) = O(h^2)$$

(5.5-1)

And for quadratic shape functions,

$$E(\Phi) = O(h^3) \quad (5.5-2)$$

Where E is the error, O means “of the order” and h is the linear dimension of the elements. This simple analysis is only true for square elements, but it is reasonable to assume the worst case and use the largest dimension for h . Unfortunately, these formulae only give the order of the error, the actual error is dependent on the solution, or more precisely on the geometry of the model in the vicinity of the point. As an example, consider a point close to the corner of a magnetised steel cube, the field will be weakly singular at the corner. Given the same size discretisation over the whole space, the errors will be far larger close to the edges and corners of the cube. This is because the low order polynomials used in the finite elements which are not good at approximating the singularity. Calculating the magnetic field from the potential solution generally results in larger errors in the field than there were in the potential.

Differentiation of the finite element shape functions to determine the field gives an error in the field that is worse by $O(h^{-1})$. In the case of linear shape functions, this results in an error in the field $O(h)$. In the ST SOLVER special facilities have been included in order to reduce the errors in the fields that are computed from potential solutions. Two methods are available that increase the field precision; the best method depends on the problem being solved. Nodal weighted averaging improves the field accuracy to $O(h^2)$. The volume integration technique does not improve the order of the error, but it enables the variation of the field to be calculated very accurately remote from steel or dielectric regions.

It is essential that the user of a finite element program to carry out a number of analyses to examine the effect of element size on the solution. Using the ideas introduced above it is clear that the best approach is to solve the same model with two levels of finite element discretisation or with the same discretisation by using linear elements in one case and quadratic elements in the other. Taking as an example the use of two levels of discretisation, such that the element dimensions are halved in the second case, the case with the larger number of

elements will have solution errors that are 4 times smaller (the errors in the fields evaluated by differentiation of the shape functions will be halved). Examination of the changes between the two solutions will give a good estimate of the discretisation errors, but not, as pointed out in the previous section any indication of the accuracy of the model.

This approach is very good for two-dimensional discretisation, but in three dimensions, the 8-fold increase in the number of nodes quickly becomes prohibitive for all but the simplest geometries. When increasing the overall discretisation becomes too expensive, it is necessary to carry out more trial analyses, in each case choosing particular regions of increased discretisation to determine the sensitivity of the solution to the change in element size. An experienced user will have learnt how to minimise the number of trials as a result of carrying out this type of experiment on a number of different geometries.

5.5.5 The Data Command Input File

The COMI input command file allows Opera-2d commands to be read from a file. Pre-processing commands for our model are stored in such a file. The file is prepared using the editor.

The significance of the command input file is that the series of models required in our study to be generated simply by altering the appropriate design parameters and calling the associated data file using the COMInput command. This Opera-2d facility simplifies pre-processing (and post-processing) by eliminating the tedious and time consuming operation of typing Opera-2d commands for every model, using the terminal keyboard. The most important steps of the data commands and units are already discussed in this chapter.

5.6 MATHEMATICAL MODELLING AND DESIGN OF HIGH-SPEED ACTUATORS

High-speed sorting machines based on optical properties are in the forefront of bulk sorting of many food products (rice, peanuts, coffee, peas, beans, etc.) [3-

9]. The non-contact sensor technology used to identify unwanted product items is based on optical techniques such as light transmittance, surface reflectance, and optical absorption. Most sorting machines of this type rely mainly on colour differences between 'accept' and 'reject' products and other physical properties that are detectable optically (e.g. shape, colour). Considerable progress has been made in recent years in the development, design and implementation of suitable optical components, detector arrays, signal/image processing hardware/software and control circuitry for these sorting machines. Depending on the food products and the nature of contaminants they contain, monochromatic, bichromatic and trichromatic optical sub-systems are readily used often for simultaneous colour and shape discrimination [7, 9]. These are combined with high-sensitive silicon CCD and/or, typically germanium linear detector arrays to obtain high-speed and high-resolution bulk sorting.

Fig. 5.6-1 shows the schematic diagram of an optical sorting machine showing the optical and ejector sub-system.

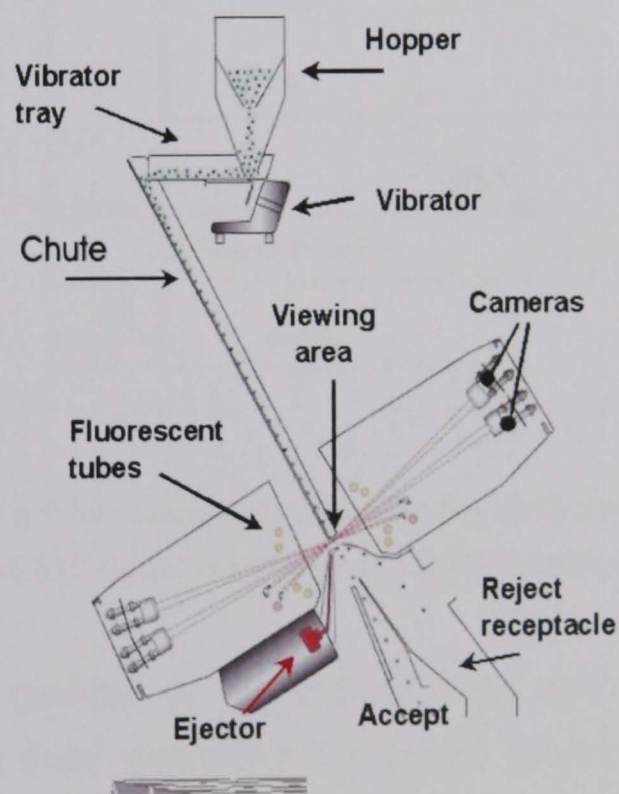


Fig. 5.6-1. Schematic diagram of an optical sorting machine showing the optical and ejector sub-systems

It is essentially an on/off valve actuator whose active components comprise an excitation coil wound around a magnetic core that attracts or releases a movable valve plate depending on the excitation state of the coil. Very tight

design and rigorous performance specifications make these ejectors used in high-speed sorting applications unique in terms of their design, manufacture and reliable exploitation. Typically, an individual ejector fits into an array of 32, 64, 96 or 128 ejectors to maintain the maximum packing density. They are often packaged in serviceable modules of two, four or more ejectors.

Fig. 5.6-2 shows the schematic diagram of a one of the designs of a high speed solenoid actuator used as ejector valves mentioned above. All these factors put severe constraints on a number of the geometric dimensions (e.g. TCL, TV shown in Fig. 5.6-2) of individual ejectors, some of which are directly linked to their overall lifetime and the ‘resolution’ of the optical sorting to be carried out.

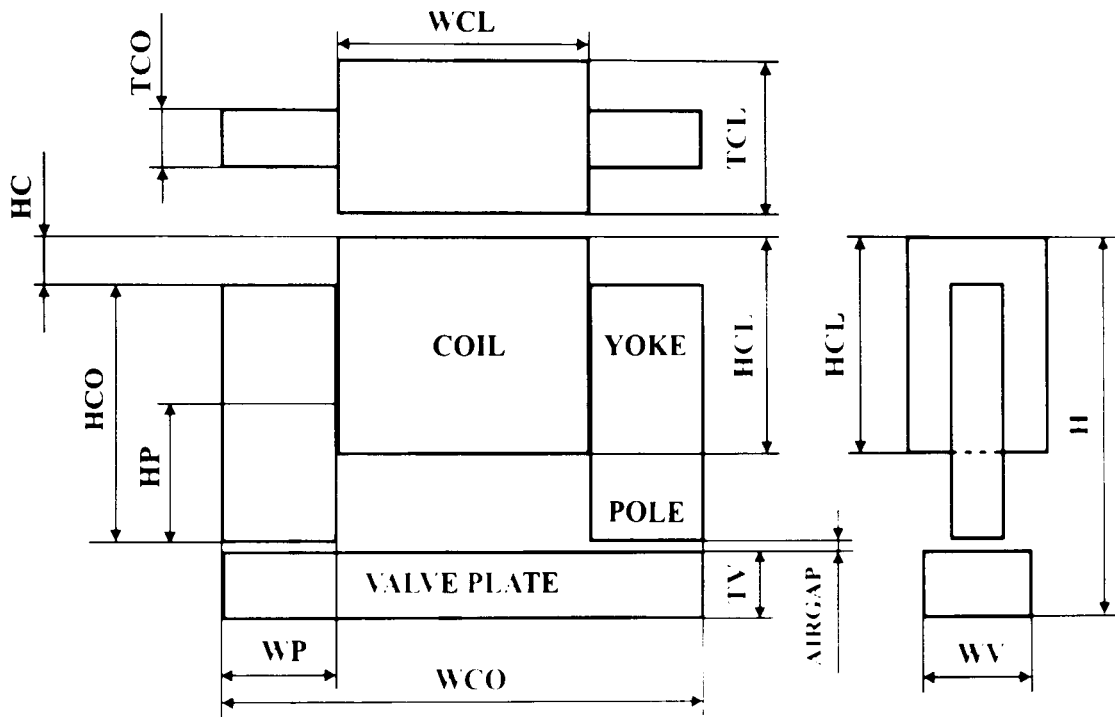


Fig. 5.6-2. Simplified schematic showing the main constructive features of a high speed EM actuator used as an ejector valve in an optical sorting

EM actuators rarely operate in the steady state and in various operational factors like start-stop duty, operating frequency, response time and damping. They have a significant influence on their designs. The EM part of the system is represented by electric and magnetic circuits with self-inductance, resistance and reluctance which are subject to variations, in general, due to eddy currents, saturation conditions, motional electromotive force (EMF), demagnetisation and hysteresis. The mechanical part is represented by friction, damping, elasticity and inertia as well as external forces. Together these two parts form an

equivalent electromechanical system which has to be optimised against the performance requirements and the complex behaviour of which is subject to static and dynamic analyses of these actuators.

For high frequency EM ejectors, the thermal problem of temperature distribution and heat dissipation are of vital importance. Like all other electrical devices, they generate losses (e.g. Ohmic loss in the winding, core and any circulating-current losses, etc.) manifested in the form of heat and temperature rise which may be considered to be one of the dominant factors in limiting the life of most high speed actuators. Temperature-rise may significantly increase the winding resistance, impairing control. The frequency response may be altered because both the electrical and the mechanical time constants are temperature sensitive. Often, when tightly packed, ejectors may create serious problems of heat sinking from individual units.

Also the diverse combination of materials used and the very extensive duty cycles may give rise to a myriad of thermal problems, unique only to high-speed actuators. The solutions to these problems will have a direct impact on the cost, size, reliability and feasibility of a given design. Compared to conventional solenoid actuators, the nonlinear and transient EM, thermal, and motional problems being solved in the above ejector valves pose substantial challenges because of their high frequency of operation and the requirement for a continuous and fail-safe duty cycle.

In general, the mathematical model of the above electromechanical system can be adequately represented by the following four differential equations given below. In summary, these represent equation (5.6-1) an electrical circuit equation for the excitation coil and control circuitry, equation (5.6-2) a nonlinear magnetic field equation (Poisson's equation) for the flux, the change of which changes the EM energy storage in the system and produces, the magnetic force, equation (5.6-3) a mechanical equation for this force, load (e.g. pneumatic force), friction, inertia, acceleration, speed and displacement, and equation (5.6-4) a nonlinear thermal diffusion equation for the conduction of heat produced by electrical power losses [99-106].

$$V(t) = iR + N \frac{d\lambda(i, z)}{dt} \quad (5.6-1)$$

$$\text{curl}(\nu \text{ curl } \mathbf{A}) = \mathbf{J} - \sigma \frac{\partial \mathbf{A}}{\partial t} + \sigma \mathbf{V} \times (\text{curl } \mathbf{A}) \quad (5.6-2)$$

$$F_m(i, z) = m \frac{d^2 z}{dt^2} + B \frac{dz}{dt} + Kz + F_e \quad (5.6-3)$$

$$\rho C \frac{\partial T}{\partial t} - \nabla \cdot [k(T) \nabla T] = q^B \quad (5.6-4)$$

In the above equations $V(t)$, i and $\lambda(i, z)$, and z are the applied voltage, coil current, flux linkage with the coil, and the displacement of the valve plate respectively, R and N are the coil resistance and the number of turns in the coil, \mathbf{J} , \mathbf{A} , \mathbf{V} are the coil current density, magnetic vector potential, and the plunger (valve plate) velocity; m , B , K , F_m and F_e are the mass of the valve plate, viscous damping coefficient, spring constant, magnetic force and the load force respectively; and T , and q^B are the temperature and the internal rate of heat generated per unit volume respectively. The material parameters ν, σ, ρ , C and k denote the magnetic reluctivity ($\nu=1/\mu$, μ is the permeability), the electric conductivity, density, specific heat and the thermal conductivity respectively.

In general, these equations are nonlinear and inseparable. The current produced by equation (5.6-1) creates the magnetic field given by equation (5.6-2) and produces the magnetic force which causes the displacement, speed and acceleration of the actuator obtained from equation (5.6-3). The current also generates the heat (per unit volume) and the resulting temperature distribution given by equation (5.6-4). There are two main approaches to the coupled solution of these equations: the direct coupled approach and the indirect coupled approach, neither of which alone is suitable to incorporate the whole array of factors which are expected to be encountered in the practical exploitation of high-speed ejector valves. These assume the necessity for qualitative and quantitative assessments of those factors that introduce nonlinearities in the system, in order to justify the use of one (or several) of these methods for modelling and simulation purposes.

For example, if the motional and eddy-current effects are negligible, the winding inductance can be taken as constant and the decoupling of the equations would be adequate for dynamic analysis. On the other hand, the direct coupled approach would be more appropriate if the eddy-current effects are negligible, but saturation and motional nonlinearities are prominent. Thus a methodology which includes the provision for using both coupled or/and decoupled solutions of electromechanical equations by *a priori* qualitative and quantitative justification would be most appropriate. The methodologies for modelling and design of EM ejector valves are based upon the modelling and computation of the 2D/3D nonlinear magnetic field distribution using the numerical finite element (FE) technique [107-111]. This involves the steady-state and transient solutions of the nonlinear Poisson's equation for which there are no analytical solutions.

The results are used for design optimisation and for investigating the effects of various geometric, material, EM and mechanical parameters on the output performance of ejectors. The thermal modelling involves the development of 2D/3D thermal models and the FE solution of the steady-state and/or transient heat transfer equations given by equation (5.6-4) above. The heat sources needed for this are given by the various losses mentioned above.

The coupling of the magnetic field and the thermal equations (owing to the dependence of the power density on the magnetic vector potential and the temperature dependence of the magnetic permeability and electric conductivity) may be realised either by indirect coupling (in which the equations are solved separately and coupled by means of power density and an iterative process is used to compute the power density and the temperature distribution) or by direct coupling in which the equations are solved simultaneously. The prime aim here is to obtain a vital insight into the thermal behaviour of the ejector valves and to enable quantification of the effects of various factors that affect such behaviour. The FE models also enable the simulation of possible modes of thermal failure and create an essential basis for the design of a predictable, thermally stable and reliable actuator sub-system [112-115].

Following the field computation, the magnetic force \mathbf{F} (a major design parameter) was calculated using the second Maxwell stress tensor \mathbf{T} due to magnetic field [7, 8]. \mathbf{T} is calculated from the tangential component of magnetic field intensity, H_τ and the normal component of the flux density, B_n on a closed surface S in air surrounding the valve plate. The surface density \mathbf{F}_ρ of the force \mathbf{F} is defined as the divergence of Maxwell's stress tensor \mathbf{T} :

$$\mathbf{F}_\rho = \text{div} \mathbf{T} \quad (5.6-5)$$

The surface force density \mathbf{F}_ρ can be defined as the sum of its normal $\mathbf{F}_{\rho n}$ and tangential $\mathbf{F}_{\rho \tau}$ components:

$$\mathbf{F}_{\rho n} = \frac{1}{2} \left(\frac{1}{\mu_0} B_n^2 - \mu_0 H_\tau^2 \right) = \frac{1}{2\mu_0} (B_n^2 - B_\tau^2) \quad (5.6-6)$$

$$\mathbf{F}_{\rho \tau} = H_\tau B_n = \frac{1}{\mu_0} B_n B_\tau \quad (5.6-7)$$

For the closed surface S surrounding the valve plate, the total force \mathbf{F} is calculated by integrating the Maxwell stress tensor \mathbf{T} on this surface:

$$\mathbf{F} = \oint_S \mathbf{T} \cdot \mathbf{n} \, ds \Rightarrow \int_S \mathbf{F} \, ds = \oint_S \left[\frac{1}{2\mu_0} (B_n^2 - B_\tau^2) \mathbf{n} + \frac{1}{\mu_0} (B_n B_\tau) \boldsymbol{\tau} \right] ds \quad (5.6-8)$$

This means the normal \mathbf{F}_n and tangential \mathbf{F}_τ components of the force \mathbf{F} :

$$\mathbf{F}_n = \frac{1}{2} \oint_S \left(\frac{1}{\mu_0} B_n^2 - \mu_0 H_\tau^2 \right) ds = \frac{1}{2\mu_0} \oint_S (B_n^2 - B_\tau^2) ds \quad (5.6-9)$$

$$\mathbf{F}_\tau = \oint_S H_\tau B_n \, ds = \frac{1}{\mu_0} \oint_S B_n B_\tau \, ds \quad (5.6-10)$$

Besides Maxwell stress tensor, there exist two other methods for the calculation of magnetic force – the virtual work and magnetizing current methods. Although in general these methods give results of comparable accuracy. The stress tensor method was used in this work because of the relative ease of its implementation. In order to increase the accuracy, at least two layers of finer elements were used in the air gap and the surface of integration was chosen in such a way as to completely surround the movable valve plate and lie

completely in air. This increases accuracy by reducing the effects of the tangential components of field vectors at the boundary of high and low-permeability FE regions.

5.6.1 Practical Elements of an Electromagnetic Actuator

Comprehensive integrated functional and physical models can fully describe a real system. This modelling approach was therefore used as the basis or backbone of a computer orientated design methodology. Simplifying assumptions had to be made in idealising the real systems and secondary effects neglected unless they were sufficiently relevant for most designs. In practical design situation secondary effects as well as other practical factors such as material constraints, manufacturing limitations (tolerance, dimensions, etc) have to be considered in order to take action to compensate or minimise their effect upon the design.

For the purpose of developing modelling methodologies and 2D FE models of actuators mentioned earlier was considered. Two types of electromagnetic actuator devices are going to be reviewed in this section (C-core & E-core).

Design constraints in a design exercise from sources such as:

- (a) Cost considerations,
- (b) Performance requirements,
- (c) Material properties,
- (d) Dimensional and geometric limitations.

Cost constraints are the economic limits set by the allocated budget for the design. Minimisation of these constraints from material, manufacturing, testing and developing turns into economic gain and marketing advantages.

Computer orientated design strategies can be used to minimise material cost and to reduce developing costs by minimising prototypes.

For determination of the design parameters, both analytical and numerical techniques have been employed. A general-purpose electromagnetic field analysis CAD software package (VF-Opera) that uses finite element methods has been used to model and solve the magnetic field distribution in a range of design variants of the device [10]. The design parameters are iteratively refined, ultimately resulting in the optimum design.

Performance constraints are either inherent design constraints or specification generated constraints. Inherent design constraints can be avoided by the appropriate choice of design. Specification generated constraints have to be met or at least be compromised with in order to attain the best possible design.

Material constraints are the limitations inherent in the materials. Choice of the materials for a given design specification is hence of paramount importance. A computer design approach allows comparison of performance for different materials. Magnetic materials have been studied extensively in chapter 4. From this study we have chosen the right magnetic materials for the actuator design.

Dimensional and geometric constraints are specification generated constraints or topologically dictated constraints. Dimensional requirements have normally to be met. Dimensional minimisation usually falls into material cost minimisation.

Modelling investigations were carried out to investigate C-core and E-core electromagnetic actuators. Modelling results demonstrate satisfactory regulation of the electromagnetic actuator force to the desired trajectories, for various input current, air gap and orientation. This addresses a key outstanding issue in development of high performance actuation system.

5.7 DESIGN VARIABLES OF C-CORE AND E-CORE ACTUATORS AND THEIR OPTIMISATION

In a systematic procedure of design once a design concept is chosen, the next step is to ascertain the variables of dimension and material property called the design variables which a designer can manipulate to produce a successful design,

For an electromagnetic actuator the important variables which a designer can choose are:

- (a) Size, shape and the number of turns of the coil,
- (b) Material of the core,
- (c) Thickness of the valve plate,
- (d) Length of the core,
- (e) Air gap distance between core and the valve plate,
- (f) Thickness of the core,
- (g) Width of the pole.

These variables can play an important part in design. By doing a sensitivity analysis as described in this section, one can pick out the most sensitive variable, in terms of meeting a particular objective e.g. sensitivity, non-linearity etc.

From the analysis, it has been found that thickness of the valve plate is the one of the sensitive parameter. However in the sensitivity analysis the valve plate thickness is not constant over the whole range of the variable, the factor needs to be used carefully over the whole range.

Alternatively, one can investigate the sensitivity of a particular variable over the range and find out the optimum value for a particular design specification.

By using the model developed, an investigation on the sensitivity of three design variables thickness of the valve plate, height of the yoke, width of the pole, has been investigated, Fig. 5.7-2 shows the sensitivity of the valve plate thickness.

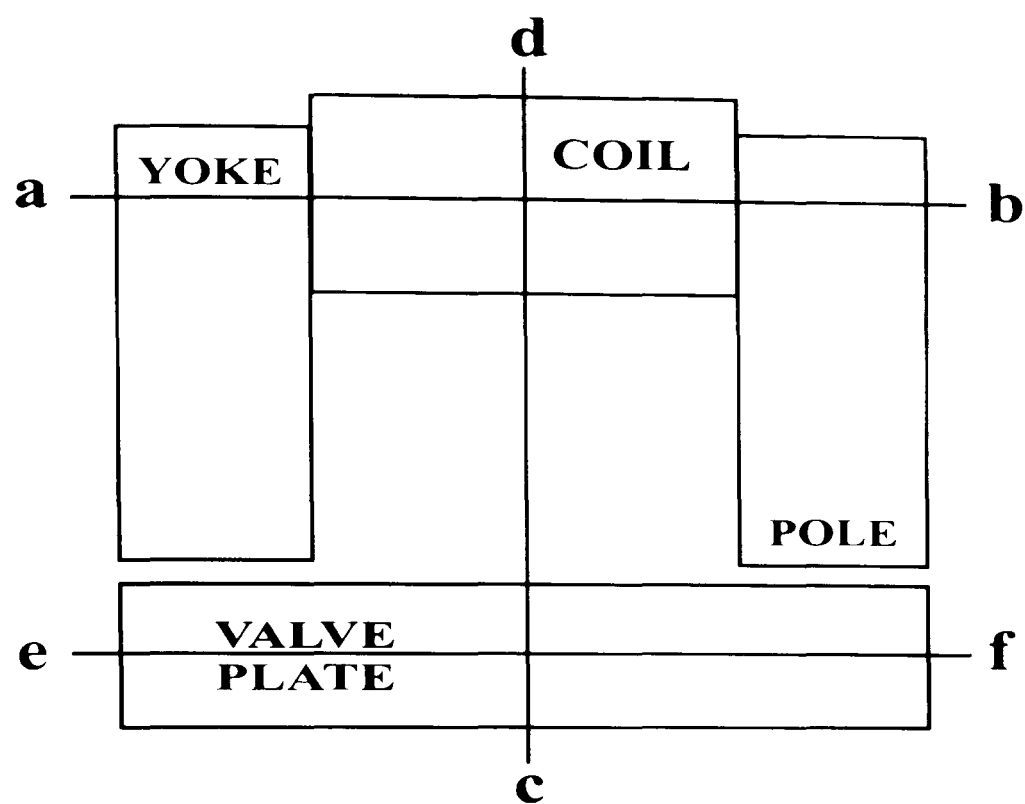


Fig. 5.7-1. Schematic of the EM actuator, showing the lines ab, cd and ef along which magnetic flux densities are calculated

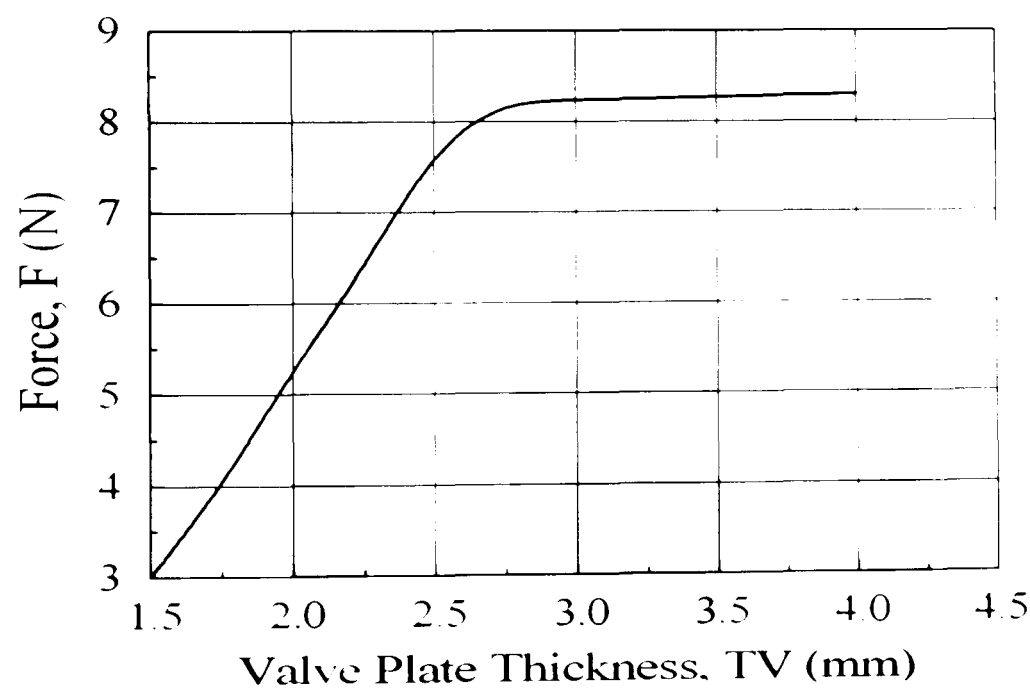


Fig. 5.7-2. Variation of force with valve plate thickness for c-core actuator, material for magnetic circuit Radiometal: 4550.

In the Fig. 5.7-2 the valve plate thickness is given as fraction of total length of actuator, Thus the results can be used for scaling of the device. From a design point of view this is an important consideration, because there is a remarkable improvement in the force of the device, if the valve plate is designed at the optimum thickness.

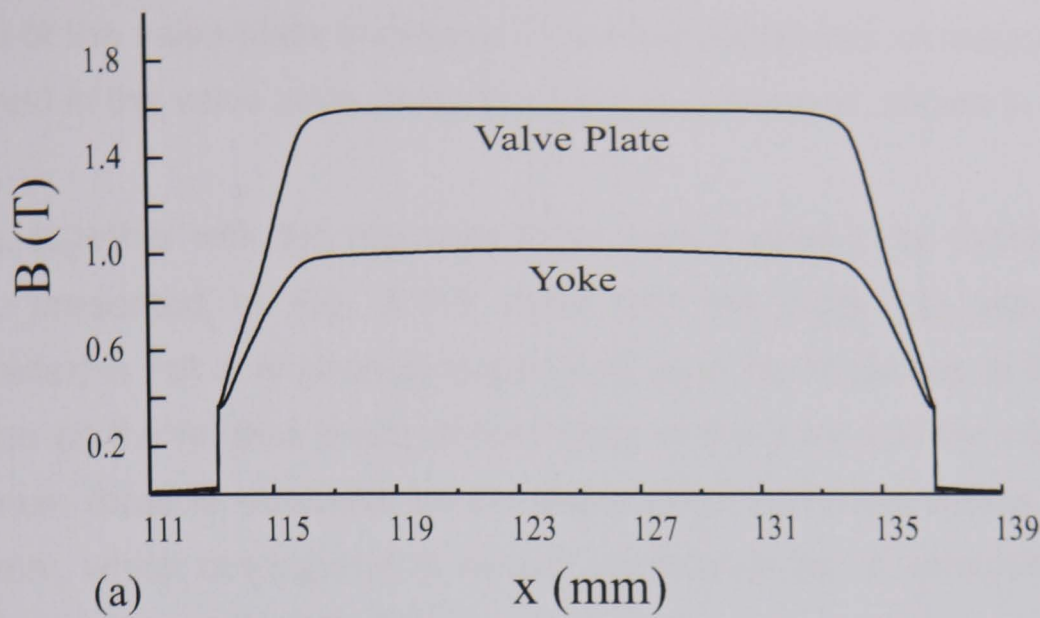


Fig. 5.7-3. Field distribution along the lines ab (yoke) and ef (valve plate); TV = 4.0 mm, material for magnetic circuit Radiometal-4550

Fig. 5.7-3 is the flux density distribution of the electromagnetic actuator along the line ab and cd in the Fig. 5.7-1 for a given thickness of the valve plate (TV=4.00 mm, HY=2.5 mm).

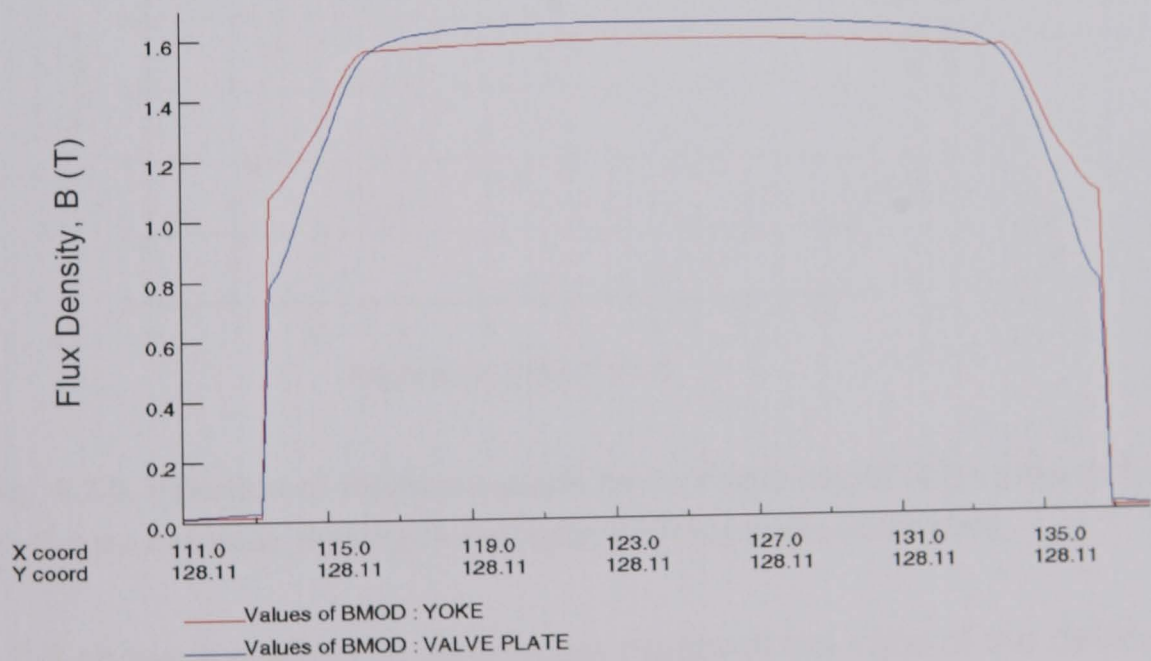


Fig. 5.7-4. Field distribution along the lines ab and ef; TV = 2.5 mm, material for magnetic circuit Radiometal-4550.

Fig. 5.7-4 shows the magnetic flux density plot in the yoke (HY=2.5 mm) and valve plate (TV=2.5 mm) for an electromagnetic actuator.

The modelling results are presented in Figs. 5.7-2 - 5.7-4, which show the effects of the valve plate thickness TV on the distribution of magnetic flux in the yoke and in the valve plate along the lines ab , cd and ef , shown in Fig. 5.7-1.

These, together with the magnetic force versus valve plate thickness, $F=f(TV)$ curve, presented in Fig. 5.7-3 show that the force (an important design parameter) is not only strongly dependent upon the thickness of the valve plate but also on the relative levels of saturation in the yoke and the valve plate. The maximum force is obtained for the valve plate thickness values between 2.5-2.75 mm, which correspond to almost identical levels of saturation in the yoke and in the valve plate (Fig. 5.7-4).

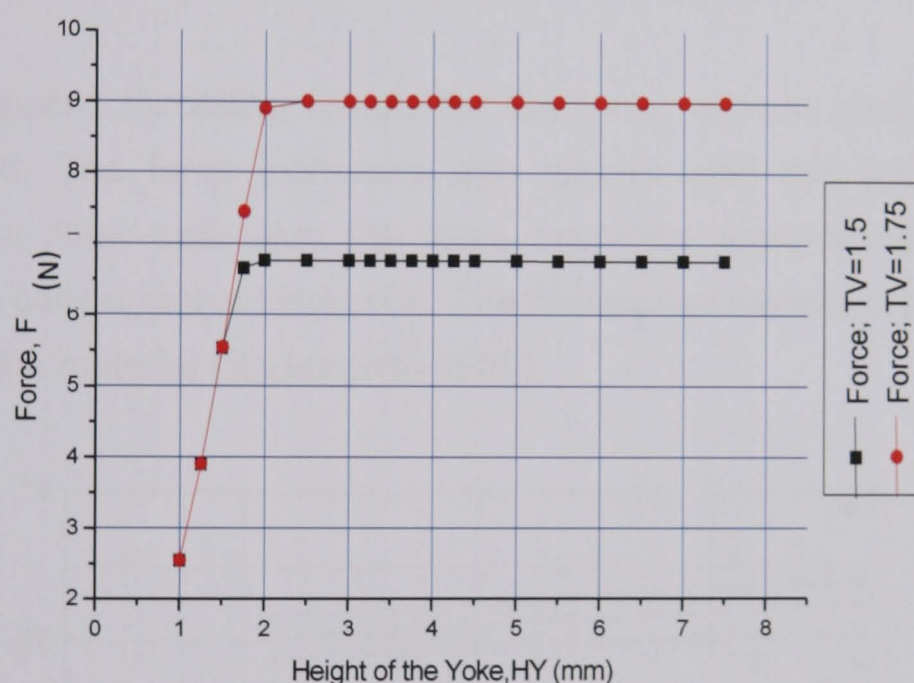


Fig. 5.7-5. Variation of electromagnetic force, F with height of the yoke (HY) for C-core Actuator, material for magnetic circuit Radiometal-4550.

Fig. 5.7-5 shows the effect of varying the height of the yoke of the device. It can be seen that force increases and as actuator's height of the yoke increases for each individual curves. This was carried out to find two different values of valve plate thickness. It is clear from our analysis that the force increases with the height of the yoke and also the height of the yoke (HY) approximately equal to thickness of the valve plate (TV), reaches the maximum value.

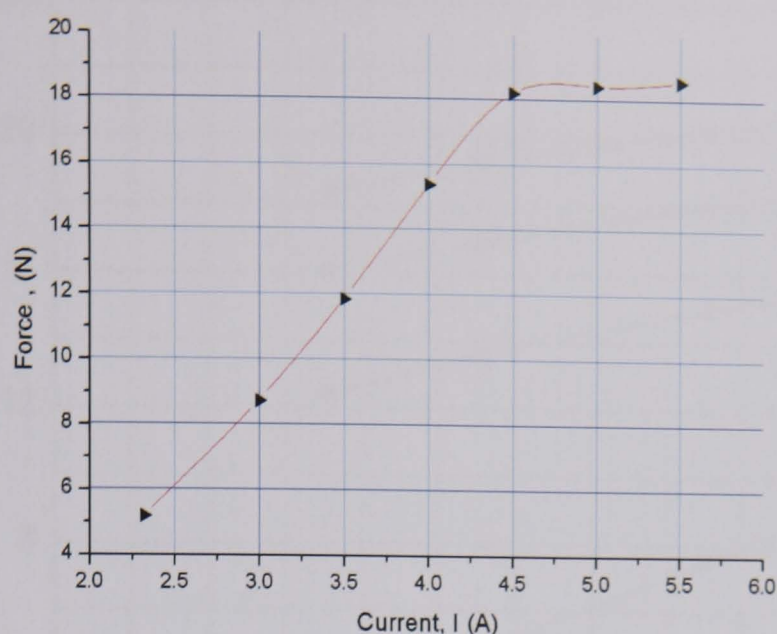


Fig. 5.7-6. Variation of electromagnetic force, F for different current inputs, material for magnetic circuit Radiometal-4550.

The computed modelling results for the force, current analysis are shown in Fig. 5.7-6. The force increases with current until the flux density up until saturation. After saturation the force becomes approximately constant even when the coil current is increased. The limiting flux density is defined by the B-H curve of the material (Radiometal-4550).

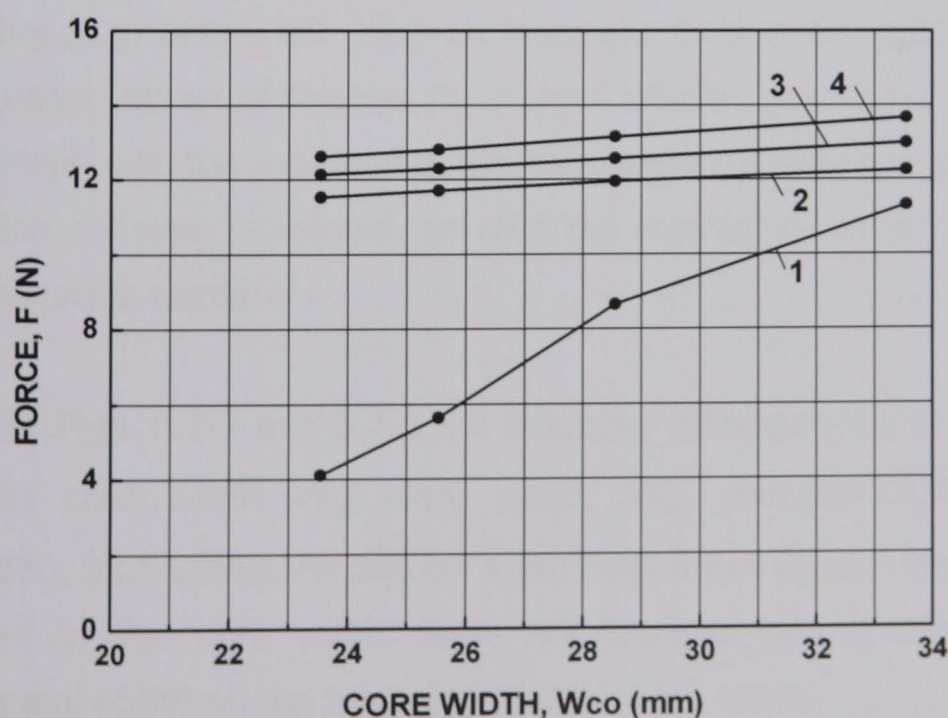


Fig. 5.7-7. Variation of electromagnetic force, F with the width W_{co} of the valve core for various excitation currents I : 1 – $I=0.5$ A, 2 – $I=1$ A, 3 – $I=1.5$ A, 4 – $I=2$ A. Material for magnetic circuit Radiometal: 4550.

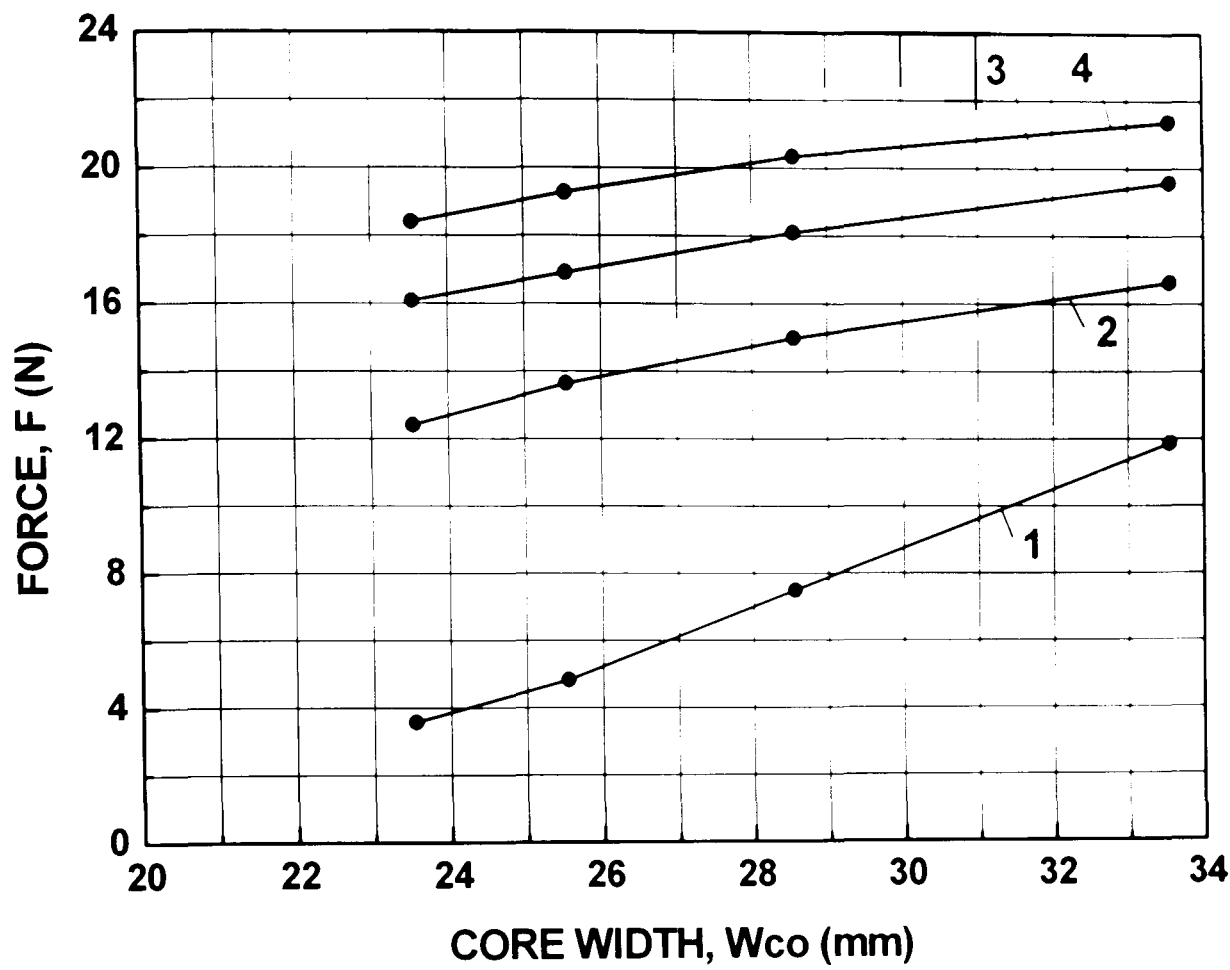


Fig. 5.7-8. Variation of electromagnetic force, F with the width W_{co} of the valve core for various excitation currents I : 1 – $I=0.5$ A, 2 – $I=1$ A, 3 – $I=1.5$ A, 4 – $I=2$ A. Material for magnetic circuit: Armco.

Modelling studies were also carried out to investigate the effects of core geometry (e.g. core width W_{co}) on magnetic force produced by various designs of the valve. Some of the results of such studies are shown in Figs. 5.7-7 and 5.7-8. Here, with the increase in the core width the effective cross-section of the excitation coil was increased, so also the number of turns that could be put in this new cross-section.

Thus, for Figs. 5.7-7 and 5.7-8 the following combinations of number of turns N and the core width W_{co} were used: W_{co} (mm)/ $N=23.55/191$, $25.55/225$, $28.55/286$, $33.55/388$). As can be seen from these figures for larger currents an increase in the core width does not have a strong effect (especially for Radiometal 4550) on the force produced by the valve.

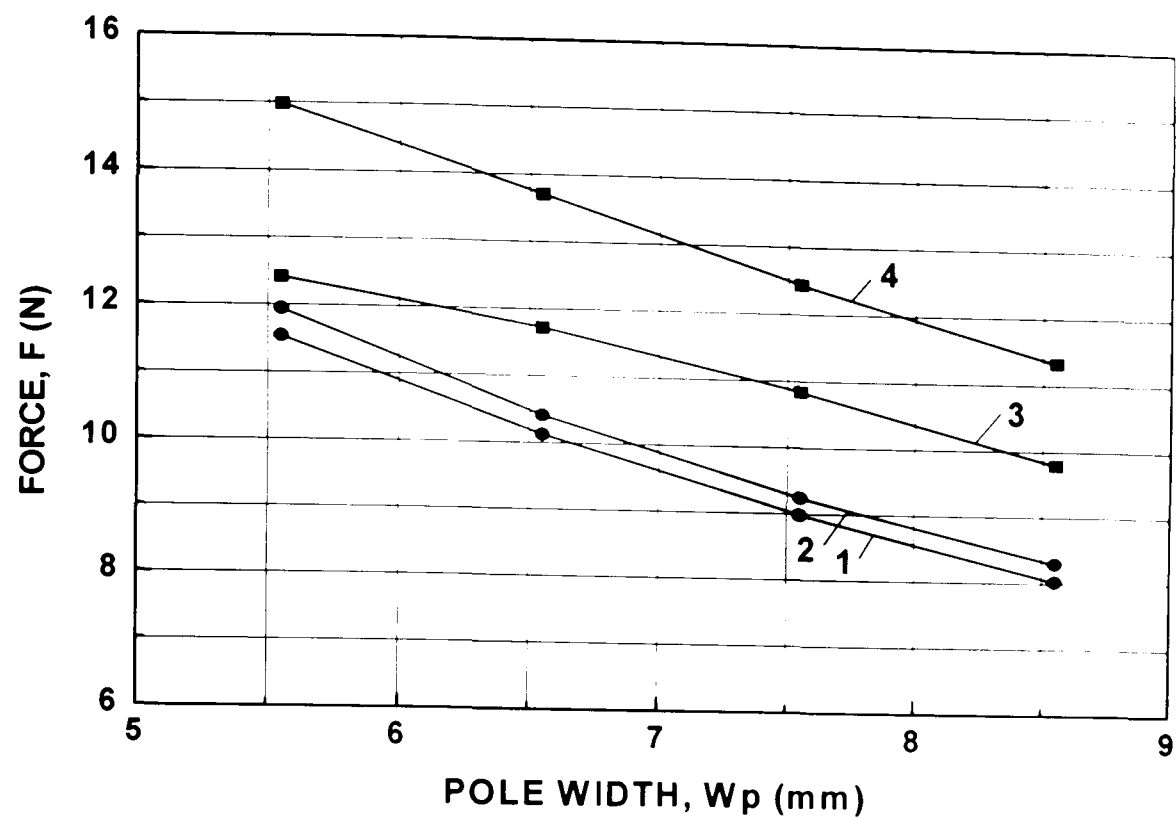


Fig. 5.7-9. Variation of electromagnetic force, F with the valve pole width W_p for various materials of the magnetic circuit (excitation current $I=1$ A): 1 – Radiometal 4550, effective area of excitation coil/ $N=14.43\text{ mm}^2/191$, 2 – Radiometal 4550, $21.45\text{ mm}^2/286$, 3 – Armco, $14.43\text{ mm}^2/191$, 4 – Armco, $21.45\text{ mm}^2/286$.

Fig. 5.7-9 shows the effects of pole width W_p on magnetic force produced by various designs of the valve. Here the pole width was increased by a step of 1 mm from nominal 5.55 mm to 8.55 mm for two different initial core widths (W_{co}): 23.55 mm, 28.55 mm. These dimensions were also increased (by a step of 2 mm) with the increase in the pole width. The changes in the effective areas of the excitation coil A for these two initial core widths were taken into account by using appropriate number of turns in simulation studies. The table 5.7-1 below summarises the geometric parameters used for Fig. 5.7-9.

W_p	W_{co} ($A=14.43\text{ mm}^2$, $N=191$)	W_{co} ($A=21.45\text{ mm}^2$, $N=286$)
mm	mm	mm
5.55	23.55	28.55
6.55	25.55	30.55
7.55	27.55	32.55
8.55	29.55	34.55

Table 5.7-1 Geometric variables used for FE simulation results shown in Fig. 5.7-9.

5.8 INVESTIGATION OF C-CORE-I ACTUATOR DESIGN

The body of the actuator is demarcated into simple geometric shapes as shown in Fig. 5.8-1 for the purpose of modelling. It consists of the ferromagnetic core with valve plate; and the winding tightly wound around the core. Generally, the analysis problem is given the core iron geometry ,coil winding configuration, the position of the plunger, and the currents in the winding coils.

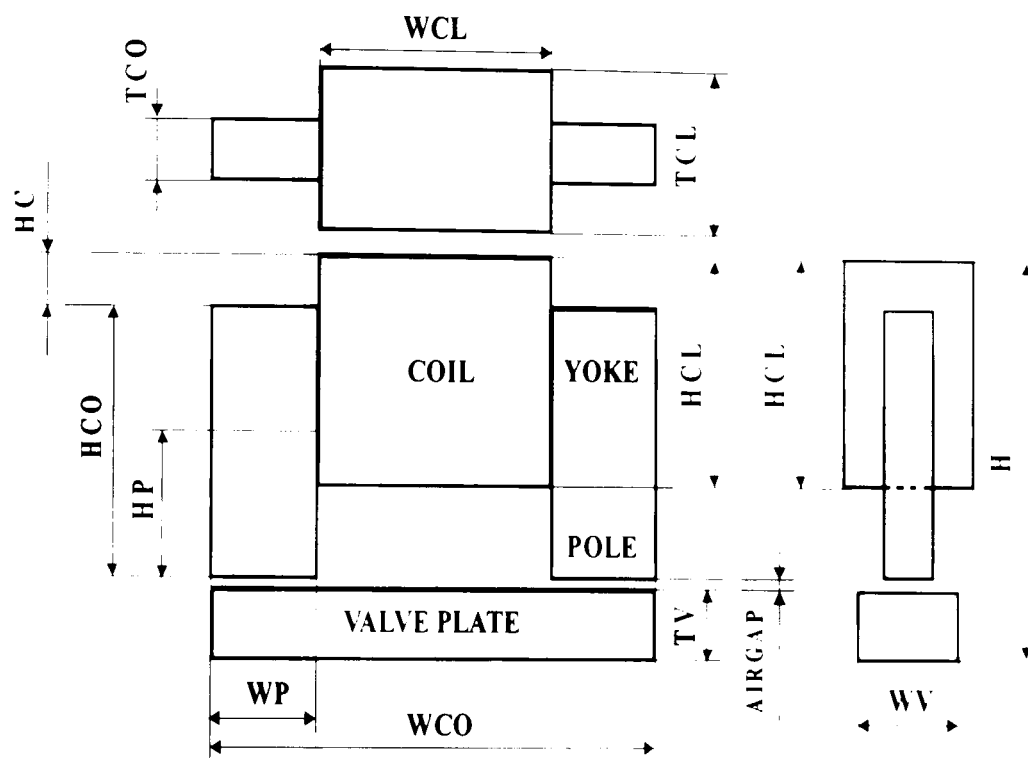


Fig. 5.8-1. Simplified schematic showing C-core-I actuator

Having established that the simulation procedures for the actuator were accurate and reliable, the electromagnetic actuator model was considered for analysis. The model was created using command input file in Opera-2d. The command input file was written as a program, with all parameters defined at the beginning; followed by a listing of all command procedures in order to generate the whole model. The command input file can be seen in appendices.

The set parameters units for an electromagnetic Problem are:

Length	MM (millimetre),
Flux density	TESLA (tesla),
Field strength	AM (ampere metre ⁻¹),
Potential	WBM (weber meter ⁻¹),
Conductivity	SM (siemen meter ⁻¹),

Source density	AM2 (ampere metre ⁻²),
Power	WATT (watt),
Force	NEWTON (Newton),
Energy	JOULE (joule),
Mass	KG (kilogramme).

By typing \$ COMI, the command input file is decoded line by line. Hence the regions become apparent one at a time until the entire model has been generated. Modelling approach has been adopted to set up the 2D model. During the course of model development substantial effort has been put into dividing the model and free space into number regions. This helps us to define a good mesh in the model and free space.

The 2D FE model of the actuator is built by defining all the geometric features of the actuator on a 2D 'base plane' in X-Y coordinates.

The choice of material for the core once again is largely dependent on performance and, of course, the cost. High permeability is needed to ensure proper flux guidance and minimum absorption of MMF. The magnetic materials have already been discussed in chapter 4.

The coil has been made up 191 turns with solid enamelled copper wires. The wire has a diameter of 0.3 mm. The cross-section of the coil has a nearly rectangular shape. The core coil and valve plate are modelled in X-Y symmetry in Opera-2d by drawing their exact geometry as a set of non-overlapping regions. Fig. 5.8-2 shows the 2D FE model development of the C-core actuator.

Dimensions	WCO	WP _L	WP _R	TV	WCL	HC	HCL	WV	TCO	HP	gap
Unit	mm	mm	mm	mm	mm	mm	mm	Mm	mm	mm	mm
C-core	23.55	2.78	2.78	2.50	17.15	0.65	4.08	3.50	2.20	6.22	0.1

Table 5.8-1 C-core model-I dimensions

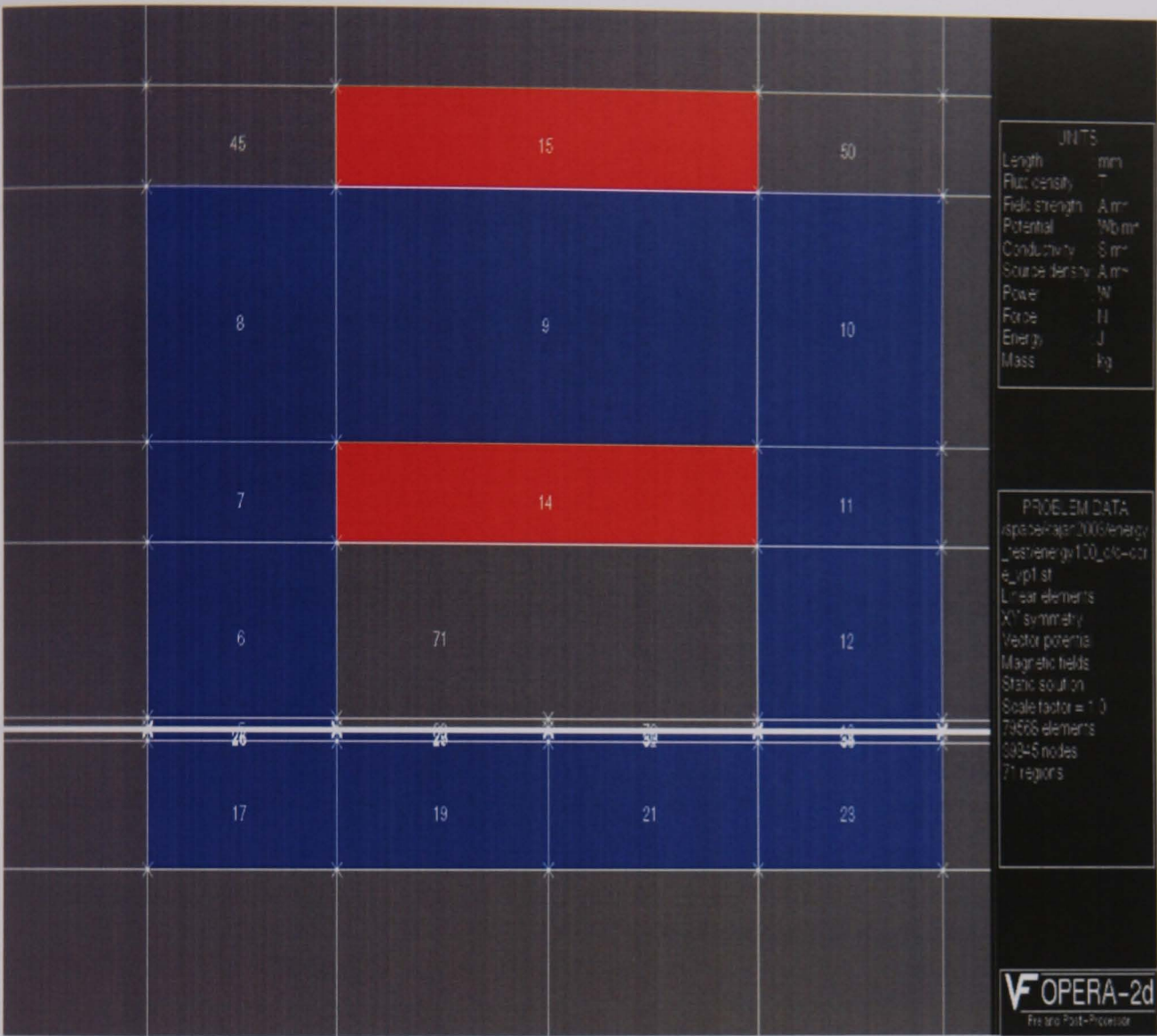


Fig. 5.8-2. C-core- I Opera-2d model

The typical Opera-2d model shown in Fig. 5.8-2 contains 80 k elements and 71 regions including the air regions surroundings of the actuator. For all modelling purpose commercial software package Opera-2d/3d on Sun Blade 2000 workstations operating under Unix was used. The linear solution requires only about 5-10 minutes running 12-18 iteration to solve the problems. Also the nonlinear solution takes about 20-35 minutes to run approximately 30-40 iteration to solve the most of the problems.

It has been used to calculate the magnetic field distribution in the model for various linear and non-linear cases. Running the static analysis program where the finite element method is used to average field values at nodes produced an RMS error of 0.86% indicating that the field values at nodes are continuous. Hence the potential solutions derived from partial differential equations are quite

accurate. The equipotential lines for the model show continuity and direction of contours which can be seen on Fig. 5.8-3.

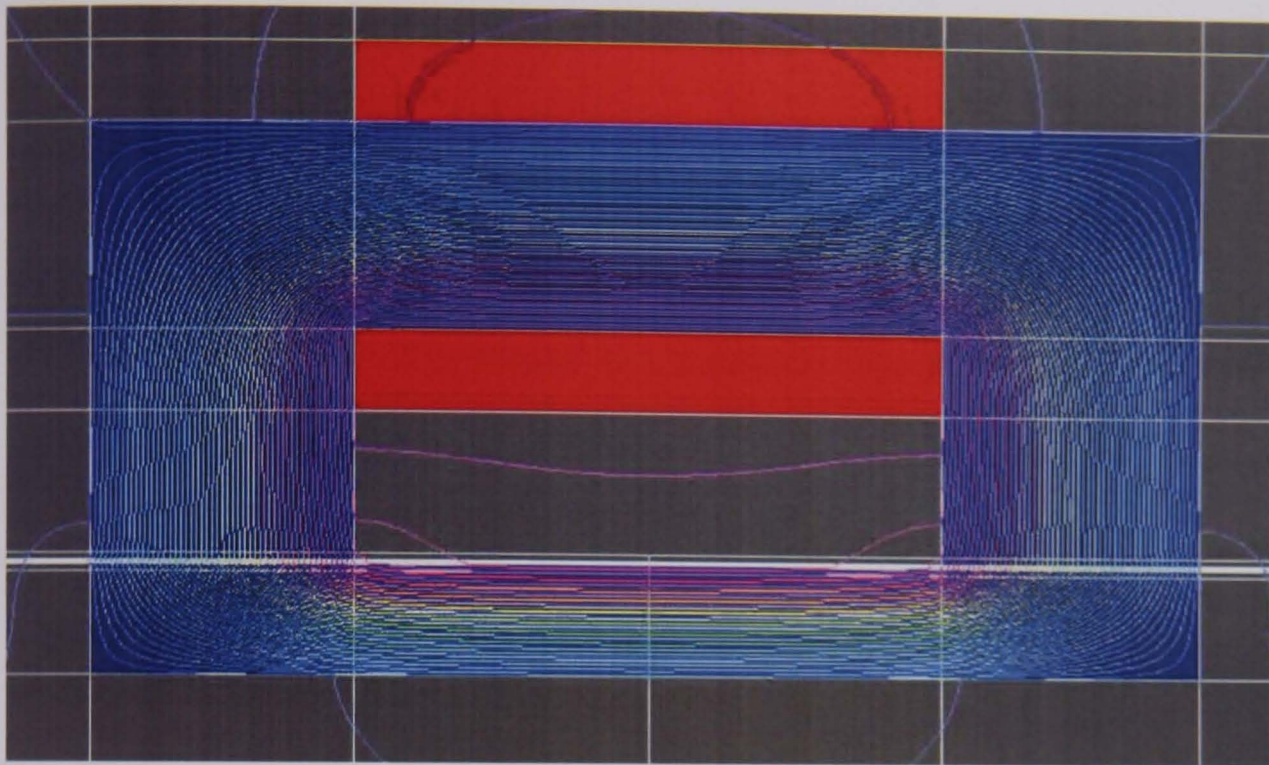


Fig. 5.8-3. C-core-I model field lines

Through this modelling investigation, the total linear force produced by the actuator is 64.59 N.

By running current through the coils that are wrapped around the yoke of actuator, a magnetic flux is created within the model. This flux is driven around the magnetic circuit that is completed by the target material. When the magnetic field passes through the air gaps to the target material, an attractive force is generated.

Magnitude of this force is given by equation (2.8-16),

$$F = \frac{\mu_0 A (NI)^2}{4\delta^2}$$

Method	Force (N)
Analytical	64.59
Opera-2d (linear)	60.04

Table 5.8-2 C-core-I force

Comparison of the FE modelling results with the corresponding analytical results, obtained for the C-core model-I is described in this section and is tabulated in the Table 5.8-2. The good agreement is obtained in this case between analytical and numerical method results. This established confidence in the modelling methodologies and in the 2D FE models help to realise these methodologies for further simulation studies.

The 2D model in Fig. 5.8-2 was used to carry out extensive non-linear simulation studies to investigate the actuator. The Fig. 5.8-4 is showing the distribution of magnetic flux density in the core and the valve plate for non-linear analysis.

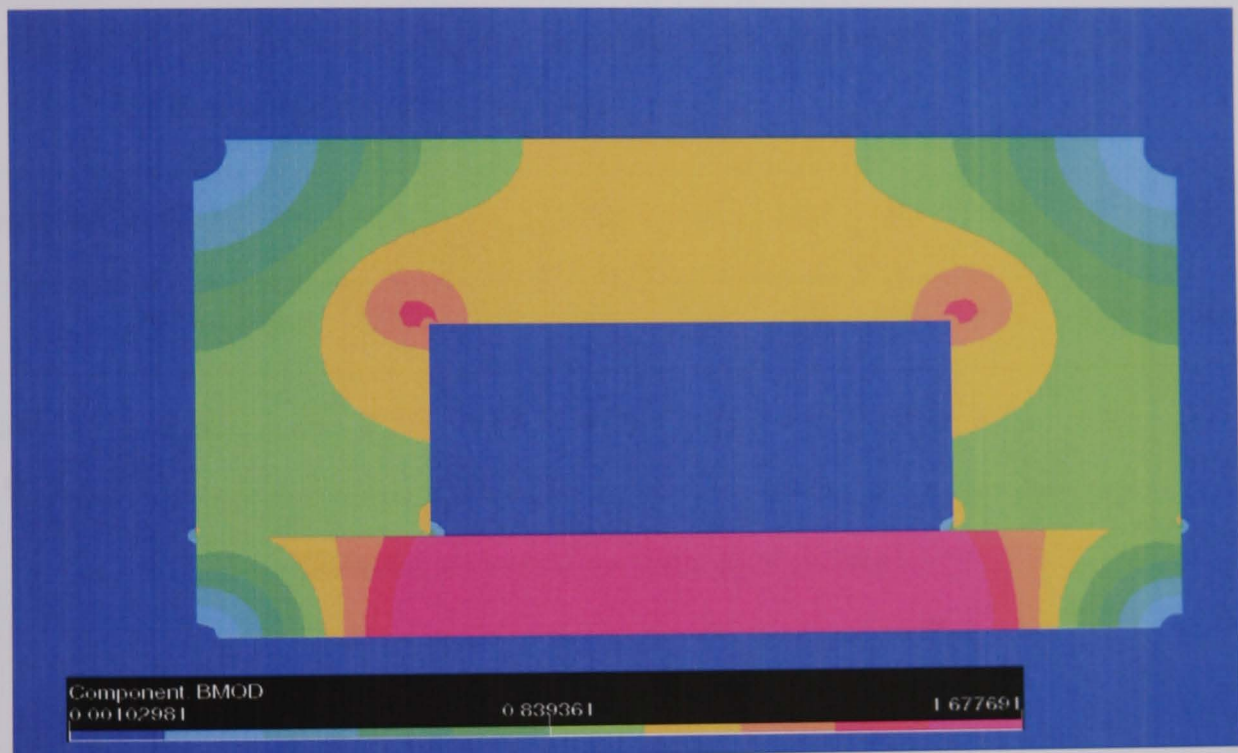


Fig. 5.8-4. C-core-I contour plot

The flux density in the core is 0.8 T and the valve plate is 1.6 T. The valve plate in this model is fully saturated (material:Radiometal-4550). The study of the effects of saturation conditions in the valve plate on the magnitude and distribution of magnetic field in the air closer to valve plate constituted a particular interest.

The net force on the valve plate is obtained by creating a surface totally enclosing the valve plate (Region 17-23 in Fig. 5.8-2) and integrating the magnetic stress over that surface. The net force produced by this model is 9.06 N.

5.8.1 Investigation Of C-Core-II Actuator Design

The model created in section 5.8 was modified to reduce the size of the actuator and different value of number of turns and current. The command input file originally created was modified to achieve the appropriate model which meant that reconstruction of the geometry from first principle operation was conveniently avoided. Alterations to region parameters and other parameters (i.e. Number of turns, current, etc) were made in the command input file. The command input file was read by ‘PP’ (pre and post processing), in Opera-2d. Once the model data was correctly specified, the files would be transferred by selecting ‘ST’ for field analysis as described earlier.

The body of the actuator is demarcated into geometric shape as shown in Fig. 5.8-5 for the purpose of modelling.

Dimensions	WCO	WP _L	WP _R	TV	WCL	HC	HCL	WV	TCO	HP	gap
Unit	mm	mm	Mm	mm	mm	Mm	mm	mm	mm	mm	mm
C-core	23.55	2.78	2.78	2.50	17.15	0.65	4.08	3.50	2.20	6.22	0.1

Table 5.8-3 C-core-II model dimensions

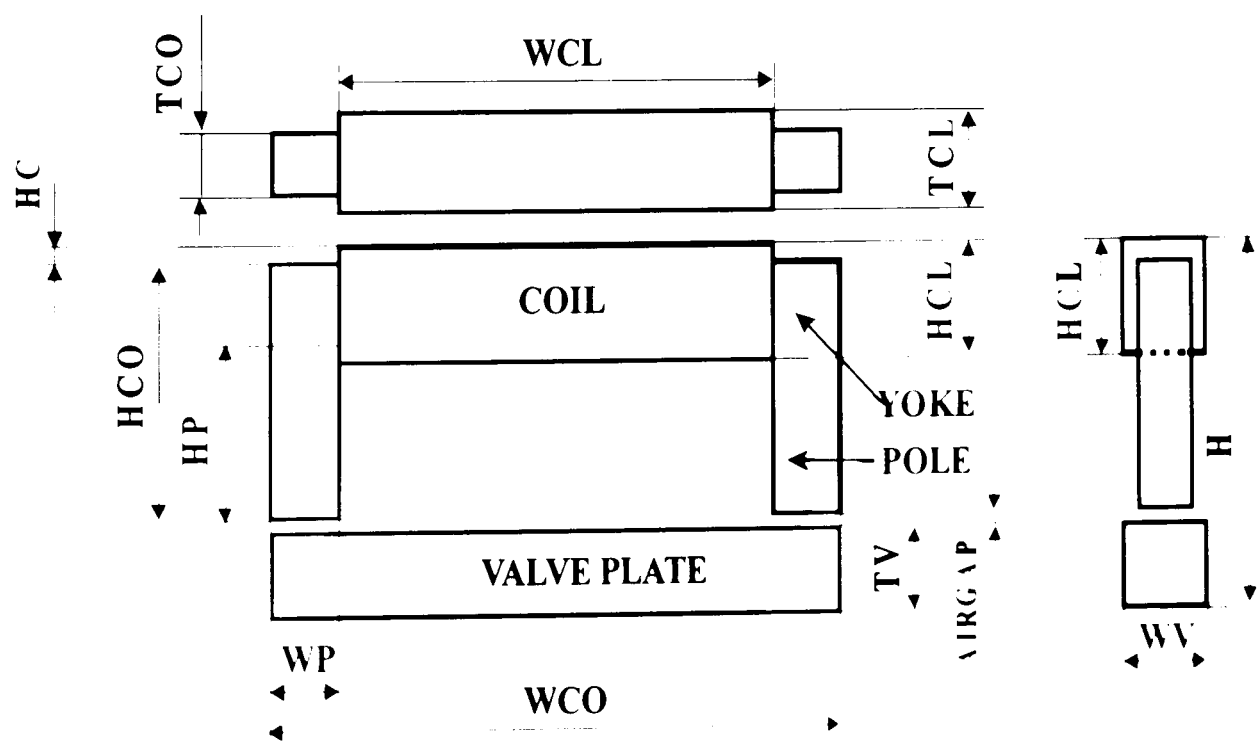


Fig. 5.8-5. C-core-II model

The width of this model is remaining same as in the model one. The rest of the parameters are listed in the Table 5.8-3.

To calculate the total force on a body, in this case the force on a plunger, an integration surface around the body is defined. Working in two dimensional space, Opera-2d calculated the total force on a body by performing a series line integral in Fig. 5.8-6, encircling on valve plate region.

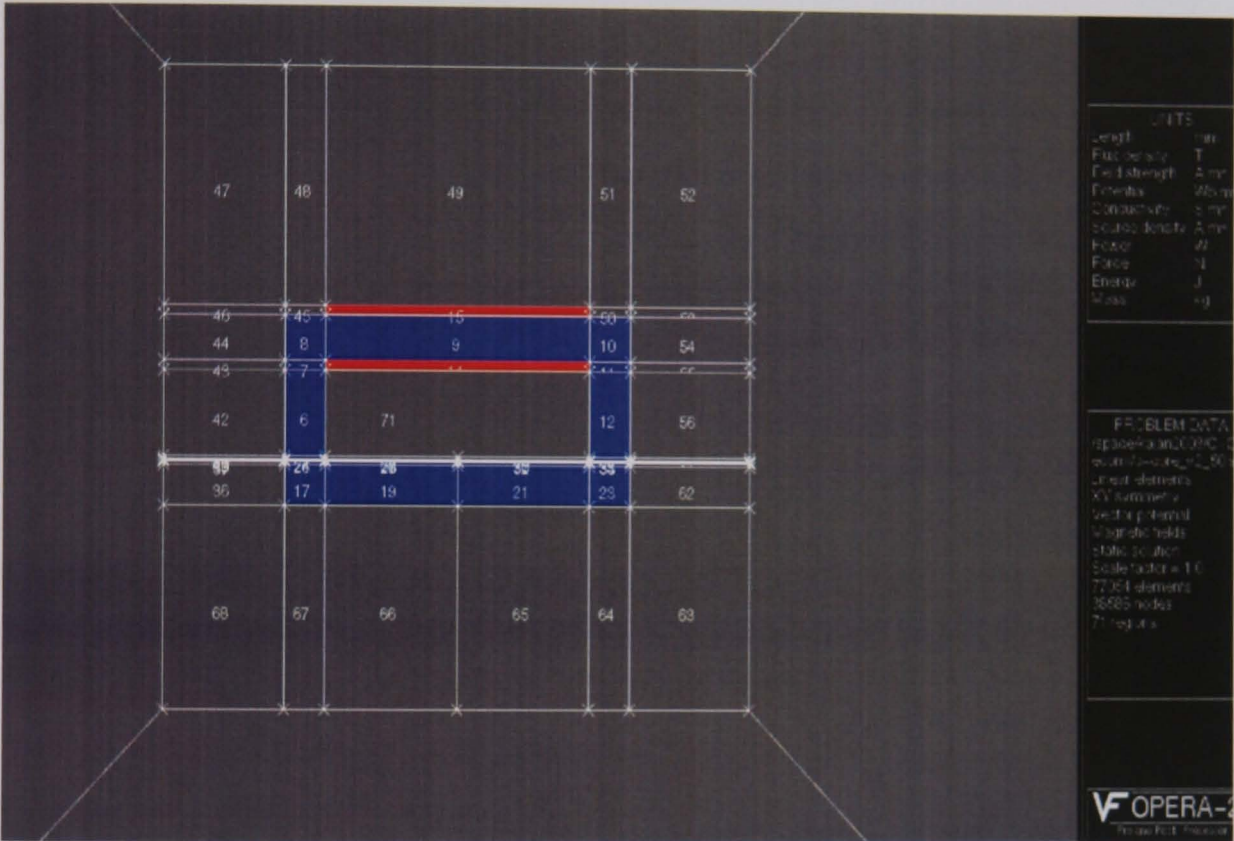


Fig. 5.8-6. C-core-II Opera-2d model

Method	Force (N)
Analytical	10.27
Opera-2d (linear)	9.41

Table 5.8-4 C-core-II force

Comparison of the FE modelling results with the corresponding analytical results, obtained for the C-core model-II described in this section is tabulated in the Table 5.8-4. In this model also an acceptable agreement was obtained between analytical and numerical method results.

The investigation is carried out by 2D FE modelling and computation of non-linear magnetic field distribution in the design shown in Fig. 5.8-7.

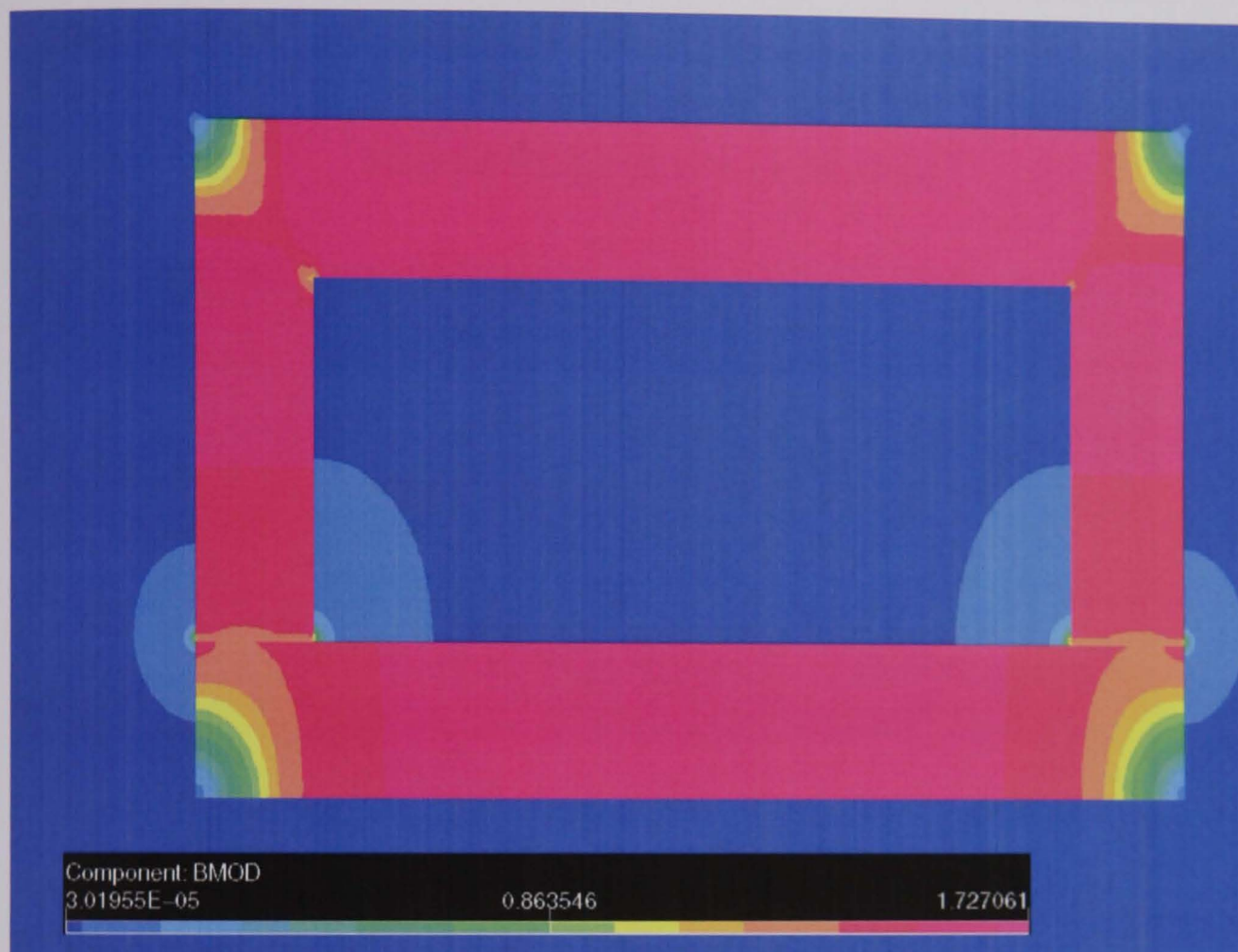


Fig. 5.8-7. C-core-II model contour plot

The investigation is carried out by 2D FE modelling and computation of non-linear magnetic field distribution in the design shown in Fig. 5.8-7.

To determine the force, we used the Opera-2d in non-linear solution. Fig. 5.8-7 shows the saturated core and plunger contour plot. According to Opera-2d, the force produced by this model is 8.28N.

5.8.2 Investigation Of C-core- III Model Design

Fig. 5.8-8 shows the cross section of the C-core solenoid under investigation. The proposed method (section 5.8) has been applied to solve the problem.

Dimensions	WCO	WP _L	WP _R	TV	WCL	HC	HCL	WV	TCO	HP	gap
Unit	mm	mm	mm	mm	mm	mm	mm	mm	mm	mm	mm
C-core	24.05	5.83	5.83	3.00	12.39	2.18	10.19	2.50	2.50	6.17	0.1

Table 5.8-5 C-core-III model dimensions

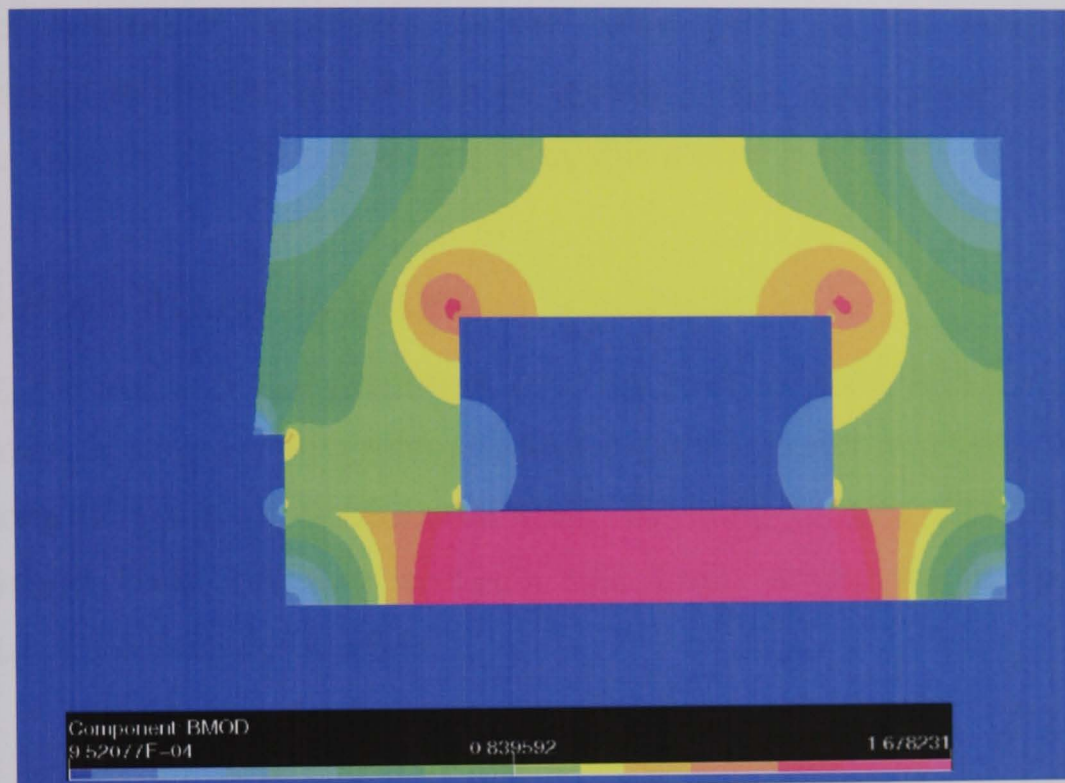


Fig. 5.8-8. C-core-III model contour plot

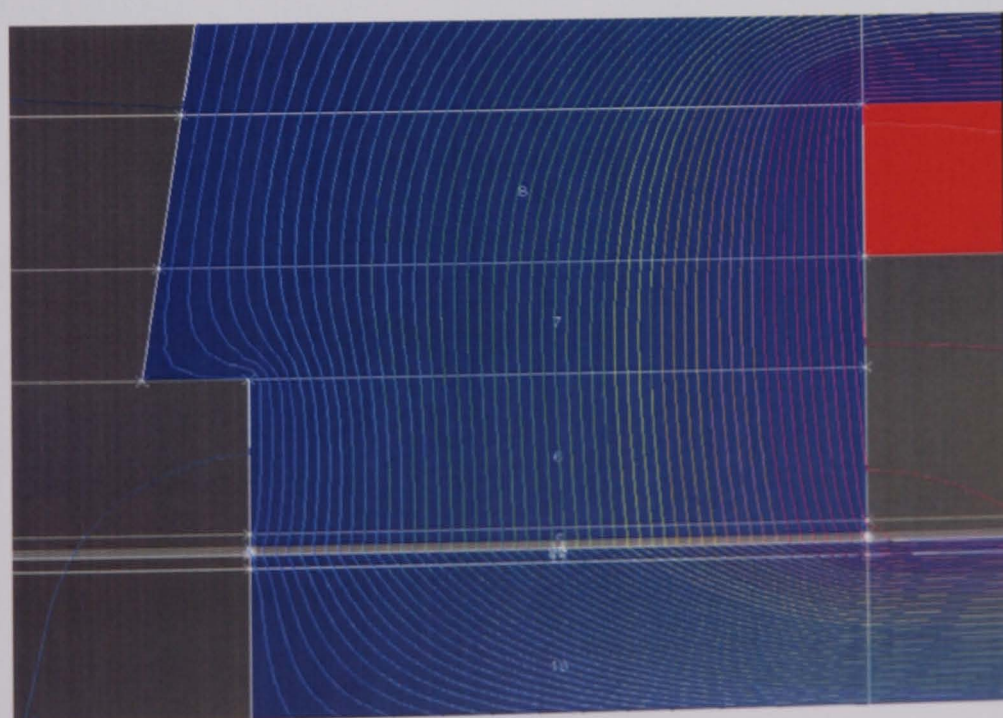


Fig. 5.8-9. Equipotential line contours of vector potential

For all modelling purpose commercial software package Opera-2d from vector fields, running on Sun workstation has been used. The modelling results are presented in Figs. 5.8-8 to 5.8-9 which show the effects of the material, geometry and saturation nonlinearities in the C-core-III model investigated.

The flux density in the core is 1.15 T and in the valve plate is 1.55 T. Valve plate in this model is fully saturated (material: Radiometal-4550). The study of the effects of saturation conditions in the valve plate on the magnitude and distribution of magnetic field in the air closer to the valve plate constituted a particular interest. The force generated by this model is 8.36 N.

5.9 E-CORE SOLENOID VALVE

Providing the ability of fast response and high traction force, and being a simple construction, a different structure solenoid E-core actuator has been developed. The E-core is made of Radiometal-4550. Working on this development, the computerized finite element analysis has been employed to analyse the behaviour of the actuator models.

5.9.1 Investigation of E-Core-I Model Design

Fig. 5.9-1 shows a design of an E-core with two planar coils connected in series for generating a magnetic flux. The dimensions of E-core-I are shown in Table 5.9-1.

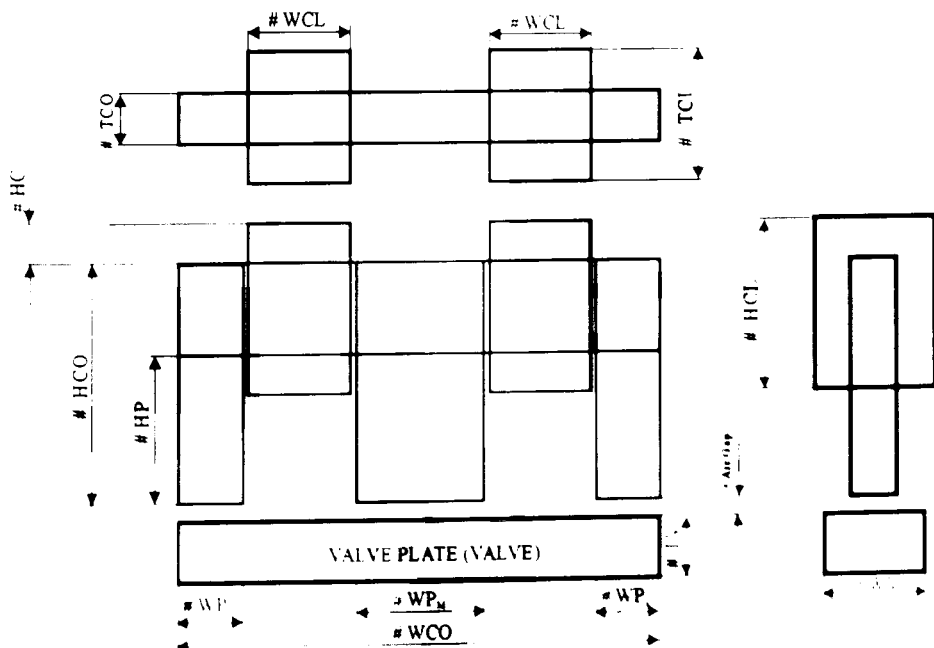


Fig. 5.9-1. E-core solenoid valve

Before go to our modelling, we will summarize the various situation what we hope to model and the values we hope to calculate for each. For this particular model

Dimensions	WCO	WP _L	WP _R	WP _M	WCL	HC	TV	WV	TCO	HP	gap
Unit	mm	mm	mm	mm	mm	mm	mm	mm	mm	mm	mm
E-core	25.60	3.40	3.40	6.80	6.00	1.80	3.00	5.40	2.50	7.30	0.10

Table 5.9-1 E-core- I model dimensions

we set 130 turns and 1.47A current to make a total MMF of 381 ampere-turns. To accommodate 130 turns we have to calculate the height of the coil (HC). Because the core window must be large enough to accommodate the number of turns of copper wire required to reach the specified inductance. A large DC inductor is often limited by the core’s saturation point. The number of turns can be calculated as we discussed in section 2.6.5. Table 5.9-1 shows the entire dimension for the Fig. 5.9-1 of the E-core actuator.

As we discussed in section 5.5, we are using the Opera-2d for modelling this device. Fig. 5.9-2 shows the 2D geometric model of the E-core model.

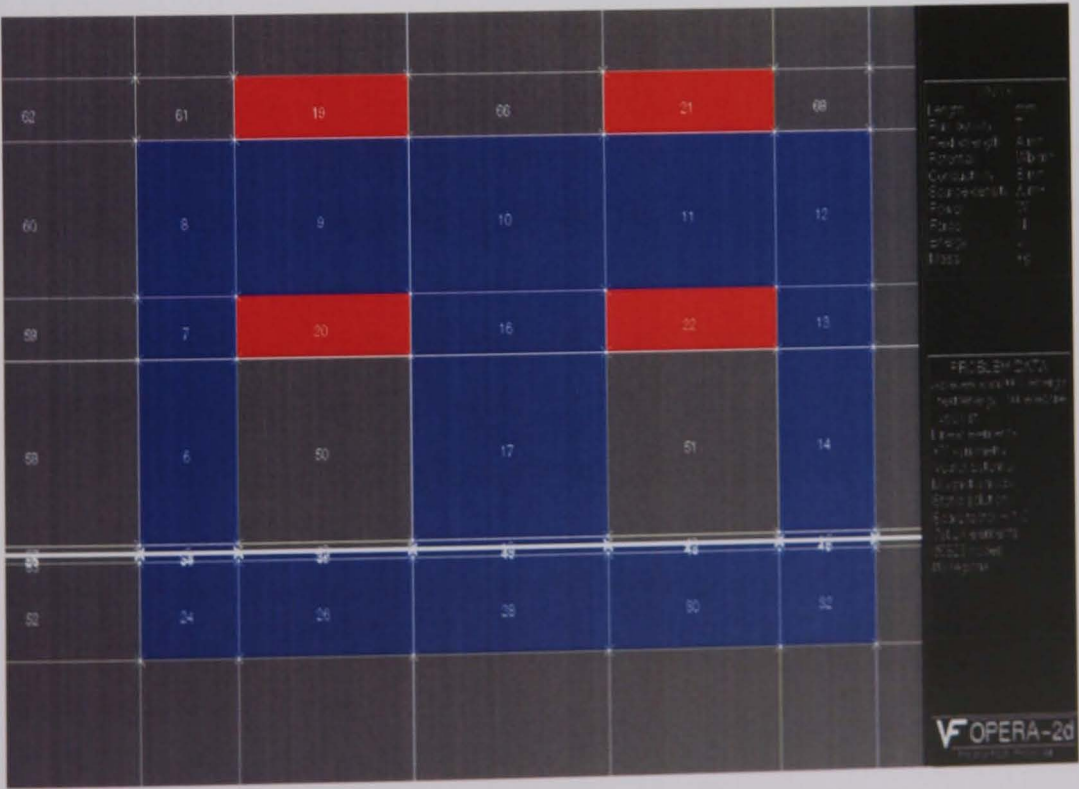


Fig. 5.9-2. E-core-I Opera-2d model

This Opera-2d model of E-core actuator shown in Fig. 5.9-2 contains 74 k elements including the air regions surrounding the actuator. It has been used to calculate the magnetic field distribution in the actuator for various linear and non-linear magneto static cases.

By running current through the coils that are wrapped around the yoke of actuator, a magnetic flux is created within the actuator material. This flux is driven around the magnetic circuit that is completed by the target material. When the magnetic flux passes through the air gaps to the target material, an attractive force is generated.

Magnitude of this force is given by equation (2.8-16),

$$F = \frac{\mu_0 A (NI)^2}{4\delta^2}$$

Method	Force (N)
Analytical	19.50
Opera-2d (linear)	18.61

Table 5.9-2 E-core-I force

Comparison of the FE modelling results with the corresponding analytical results, obtained for the E-core model-I described in this section is tabulated in the Table 5.9-2. The good agreement is obtained in this case between analytical and numerical method results. This established confidence in the modelling methodologies and in the 2D FE models that were developed to realise these methodologies for further simulation studies.

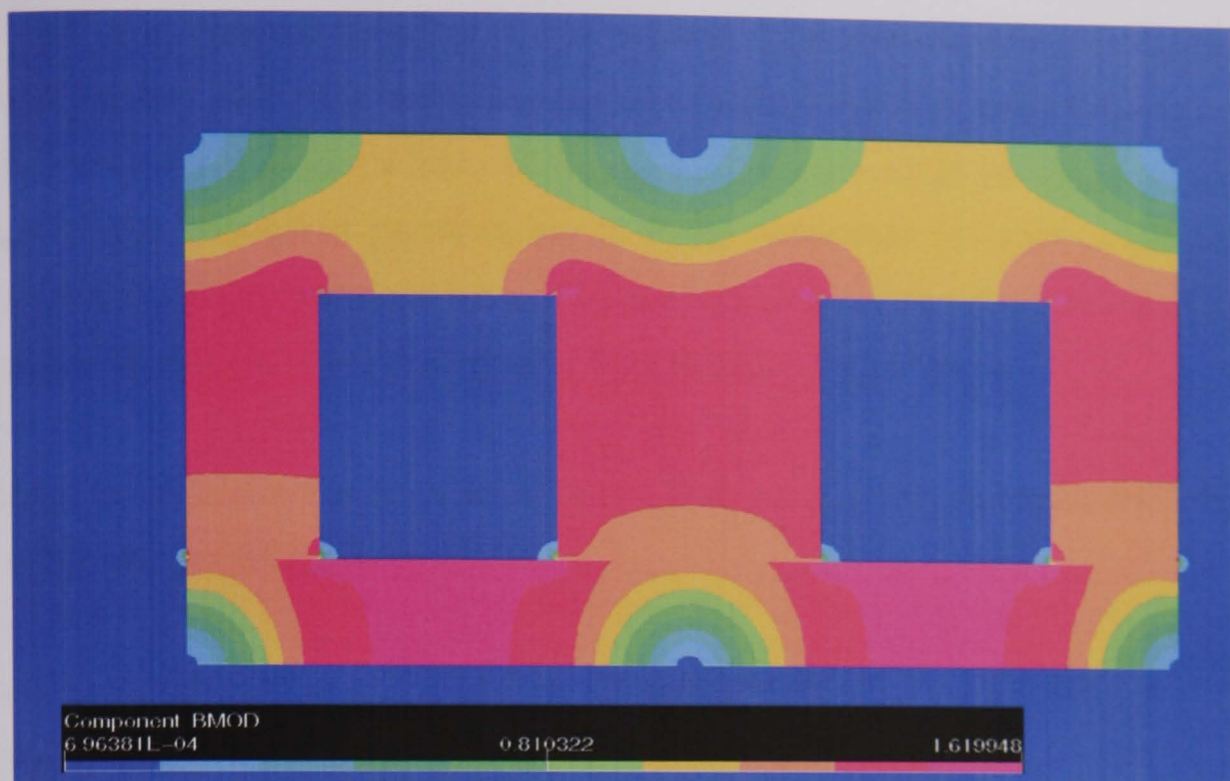


Fig. 5.9-3. E-core-I model filled zone contours of magnetic flux density

The 2D E-core-I model in Fig. 5.9-1 was used to carry out extensive non-linear simulation studies to investigate the actuator. The Fig. 5.9-3 has been shown that the distribution of magnetic flux density in the core and the valve plate.

The flux density in the core is 1.4 T and the valve plate is 1.6 T. Valve plate in this model is fully saturated (material: Radiometal-4550). The study of the effects of saturation conditions in the valve plate on the magnitude and distribution of magnetic field in the air closer to valve plate constituted a particular interest.

The net force on an object is obtained by creating a surface totally enclosing the valve plate and integrating the magnetic stress over that surface. The force produced by this model is 19.52 N.

5.9.2 Investigation of E-core-II Model Design

The technique used to create the model in the section 5.9.1 is applied here. The device described in Fig. 5.9-1 is going to be modelled in this section with different dimensions. We adopt the dimensions from the section 5.8-1, C-core model-II to create this model. Before going to the modelling, we will summarize the entire parameters and material properties needed to create this model.

The coil core window must be large enough to accommodate the number of turns of copper wire required to reach the specified MMF. A large DC inductor is often limited by the core’s saturation point. The core must be large enough in size and low enough in permeability to avoid saturation (or shift in inductance below the minimum required level). These factors increase the turns and length of copper wire required, causing wire loss to become an issue.

In order to calculate the number of turns first we have to calculate the width of the coil window (WCL).

Reaming length for the coil = $23.55 - (2.78+2.78+5.56) = 12.43 \text{ mm}$
Available length for one coil = $12.43 / 2 = 6.22 \text{ mm}$
WCL = 6.22 mm

The dimensions of E-core-II are shown in Table 5.9-3

Dimensions	WCO	WP _L	WP _R	WP _M	WCL	HC	HCO	TV	TCO	HP	gap
Unit	mm	mm	mm	mm	mm	mm	mm	mm	mm	mm	mm
E-core	23.55	2.78	2.78	5.56	6.22	0.65	8.98	2.50	2.20	6.22	0.10

Table 5.9-3 E-core-II dimensions

In section 2.6.5 we discussed about how to calculate the number of turns fit into the coil window. From the derived calculation we can wind 50 turns in one coil window.

As we discussed in section 5.5, we used Opera-2d for modelling this valve. Fig. 5.9-4 shows the diagram of the valve plate and core geometry. Input current for this model is 2.312 A. We used Radiometal-4550 to create this model.

modelling methodologies and in the 2D FE models that were developed to realise these methodologies for further simulation studies.

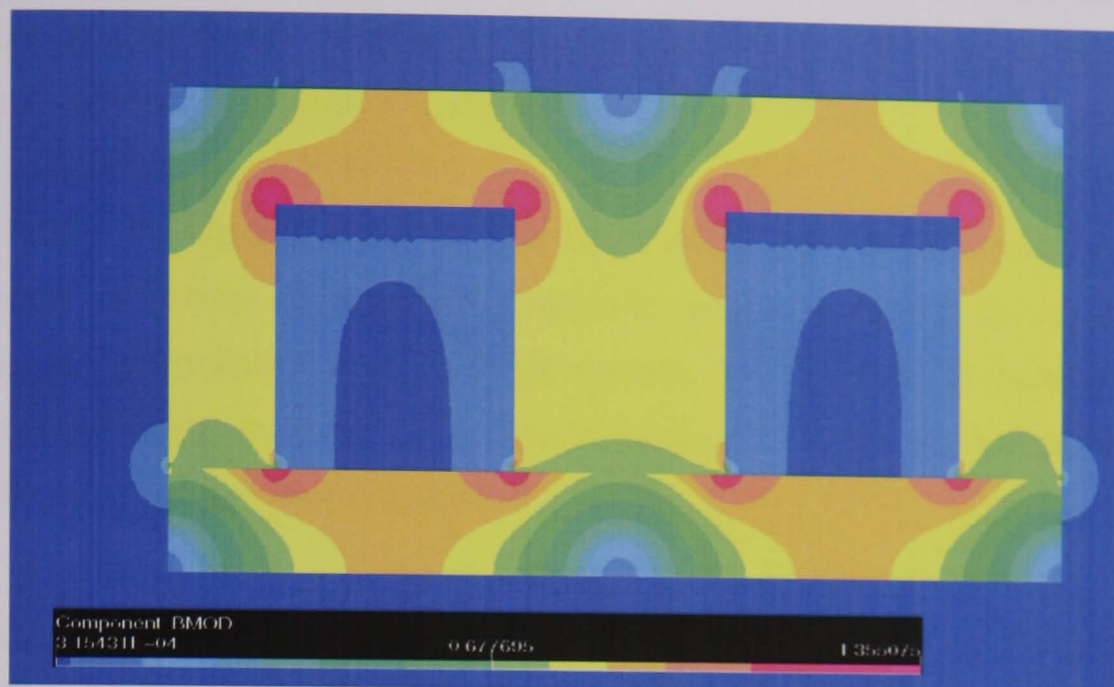


Fig. 5.9-5. E-core-II contour plot of flux density

The magnetic material's B-H characteristics are defined in the Opera-2d to calculate the flux density in the air-gap for the non-linear static solution of the model. The contour plot of the flux density is shown in the Fig. 5.9-5. Opera-2d non-linear simulation result give 5.18 N force for this E-core-II model.

5.10 ANALYZING C-CORE-II AND E-CORE-II ELECTROMAGNETIC ACTUATOR

In this section we considered four different types of electromagnetic actuators. Our research mainly concern about the C-core model-II (section 5.8-1) and E-core model-II (section 5.9-2) actuators.

The both models have the same number of turns in the driving coils and the same current this will create a very similar amount of magnetic flux as we expect. However the magnetic flux density is observed to be approximately half in the E-core model due to the area of the air gap being double. The same amount of flux has twice as much area to flow through. This means that the flux density is about half in the E-core as in the C-core.

The fundamental difference between the models are the E-core has the extra iron part in the core (middle pole, WPM). The total area of the air gap is twice as much as in the C-core due to this. Therefore our comparison and discussion will be focusing only these models. In section 5.8-1 and 5.9-2 we developed 2D models to analyze the system using finite element method.

Vector fields (Opera-2d) software has been employed for field analysis. Nodal formulation in terms of modified magnetic vector potential is used. Circuit equation is incorporated into the FEM system. Non-linearity is handled by the Newton-Raphson's method. The electromagnetic force is computed using Maxwell stress tensor [Appendix A].

5.10.1 C-Core-II Analysis

Fig. 5.10-1 shows the 2D model with the finite element mesh for the actuator. The model is built up using a number of regions to define yoke, the coil, poles, plunger and the surrounding air.

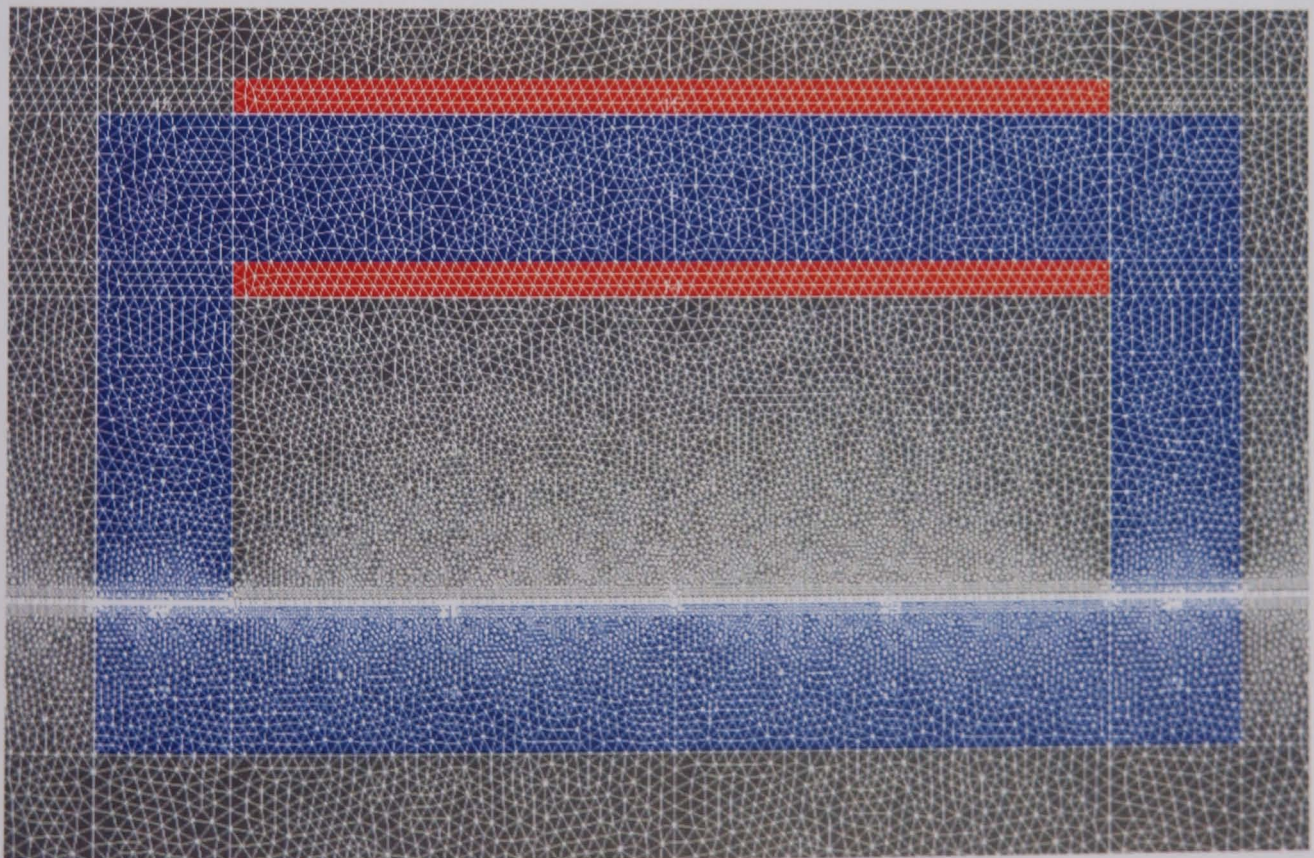


Fig. 5.10-1. C-core-II actuator model mesh

The results obtained for the system are in Fig. 5.10-1 and they are tabulated in Table 5.10-1.

Source	Force N
Opera- 2d	8.2831
Analytical	10.18

Table 5.10-1 C-core-II force

To verify the results we use force, energy relationship as we discussed in section 3.5.1.The mechanical result done by the force acting on the plunger during the time interval can be written as in equation (3.5-1),

$$dW = Fdx$$

From equation (3.5-1)

$$F = \frac{\partial W}{\partial x} = \frac{\Delta W}{\Delta x} \tag{5.10-1}$$

Case One: Air gap = 0.1 mm

The energy stored in the air gap $\int \frac{B.H}{2} ds = 3.72905 \times 10^{-4} \text{ Jmm}^{-1}$

Total energy stored in the model $= 3.72905 \times 10^{-4} \times 2.2 = 8.20391 \times 10^{-4} \text{ J}$

Case Two: Air gap = 0.05 mm

The energy stored in the air gap $\int \frac{B.H}{2} ds = 2.19685 \times 10^{-4} \text{ Jmm}^{-1}$

Total energy stored in the model $= 2.19685 \times 10^{-4} \times 2.2 = 4.83307 \times 10^{-4} \text{ J}$

After computing the energy, the equation (5.10-1) calculate the force in the system,

$$\begin{aligned} F &= \frac{(8.20391 - 4.83307) \times 10^{-4}}{(0.1 - 0.05) \times 10^{-3}} \text{ N} \\ &= 6.7417 \text{ N} \end{aligned}$$

The C-core model was analysed under static solution (ST) program and the results read in the post-processing stage. The finite element analysis solving potential of the elemental nodes by averaging field values and producing RMS value (root square mean error) was carried out. A number of facilities regarding field parameter variables were available to allow closer examination of the model. Integration along lines or regions of interest is an example of further processing. Hence any field quantity can be displayed along lines or as contour plots over regions. Integration and other operations are characterised by short hand definitions. i.e. the integral of magnetic field strength being BMOD. Graphical displays are allowed for a clear understanding.

The field line contours of vector potential over the whole model are displayed as shown in Fig. 5.10-2. Also the field line in the air gap is shown in the Fig. 5.10-3. In the model of a solenoid shown in Fig. 5.10-2, the flux path is unrestricted when the solenoid is excited by only one coil (C-core).

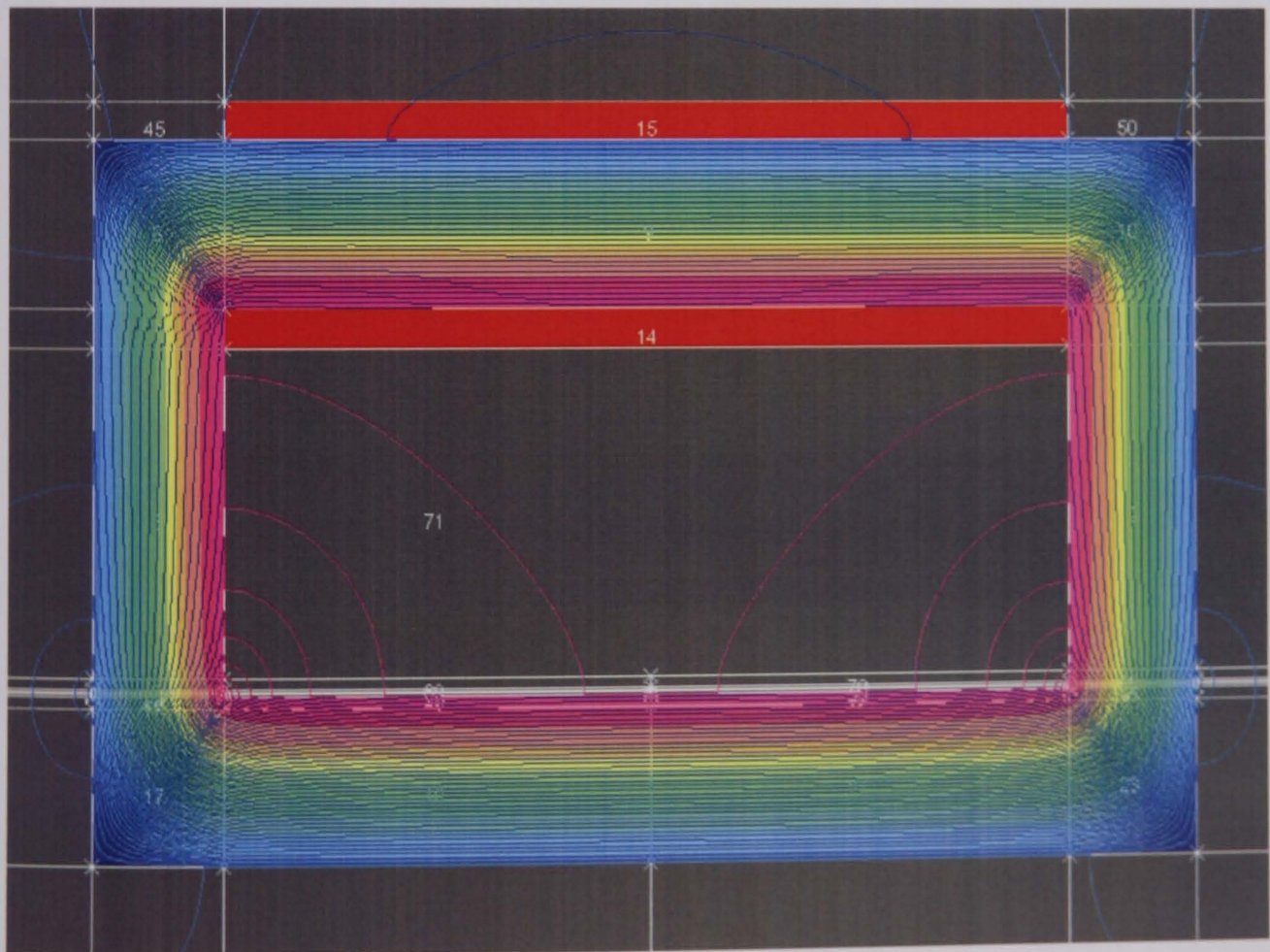


Fig. 5.10-2. C-core-II equipotential line contours of vector potential-1

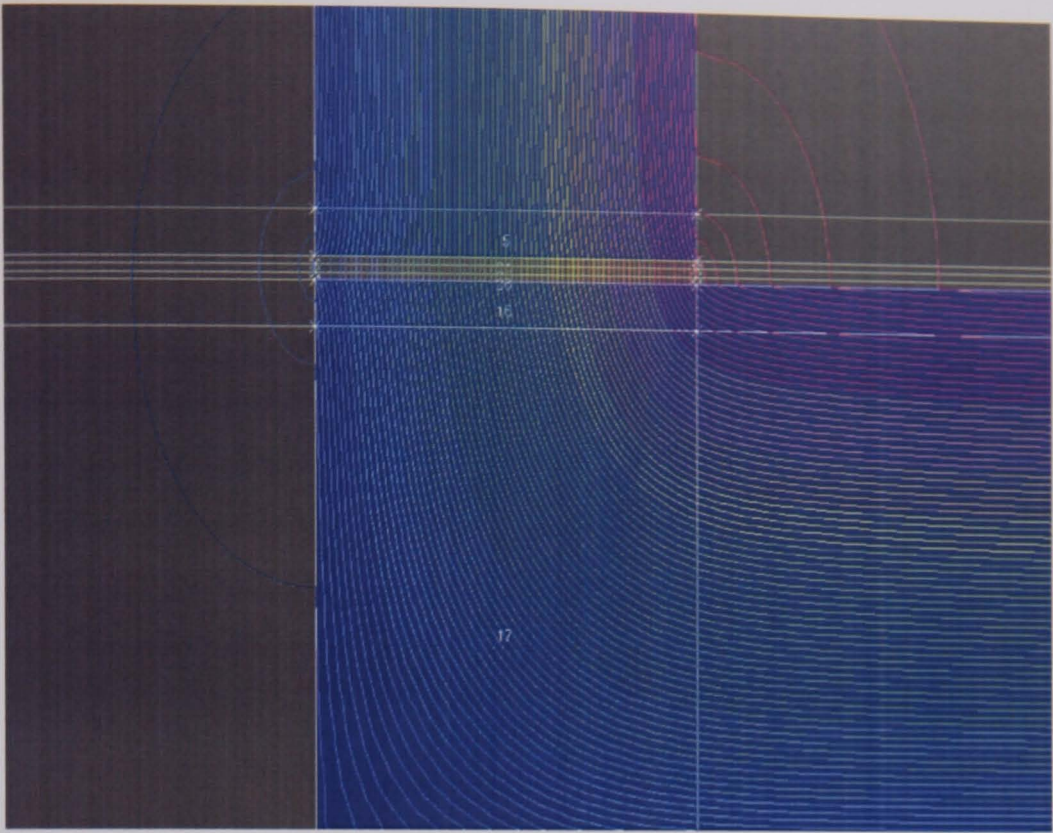


Fig. 5.10-3. C-core-II Equipotential line contours of vector potential-2

The Fig. 5.10-4 shows the magnitude flux distribution in the yoke and valve plate. The both parts are reached the maximum flux density of 1.6 T. The Fig. 5.10-4 also shows the same results.

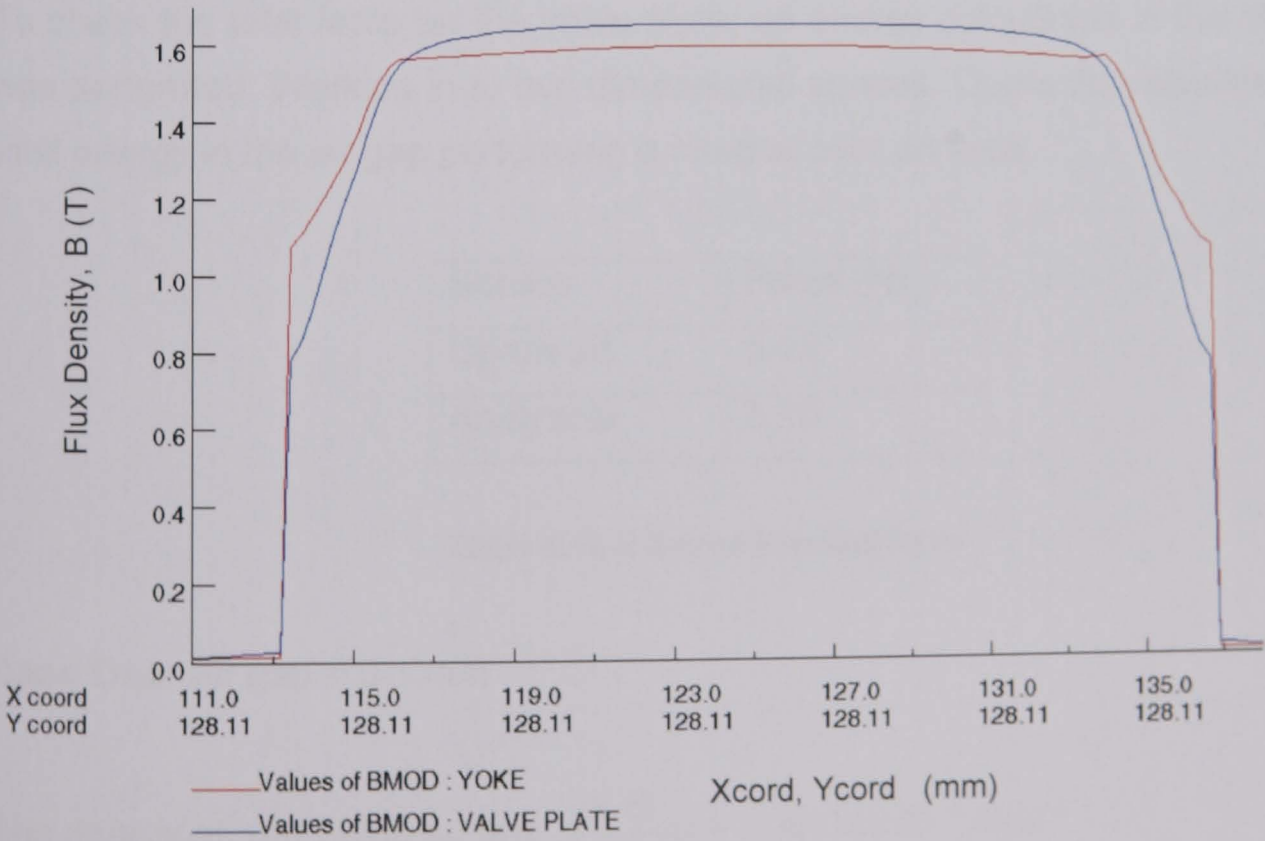


Fig. 5.10-4 C-core-II magnetic field distribution

5.10.2 E-core-II Analysis

The Opera-2d pre and post processor provide a variety of sophisticated tools to simplify the modelling process. The actuator has been modelled with the Radiometal-4550 material as shown in the Fig. 5.10-5

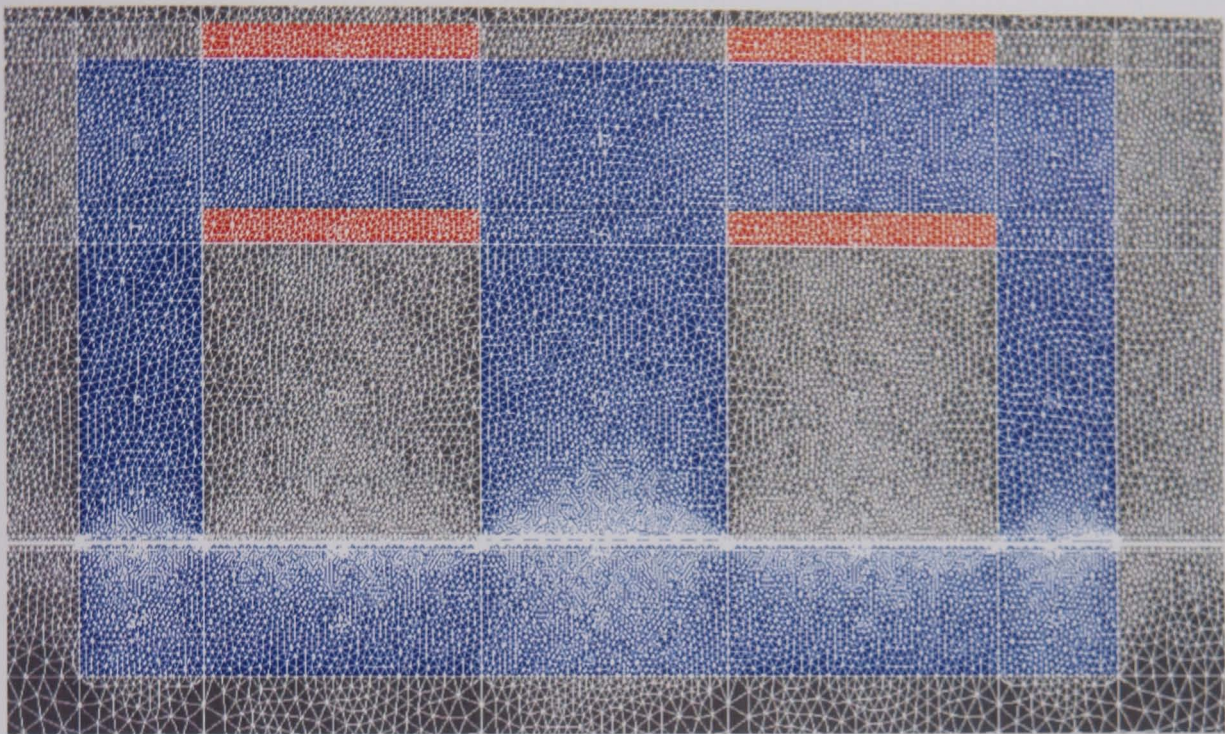


Fig. 5.10-5. The E-core-II model mesh

To check the total force on the valve plate; an energy calculation in the air gap was performed. Working in to two dimensional spaces, Opera-2d calculates the total energy in the air gap performing a integral over an area.

Source	Force (N)
Opera-2d	5.18
Analytical	5.10

Table 5.10-2 E-core-II model force

Case One: Air gap = 0.1 mm

The energy stored in the air gap $\int \frac{B.H}{2} ds = 2.36014 \times 10^{-4} Jmm^{-1}$

Total energy stored in the model $= 2.36014 \times 10^{-4} \times 2.2 = 5.192308 \times 10^{-4} J$

Case Two: Air gap = 0.05 mm

The energy stored in the air gap $\int \frac{B \cdot H}{2} ds = 4.31592 \times 10^{-4} \text{ Jmm}^{-1}$

Total energy stored in the model $= 4.31592 \times 2.2 \times 10^{-4} = 9.495024 \times 10^{-4} \text{ J}$

After computing the energy, the equation (5.10-1) calculate the force in the system

$$F = \frac{(9.495024 - 5.192308) \times 10^{-4}}{(0.1 - 0.05) \times 10^{-3}} \text{ N}$$

$$= 8.6054 \text{ N}$$

The equipotential of the model are displayed as shown in Figs. 5.10-6 and 5.10-7. These should be checked to ensure whether they agree with the expected magnetic performance of the actuator. If errors appear to be present then the model should be modified to correct the error and analysis re-run.

The response of the model to the various field operations performed, showed some promising results in Figs. 5.10-6 and 5.10-7. As expected the contour field lines followed the shape of the model smoothly.

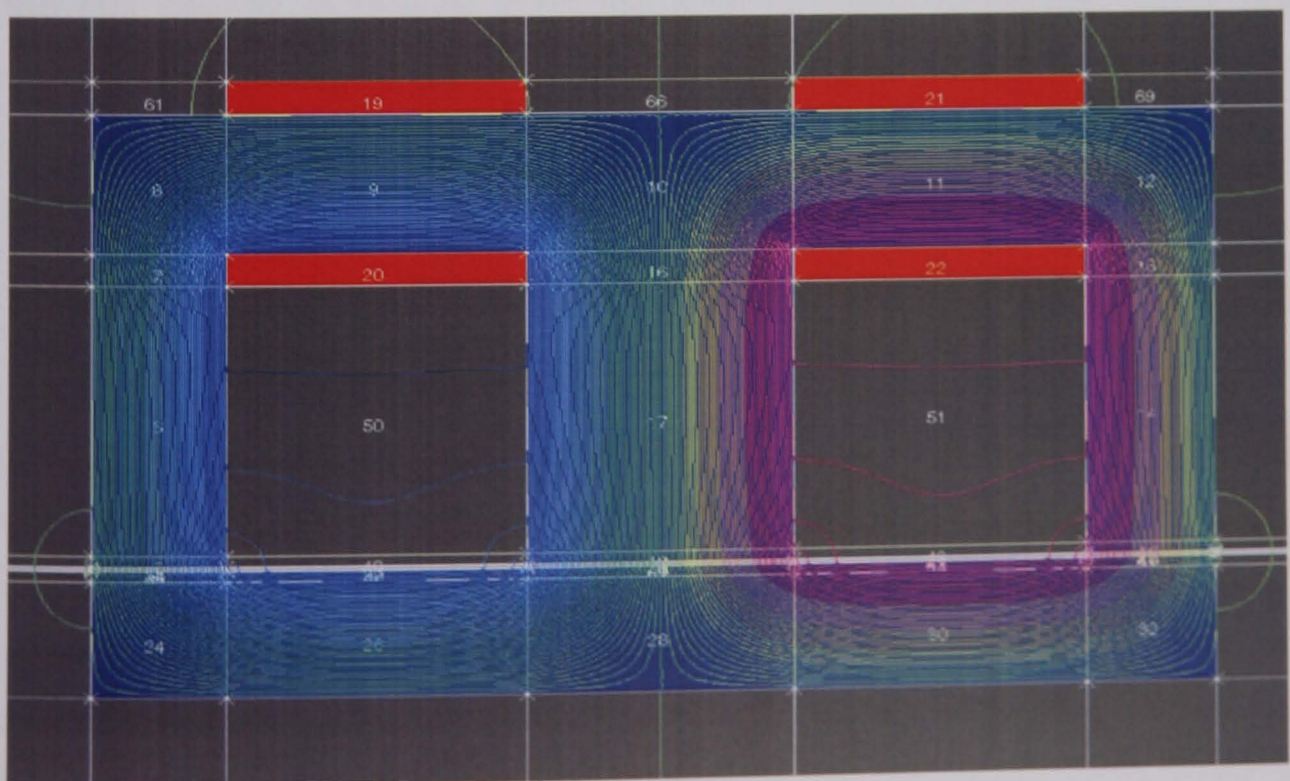


Fig. 5.10-6. E-core-II equipotential line contours of vector potential

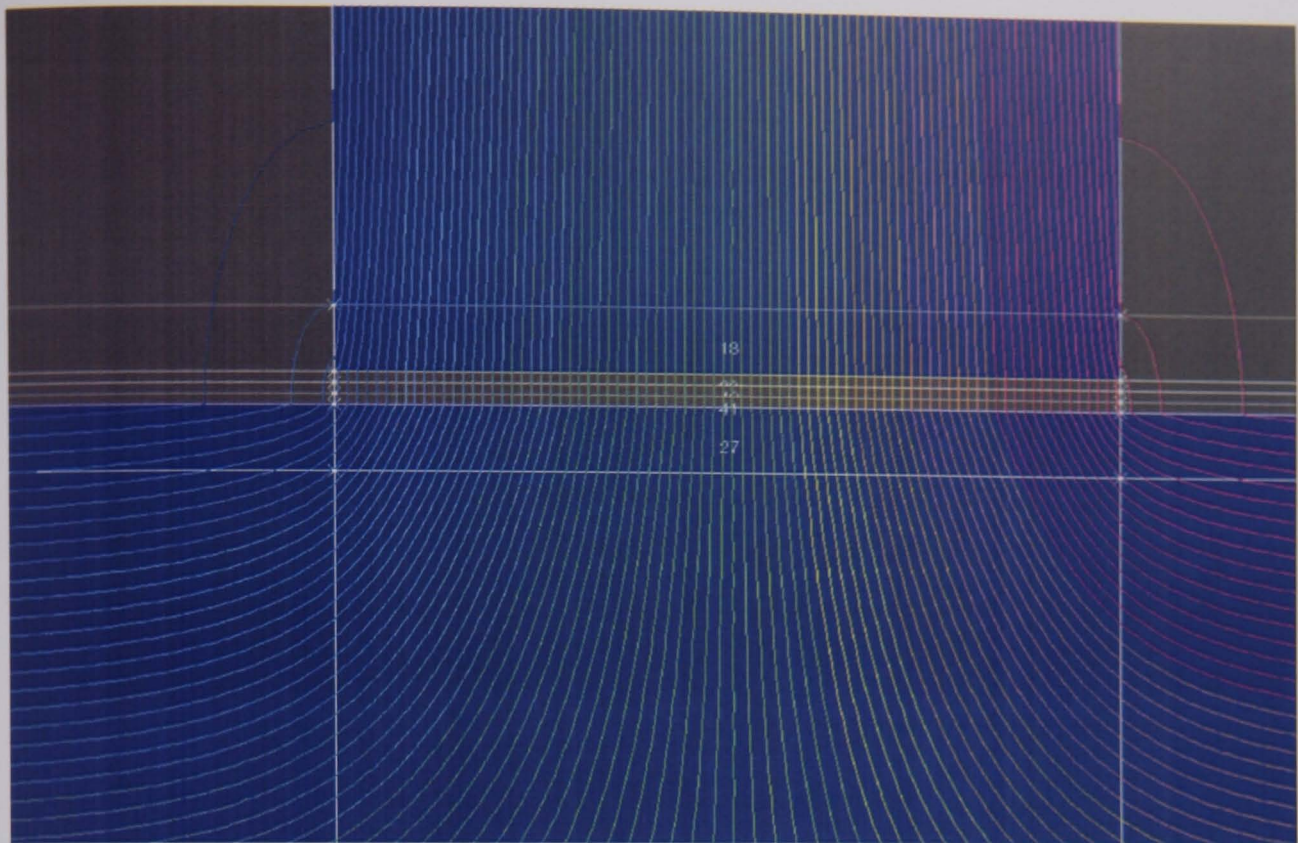


Fig. 5.10-7. E-core-II equipotential line contours of vector potential in the middle pole and air gap

Fig. 5.10-6 shows an arrangement of two coils (E-core). The winding directions are different from each in the model. Flux path do not cross, so the flux path from the excitation of each individual coil exists only in the area adjacent to that coil.

If the flux density increases, then the total flux also increases (same cross sectional area, $(\phi = BA)$). As a result of this the force acting on the plunger is increased in the model.

5.11 COMPUTATION OF 3D MAGNETIC FIELD DISTRIBUTION IN ELECTROMAGNETIC ACTUATOR

Fig. 5.11-1 shows the simplified schematic of one of several designs of a high-speed solenoid actuator used as ejector valves mentioned above. It is essentially an on/off valve actuator whose active components comprise an excitation coil wound around a magnetic core that attracts or releases a movable valve plate depending on the excitation state of the coil. The EM force produced by the actuator needs to overcome the pneumatic force which the valve plate is subjected to as a result of high-pressure air (200-550 kPa) flowing

through the valve. Very tight design and rigorous performance specifications make these ejectors for the use used in high-speed sorting applications and as unique in terms of their design, manufacture and reliable exploitation.

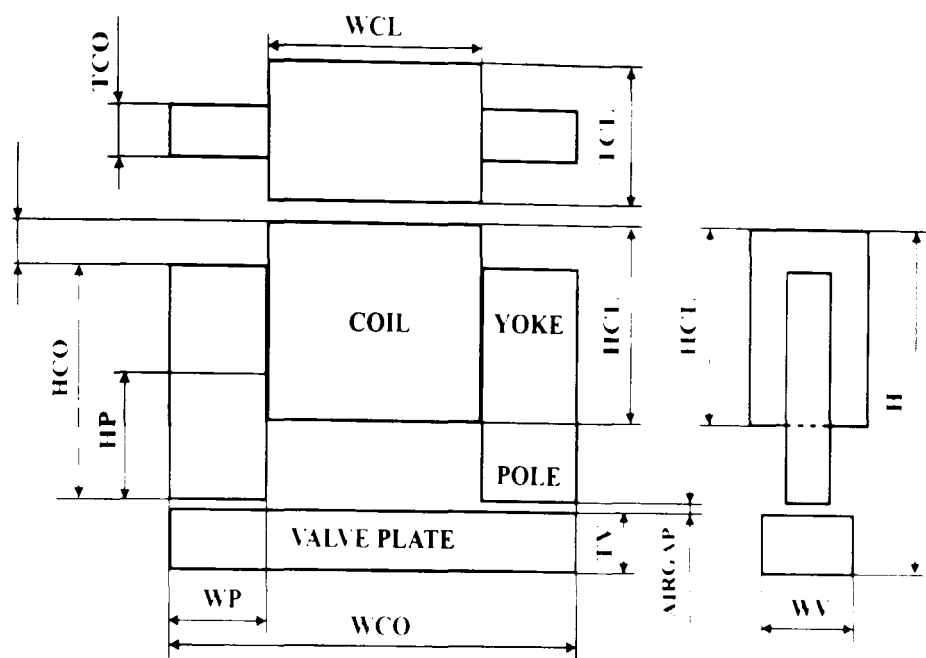


Fig. 5.11-1. Main constructive features of a long lifetime C-core EM actuator used as ejector valves in high-speed optical sorting machines.

The C-core design of the ejector valve shown in Fig. 5.11-1 poses significant problems for developing an adequate 3D FE model because of the small air gap ($\delta=0.05-0.1$ mm) compared to the rest of the valve. In order to characterize and calculate the magnetic field distribution both in the air gap and in the iron, especially in and around the pole tips and the valve plate and also to account nonlinearities due to saturation and eddy currents, a large number of volume elements are needed. This is to ensure convergence and to maintain consistent modelling accuracy for various modelling investigations. This was achieved by performing various modelling experiments to establish the appropriate number, size and distribution of volume elements in the problem domain.

On all surfaces of the rectangular air volume around the valve, Dirichlet boundary condition ($B_n=0, A=0$) was used. This is justified if the boundary surfaces are chosen sufficiently far apart so that any further repositioning of these surfaces away from the valve does not appreciably change the FE solution.

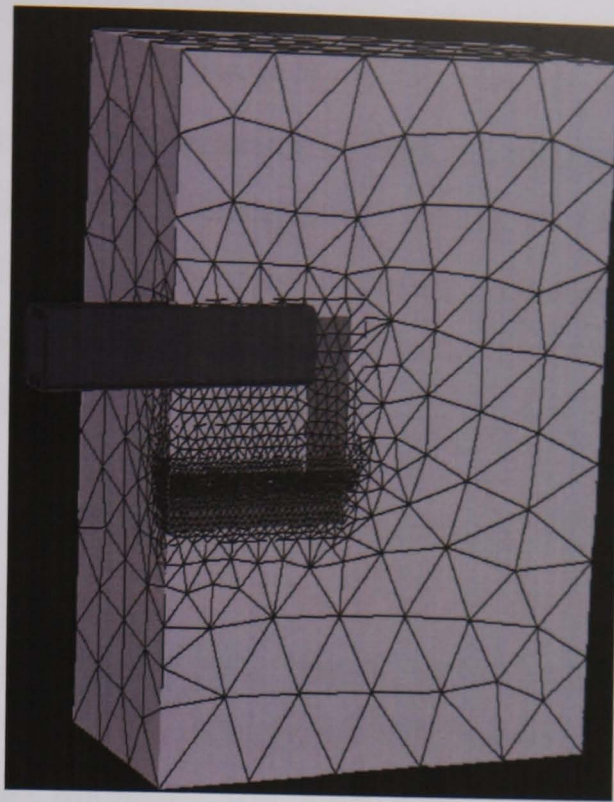


Fig. 5.11-2. Typical 3D finite element (FE) model of the EM actuator shown in Fig.5.11-1 (1/4 of the full model)

A typical 3D FE model is shown in Fig. 5.11-2 which consists of approximately 250k tetrahedral elements, most of which are concentrated in the regions of the air gap, pole tips and the valve plate (Fig. 5.11-3). For all modelling purposes commercial software package Opera-3d was used.

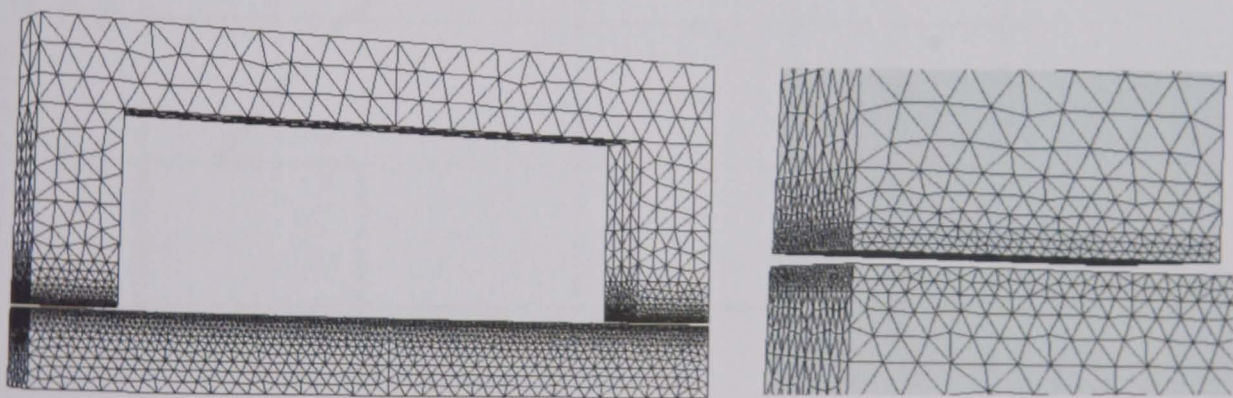


Fig. 5.11-3. FE discretization of the 3D problem domain showing the distribution of elements (a) in the iron and (b) finer mesh in and around the pole tips.

Following an extensive 2D modelling study of the nonlinear magnetic field in the EM valve actuator shown in Fig. 5.11-1, 3D FE models described above had been used to investigate the effects of 'z-direction' magnetic field distribution on various performance parameters, especially on the magnetic force produced for a given excitation current. Further modelling studies were carried out to quantify

the leakage and fringe field effects on the actuator performance. The need for delivering a relatively large force and a very fast response time under multibillion cycle operational regimes at 300 Hz puts an added importance on some of the crucial design parameters. Some of the effects, which would otherwise play a minor role in low-frequency actuators operating under duty cycles far below that is required of the actuator discussed here, are likely to be magnified under multibillion duty cycles.

Some of the modelling results are shown in Figs. 5.11-4 - 5.11-7. The Fig. 5.11-4 shows the effect of the height of the yoke on magnetic force F . It shows a strong dependence of F on the yoke height, most likely attributable to change in the saturation conditions. This is significant from the design point of view since one of the aims is to minimize the thickness of the yoke (TCO) and hence increase the packing density leading to an increase in the resolution of optical sorting. This means the cross sectional area of the yoke can only be increased by increasing the height of the yoke which, as shown in Fig. 5.11-4 has a positive effect on the force produced.

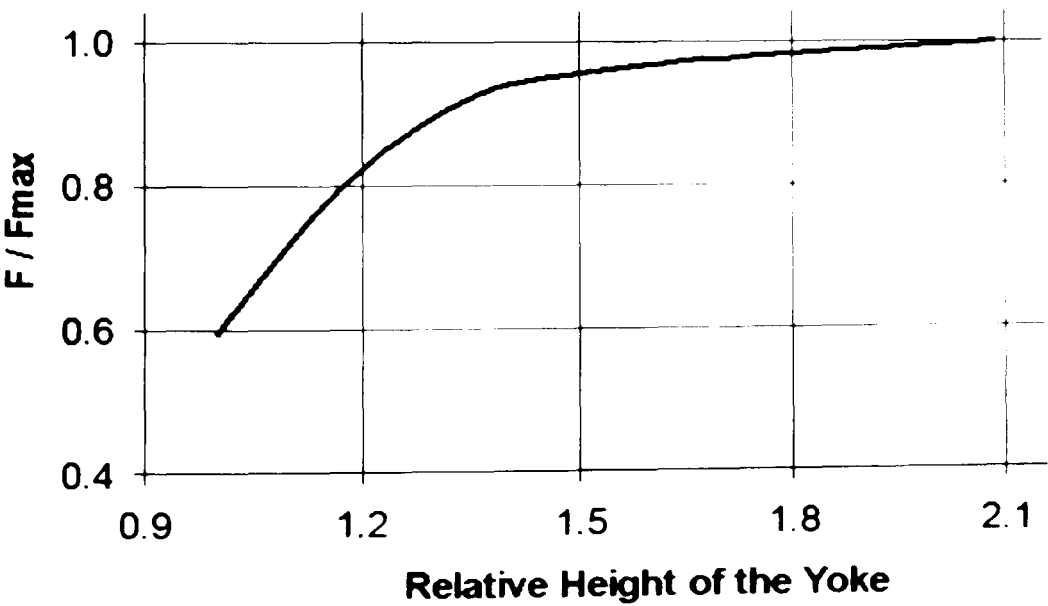


Fig. 5.11-4. FE modelling results: variation of EM force with height of the yoke (HCO-HP); excitation current $I=1.7$ A, air gap $x=0.1$ mm.

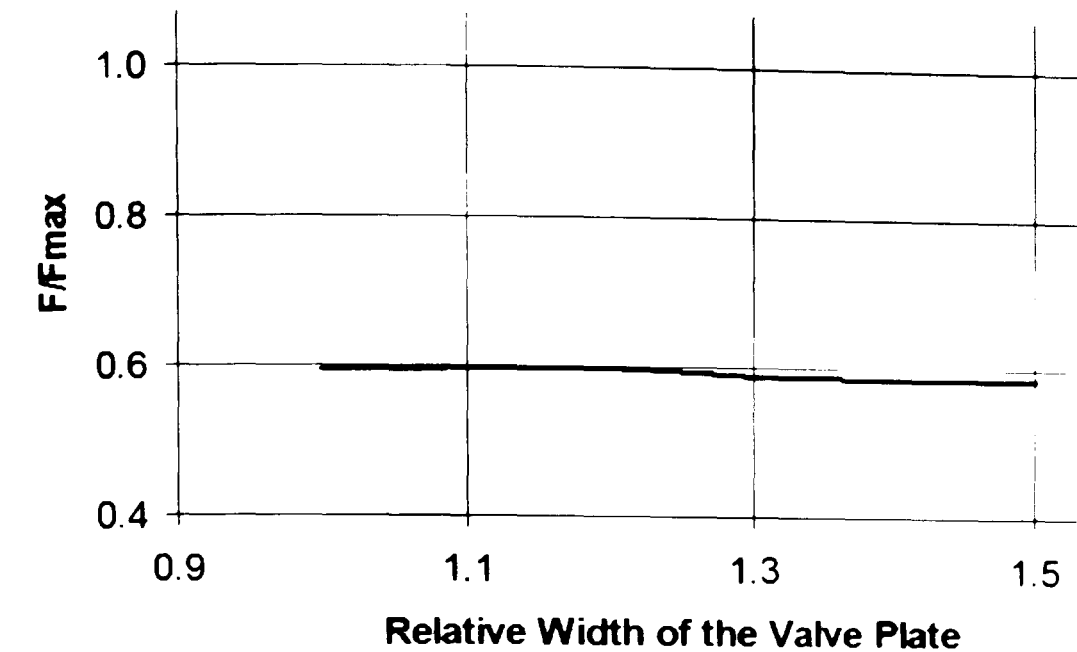


Fig. 5.11-5. FE modelling results: variation of EM force with the width of the valve plate (WV).

The increase in the width of the valve plate (WV) does not seem to result in an increase in the leakage and fringe field effects leading to reduction in the force (Fig. 5.11-5). The thickness of the valve plate (TV) also plays an important role. Modelling studies [7] have shown that the force is not only strongly dependent on the thickness of the valve plate but also on the relative levels of saturation in the yoke and the valve plate. Maximum force is obtained for TV which corresponds to an almost identical level of saturation in the yoke and the valve plate (Fig. 5.11-7).

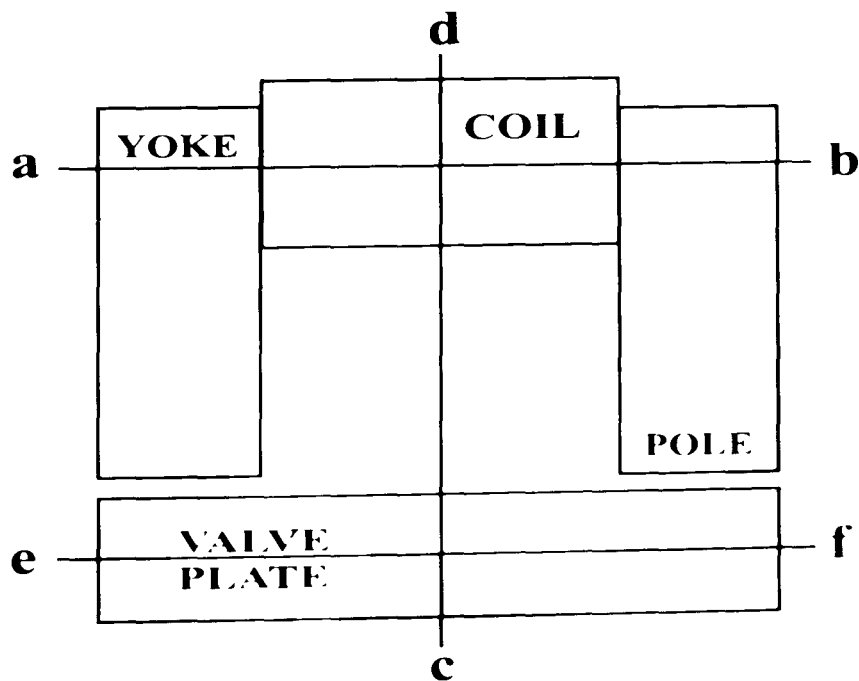


Fig. 5.11-6. Schematic of the EM actuator showing lines ab, cd and ef along which magnetic flux densities are calculated in Fig. 5.11-6. (not drawn to scale).

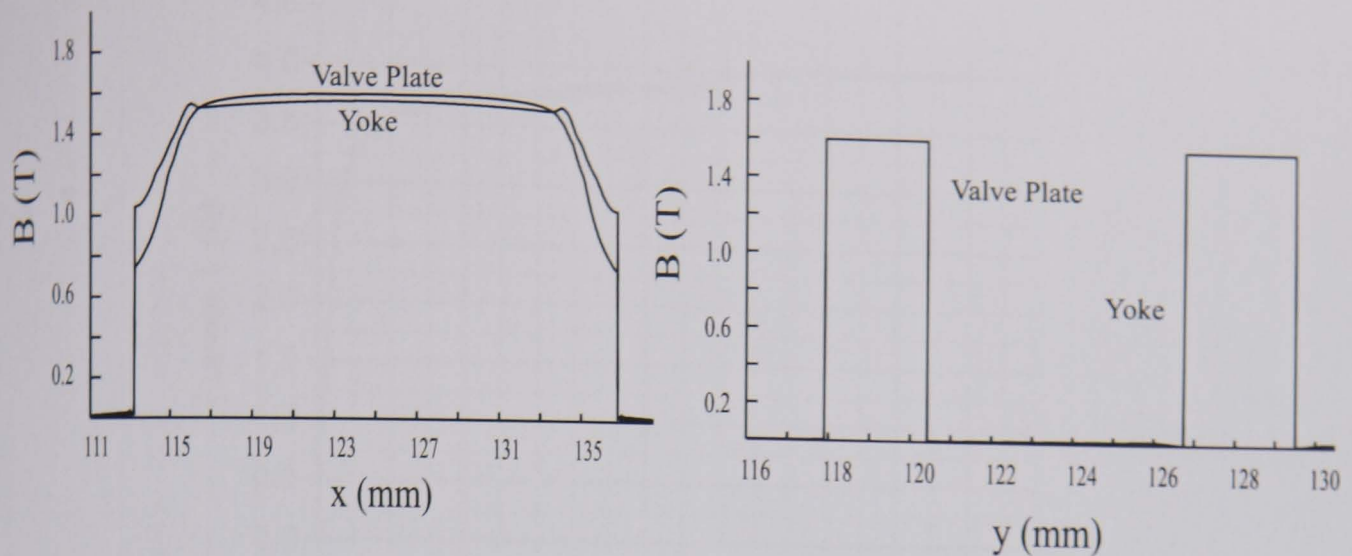


Fig. 5.11-7. Effects of the valve plate thickness T_V on magnetic field distributions in the yoke and the valve plate (a) along the lines ab and ef respectively and (b) along the line cd shown in Fig. 5.11-6.

Various 3D FE models of the above ejector valves have been used to investigate any '3D' effects that could have a detrimental effect on the valve performance (e.g. force produced). Fig. 5.11-8 shows an example of such a model. It also shows the small amount of fringe field effects in the air underneath and around the poles. Initially, some inconsistencies had been found for some of the materials in terms of the force calculated by 2D and 3D modelling and the force values calculated from some of the 3D. The analysis did not seem to agree with those obtained from 2D simulations although there were no visible significant 3D effects seen from the 3D modelling results. This is now being addressed by adopting an alternative approach to 3D model set up which gives increased flexibility and greater control over model discretisation improving accuracy.

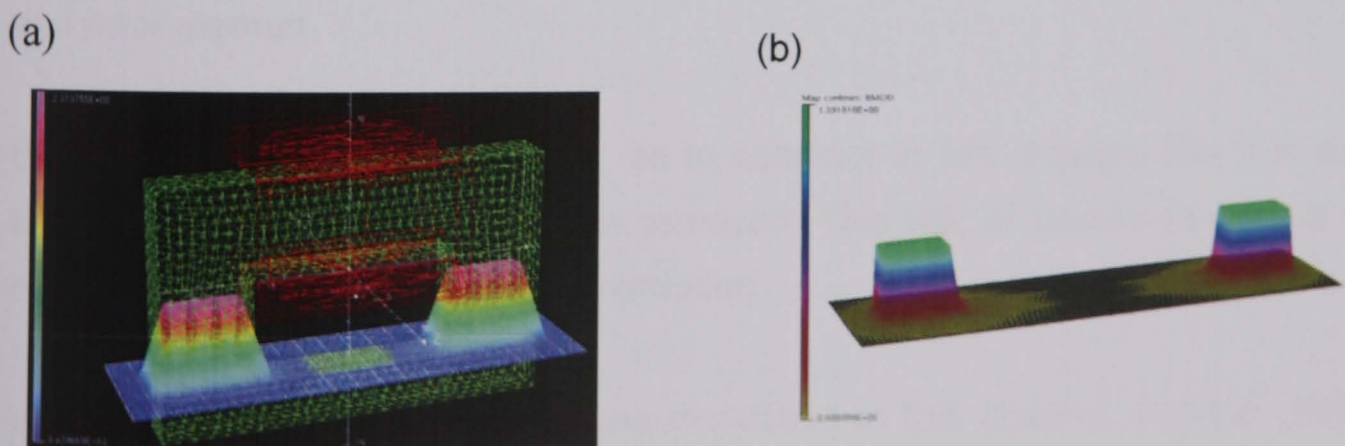


Fig. 5.11-8. Typical 3D finite element model of the newly designed 'C-core-II valve' (a) showing fringe field effects in and around the air gap (b) showing fringe field effects in and around the air gap

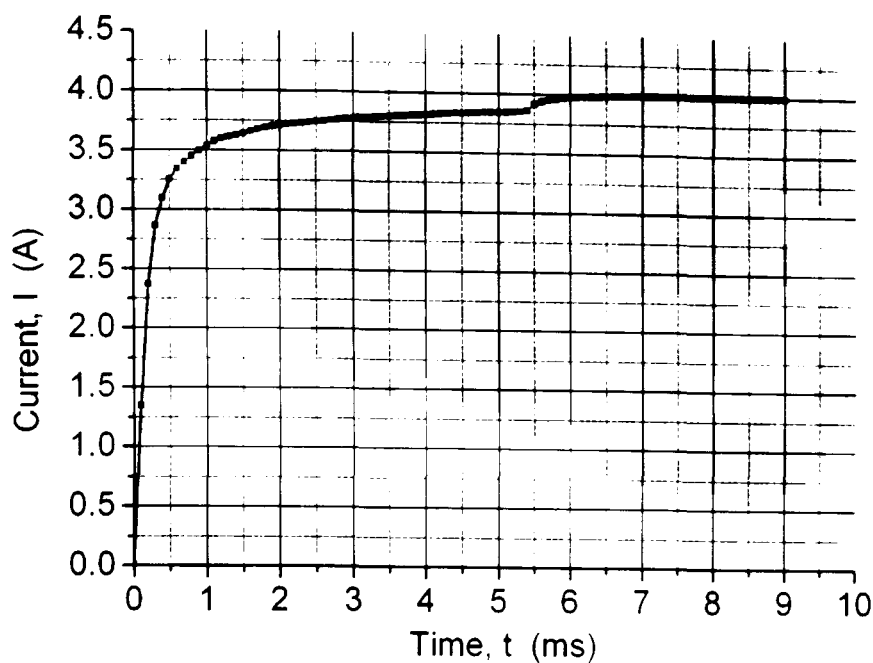


Fig. 5.11-9. Current rise in the excitation coil for the ‘C-core-II valve’ calculated from coupled solution of electric circuit and magnetic field equations

The coupled solution of the electric circuit and magnetic field equations gives the current transient in the excitation coil (Fig. 5.11-9) as it is switched ‘on’ and ‘off’. This defines the vital dynamic performance of ejector valves. From these solutions the inductance of the excitation coil was calculated for various saturation conditions of the magnetic circuit (0.1 - 0.6 mH).

5.12 SUMMARY

In this chapter various approaches to the design of electromagnetic actuators using mathematical model developed earlier in this work have been investigated. As mentioned earlier, in the past such designs were based on trial and error method.

By adopting a systematic method, as to consider in this chapter, this trial and error in the design process can be removed. This will, of course save a lot of costly and time consuming experimentation.

Various 2D/3D design investigations discussed in this chapter, provide useful information for a process of design. They help to choose a sensitive design variable and give one a useful insight into the way in which various design variables play off against each other and contribute to the output of the device.

A comprehensive and exhaustive study for optimising the design variables for an electromagnetic actuator design has been carried out. Various factors that need to be considered for a design have been discussed in this chapter. Useful design information that can be used for such a design process has been studied.

Chapter 6

INVESTIGATION OF ELECTROMAGNETIC ACTUATOR DESIGN CONCEPT

6.1 INTRODUCTION

The requirement for accuracy in the field of measurement and instrumentation has seen the development of many percentage precision devices. Technology has risen to levels where standards have needed to be equally met. Continued research and study regarding the modified new designs led to the production of higher quality products.

This chapter presents some of the results of investigation of various designs of actuators. The investigation is carried out by 2D finite element (FE) modelling and computation of non-linear magnetic field distribution in various designs of such actuators. In this section various designs of a particular concept were investigated by changing the number of design manipulative variables e.g. air gap distance, current. These factors ultimately define the overall size and performance of the actuators investigated in this chapter.

Modifying an existing design or creating an entirely new one can sometimes pose problems of a different kind, depending on various factors in the design process and the cost of time. Modelling of hardware devices has more recently found application in the form of CAD (computer aided design) packages.

6.2 C-CORE ELECTROMAGNETIC ACTUATOR

An investigation regarding an electromagnetic actuator will be used in food sorting machines to confirm the concern of these tests. Below is shown an C-core actuator in Fig. 6.2-1.

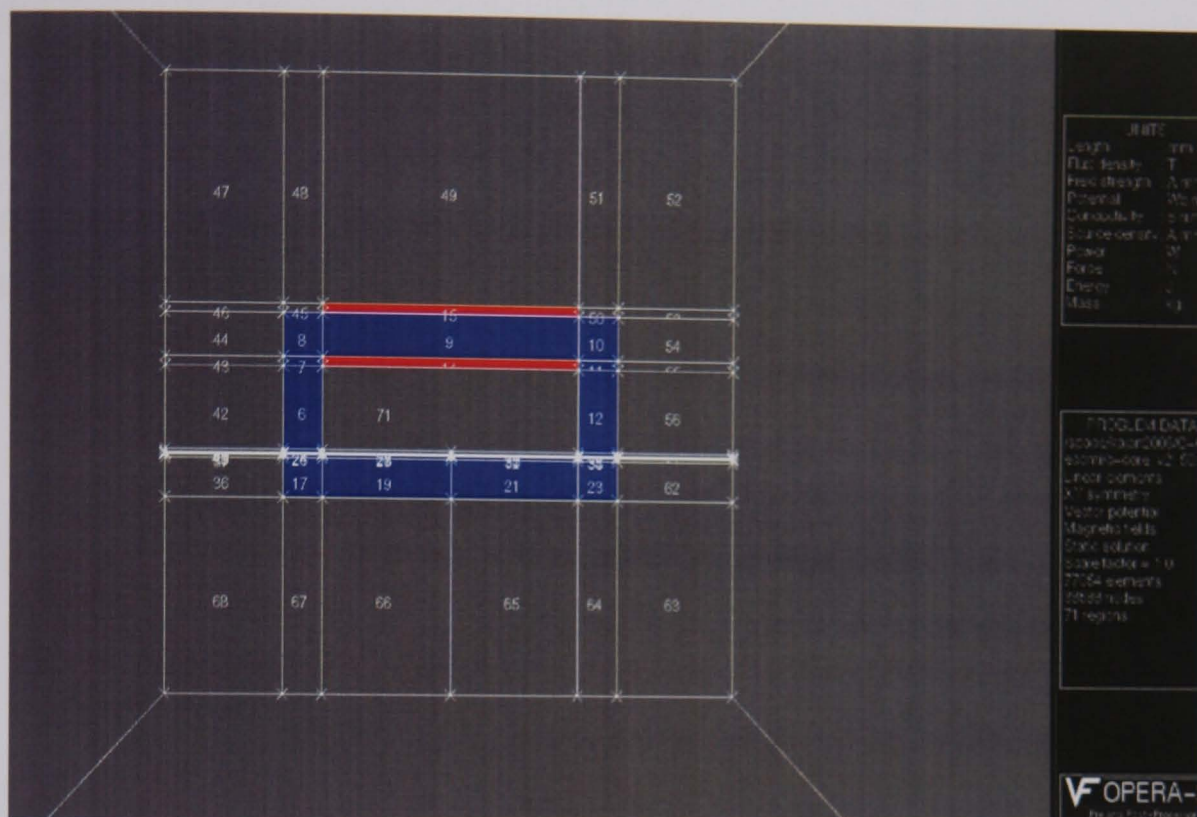


Fig. 6.2-1. C-core-II electromagnetic Opera-2d model

An analysis of the actuator using finite element modelling technique has been conducted in order to determine, and to characterise performance under conditions of interest.

The design of the actuator has been modelled using Opera-2d, where the aim has been modified to various features of the model, by simulating response under different conditions, and indeed identifying any characteristics behaviour. All work carried out has been the result of using an electromagnetic vector fields package, namely Opera-2d. The main advantage feature of these packages is their computational efficiency under simulation methods and provision of graphical displays for varied parameter values. In this way the actual hardware device does not undergo repeated physical dismantling and reconstruction, as even complex alterations can be simulated and the results be achieved in a matter of hours.

6.2.1 Force, Current Analysis for Different Air Gap

Using the modelling methodologies and C-core-II FE model designs of solenoid valve simulated to investigate their performance in terms of electromagnetic force, F is produced by a given design. For this, the effects of various electric (excitation current I), and air gap, δ (#gap)) and material parameters (Radiometal 4550, Armco, Hyperm 0 and Hyperm 0) were investigated. This was done, to investigate the effects of the above design parameters on the static performance of the valve. The results of these investigations are given in this section.

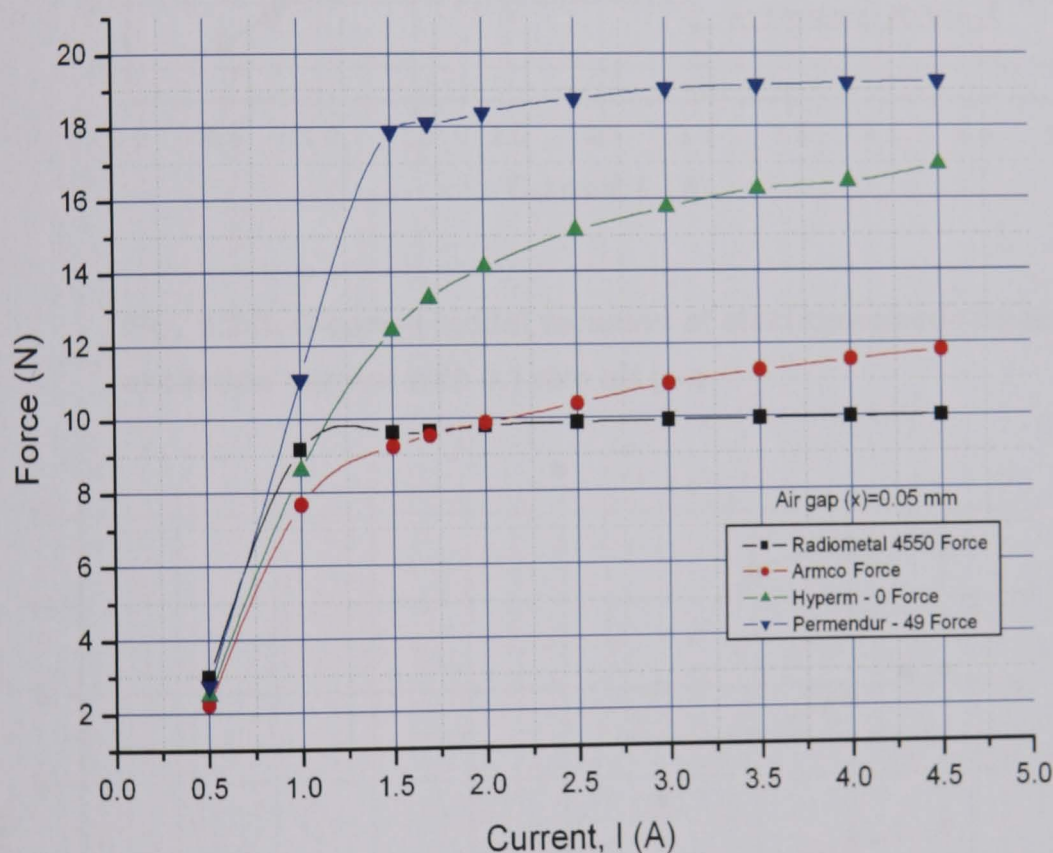


Fig. 6.2-2. C-core-II model variation of electromagnetic force for different excitation current with 0.05 mm air gap

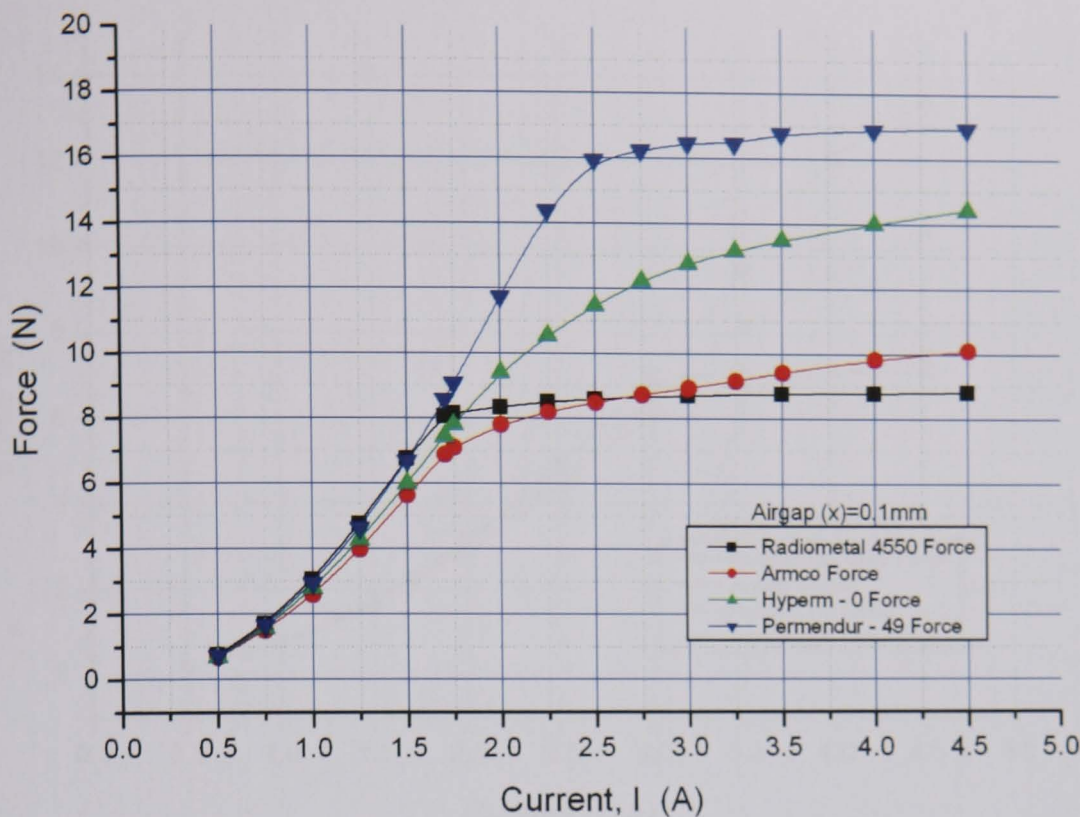


Fig. 6.2-3. C-core-II model variation of electromagnetic force for different excitation current with 0.1 mm air gap

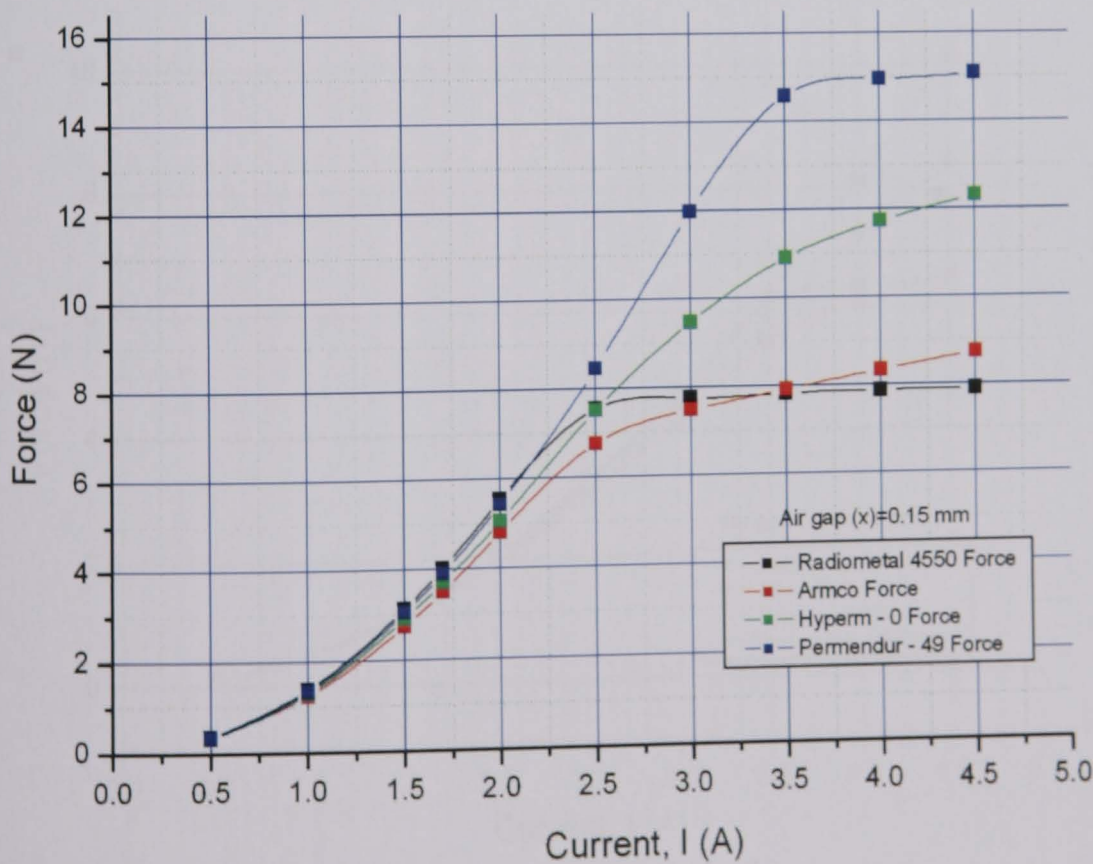


Fig. 6.2-4. C-core-II model variation of electromagnetic force for different excitation current with 0.15 mm air gap

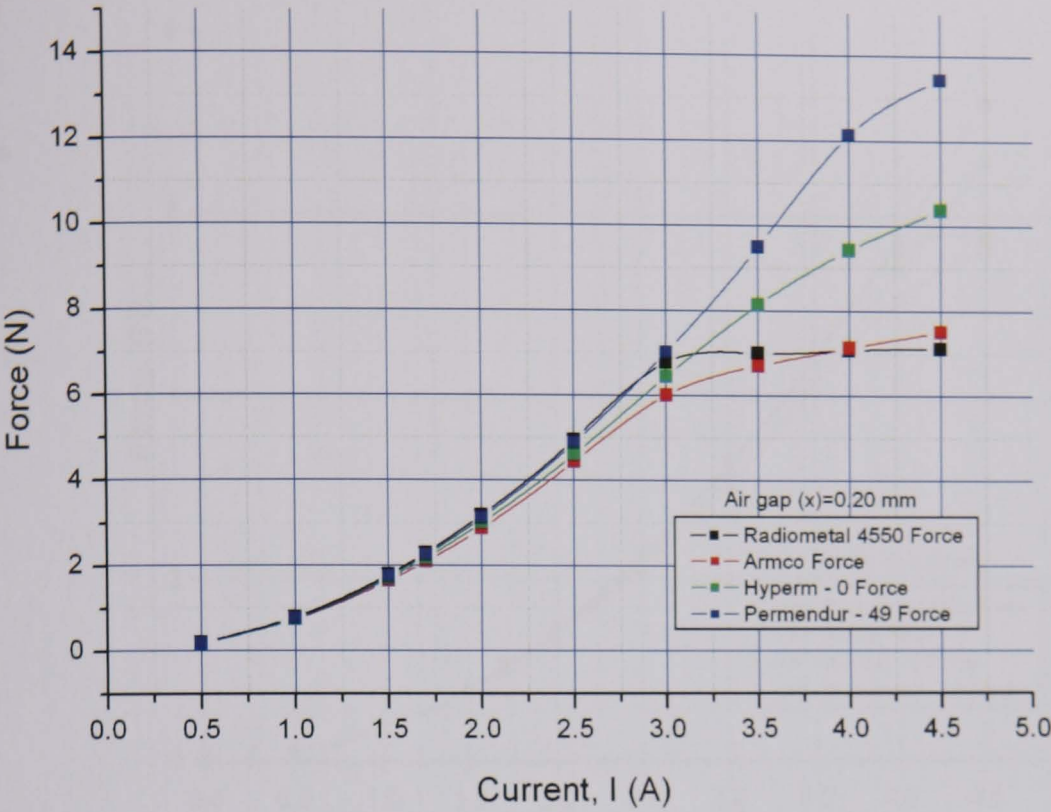


Fig. 6.2-5. C-core-II model variation of electromagnetic force for different excitation current with 0.20 mm air gap

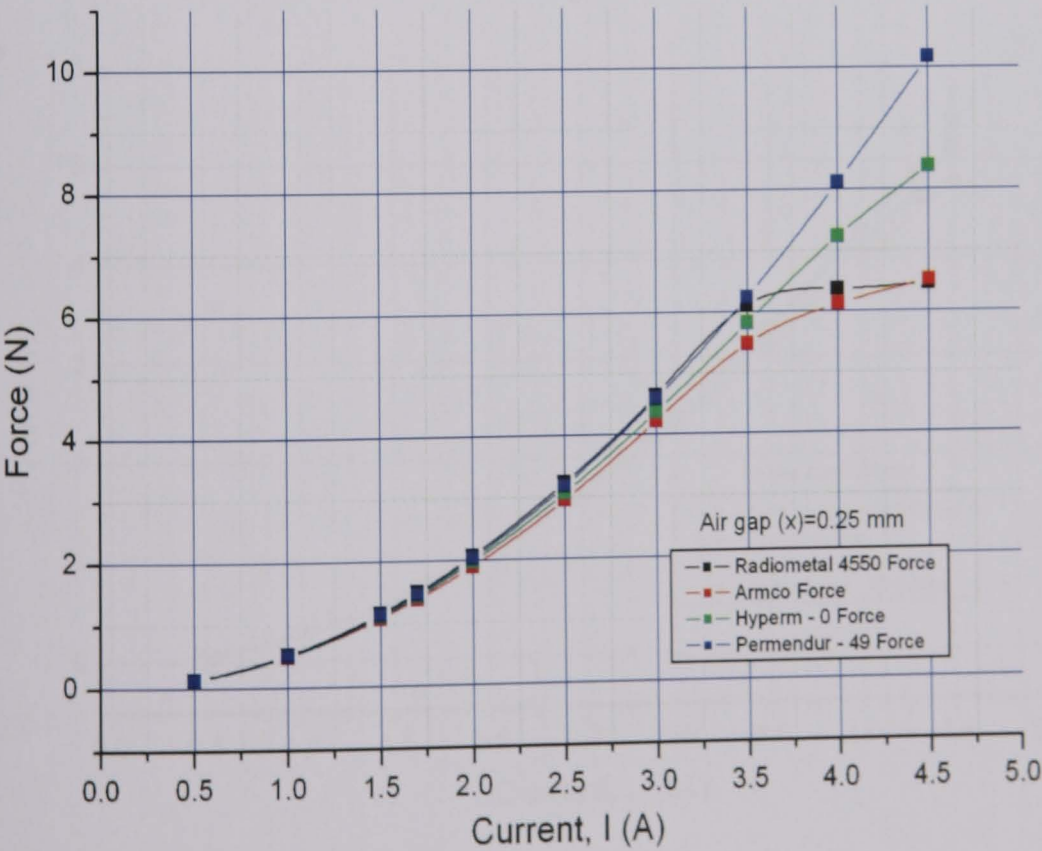


Fig. 6.2-6. C-core-II model variation of electromagnetic force for different excitation current with 0.25 mm air gap.

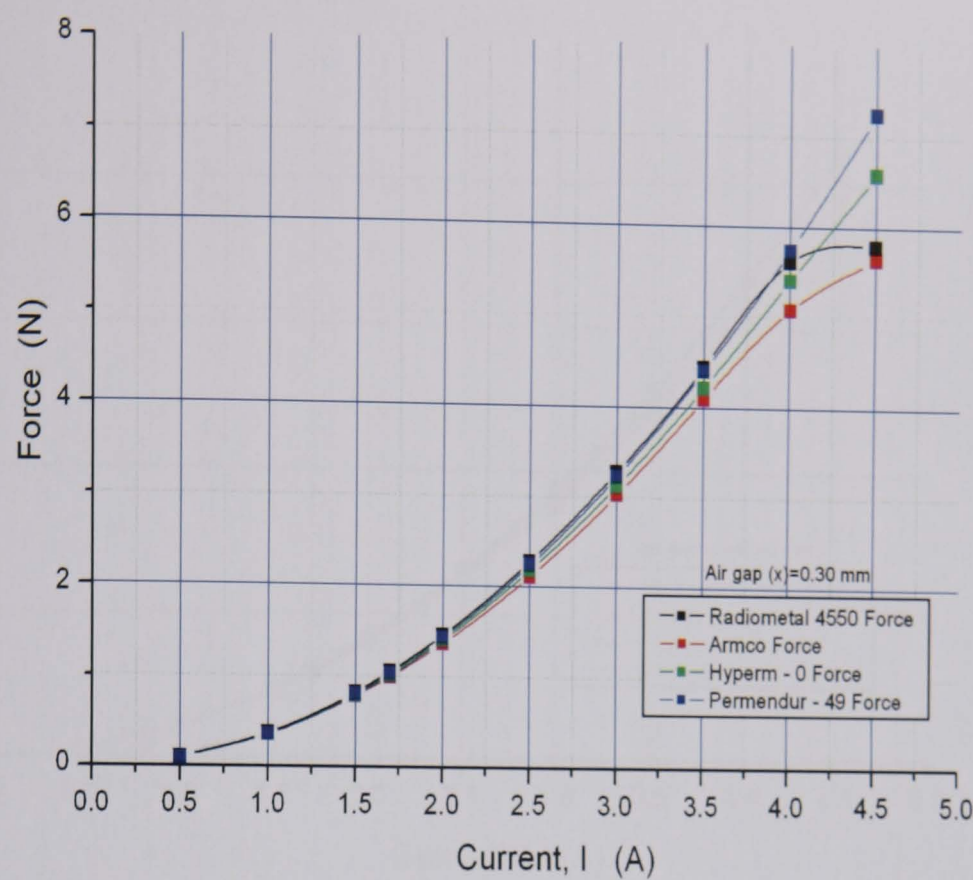


Fig. 6.2-7. C-core-II model variation of electromagnetic force for different excitation current with 0.30 mm air gap

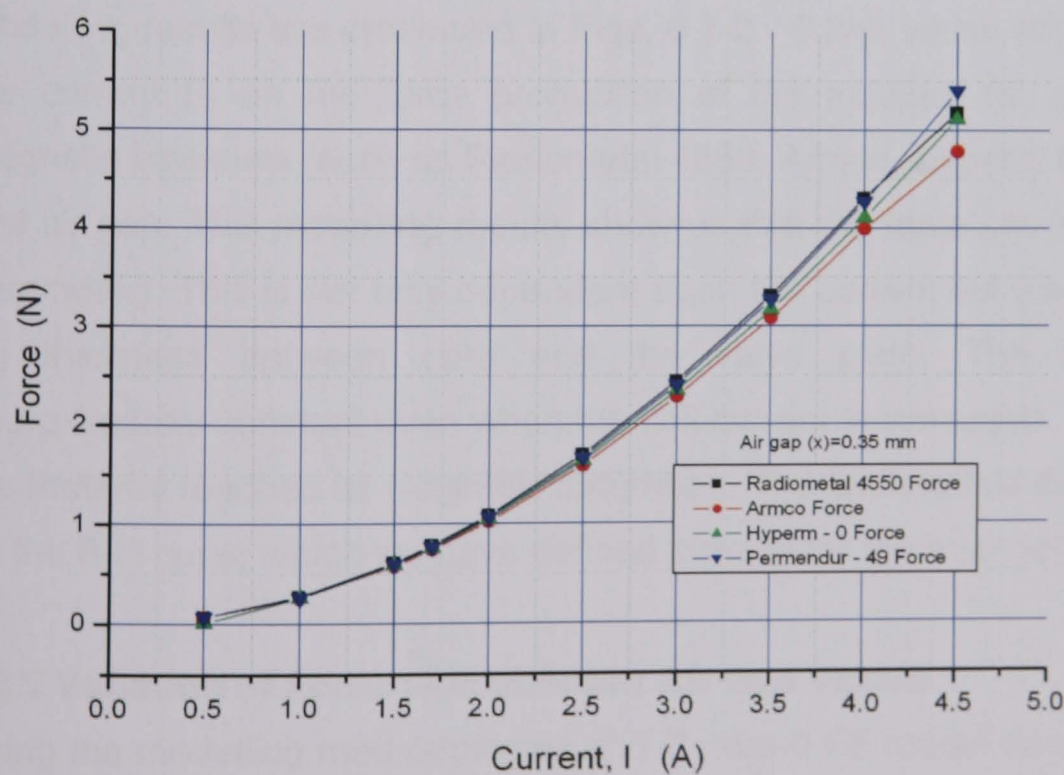


Fig. 6.2-8. C-core-II model variation of electromagnetic force for different excitation current with 0.35 mm air gap

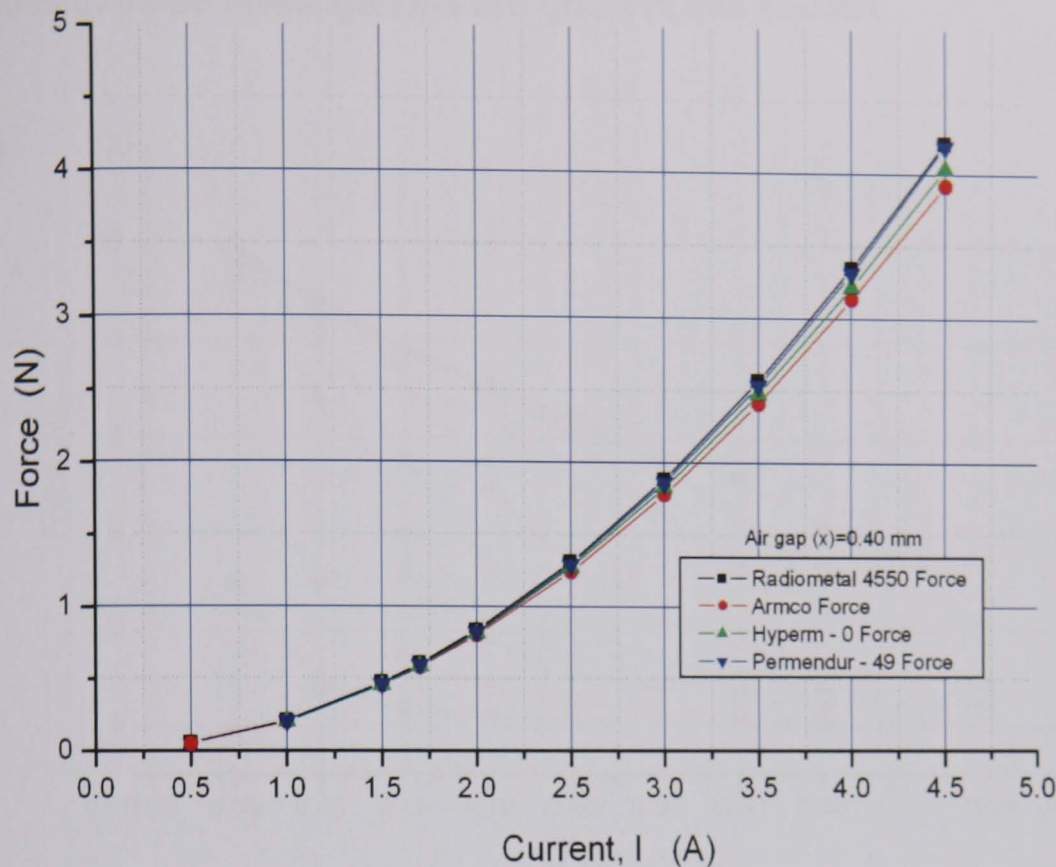


Fig. 6.2-9. C-core-II model variation of electromagnetic force for different excitation current with 0.40 mm air gap

Modelling results are presented in Figs. 6.2-2 - 6.2-9, which show the effects of the current (i) on the force production of the actuator for different type of magnetic materials (such as Radiometal 4550, Armco, Hyperm 0, Permedur-49) and air gap. This modelling results show us that the force (an important design parameter). This is not only dependent upon the current but also on the air gap (δ) thickness between core and the valve plate. The force becomes approximately constant even when the coil current is increased. This is because the material reaches its magnetic saturation. The limiting flux density is defined by the B-H curve which we have defined already for the material.

6.2.2 Variation of Force with different Air Gap Values

Using the modelling methodologies and C-core-II FE model designs of solenoid valve simulated to investigate their performance in terms of electromagnetic force, F is produced by a given model design. For this the effects the air gap and material parameters (Radiometal 4550, Armco ingot iron, Hyperm 0 and Permendur-49) were investigated. This was done, to investigate the effects of

the C-core-II design parameters on the static performance of the valve. The results of these investigations are given in this section.

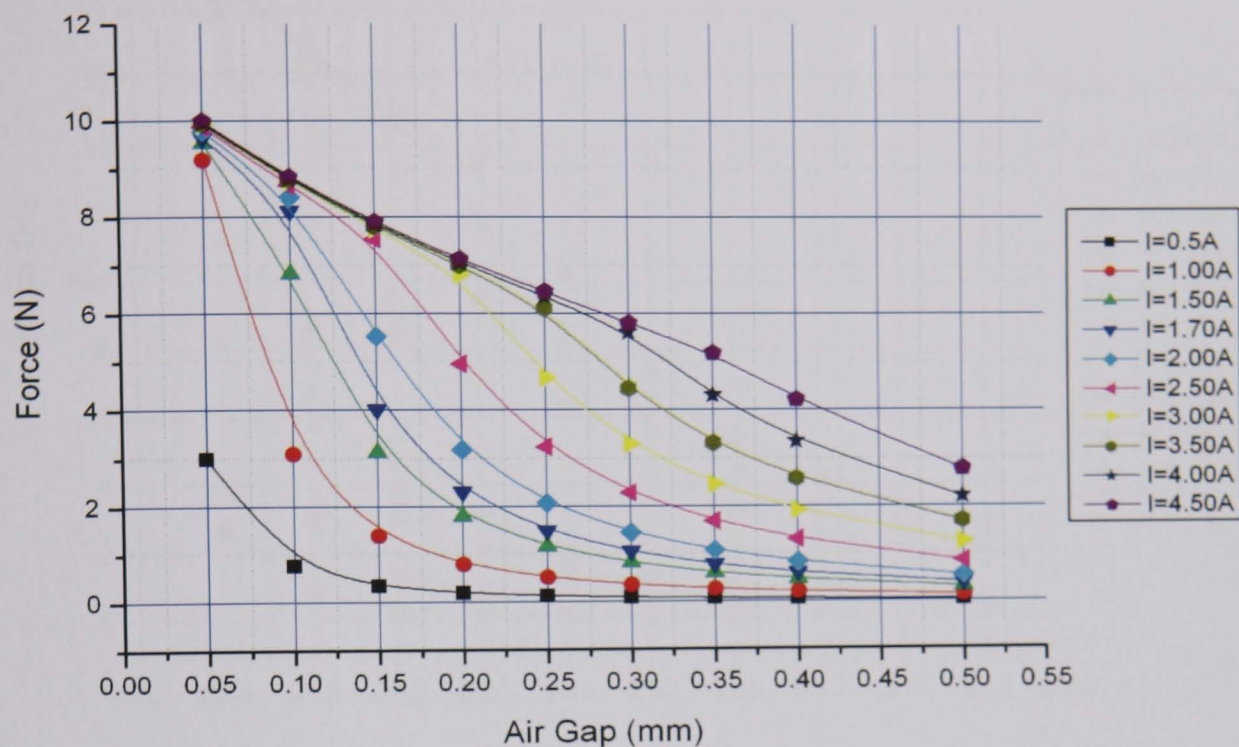


Fig. 6.2-10. C-core-II model variation of electromagnetic force for different air gap distance with Radiometal-4550

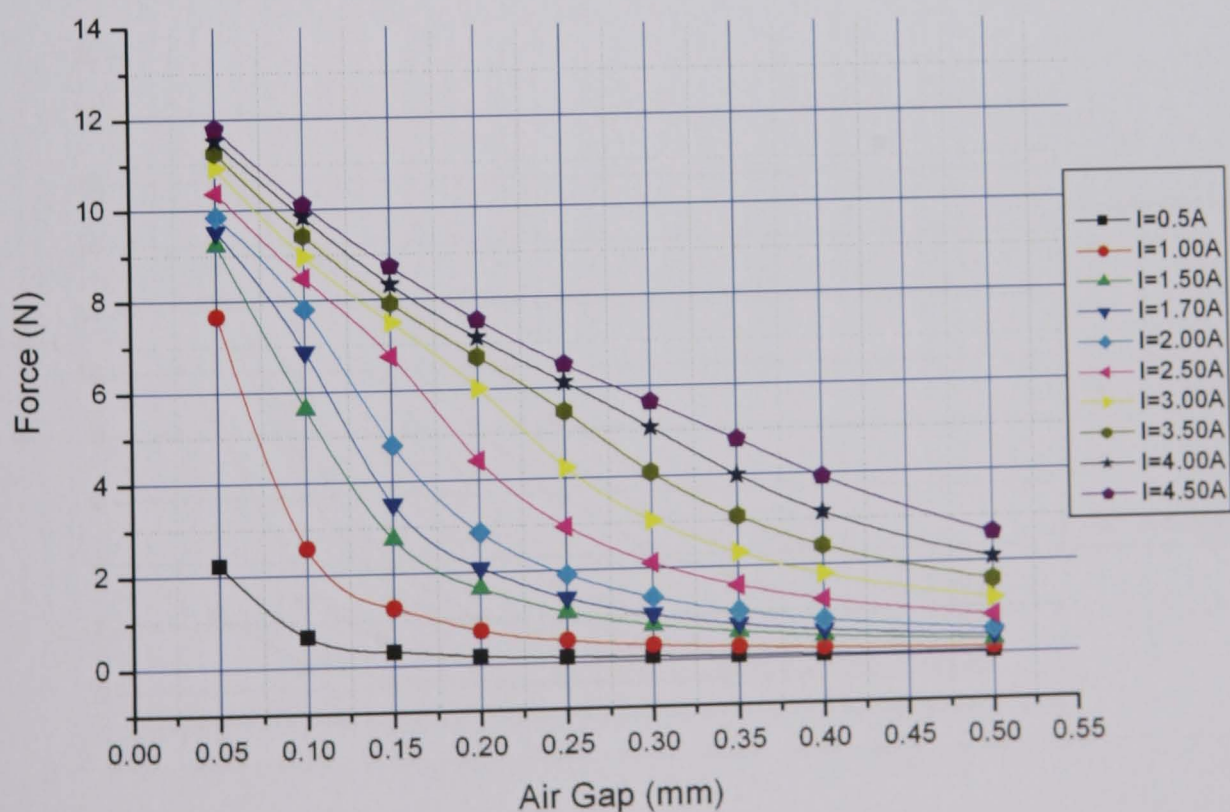


Fig. 6.2-11. C-core-II model variation of electromagnetic force for different air gap distance with Armco

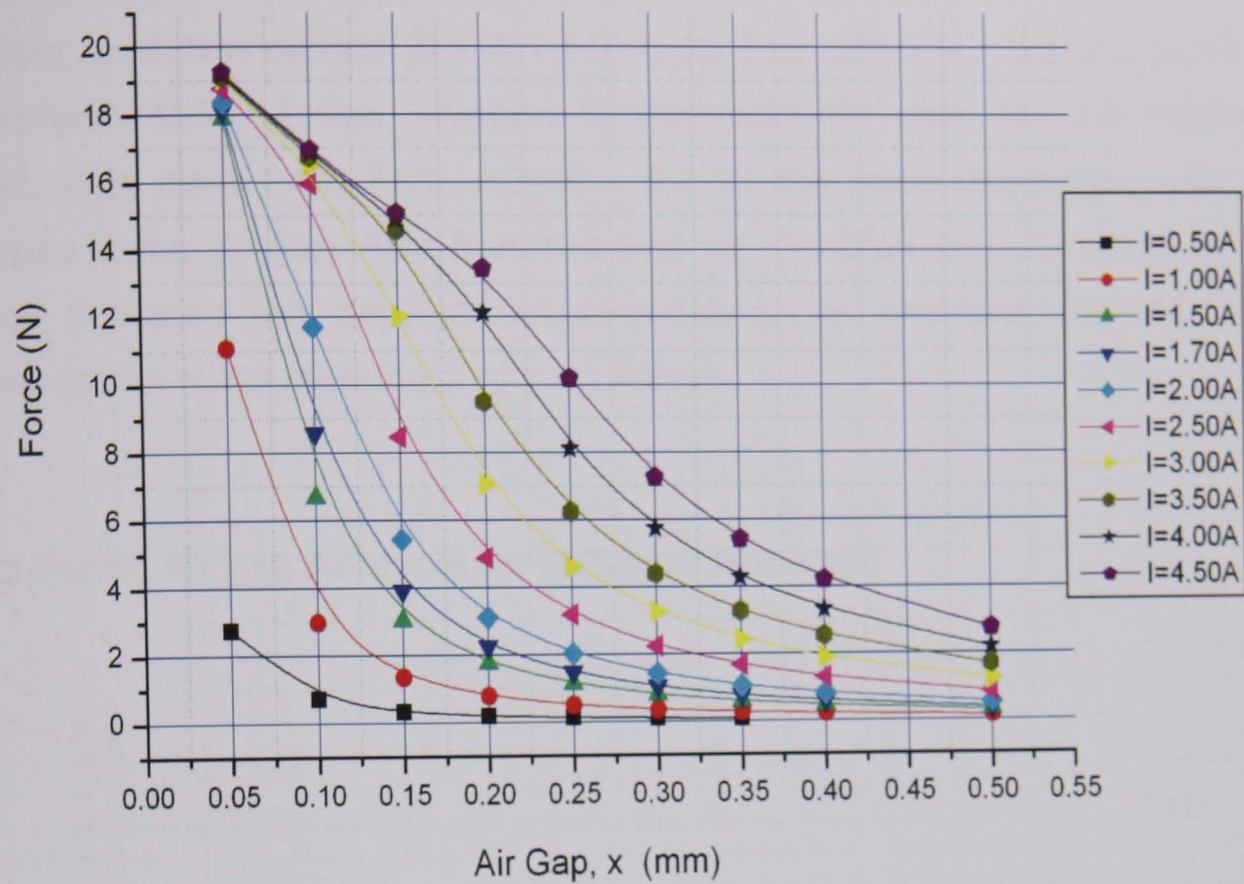


Fig. 6.2-12. C-core-II model variation of electromagnetic force for different air gap distance with Permendur-49

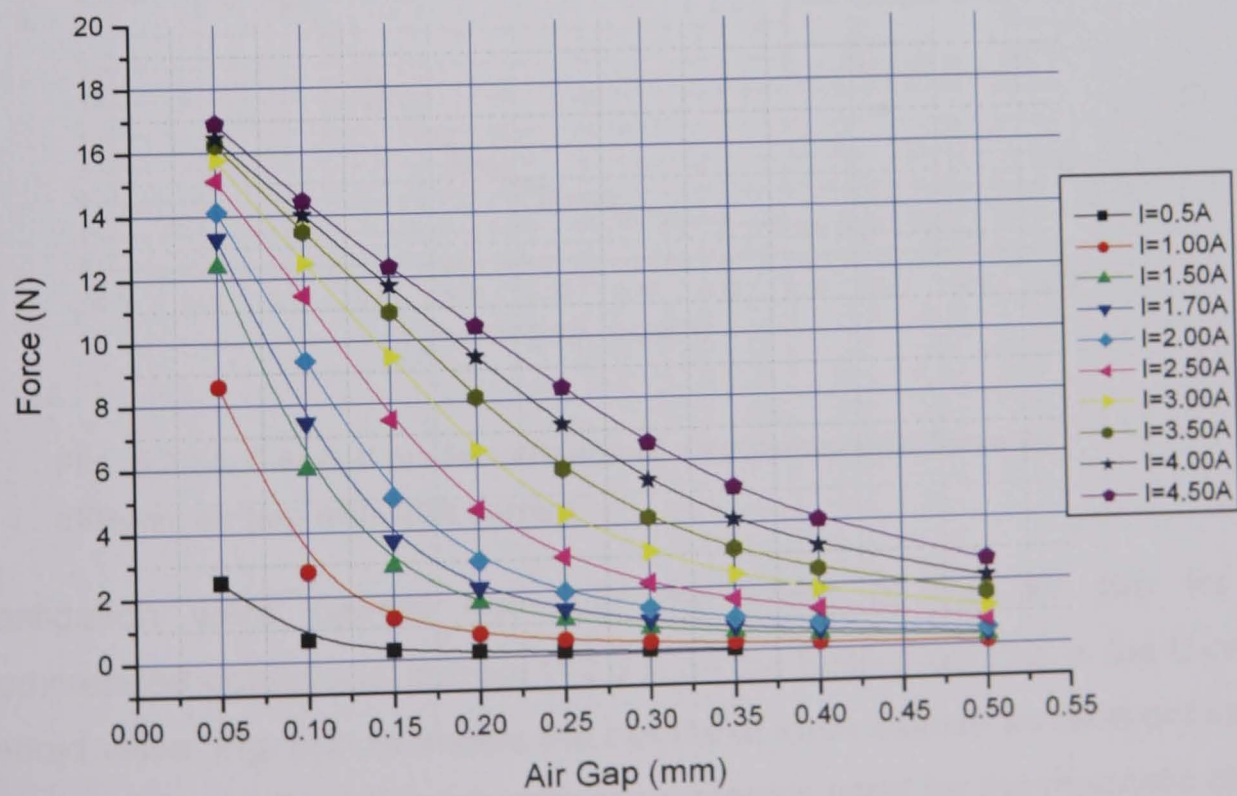


Fig. 6.2-13. C-core-II model variation of electromagnetic force for different air gap distance with Hyperperm-0

Simulation studies were also carried out to investigate the effects of air gap (δ) on the force produced by the valve. Figs. 6.2-10 - 6.2-13 show the results for different excitation current (0.5 A - 5.0 A) for four different materials (such as Radiometal 4550, Armco, Hyperm 0, Permedur-49) used for the magnetic circuit. It is clear from Figs. 6.2-10 - 6.2-13 the force decreases with the increase in the air gap. Also from this test we identified the robustness of the valves designed (air gap) in accommodating, for example, manufacturing tolerances for mass production of such valves.

6.2.3 Force, Air gap Analysis for Different Materials

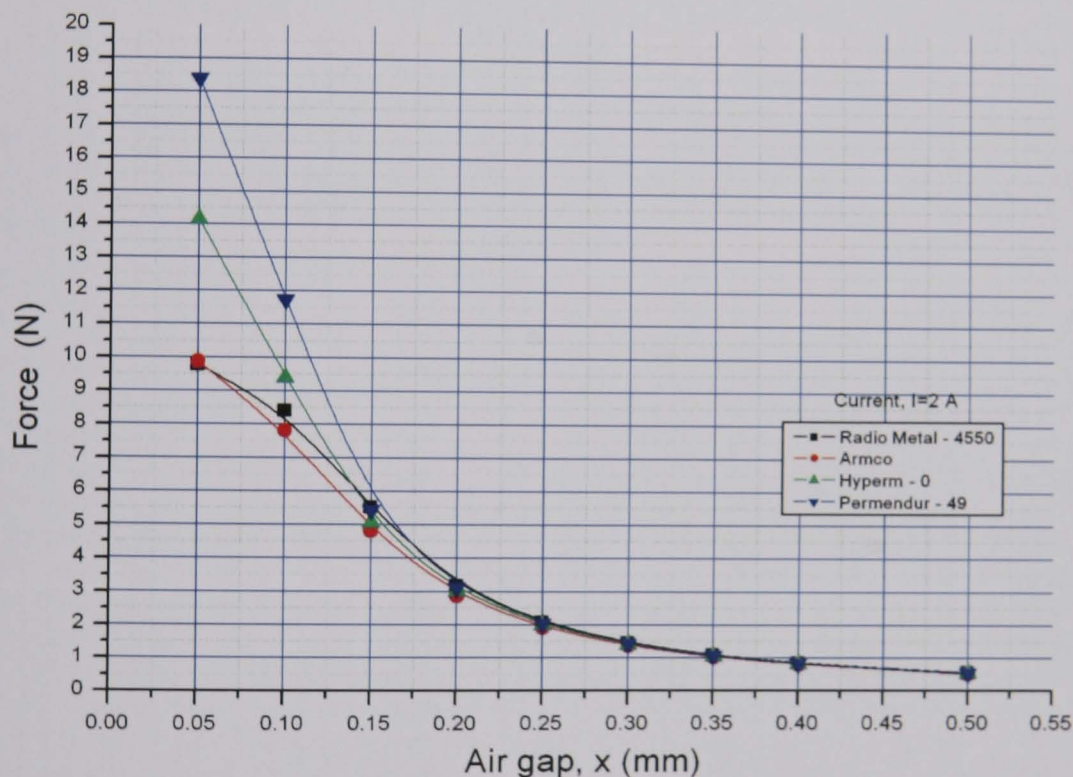


Fig. 6.2-14. C-core-II model variation of electromagnetic force for different air gap with $I=2\text{ A}$ current

Investigation were carried out over the effect of the air gap for the recommended operational current $I=2.0\text{ A}$ on the force produced in the C-core-II solenoid valve. Fig. 6.2-14 shows the results of such studies for different values of air gaps (δ) and for different magnetic materials used for the magnetic circuit. As it can be seen from Fig. 6.2-14, the force produced by the solenoid (for $\delta=0.1\text{ mm}$) far exceeds the design specification ($F \geq 8\text{ N}$). It also shows that for the magnetic circuit made of Hyperm-0 and Permedur-49 produce more force for

current $I=2.0$ A; because of higher saturation flux density of Hyperm-0 and Permendur-49. Also these modelling results show us that we can obtain the maximum force for a given current when the air gap is small.

6.3 E-CORE ELECTROMAGNETIC ACTUATOR

Investigations were carried out on some of the alternative design (E-core) concepts where the arrangements of coils and shape of the core are different. The investigations carried out for the E-core model are basically same as that of C-core-II model (Sections 6.2.1 - 6.2.3) Fig. 6.3-1 shown an E-core actuator.

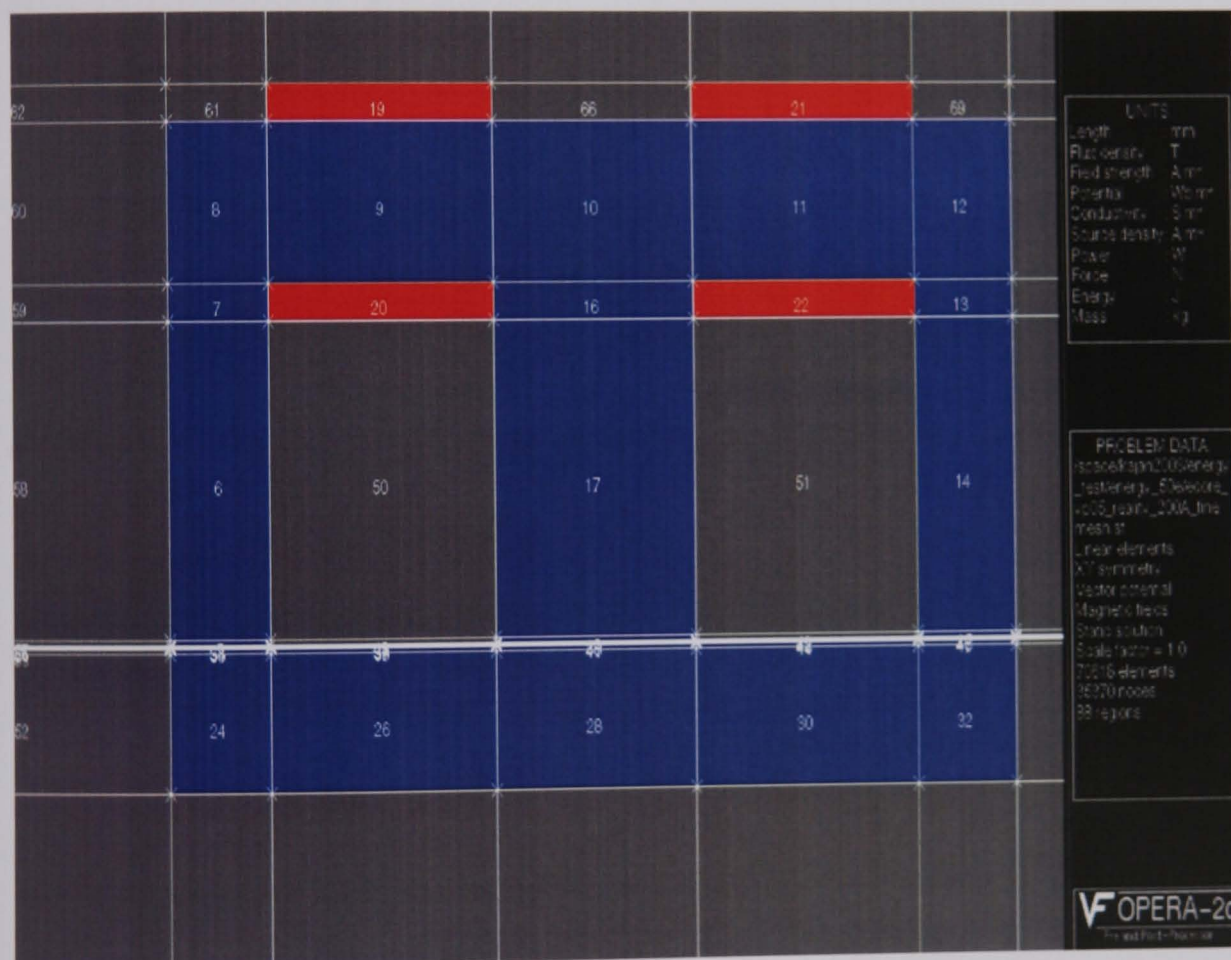


Fig. 6.3-1. E-core-II model electromagnetic actuator

6.3.1 Force, Current Analysis for Different Air Gap

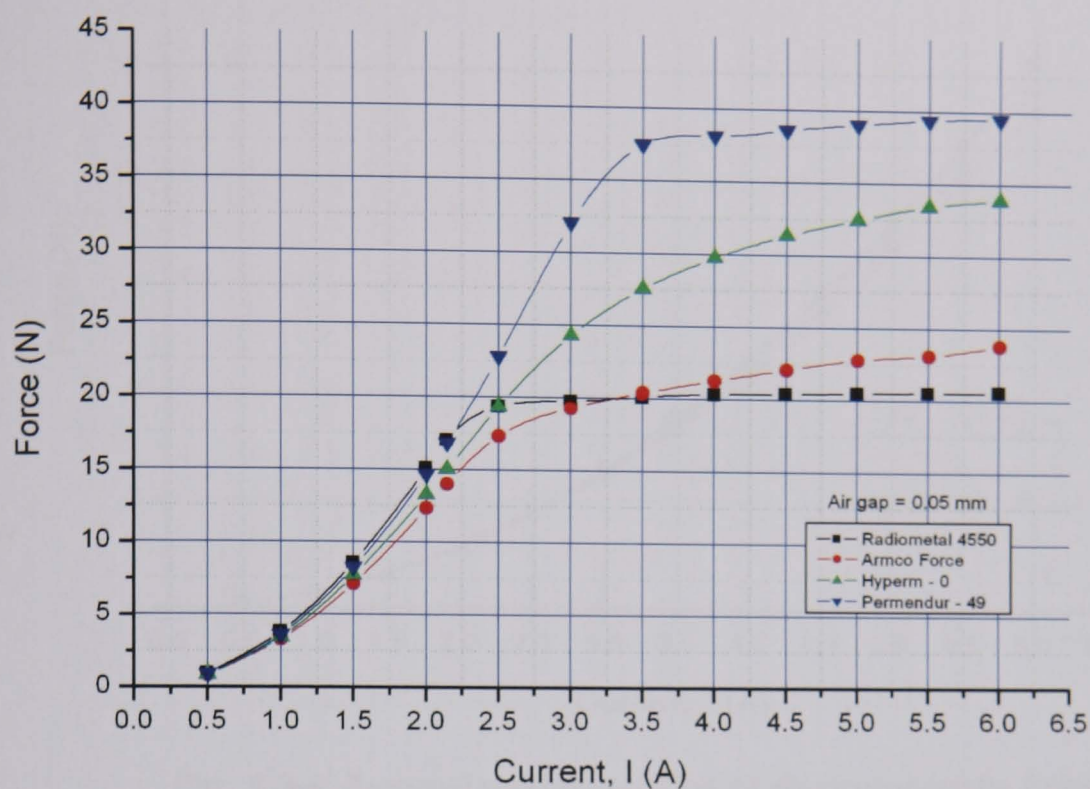


Fig. 6.3-2. E-core-II model variation of electromagnetic force for different excitation current with 0.05 mm air gap

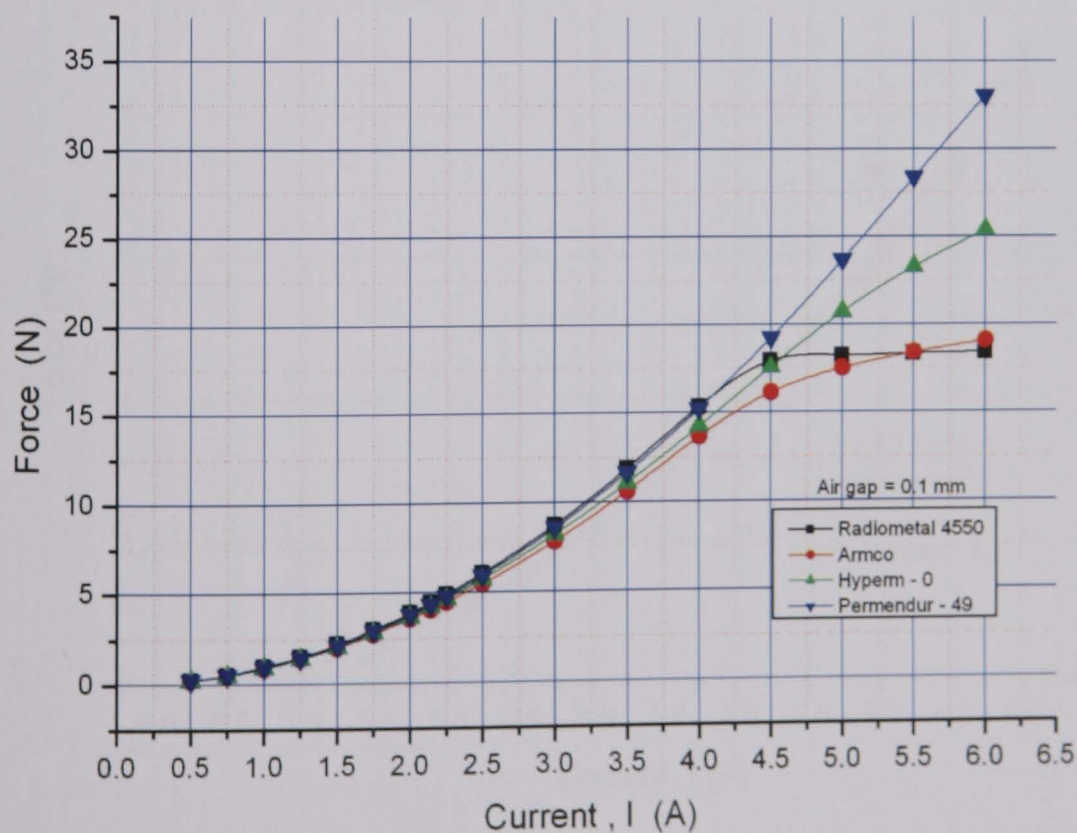


Fig. 6.3-3. E-core-II model variation of electromagnetic force for different excitation current with 0.10 mm air gap.

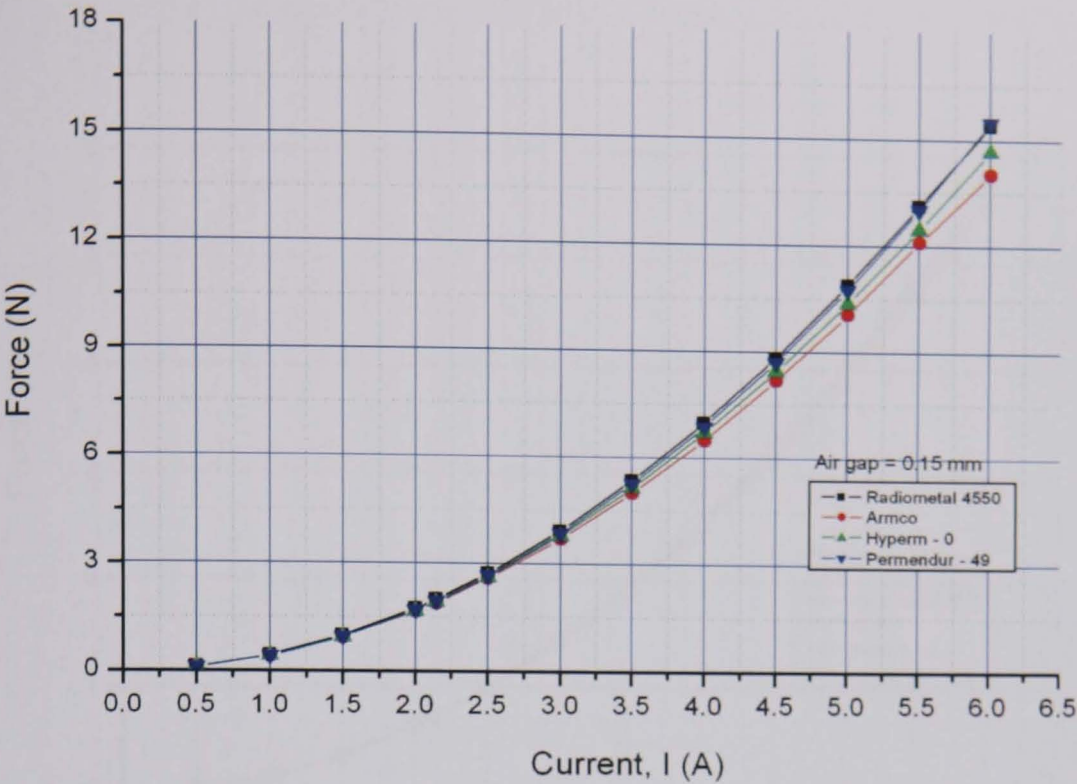


Fig. 6.3-4. E-core-II model variation of electromagnetic force for different excitation current with 0.15 mm air gap

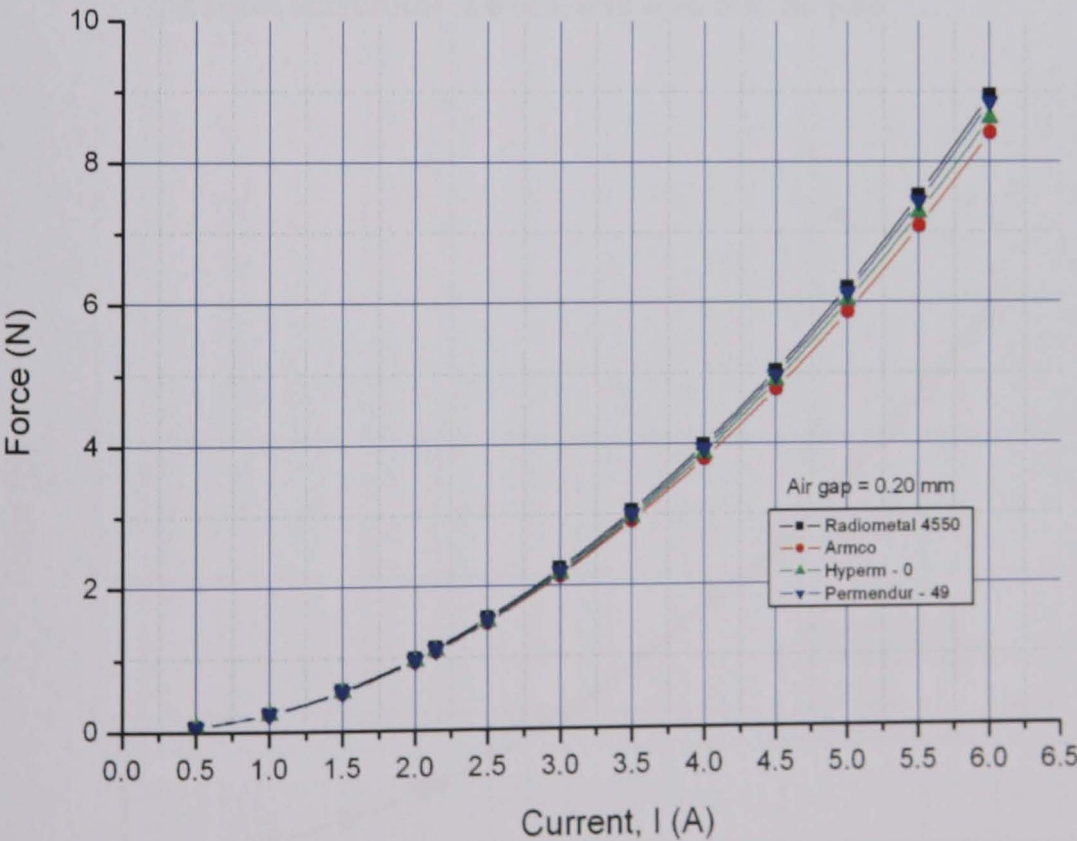


Fig. 6.3-5. E-core-II model variation of electromagnetic force for different excitation current with 0.20 mm air gap.

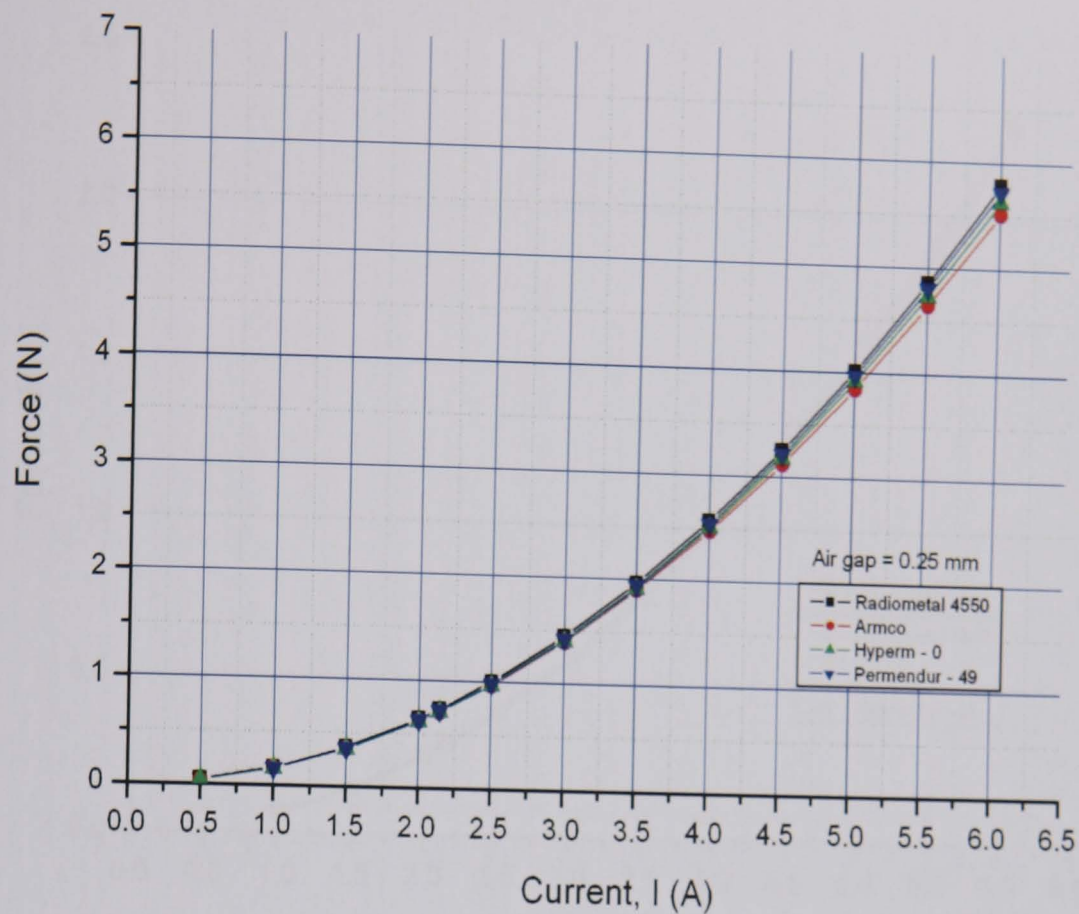


Fig. 6.3-6. E-core-II model variation of electromagnetic force for different excitation current with 0.25 mm air gap

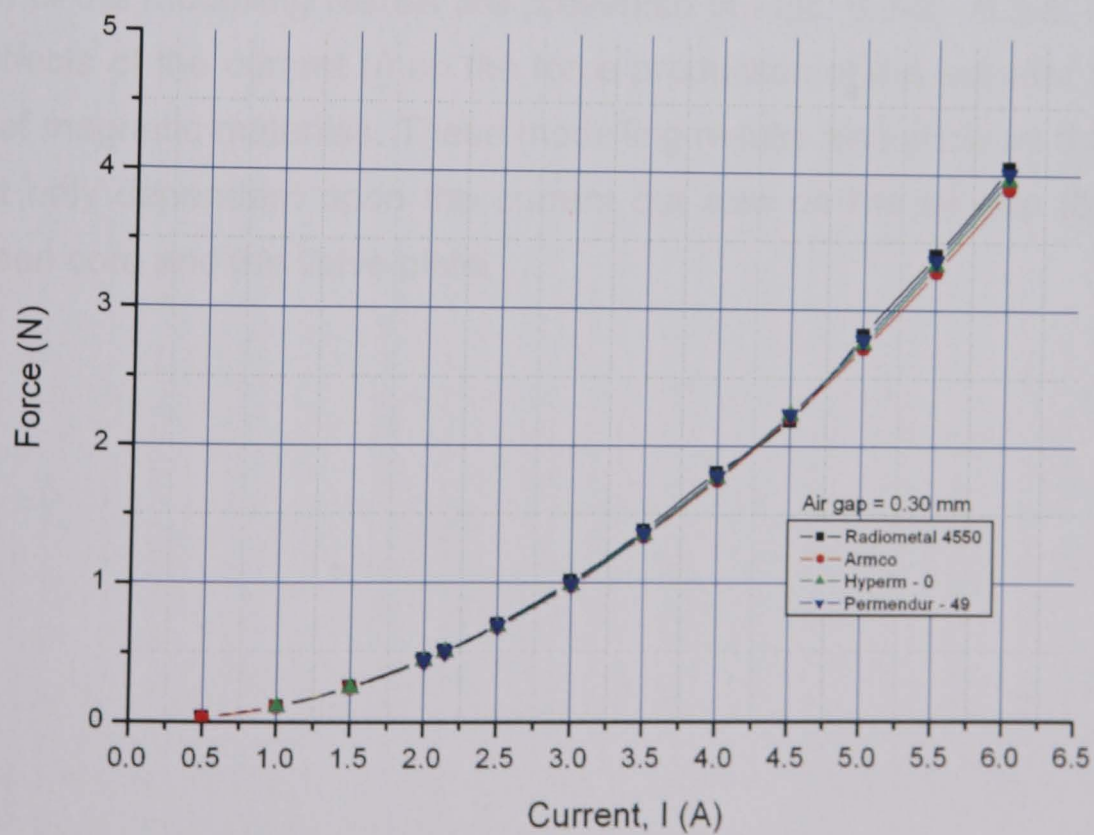


Fig. 6.3-7. E-core-II model variation of electromagnetic force for different excitation current with 0.30 mm air gap.

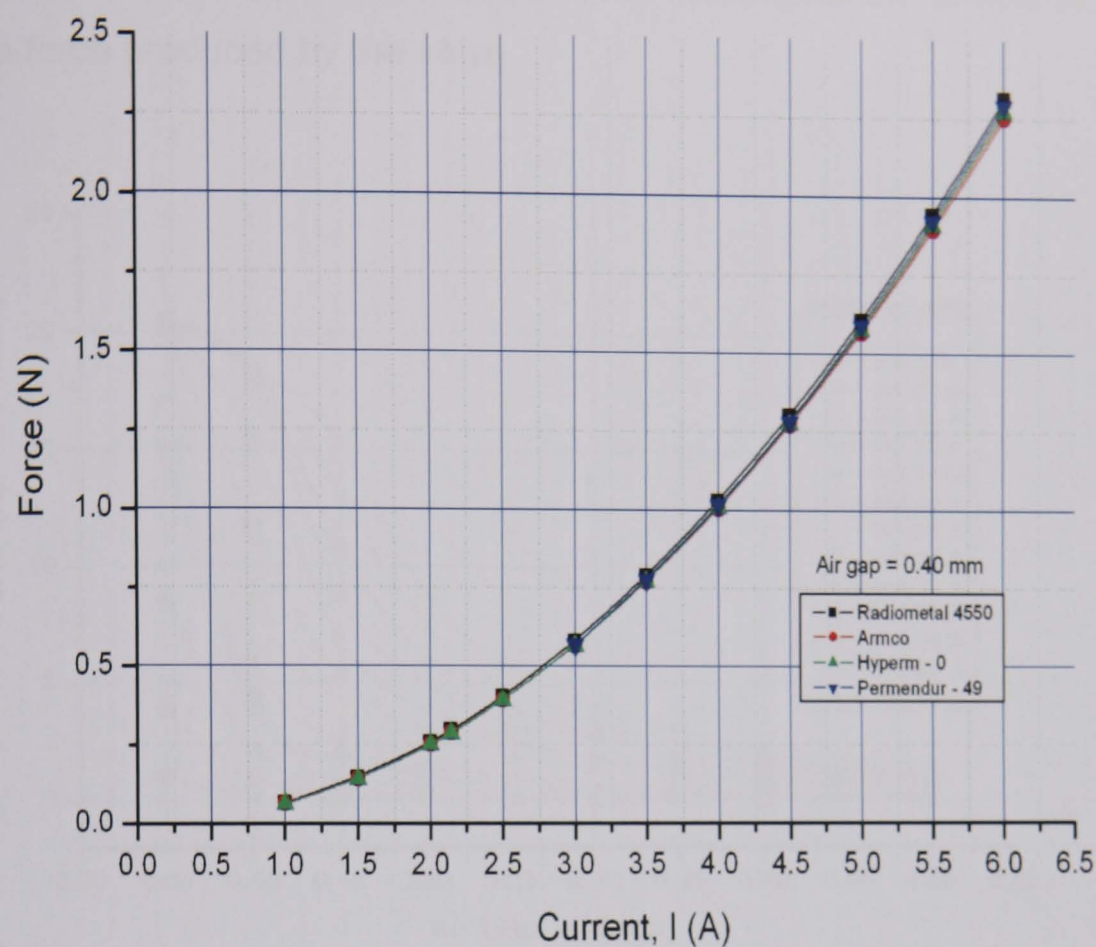


Fig. 6.3-8. E-core-II model variation of electromagnetic force for different excitation current with 0.40 mm air gap.

Some of the modelling results are presented in Figs. 6.3-2 - 6.3-8, which show the effects of the current (i) on the force production of the actuator for different type of magnetic materials. These modelling results also show us that the force is not only dependent upon the current but also on the air gap (δ) thickness between core and the valve plate.

6.3.2 Force Air Gap Analysis

Simulation studies were also carried out to investigate the effects of air gap (δ) on the force produced by the valve.

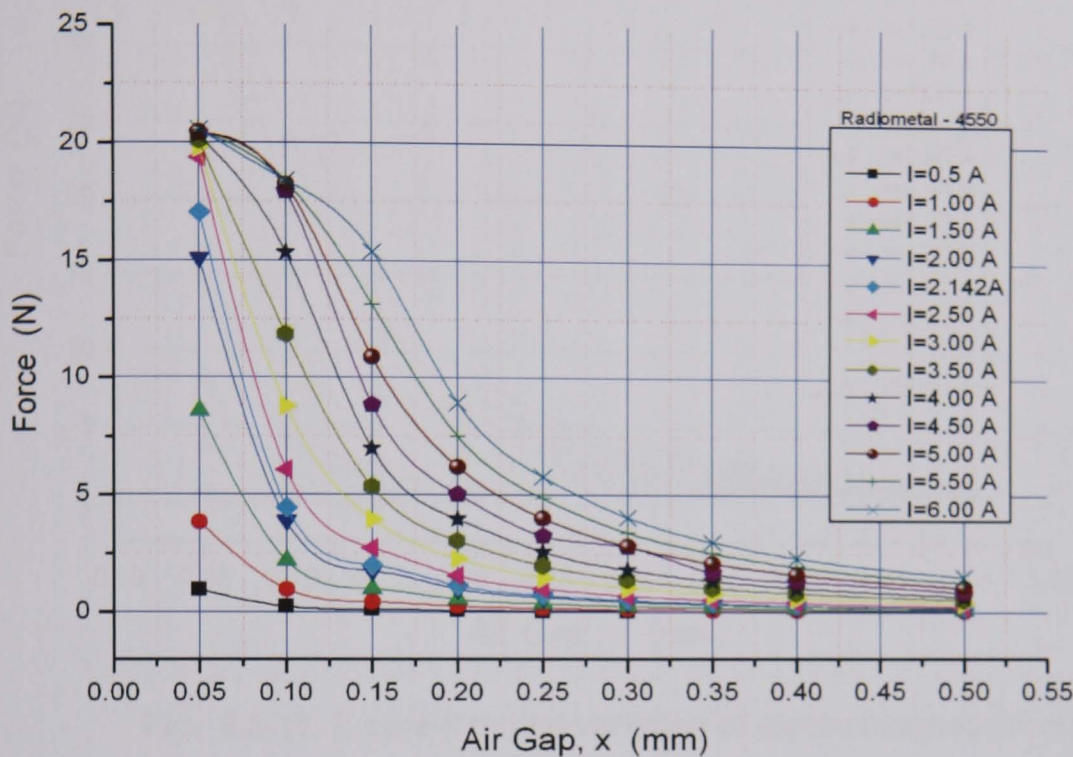


Fig. 6.3-9. E-core-II model variation of electromagnetic force for different air gap distance with Radiometal-4550

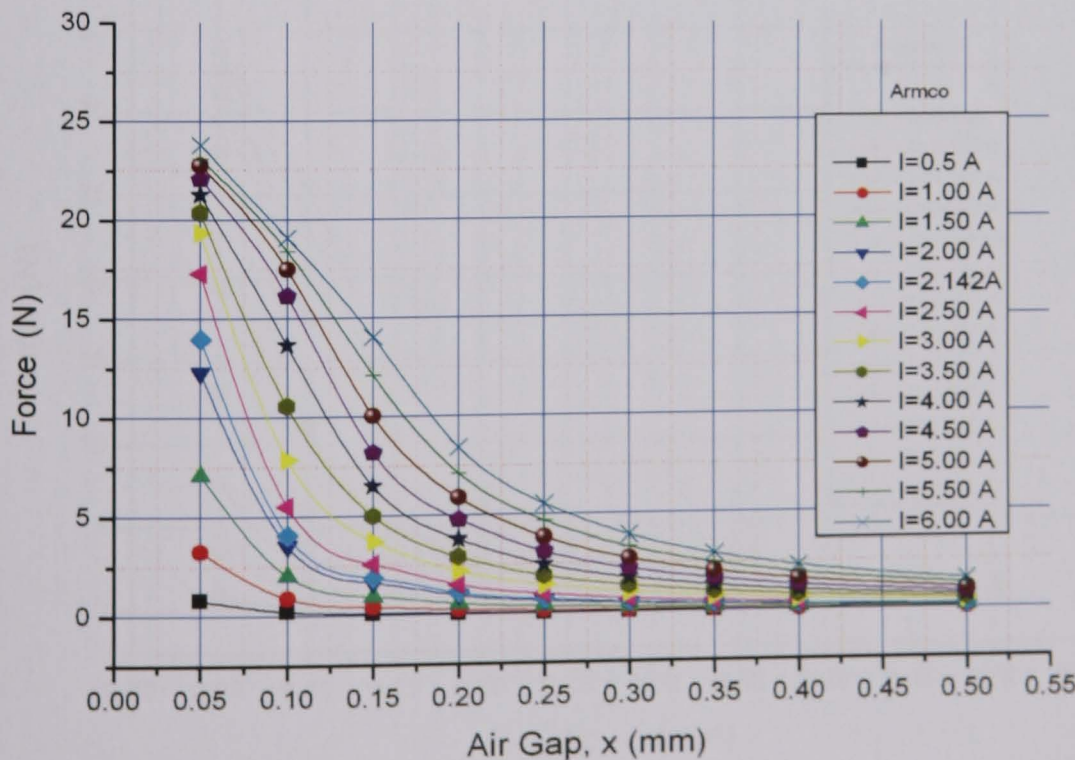


Fig. 6.3-10. E-core-II model variation of electromagnetic force for different air gap distance with Armco

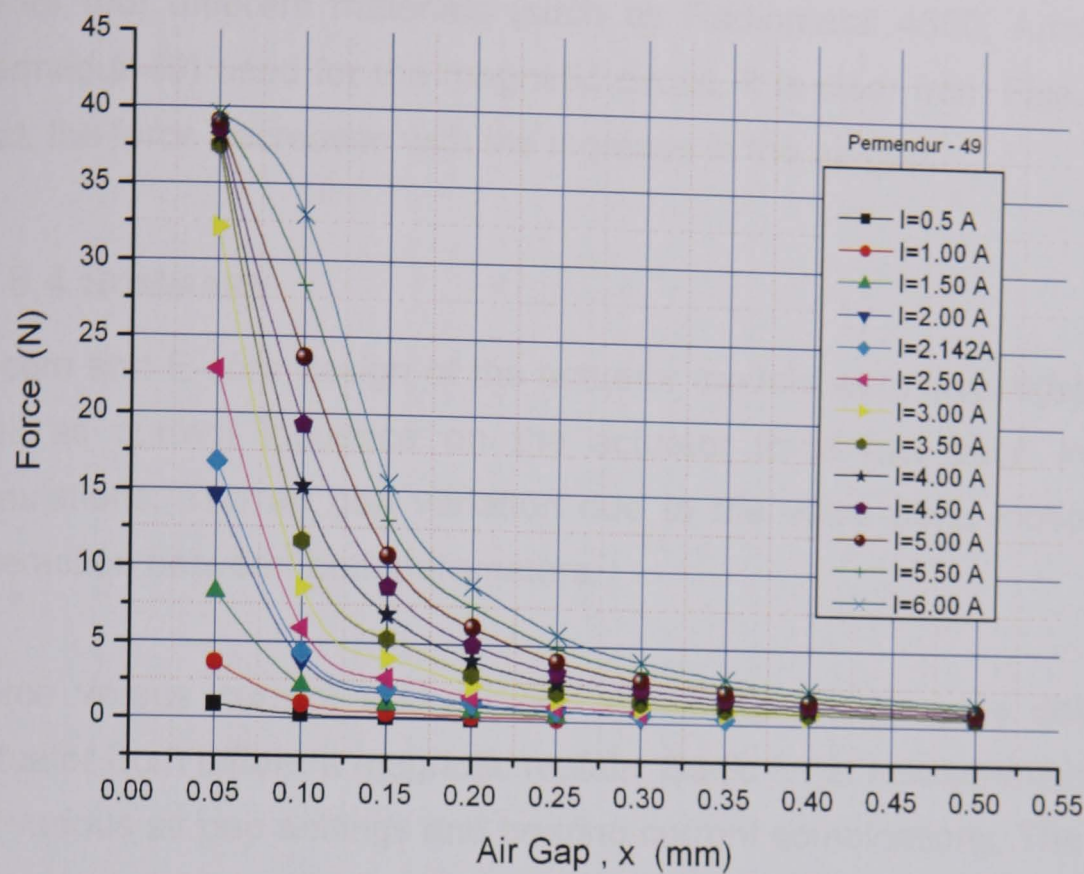


Fig. 6.3-11. E-core-II model variation of electromagnetic force for different air gap distance with Permendur-49

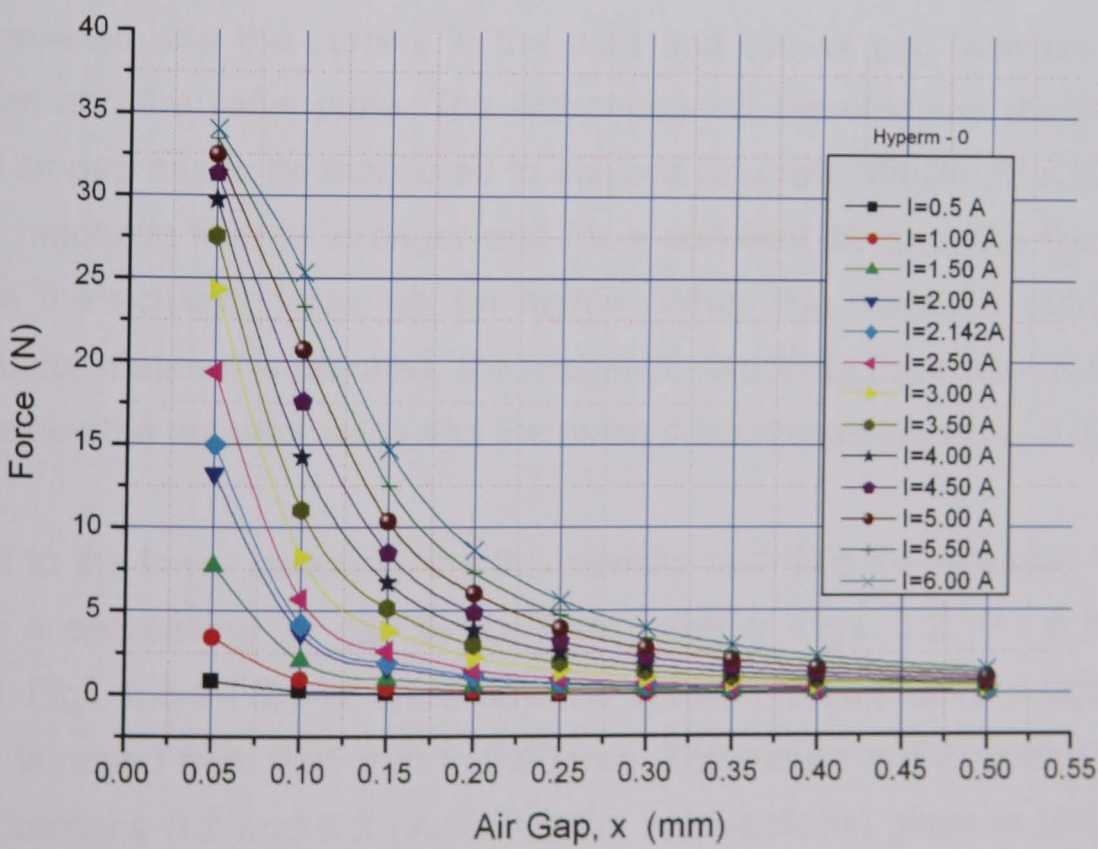


Fig. 6.3-12. E-core-II model variation of electromagnetic force for different air gap distance with Hyperm-0

Figs. 6.3-9 - 6.3-12 show the results for different excitation current (0.5 A - 6.0 A) for four different materials (such as Radiometal 4550, Armco, Hyperm 0, Permedur-49) used for the magnetic circuit. It is clear from Figs. 6.3-9 - 6.3-12 that, the force decreases with the increase in the air gap.

6.4 SUMMARY

C-core and E-core design of the actuator models were investigated. Air gap as well as current influence on the actuator force has been investigated by simulations. The air gap variation due to the valve plate motion leads to an interaction between both parameters.

Force versus current and air gap modelling results were obtained for the actuator from different magnetic metals. Static force measurements were made for various air gap settings and bearing current combinations. The resulting data were representing the force versus current and air gap relationship of the found actuator.

For the operation of the electromagnetic actuator, the most significant parameters are the current in the coils and the air gap between the actuator poles and the valve plate. The comparison to the obtained results shows that the air-gap has to be monitored to achieve accurate results. At a higher current, the magnetic field is stronger and for a constant air gap, the flux density and thus the actuator force will be higher. When the magnetic saturation of the actuator material is reached, the magnetic reluctance rises and thus the relation between the actuator force and the current decreases [sections 2.5-2 - 2.8-2].

Due to the lower reluctance the flux density and thus the actuator force will rise with a decreasing air gap in quadratic relation. Figs. 6.2-10 - 6.2-13 (C-core) and Figs. 6.3-9 - 6.3-12 show how the actuator force breaks in rapidly, if the air gap is raised from 0.05 mm to 0.50 mm. The results of FE modelling studies in the sections 6.2 and 6.3 (including the sub-sections) given in this chapter are very useful for reference for possible design changes that are recommended to maintain the overall performance of the valve design.

Chapter 7

DESIGN OF PROTOTYPES AND EXPERIMENTAL VALIDATION OF FINITE ELEMENT RESULTS

7.1 INTRODUCTION

The design stage is where theory and practice meet and compromise. The idealisations and assumptions made in the theoretical treatment of a device performance do not contain the full information required to foresee the outcome of the practical implementation of the design.

In order to make sure the computational results of numerical model is reliable and capabilities of this numerical model for predicting realistic physical processes and phenomena have to be confirmed before the model is accepted and applied to simulating in the real world problems. A numerical model is a complex system of equations wrapped with boundary conditions. It is not guaranteed to have these capabilities even it has been proven to be mathematically correct, unless they have been validated with physical model data. Numerical model validation using physical model data is a key step to confirm if a particular model is capable of reproducing true physical processes and mechanism.

This chapter deals with the validation of the design of the C-core-II electromagnetic actuator for which a set of specifications were generated by Sortex Ltd and the model was designed in this research work. Stringent design specifications are aimed at producing a high performance actuator for the highly competitive market in the sorting technology.

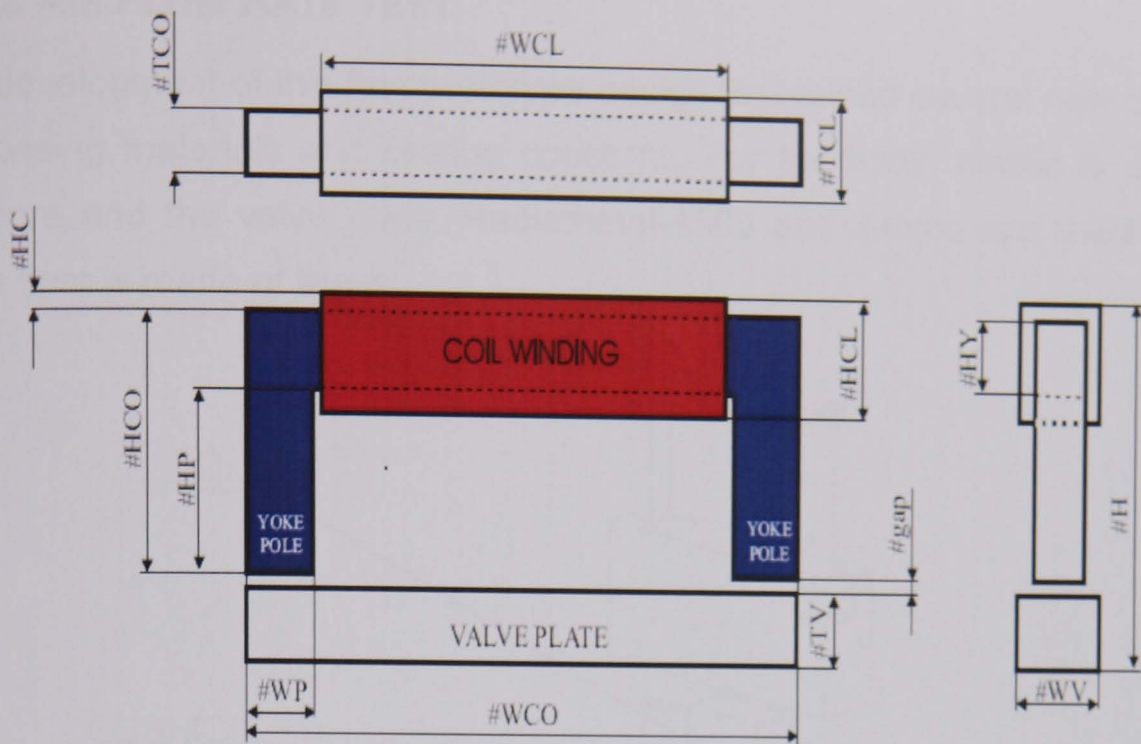


Fig. 7.1-1. Prototype design of the C-core actuator

Designs of the magnetic circuit and valve plate sub-systems were carried out with the use of the design models developed in chapter 5. The overall design strategies described in chapter 5 and chapter 6 adapted to the specific needs of this design task were followed throughout. The final design engineered to suit manufacturing practices, was implemented and tested. The performance attained was compared with the numerically predicated results and conclusion drawn about the CAD approach.

The technical specifications on C-core-II valves concern among other things the parameters:

DIMENSIONS IN MM UNLESS OTHERWISE STATED		SCALE 4:1		COIL DATA	
MATERIALS LIST		SHEET 1 OF 1		Diameter of copper wire	0.25
ARMCO		DATE			
RADIOMETAL 4550		10/02/2005		Packing Factor	0.60
HIPERCO 50					
HYPERM 0				Number of turns	136

Table 7.1-1 Coil winding technical data for C-core-II valve

The technical specifications tabulated in the Table 7.1-1 may vary according to the application. A number of designs were prototyped and tested against the Sortex design specification.

7.2 AIR FLOW RATE TEST

The development of this first prototype design test raised several new questions addressing materials and sealing concerns. For the body, plastic is used. For the core and the valve plate, Radiometal-4500 and Armco are used and the valve seat is made of brass.

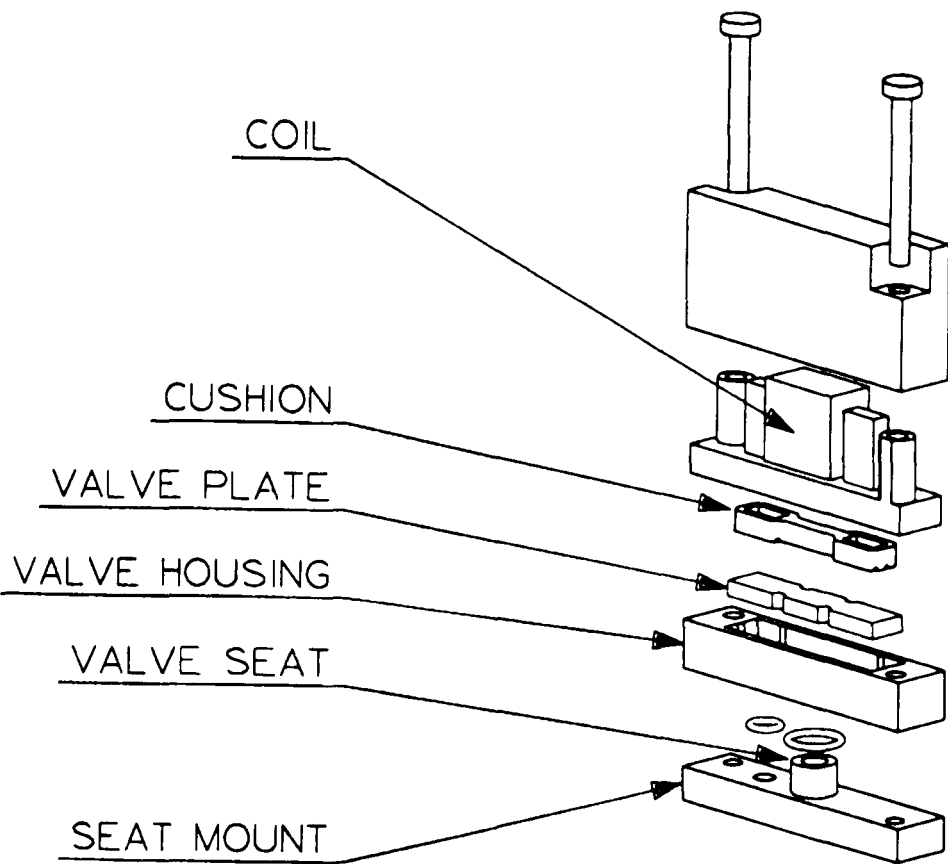


Fig. 7.2-1. Exploded drawing of the valve

The iron parts of the magnetic circuit have to be manufactured and assembled with high precision in order to fit the allowed tolerances especially for the air gaps.

Sealing concerns were a primary issue because seals would be needed to prevent the leakage of pressurized air. Unfortunately, this design had one significant problem to overcome. After sealing the valve we couldn't determine the distance between the valve plate and the poles (air gap=0.1mm). The valve seat is made of micro screw. One turn (360° of this micro screw (valve seat) give us 0.5 mm gap. To adjust the air gap to 0.1 mm we have to tighten the micro screw until the valve plate touches the poles and then we have to turn this micro screw anticlockwise 72° to get 0.1 mm air gap. The fully designed valve is shown in Fig. 7.2-2.

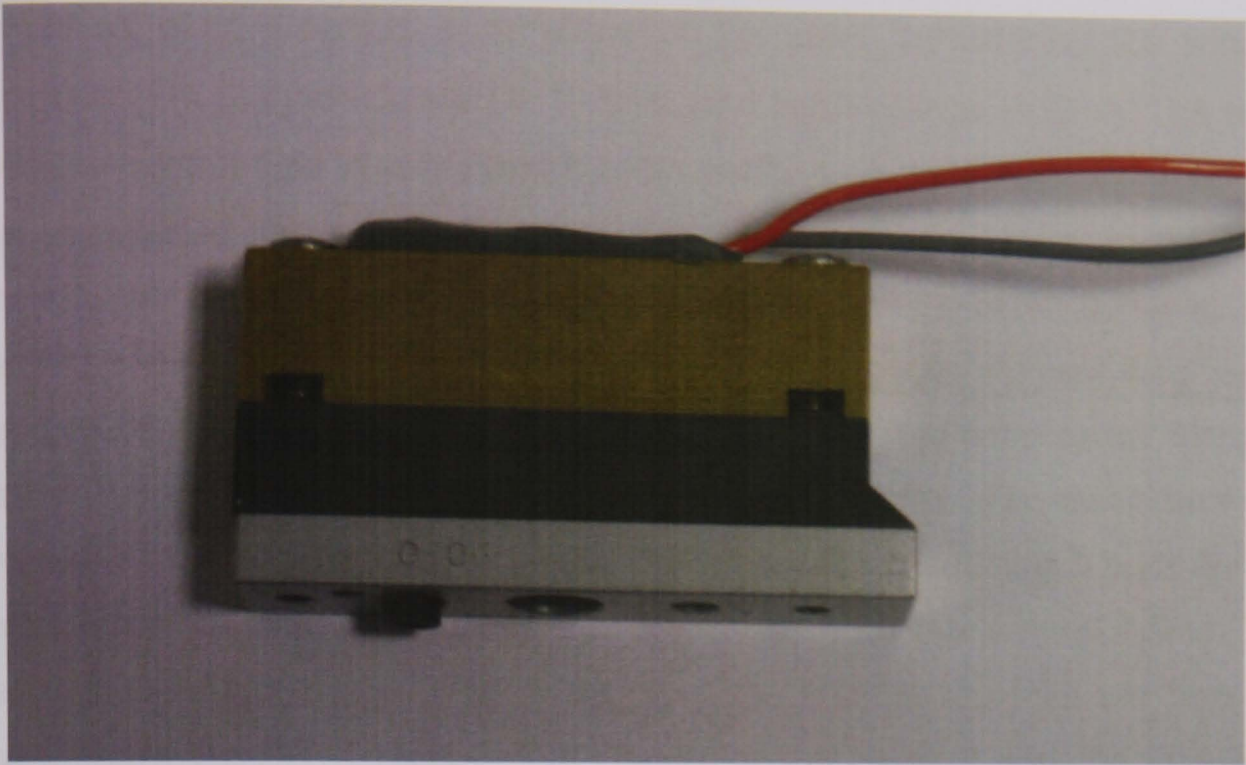


Fig. 7.2-2. C-core-II prototype ejector valve

The control of the valve is facilitated by a series of electrical components that ultimately supply voltage to coil. The control board has potentiometer adjustments for current limit and duration. Thus, the electrical time constant can be compensated. This controller board is shown in Fig. 7.2-3.

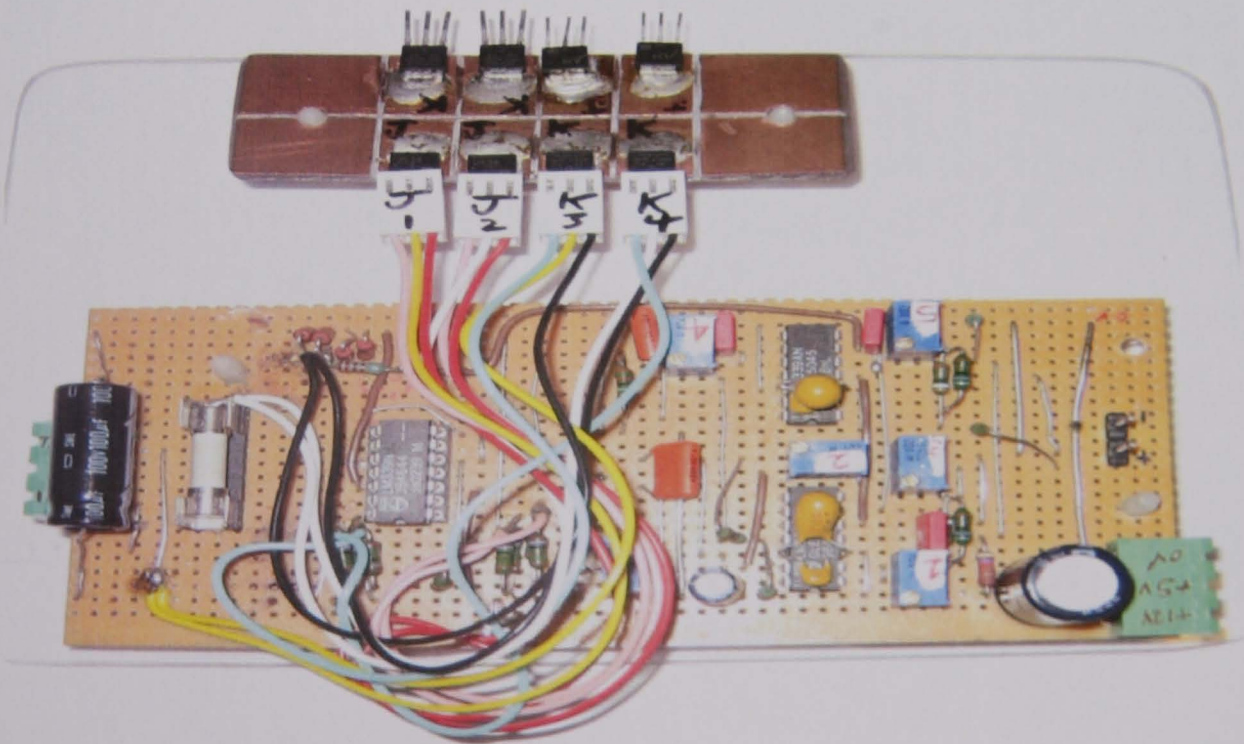


Fig. 7.2-3. Flexible driving circuit board for the valve

The flexible driving circuit board was designed and built to cope with the wide variation of such electrical parameters of the valve considering the winding resistance ($1\text{--}4\ \Omega$), inductance ($1\text{--}15\ \text{mH}$), and input voltage ($\leq 12\ \text{V}$). The valve is used to control flow to verify that it could perform as a controllable valve. The valve was tested using the control board with adjustment via potentiometers for current amplitude and duration for the pulse to hold and reverse currents. This board has facilities to deliver negative current. Negative current help us to demagnetize the magnetic circuit. Demagnetizing the magnetic circuit helps us to avoid the stiction between the valve plate and the core. The test board was powered by the TTI Thurlby Thander power supply, producing 5 volts for the control logic and 12 volts to operate the valve, from the control board. The current probe AM503 was used to measure the input to the solenoid from the control board. An HP 33120A Signal Generator was used to vary the frequency triggering the solenoid. A Kulite XTL-190M mass flow meter recorded the air flow through the valve.

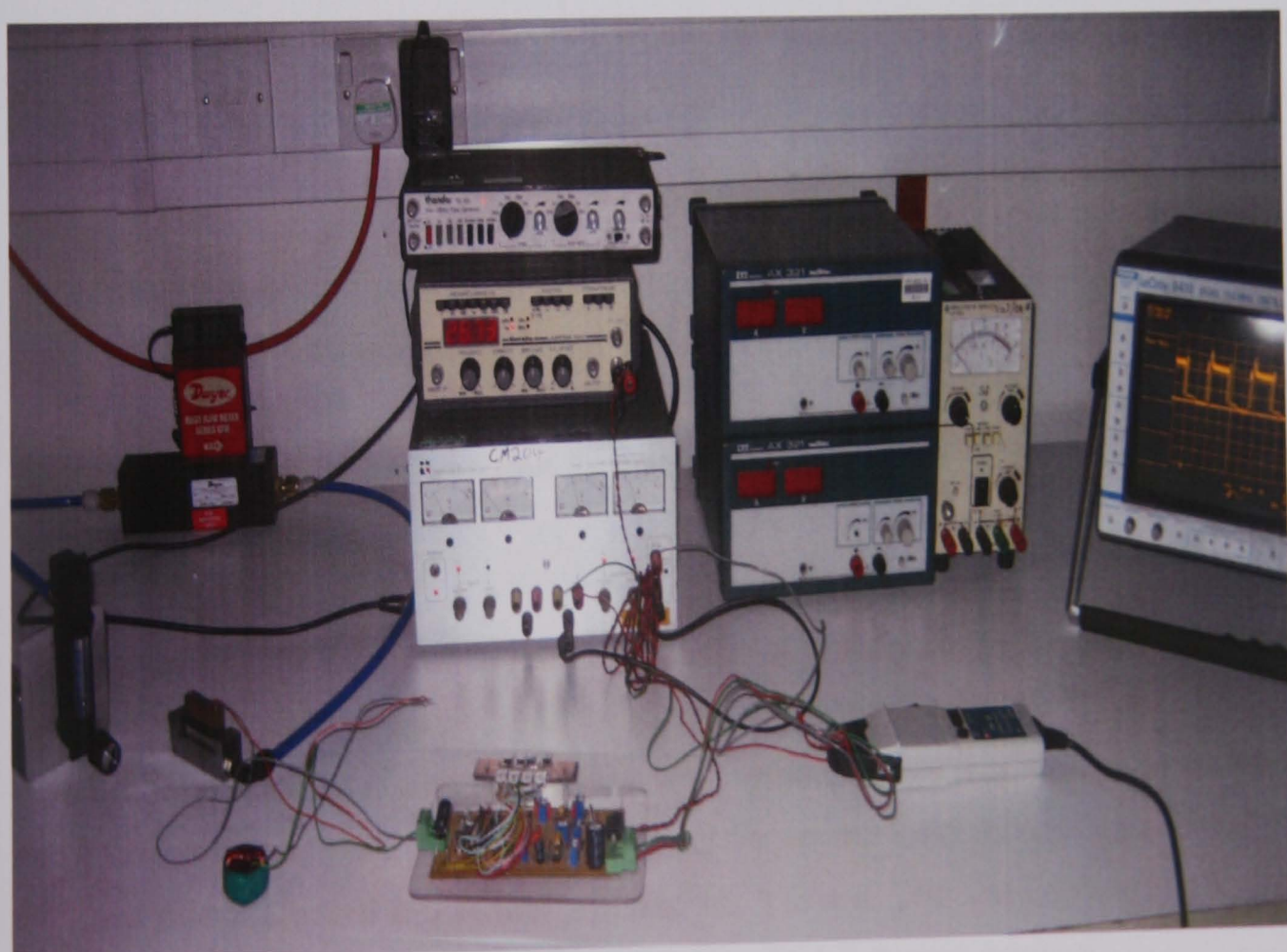


Fig. 7.2-4. Equipment setup for flow rate test

The prototypes were tested at Sortex and City University at various frequencies up to 150 Hz under specified air pressure and at current, air gap levels suggested by modelling results given in chapter 5 and chapter 6.

The test results presented in section 7.3-7.5 for individual valves showed that at lower frequencies the valves performed satisfactorily for a wide variation of excitation currents, air gaps, pressure levels, etc., confirming the robustness of the design.

However, at higher frequencies the performance tests showed the problem of 'stiction' of the valve plate with the poles. The stiction problem was attributed to residual magnetism and it was found to be more prominent in the case of prototype C-core-II that is made of Radiometal 4550 than that for prototype C-core-II that is made of Armco, although the comparison of hysteresis curves for these two materials suggested higher hysteresis effects in Armco.

The stiction problem was temporarily solved by coating the valve plate with a thin layer of non-magnetic material which increased the effective air gap and thereby reduced the effect of residual magnetism. The problem was solved for the second batch of prototypes by,

- (i) appropriately annealing the valves to minimize the effects of work-hardening (deterioration of the magnetic properties due to machining) and by,
- (ii) taking appropriate measures in the driving circuitry by introducing negative current.

To test the performance of the second batch of prototyped valve, the valve was driven with a square wave voltage. The DC voltage was 12 V, and the DC resistance was 1.2 Ω . The frequency was varied through a signal for different input frequencies from 0 to 150 Hz. In order to achieve the desired switching times, a boost current 2.5 A was applied for 1.2 ms. The valve plate movement occurred in this time. After that, the hold current 1.5 A was applied.

Pressure was measured at inlet port of the valve. This valve met the requirements for our application. The designed valve tested with a 0.10 mm air gap had a maximum flow rate of 14.5 liter per minute at 60 psi response at 150 Hz. The prototype shows a good flow rate behavior.

7.3 EXPERIMENTAL VALIDATION OF INDUCTANCE MODELLING RESULTS

The finite-element model (FEM) and computational modelling are developed for the evaluation and improvement of the dynamic performance of solenoid actuators. The model used to study the magnetic characteristics and dynamic behaviour is prototyped and ready for the experimental tests.

The aim of this task is to validate the inductance values calculated by FE modelling. This is done by performing several measurements of time constant for different current input using the prototyped valve. Validation of this FE modelling results also helps us to validate the force calculated by the FE modelling.

Force acting on the plunger is given by the equation (3.5-10) [section 3.5.1],

$$F = \frac{1}{2} i^2 \frac{dL(x)}{dx}$$

The force F and the inductance L of the actuator mainly depend on the position of the valve plate (air gap, δ) and the current (i) in the coil.

The C-core-II actuator, which was designed in this project, was used for this validation. A series of tests were carried out to investigate how the inductance of the actuator was affected by variation of air-gap between the core and the valve plate.

The following is a list of the experimental equipments used for this test.

Power Supply: A Thurlby Thandar Instruments PSU was set between 0.3 Volts and 30 Volts.

Measuring

Equipment: The output was measured using an AM503 current probe
HP54642D signal Oscilloscope and 3225 Black Star multi-
meter.

Shims Used: 0.1mm, 0.05 mm, 0.03 mm

7.3.1 C-core-II Model Radiometal - 4550 Valve Response Test

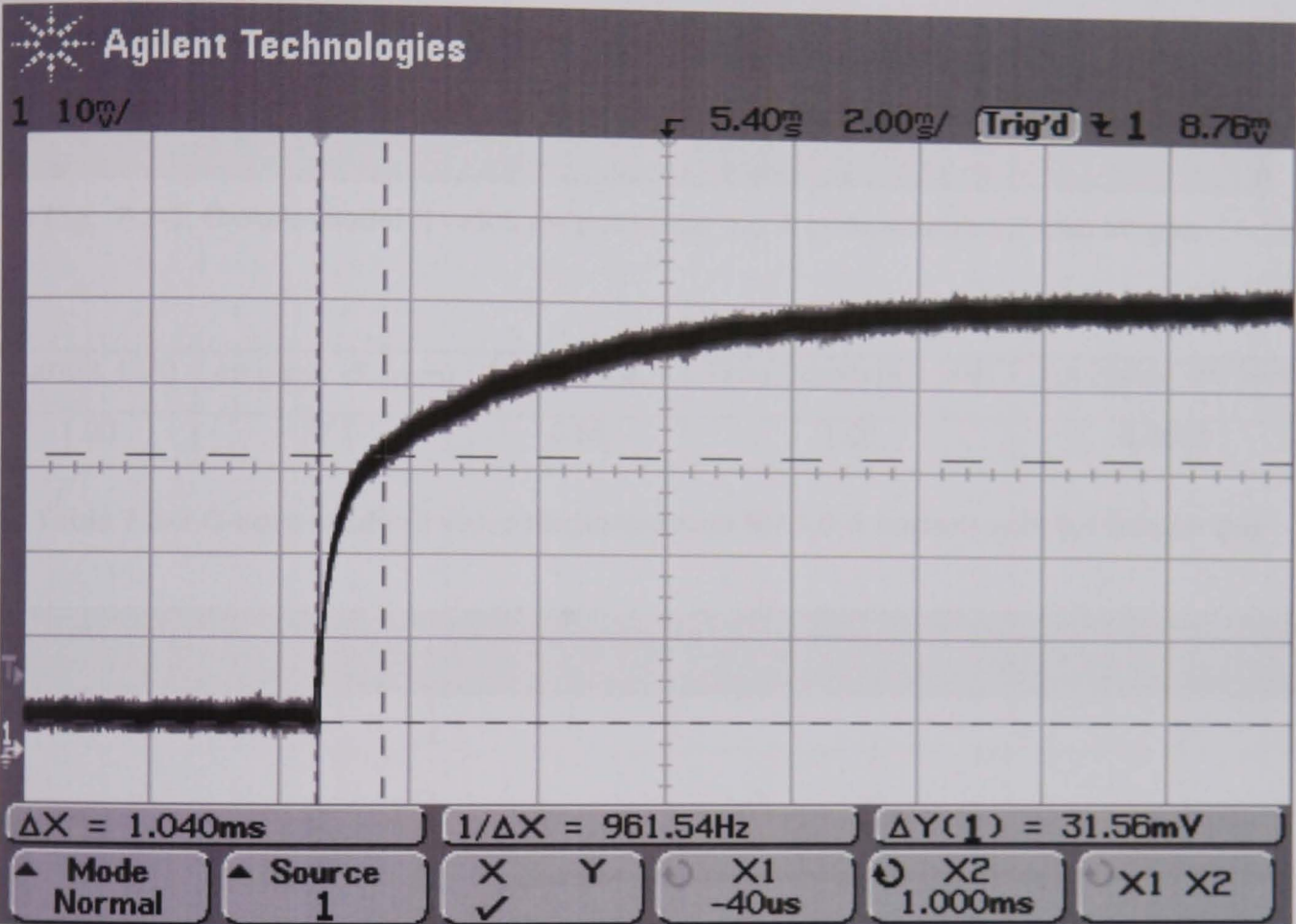


Fig. 7.3-1. C-core model-II valve response for 0.5 A current with 0.1 mm air gap

Current, I (A)	Air gap, δ (mm)	Resistance, r	Time Constant, t (ms)	Inductance, t*r (mH)
0.50	0.10	0.66	1.04	0.6884

Table 7.3-1 C-core model-II valve response data for 0.5 A current with 0.1 mm air gap

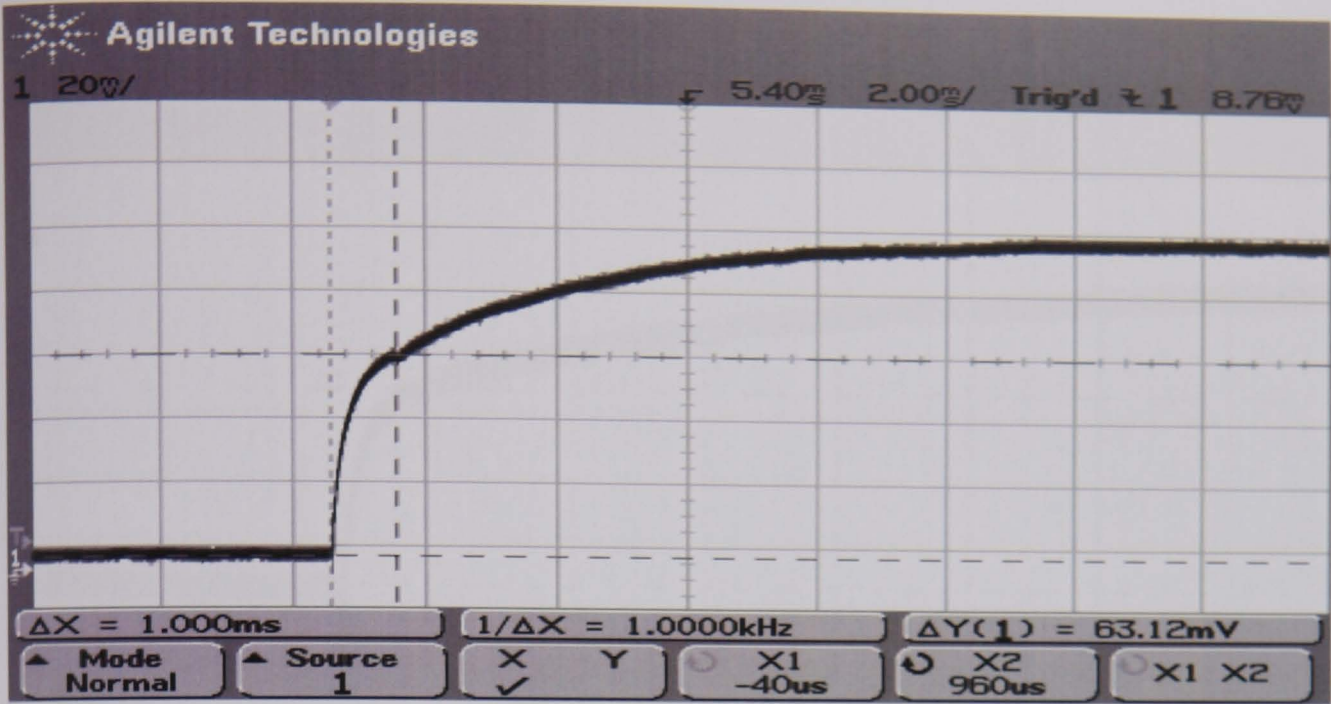


Fig. 7.3-2. C-core model-II valve response for 1.0 A current with 0.1 mm air gap

Current, I (A)	Air gap, δ (mm)	Resistance, r	Time Constant, t (ms)	Inductance, t*r (mH)
1.00	0.1	0.66	1.00	0.6600

Table 7.3-2 C-core model-II valve response data for 1.0 A current with 0.1 mm air gap

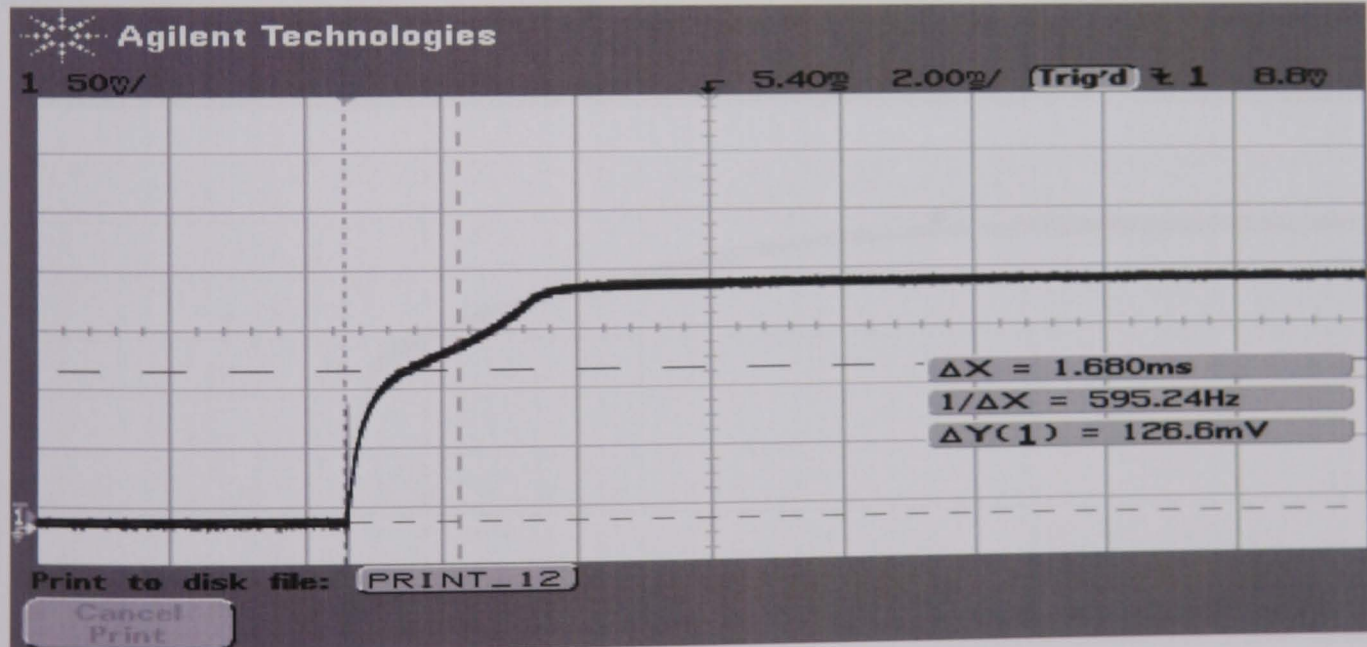


Fig. 7.3-3. C-core model-II valve response for 2.0 A current with 0.1 mm air gap

Current, I (A)	Air gap, δ (mm)	Resistance, r	Time Constant, t (ms)	Inductance, t*r (mH)
2.00	0.10	0.67	0.96	0.6432

Table 7.3-3 C-core model-II valve response data for 0.5 A current with 0.1 mm air gap

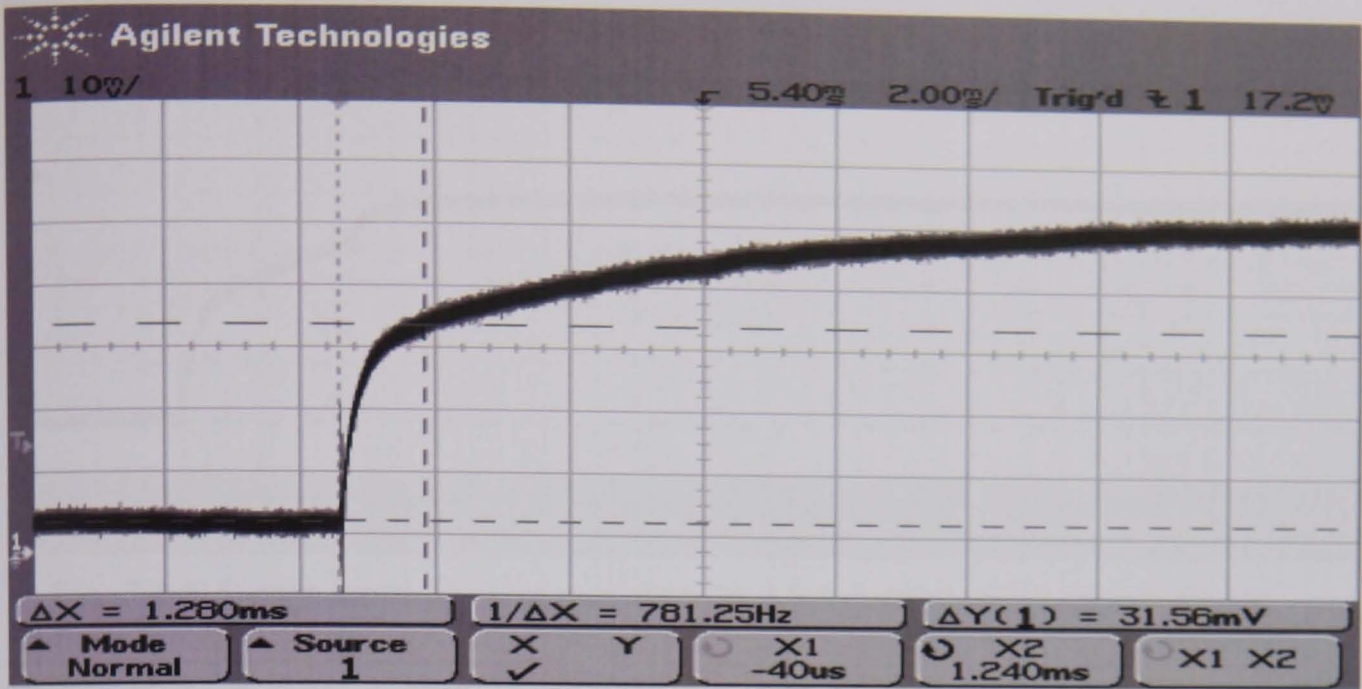


Fig. 7.3-4. C-core model-II valve response for 0.5 A current with 0.05 mm air gap

Current, I (A)	Air gap, δ (mm)	Resistance, r	Time Constant, t (ms)	Inductance, t*r (mH)
0.50	0.05	0.66	1.40	0.9240

Table 7.3-4 C-core model-II valve response data for 0.5 A current with 0.05 mm air gap

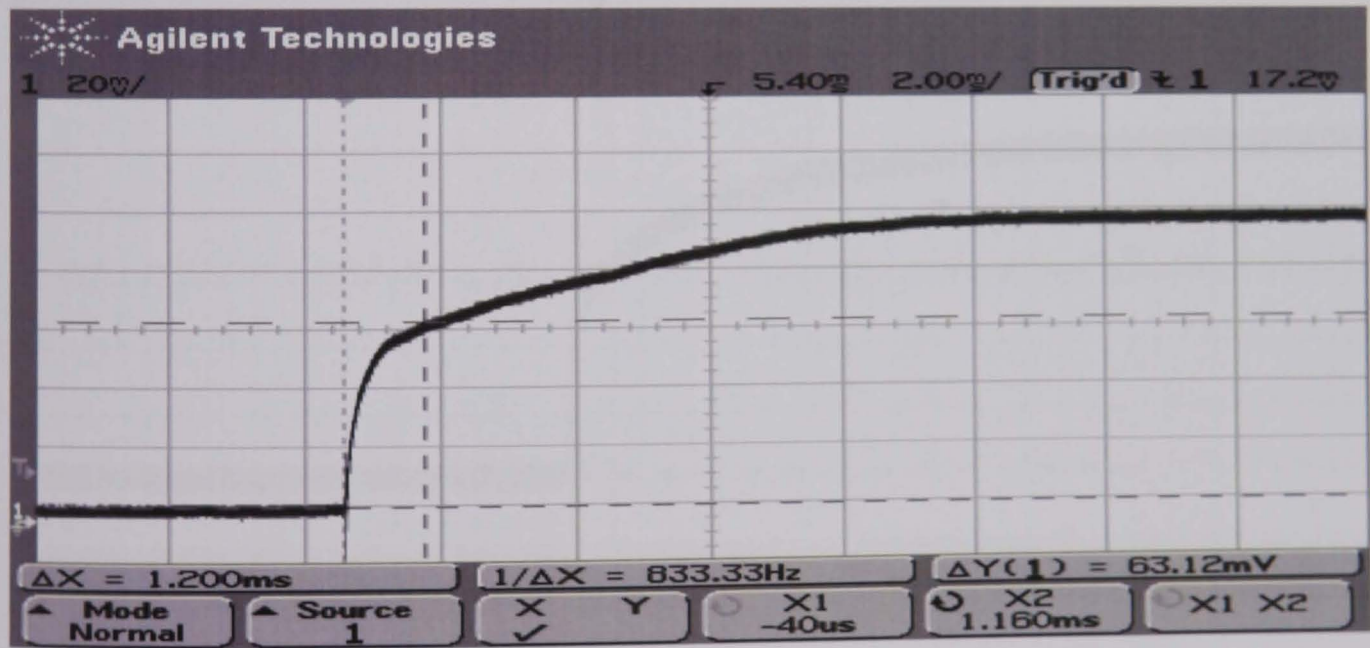


Fig. 7.3-5. C-core model-II valve response for 1.0 A current with 0.05mm air gap

Current, I (A)	Air gap, δ (mm)	Resistance, r	Time Constant, t (ms)	Inductance, t*r (mH)
1.00	0.05	0.66	1.28	0.8448

Table 7.3-5 C-core model-II valve response data for 1.0 A current with 0.05 mm air gap

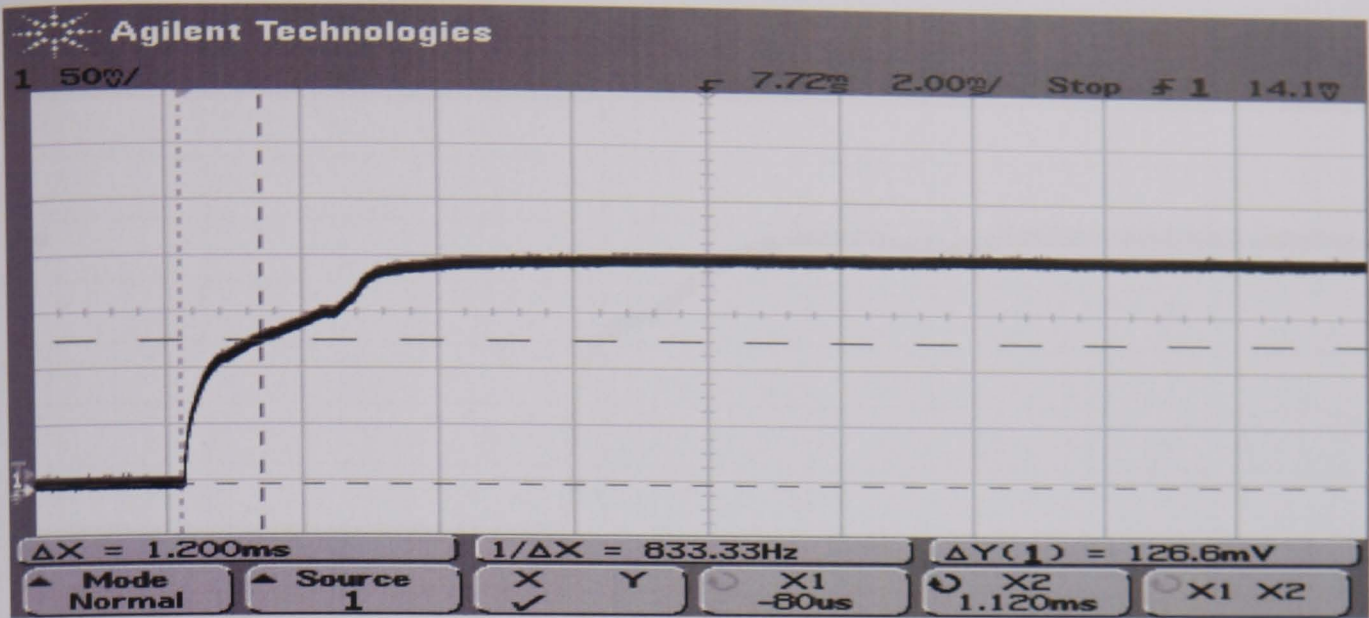


Fig. 7.3-6. C-core model-II valve response for 2.0 A current with 0.05 mm air gap

Current, I (A)	Air gap, δ (mm)	Resistance, r	Time Constant, t (ms)	Inductance, t*r (mH)
2.00	0.05	0.6850	0.88	0.8040

Table 7.3-6 C-core model-II valve response data for 2.0 A current with 0.05 mm air gap

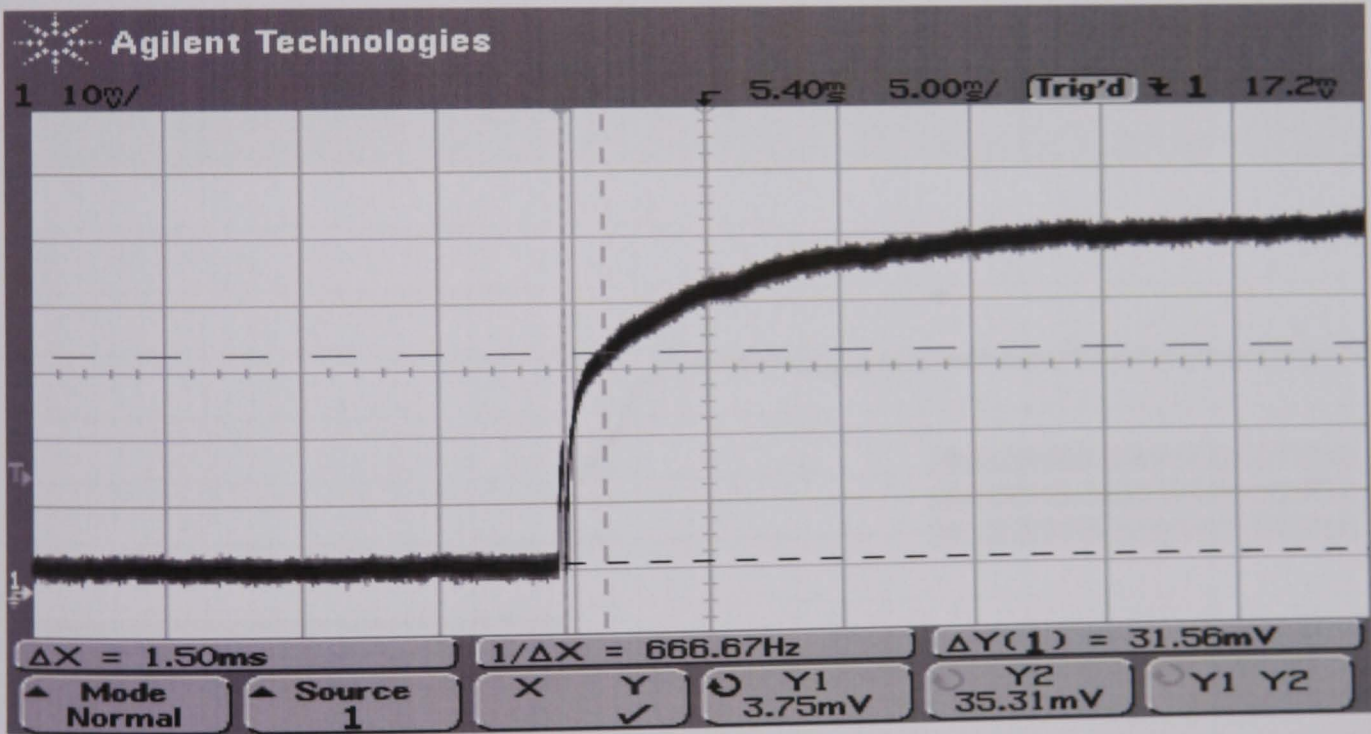


Fig. 7.3-7. C-core model-II valve response for 0.5 A current with 0.03 mm air gap

Current, I (A)	Air gap, δ (mm)	Resistance, r	Time Constant, t (ms)	Inductance, t*r (mH)
0.50	0.03	0.66	1.50	0.9900

Table 7.3-7 C-core model-II valve response data for 0.5 A current with 0.03 mm air gap

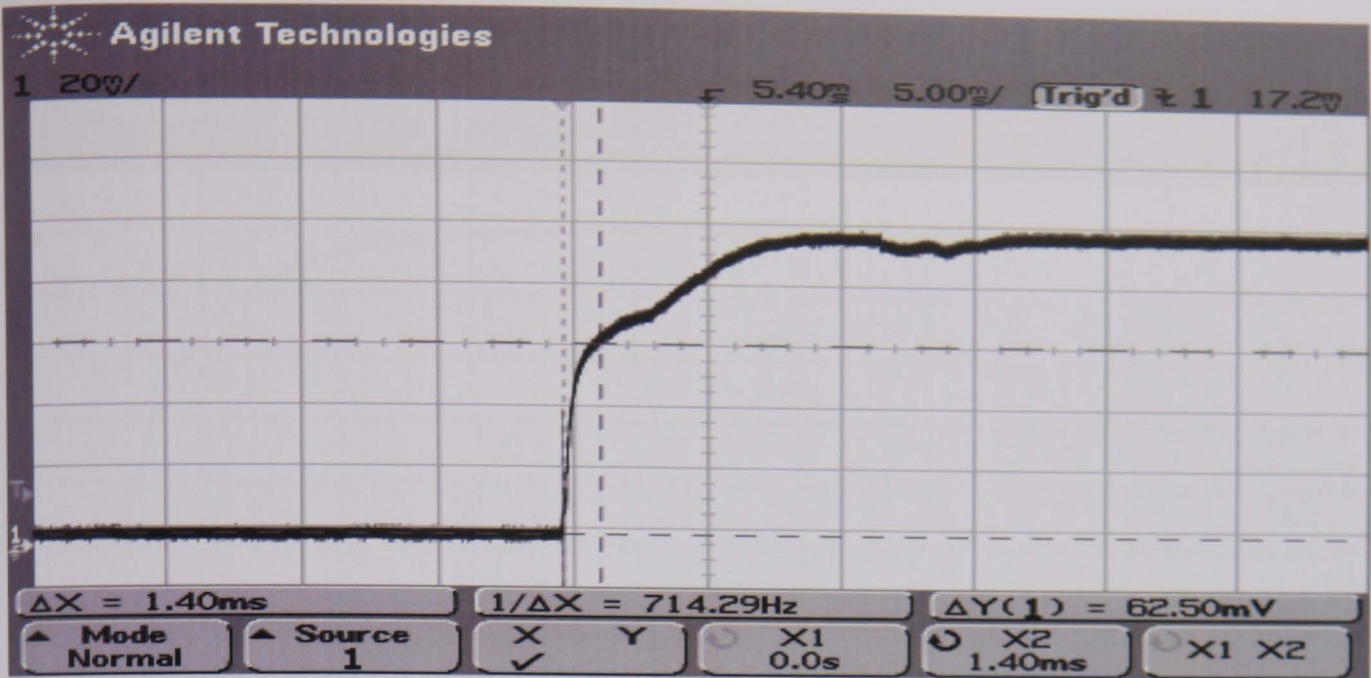


Fig. 7.3-8. C-core model-II valve response for 1.0 A current with 0.03 mm air gap

Current, I (A)	Air gap, δ (mm)	Resistance, r	Time Constant, t (ms)	Inductance, t*r (mH)
1.00	0.03	0.66	1.40	0.9240

Table 7.3-8 C-core model-II valve response data for 1.0 A current with 0.03 mm air gap

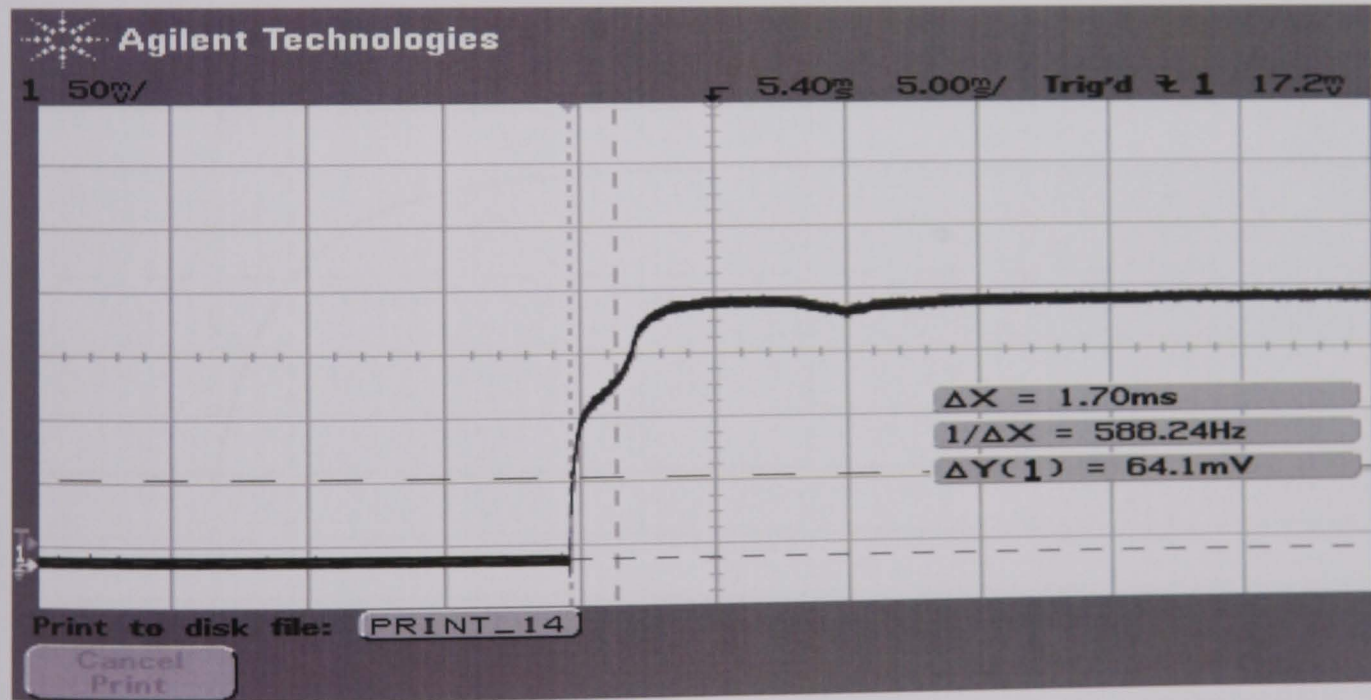


Fig. 7.3-9. C-core model-II valve response for 2.0 A current with 0.03 mm air gap

Current, I (A)	Air gap, δ (mm)	Resistance, r	Time Constant, t (ms)	Inductance, t*r (mH)
2.00	0.03	0.69	1.30	0.8970

Table 7.3-9 C-core model-II valve response data for 2.0 A current with 0.03 mm air gap

7.3.2 C-core-II Model Armco Valve Response Test

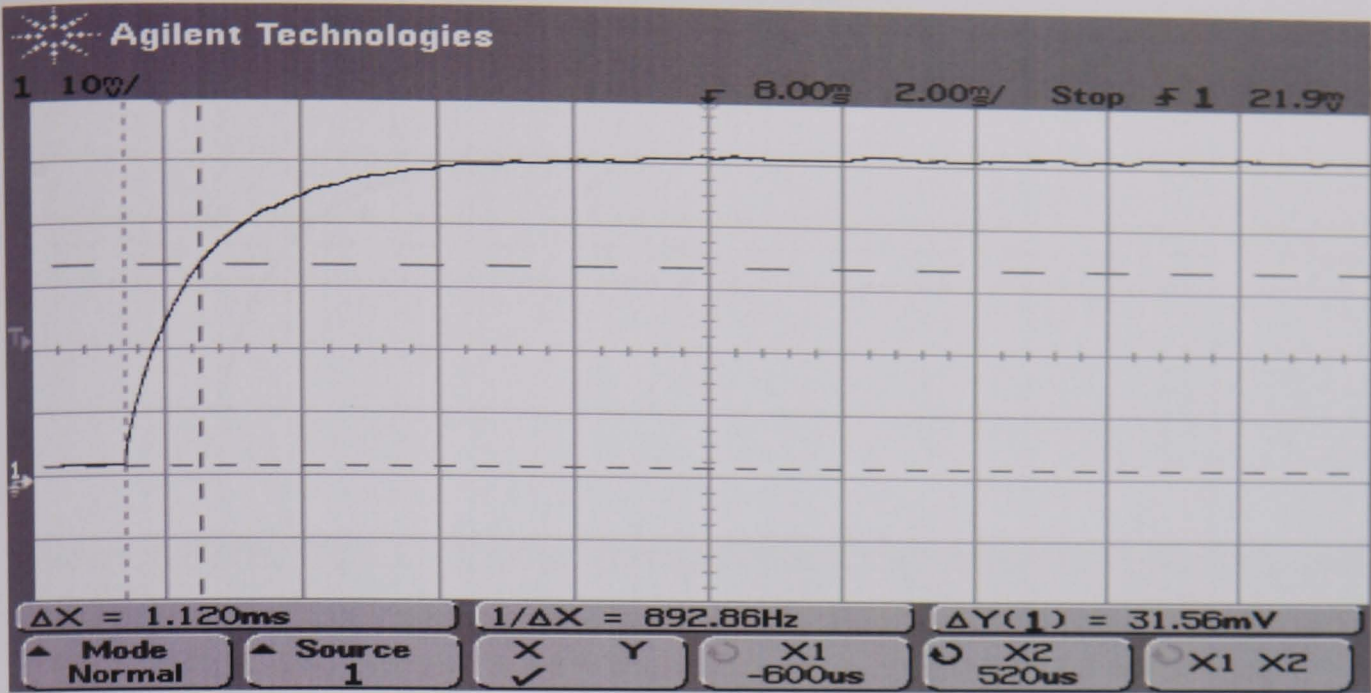


Fig. 7.3-10. C-core model-II valve response for 0.5 A current with 0.1 mm air gap

Current, I (A)	Air gap, δ (mm)	Resistance, r	Time Constant, t (ms)	Inductance, t*r (mH)
0.50	0.1	0.66	1.12	0.7392

Table 7.3-10 C-core model-II valve response data for 0.5 A current with 0.1 mm air gap

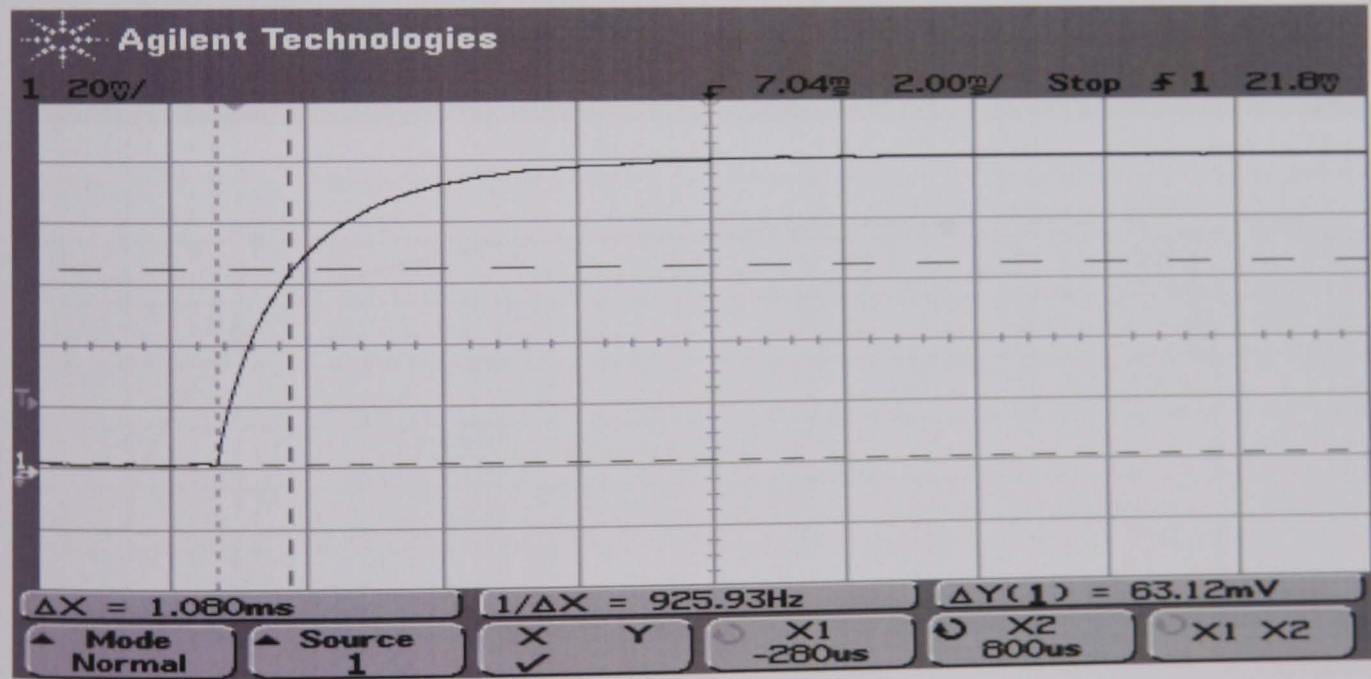


Fig. 7.3-11. C-core model-II valve response for 1.0 A current with 0.1 mm air gap

Current, I (A)	Air gap, δ (mm)	Resistance, r	Time Constant, t (ms)	Inductance, t*r (mH)
1.00	0.1	0.66	1.08	0.7128

Table 7.3-11 C-core model-II valve response data for 1.0 A current with 0.1 mm air gap

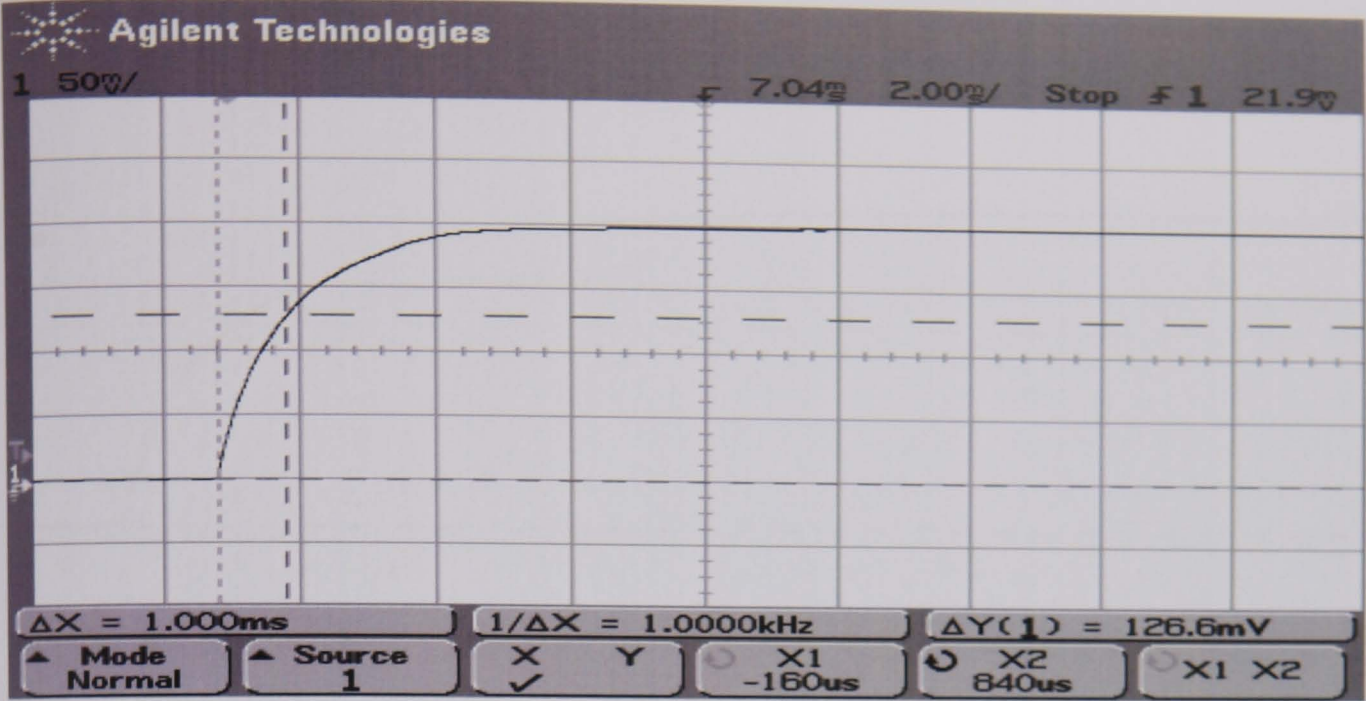


Fig. 7.3-12. C-core model-II valve response for 2.0 A current with 0.1 mm air gap

Current, I (A)	Air gap, δ (mm)	Resistance, r	Time Constant, t (ms)	Inductance, t*r (mH)
2.00	0.1	0.67	1.00	0.6700

Table 7.3-12 C-core model-II valve response data for 0.5 A current with 0.01 mm air gap

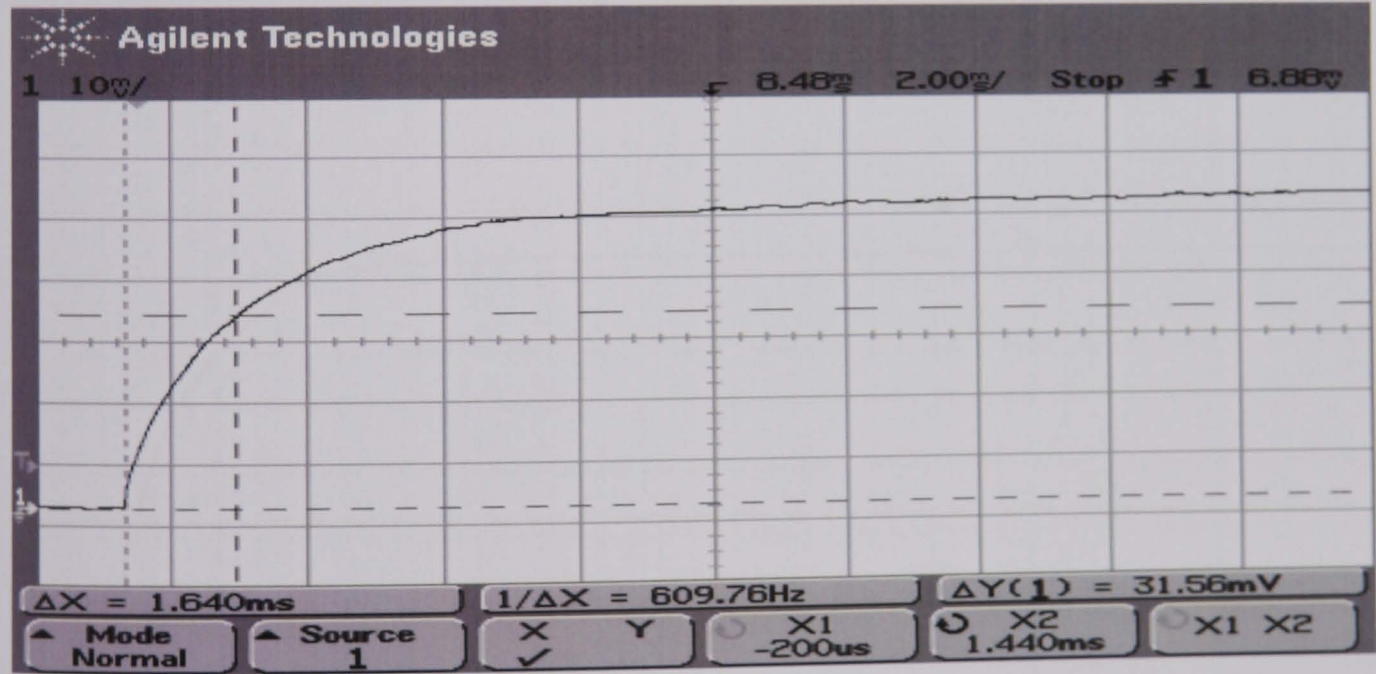


Fig. 7.3-13. C-core model-II valve response for 0.5 A current with 0.05 mm air gap

Current, I (A)	Air gap, δ (mm)	Resistance, r	Time Constant, t (ms)	Inductance, t*r (mH)
0.50	0.05	0.66	1.640	1.0824

Table 7.3-13 C-core model-II valve response data for 0.5 A current with 0.05 mm air gap

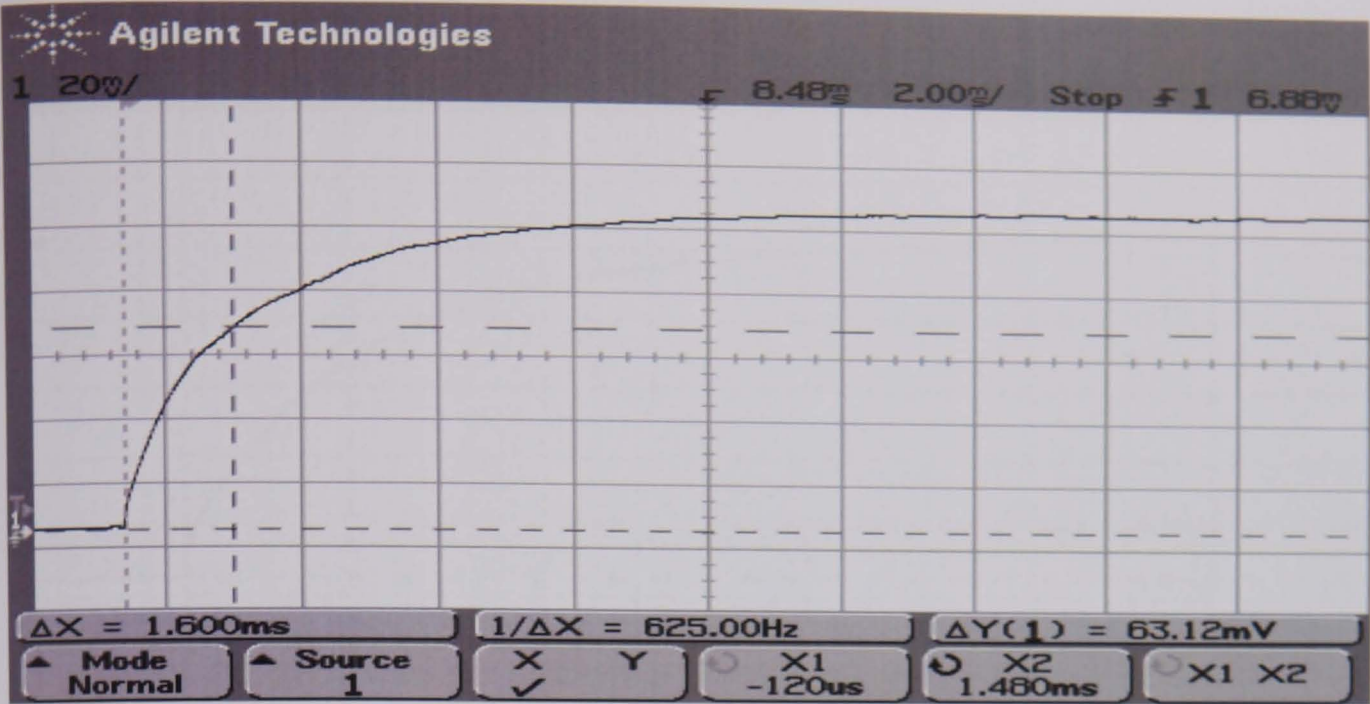


Fig. 7.3-14. C-core model-II valve response for 1.0 A current with 0.05 mm air gap

Current, I (A)	Air gap, δ (mm)	Resistance, r	Time Constant, t (ms)	Inductance, t*r (mH)
1.00	0.05	0.68	1.60	1.0880

Table 7.3-14 C-core model-II valve response data for 1.0 A current with 0.05 mm air gap

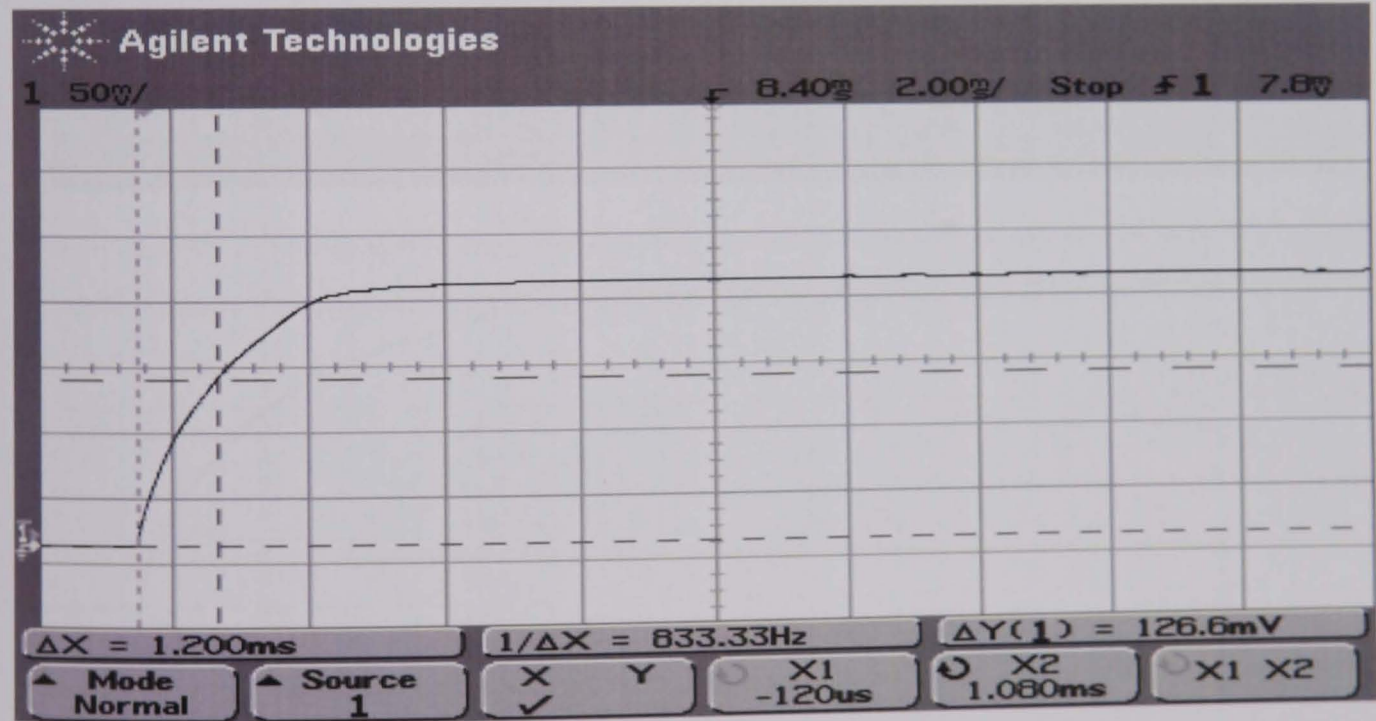


Fig. 7.3-15. C-core model-II valve response for 2.0 A current with 0.05 mm air gap

Current, I (A)	Air gap, δ (mm)	Resistance, r	Time Constant, t (ms)	Inductance, t*r (mH)
2.00	0.05	0.68	1.20	0.8160

Table 7.3-15 C-core model-II valve response data for 2.0 A current with 0.05 mm air gap

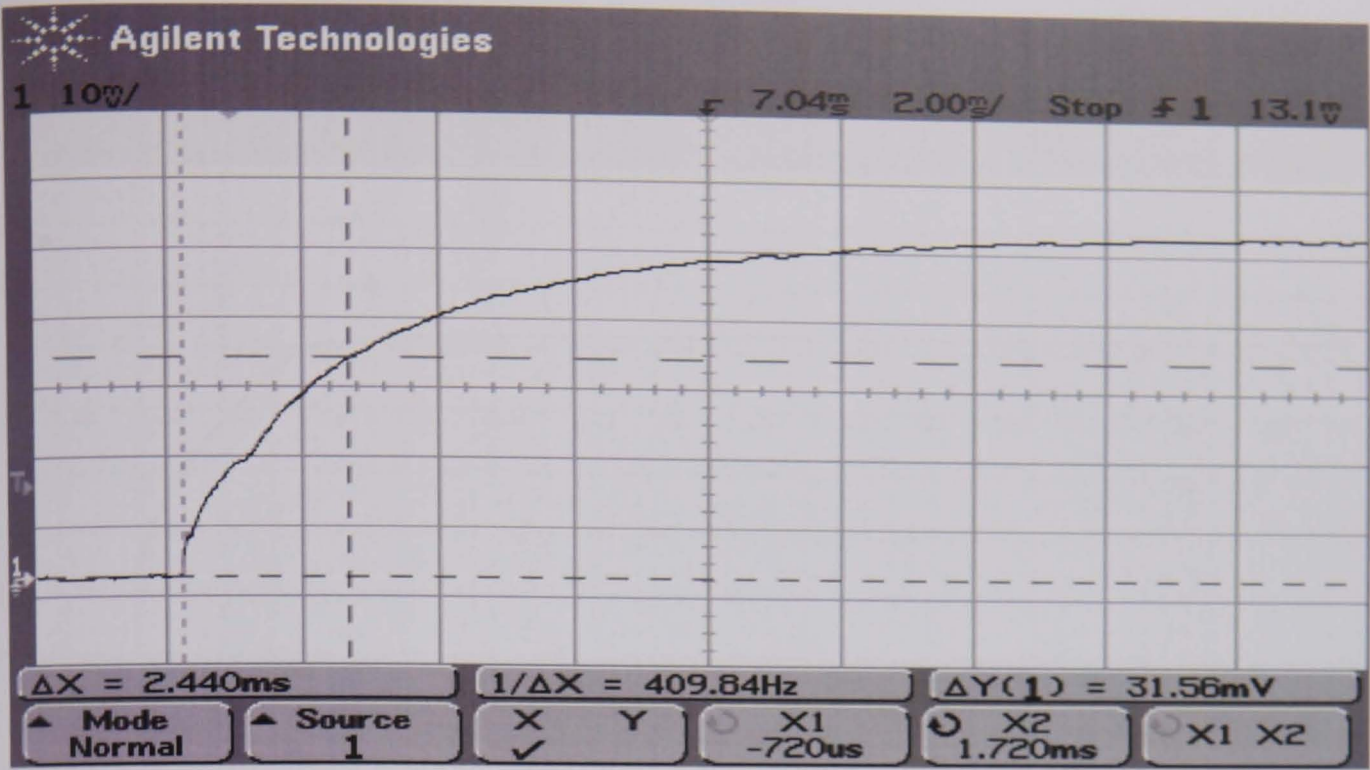


Fig. 7.3-16. C-core model-II valve response for 0.5 A current with 0.03 mm air gap

Current, I (A)	Air gap, δ (mm)	Resistance, r	Time Constant, t (ms)	Inductance, t*r (mH)
0.50	0.03	0.67	2.440	1.6348

Table 7.3-16 C-core model-II valve response data for 0.5 A current with 0.03 mm air gap

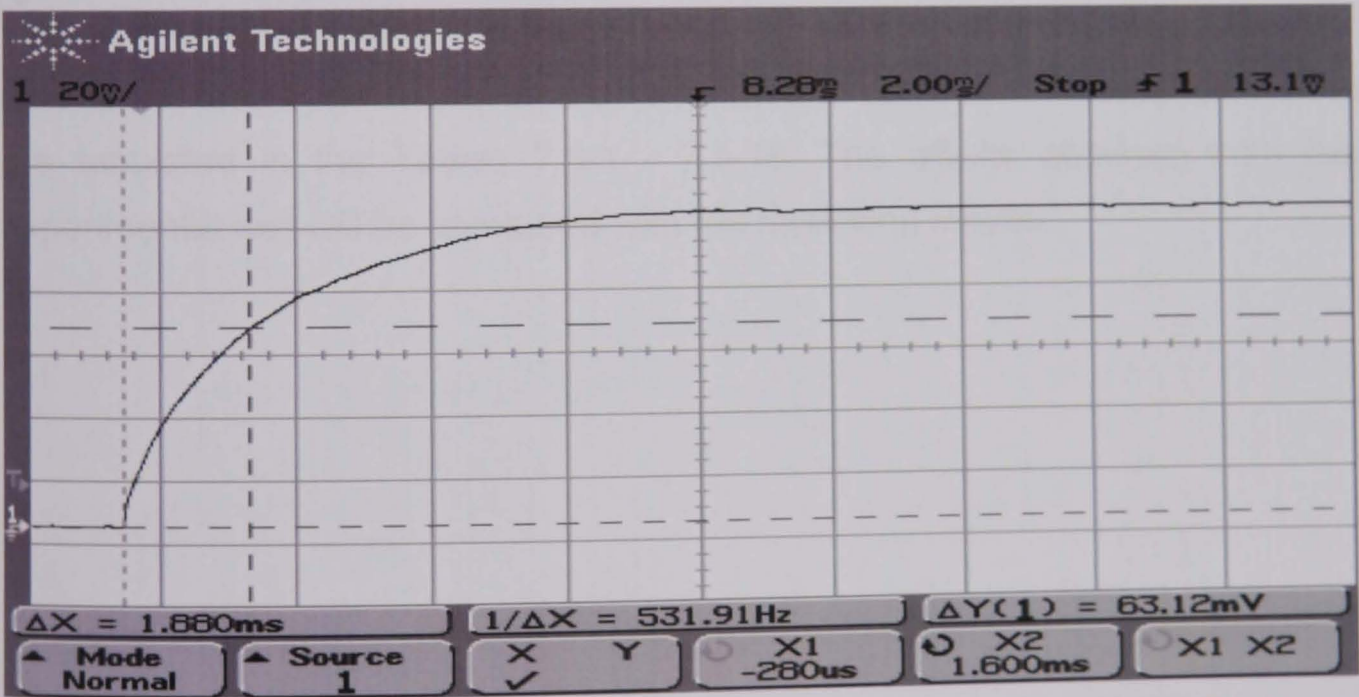


Fig. 7.3-17. C-core model-II valve response for 1.0 A current with 0.03 mm air gap

Current, I (A)	Air gap, δ (mm)	Resistance, r	Time Constant, t (ms)	Inductance, t*r (mH)
1.00	0.03	0.67	1.88	1.2596

Table 7.3-17 C-core model-II valve response / data for 1.0 A current with 0.03 mm air gap

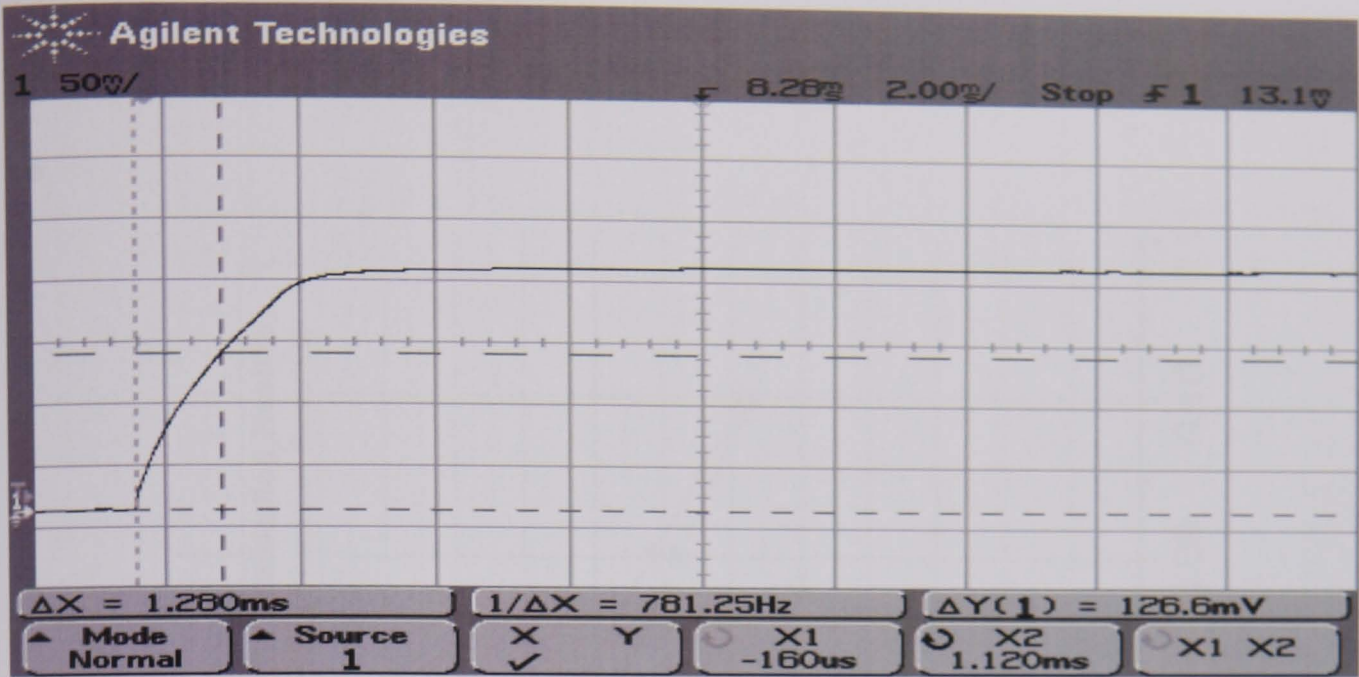


Fig. 7.3-18. C-core model-II valve response for 2.0 A current with 0.03 mm air gap

Current, I (A)	Air gap, δ (mm)	Resistance, r	Time Constant, t (ms)	Inductance, t*r (mH)
2.00	0.03	0.6750	1.280	0.8640

Table 7.3-18 C-core model-II valve response / data for 2.0 A current with 0.03 mm air gap

Figs. 7.3-1 - 7.3-18 show the results obtained from the response test. Also test main parameters measured time constantly and calculated inductance. Those are tabulated in the Tables 7.3-1 - 7.3-18. The results obtained from this experimental test will be compared with the modelling results.

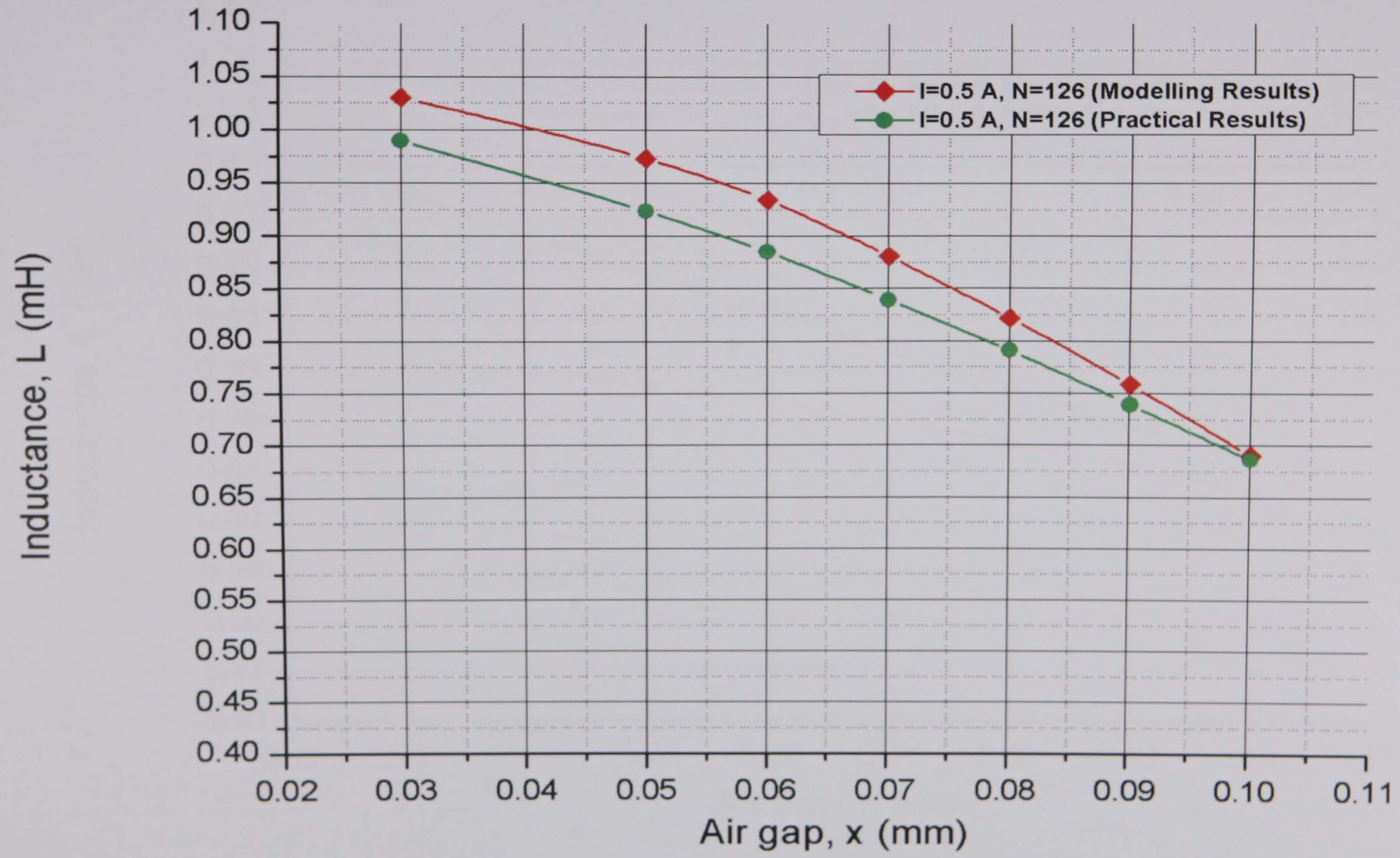


Fig. 7.3-19. C-Core-II model Radiometal-4550 inductance comparison graph for 0.5 A current

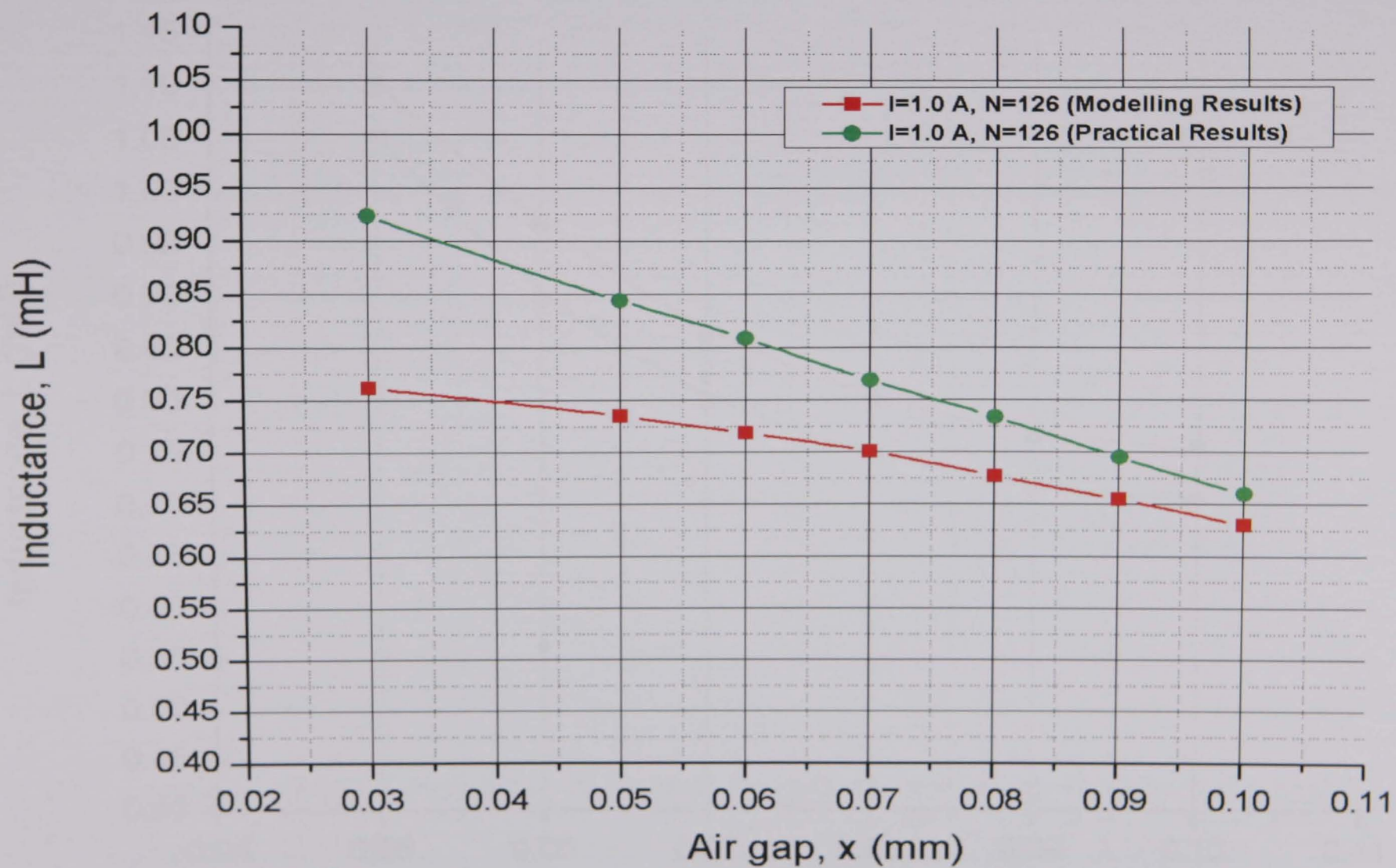


Fig. 7.3-20. C-core-II model Radiometal-4550 inductance comparison graph for 1.0 A current

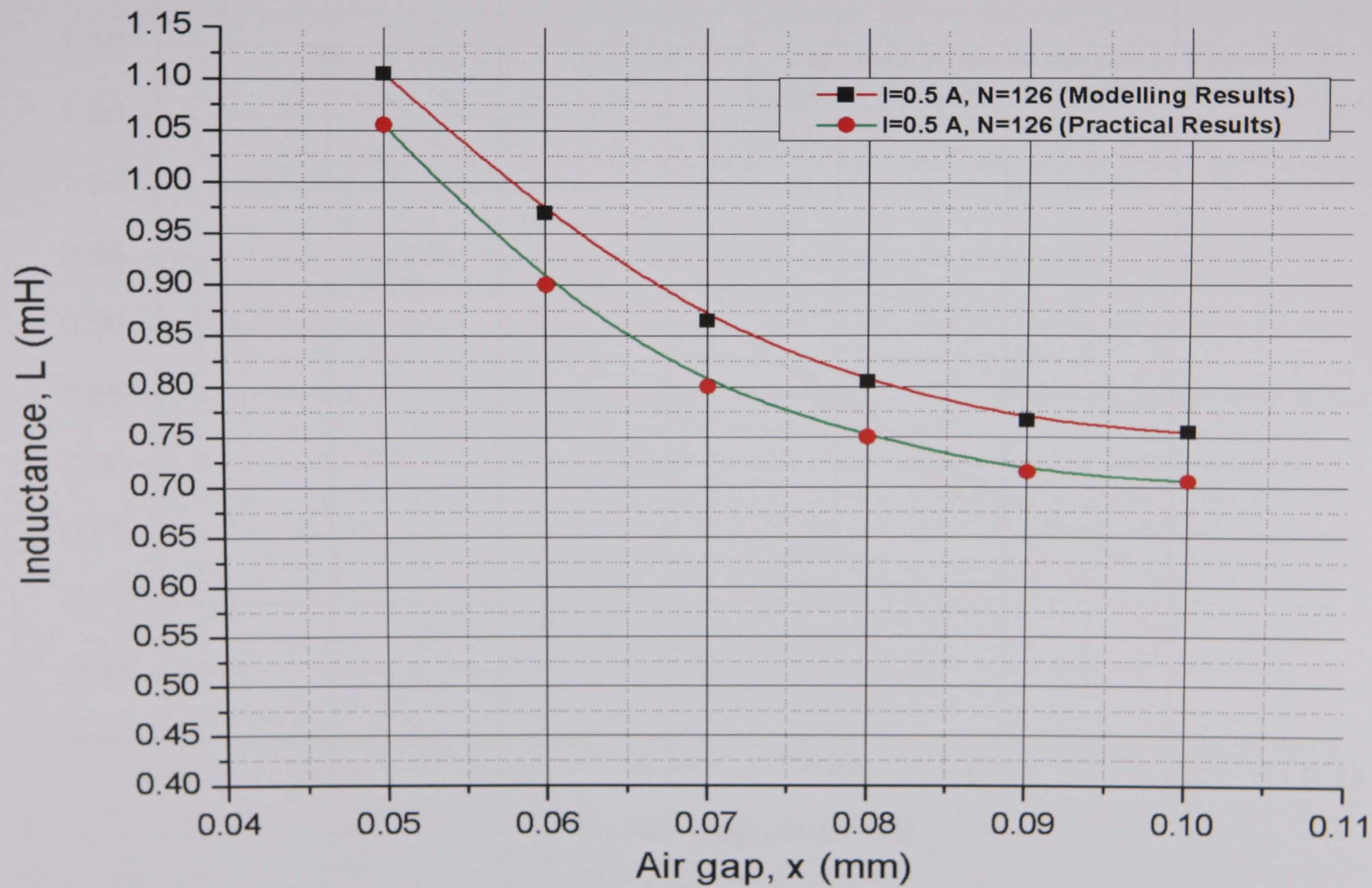


Fig. 7.3-21. C-core-II model Armco inductance comparison graph for 0.5 A current

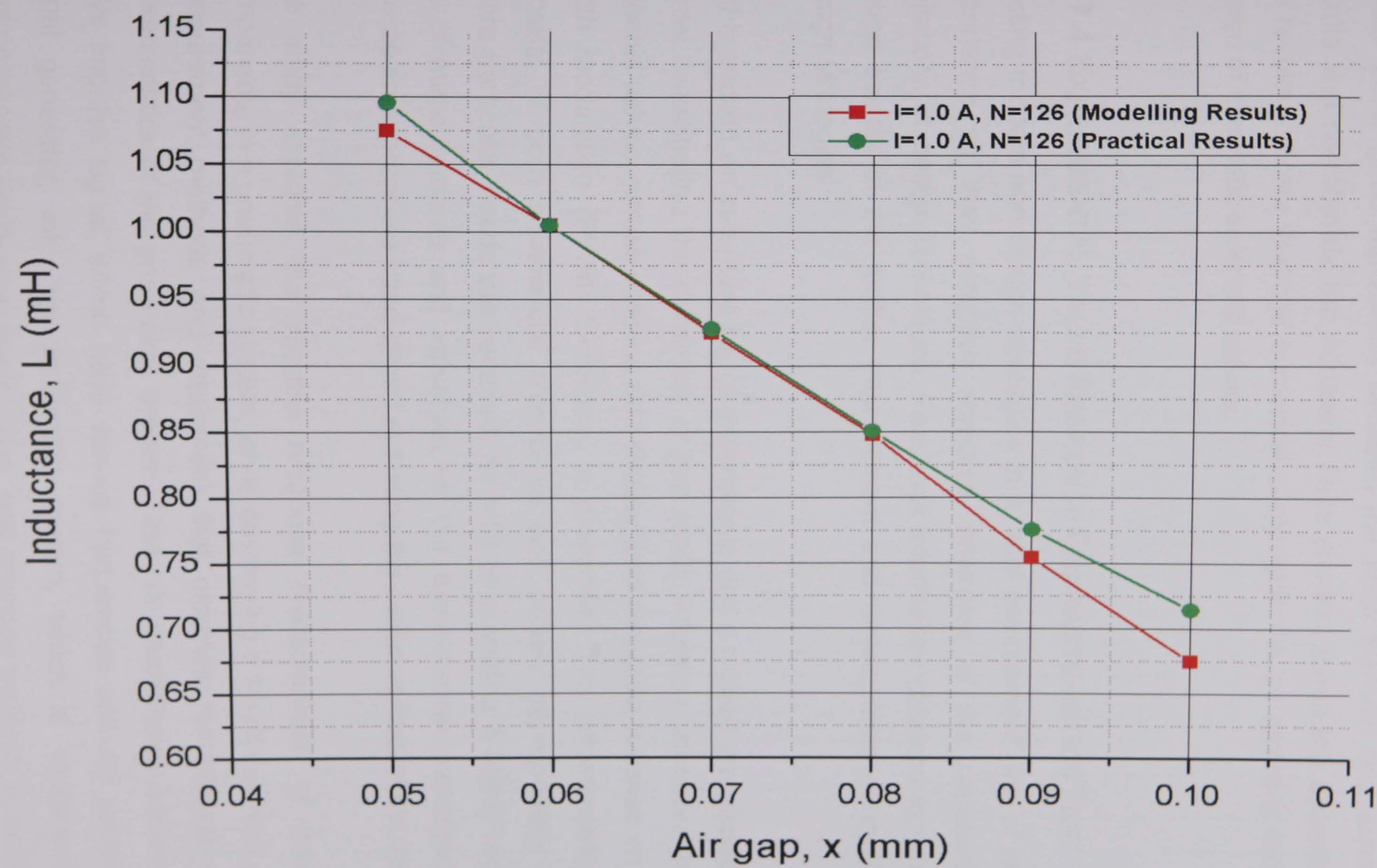


Fig. 7.3-22. C-core-II model Armco inductance comparison graph for 1.0 A current

As each experimental test was completed, the appropriate data was put into the computer programme to check the numerical and experimental agreement. The Figs. 7.4-1 to 7.4-4 show the modelling and experimental results. The test results are compared with the finite element numerical results. Most of the results show good agreement between the finite element and experimental results and corroborate the nonlinear finite element modelling approach. Also the results indicate that the numerical computation is an effective tool for the design of magnetic solenoid valves.

7.4 EXPERIMENTAL VALVE RESPONSE CHARACTERISTICS TEST

Testing models and design strategies in a "real environment" are of academic importance as they establish objective measures of the capabilities and limitations of design techniques. Feedback information obtained from practical design assists in the further improvement and development of models and design strategies.

In this section an extensive set of experiments and a related prototyped C-core model investigating the dynamics of pneumatic actuators controlled by on-off solenoid valves, whose opening and closing time response is based on a pulse width modulation (PWM) technique, is presented. The experimental set-up consists of both commercial electronics and circuits appropriately realized where particular needs are required. As well as providing a highly repeatable set of measurements and valuables for the experimental investigation also provide an appropriate base aimed at testing the performances of the valve.

The study explores the impulse response characteristics of the control components in a pneumatic system, while developing a set of the most effective measurement methods and equipment that provides the closest dynamic characteristics of the pneumatic system. First, the study inputs square current wave impulse signal, which have various frequencies and are generated by signal generator, into the pneumatic system, which is comprised of an electromagnetic valve, pneumatic pipes, and pressure sensors. In addition, the study discusses the influences of the electromagnetic valve, pneumatic pipes,

and pressure sensors on the frequency responses of the pneumatic system through the analyses of outputted pressure signals.

The original specification of the C-core valve required a response performance that included a need for a pneumatic rise time and a pneumatic fall time.

The valve was tested on a manifold mounted to test manifold with a Sortex Z series nozzle arrangements wad fitted and a high speed pressure transducer was positioned, in free air, 5 mm from the nozzle output.

The valve was powered by the TTI Thurlbsby Thander power supply. The valve was tested using this power supply for different current input. A current probe (100 mV / A) was used to measure the inputs to the solenoid from the power supply. A Thurlby Thandar Instruments PSU was set between 0.3 Volts and 30 Volts. The current response was monitored using an AM503 current probe outputting to an HP54642D signal oscilloscope. The pressure response was monitored using Kulite sensor probe mounted directly in line of output to measure the dynamic pressure.

Properties	Current, I (A)	Voltage , V(V)	Air gap, x, (mm)
Value	1.7	1.12	0.1 (approx)

Table 7.4-1 C-Core-II model Radiometal-4550 valve, I=1.7 A current test specification.

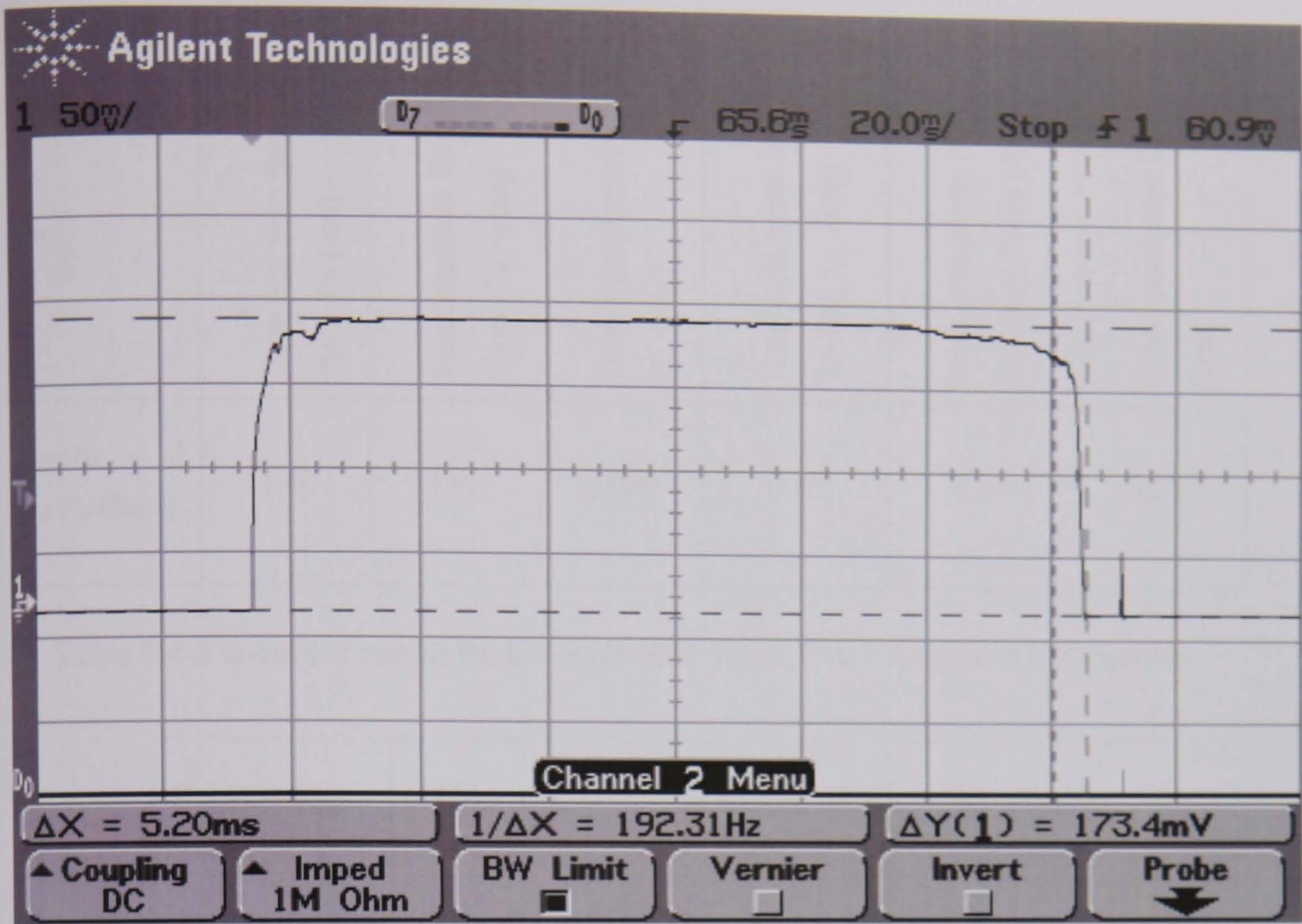


Fig. 7.4-1. C-core-II model Radiometal-4550 valve, $I=1.0$ A, current characteristic curve

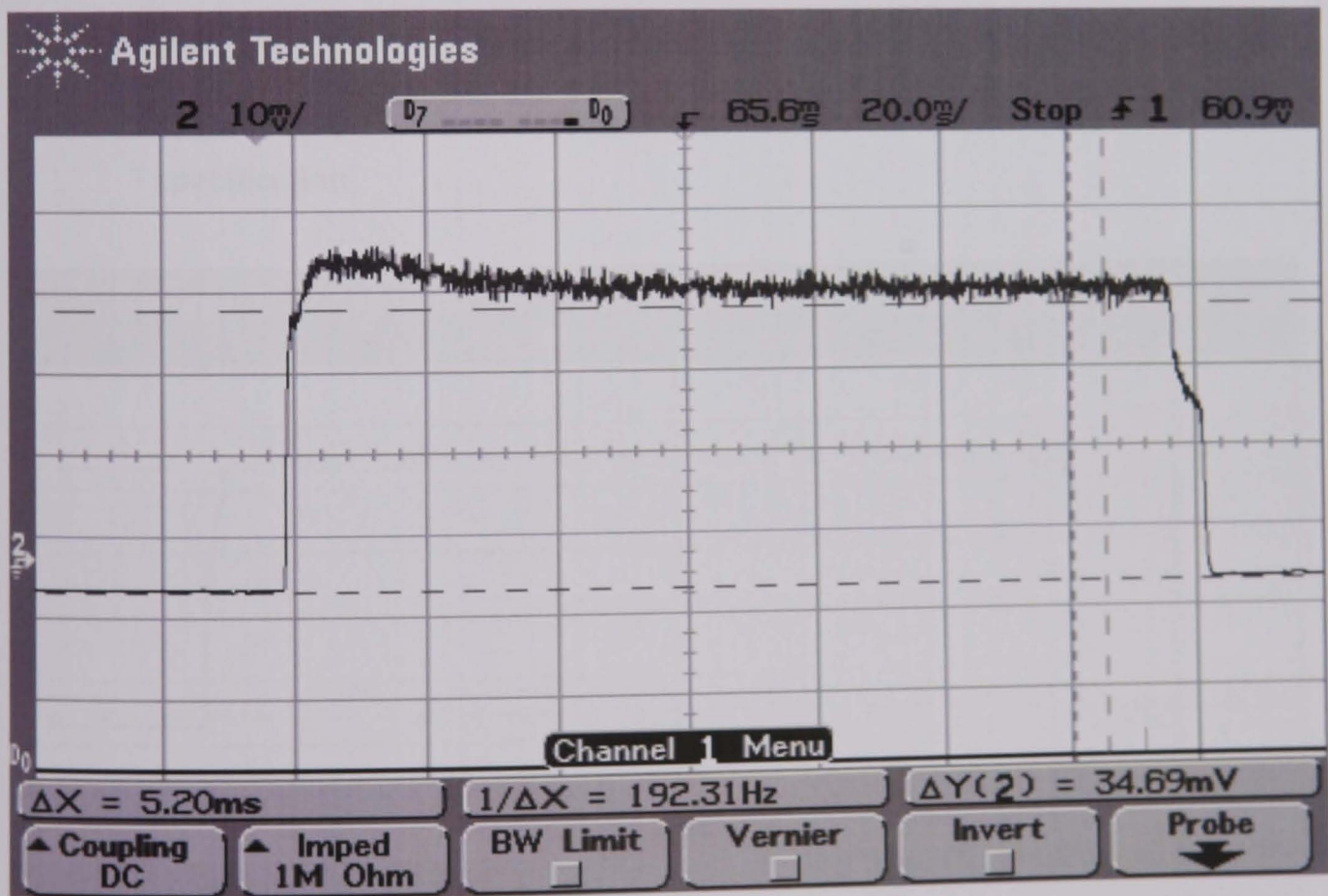


Fig. 7.4-2. C-core-II model Radiometal-4550 valve, $I=1.0$ A current pressure characteristic curve

Valve	Time signal to flow start, Ts (ms)	Time signal to flow open, To, (ms)	Time signal to full flow , Tf, (ms)	Time pneumatic rise, To-Ts (ms)	Time pneumatic full flow rise, Tf-Ts (ms)	Time pneumatic fall (ms)
C-core - II (Radio-Metal)	4.45	4.90	9.920	0.45	5.47	5.280

Table 7.4-2 C-core-II model Radiometal-4550 valve, I= 1.7 A current test results

Properties	Current, I (A)	Voltage, V (V)	Air gap, x, (mm)
Value	2.0	1.33	0.1 (approx)

Table 7.4-3 C-core-II model Radiometal-4550 valve, I= 2.0 A current test specification

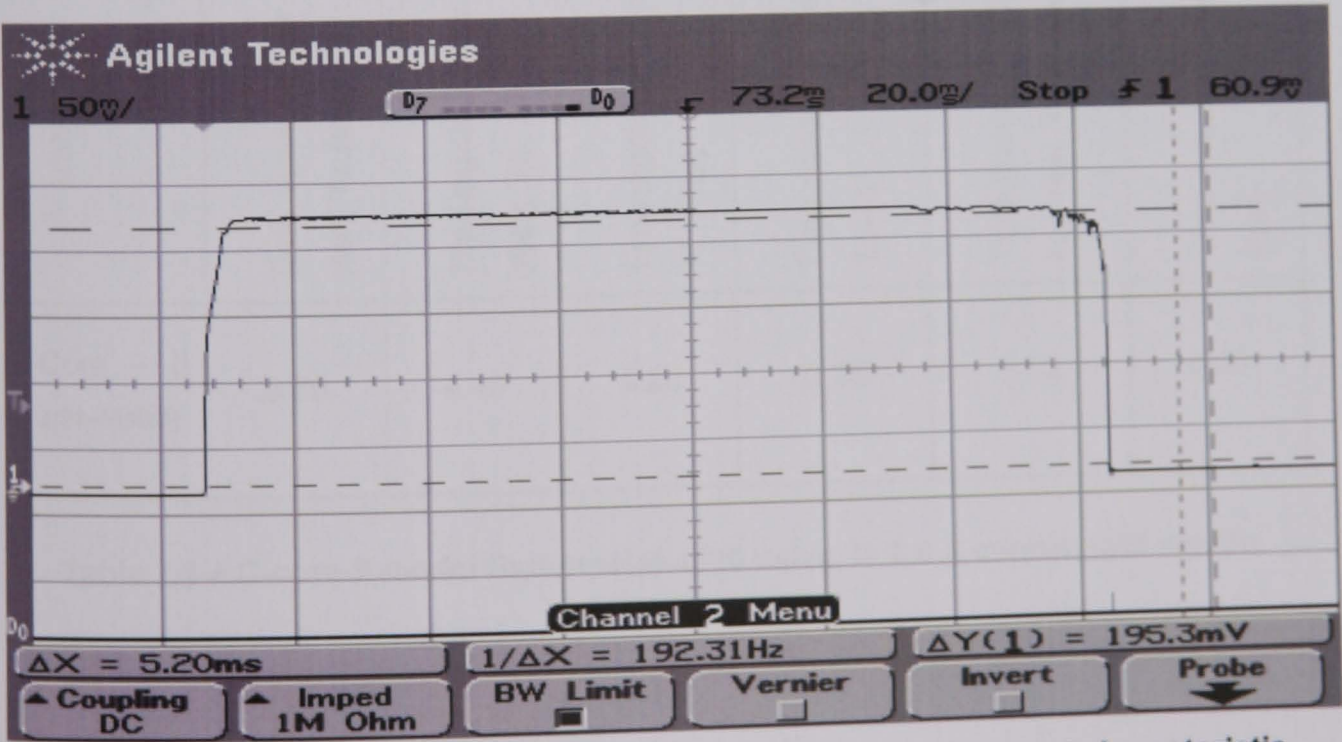


Fig. 7.4-3. C-core-II model Radiometal-4550 valve, I= 2.0 A, current characteristic curve

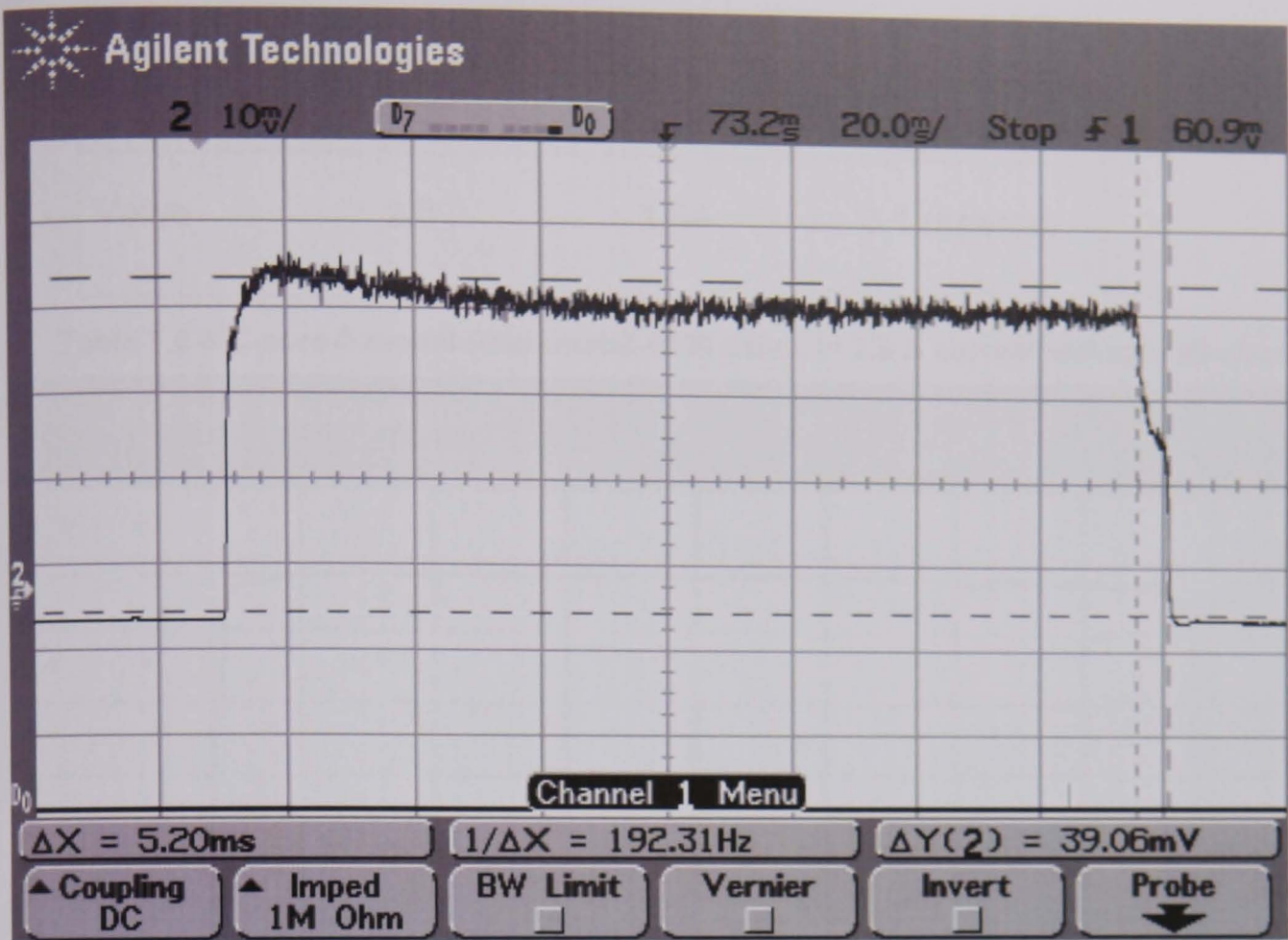


Fig. 7.4-4. C-core-II model Radiometal-4550 valve, I=2.0 A current pressure characteristic curve

Valve	Time signal to flow start, Ts (ms)	Time signal to flow open, To, (ms)	Time signal to full flow , Tf, (ms)	Time pneumatic rise, To-Ts (ms)	Time pneumatic full flow rise, Tf-Ts (ms)	Time pneumatic fall (ms)
C-Core - II (Radio-Metal)	3.88	4.16	9.20	0.28	5.32	5.20

Table 7.4-4 C-core-II model Radiometal-4550 valve, I= 2.0 A current test results

Properties	Current, I (A)	Voltage , V (V)	Air gap, x, (mm)
Value	2.5	1.64	0.1 (approx)

Table 7.4-5 C-core-II model Radiometal-4550 valve, I= 2.5 A current test specification

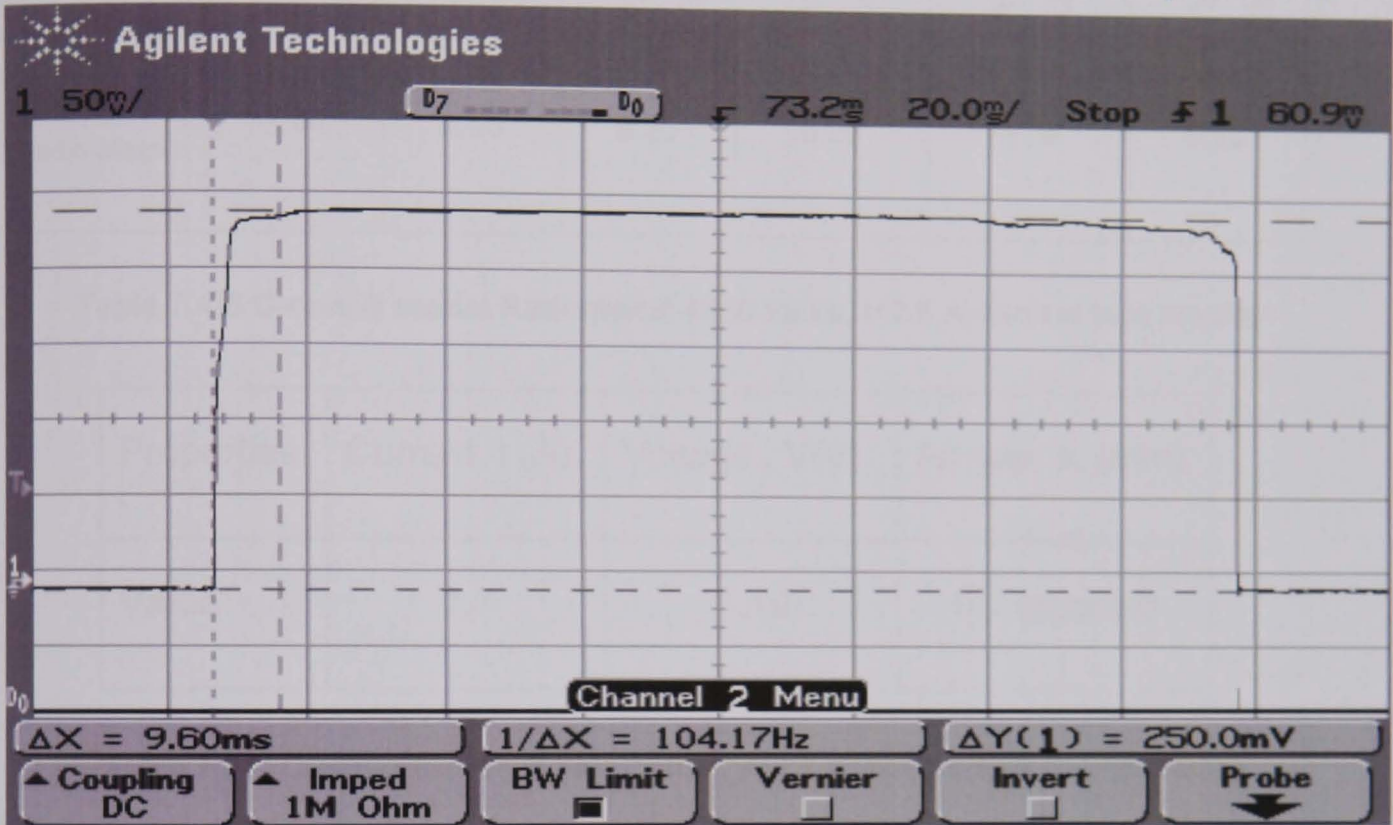


Fig. 7.4-5. C-core-II model Radiometal-4550 valve, I= 2.5 A, current characteristic curve

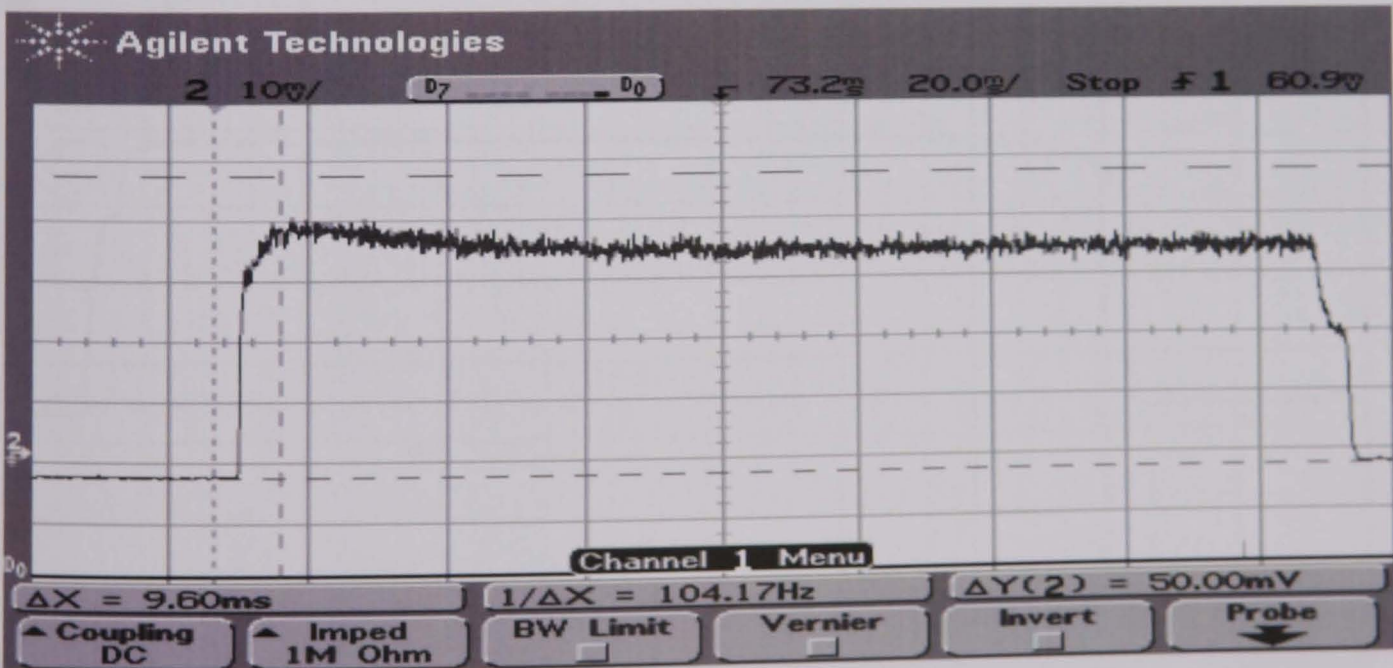


Fig. 7.4-6. C-core model-II Radiometal-4550 valve, I=2.5 A current, pressure characteristic curve

Valve	Time signal to flow start, Ts (ms)	Time signal to flow open, To, (ms)	Time signal to full flow , Tf, (ms)	Time pneumatic rise, To-Ts (ms)	Time pneumatic full flow rise, Tf-Ts (ms)	Time pneumatic fall (ms)
C-Core - II (Radio-Metal)	3.44	3.60	8.20	0.26	4.76	5.20

Table 7.4-6 C-core-II model Radiometal-4550 valve, I=2.5 A current test results

Properties	Current, I (A)	Voltage , V(V)	Air gap, x, (mm)
Value	1.7	1.19	0.1 (approx)

Table 7.4-7 C-core model-II Armco valve, I= 1.7 A current test specification

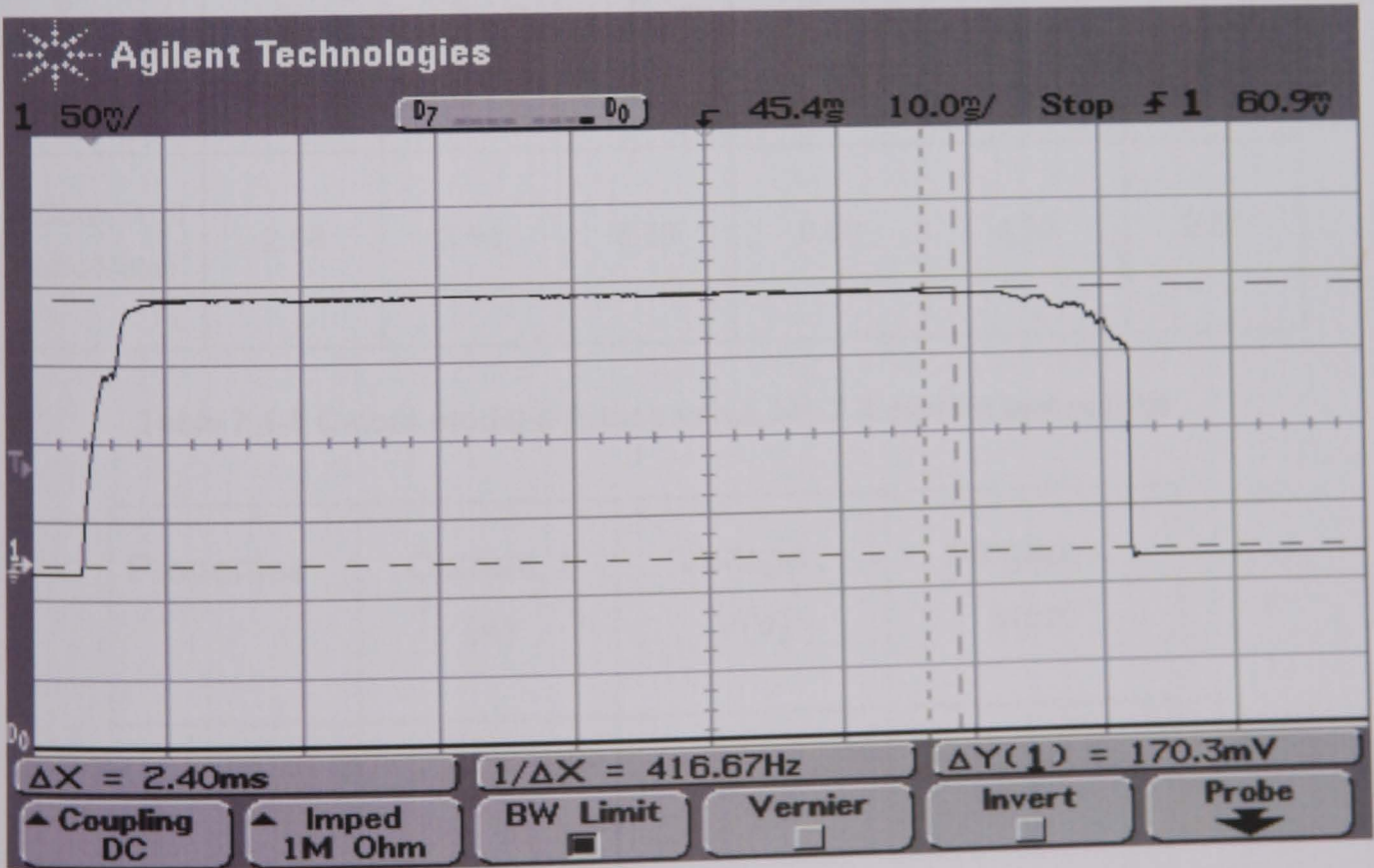


Fig. 7.4-7. C-core model-II Armco valve, I=1.7 A, current characteristic curve

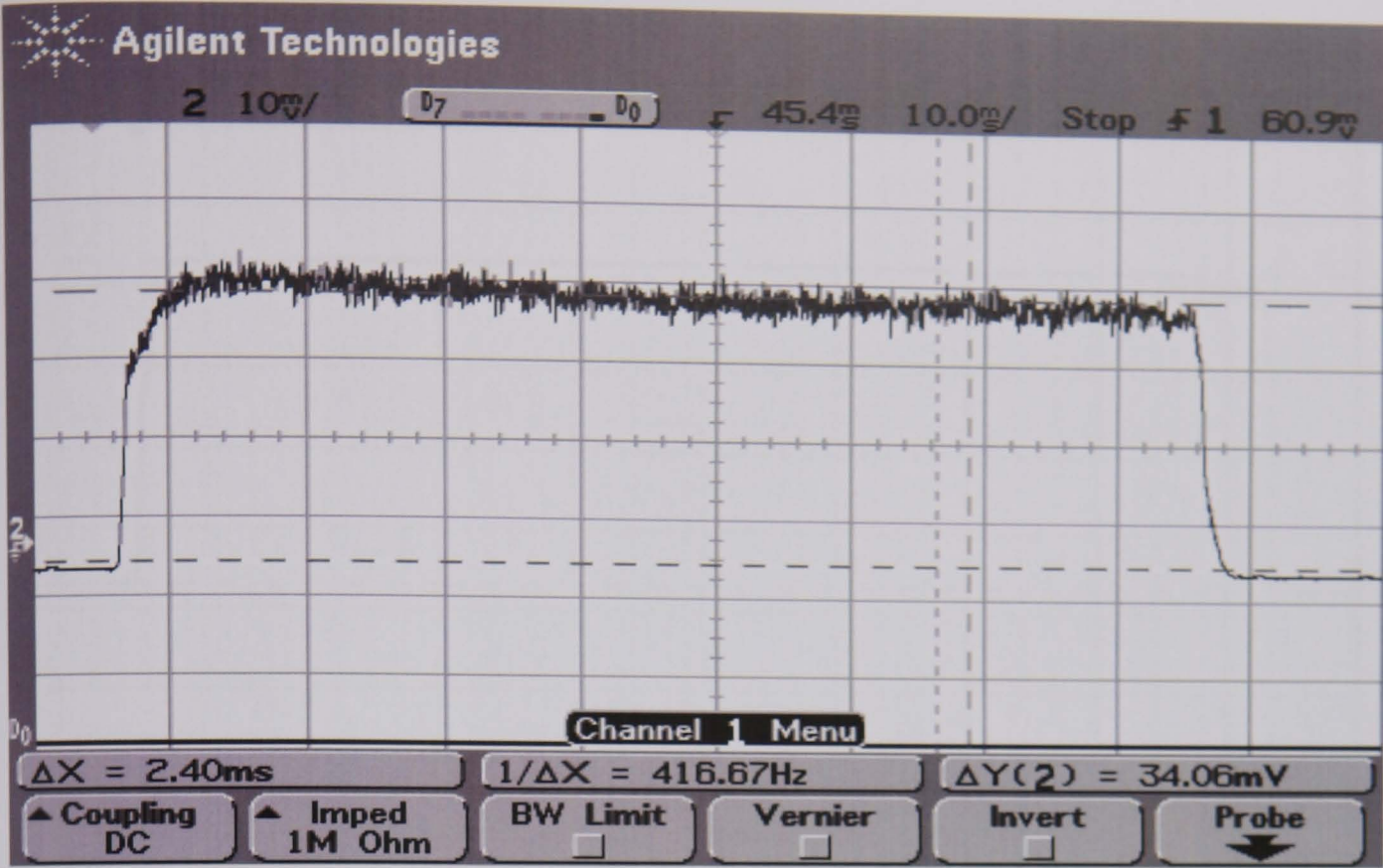


Fig. 7.4-8. C-core model-II Armco valve, I=1.7 A current, pressure characteristic curve

Valve	Time signal to flow start, Ts (ms)	Time signal to flow open, To, (ms)	Time signal to full flow , Tf, (ms)	Time pneumatic rise, To-Ts (ms)	Time pneumatic full flow rise, Tf-Ts (ms)	Time pneumatic fall (ms)
C-Core – II (Radio-Metal)	2.58	3.14	6.88	0.56	4.30	2.30

Table 7.4-8 C-core model-II Armco valve, I=1.7 A current test results

Properties	Current, I (A)	Voltage , V(V)	Air gap, x, (mm)
Value	2.0	1.33	0.1 (approx)

Table 7.4-9 C-core model-II Armco valve, I= 2.0 A current test specification

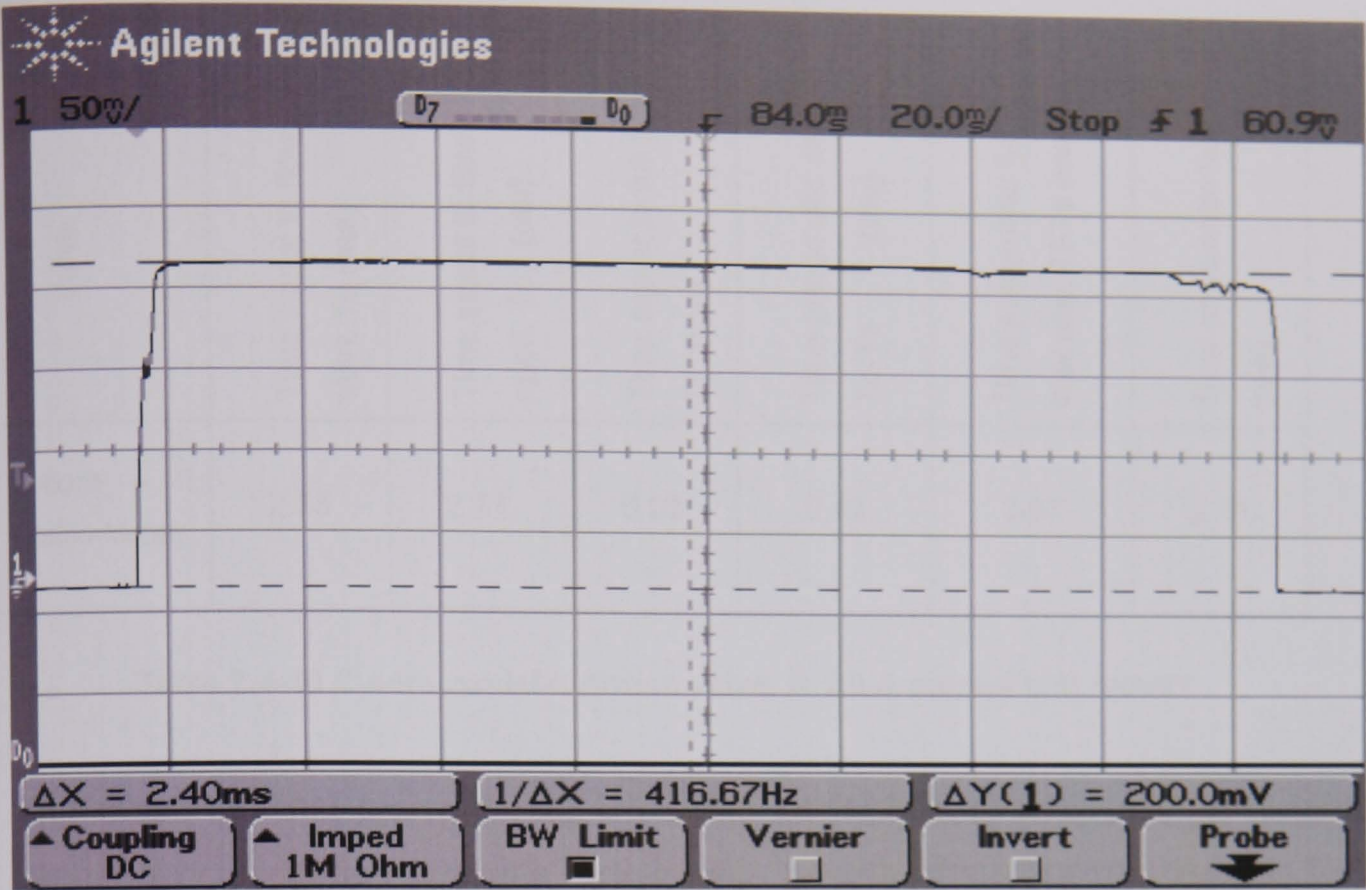


Fig. 7.4-9. C-core model-II Armco valve, $I=2.0\text{ A}$, current characteristic curve

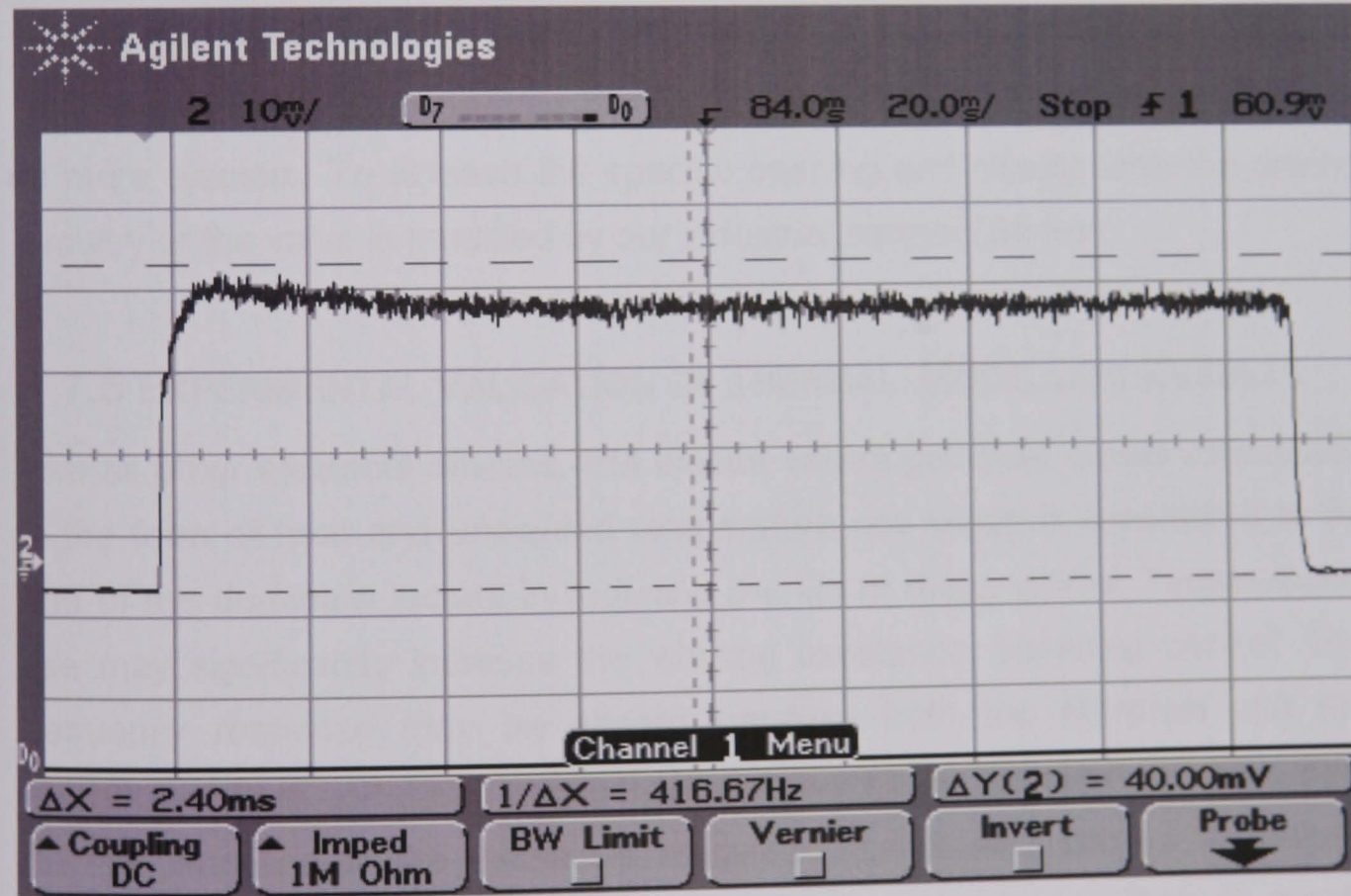


Fig. 7.4-10. C-core model-II Armco valve, $I=2.0\text{ A}$ current pressure characteristic curve

Valve	Time signal to flow start, Ts (ms)	Time signal to flow open, To, (ms)	Time signal to full flow , Tf, (ms)	Time pneumatic rise, To-Ts (ms)	Time pneumatic full flow rise, Tf-Ts (ms)	Time pneumatic fall (ms)
C-core – II (Radio-Metal)	2.35	2.77	6.02	0.42	3.67	2.11

Table 7.4-10 C-core model-II Armco valve, I= 2.0 A current test results

The response test showed that the valve performed satisfactorily for a wide variation of excitation currents, confirming the robustness of the design. This test was carried out without the drive circuit. The opening and closing time for the valves obtained were within the required limits. Typically products pass though the optical viewing station at a speed of 4 m/s and, if found defective, they are rejected approximately 7.5 ms later by a pulse of air delivered by one or more ejectors. To achieve the specific opening and closing time the driving circuitry of the valve is modified by our industrial partner (Sortex).

7.5 EXPERIMENTAL VALIDATION OF THERMAL MODELLING RESULTS

Like all other electrical devices, EM ejector valves generate losses manifested in the form of heat and unwanted temperature rise which is considered to be one of the dominant factors in reducing the life of these valves. Temperature-rise may significantly increase the winding resistance, impairing control. The frequency response may be altered because both the electrical and the mechanical time constants are temperature sensitive. Although the governing thermal limitation is the insulation, magnetic iron is also subject to thermal limitations. The tightly packed valves in the ejector banks are likely to create serious problems of heat sinking from individual valves. Also the diverse combination of materials used the very extensive duty cycles may give rise to myriad thermal problems, unique to EM ejector valves.

An effective solution to these problems will have a direct impact on the cost, size, reliability and feasibility of a given design. The methodologies for thermal modelling of ejector valves will involve the development of 2D/3D thermal models and the FE solution of the steady-state and/or transient heat transfer equations. The coupling of the magnetic field and the thermal equations may be realised either by indirect coupling or by direct coupling in which the equations are solved simultaneously. The 2D/3D thermal models and the design tools for the solution of this magneto-thermal problem, will give a vital insight into the thermal behaviour of both the individual ejectors and the ejector banks and will enable quantification of the effects of various factors that will affect such behaviour.

Methodologies have been developed, ahead of time, for the 2D thermal modelling of the above ejector valves. An experimental investigation into the thermal behaviour of the C-core-I ejector valve has also been carried out at Sortex. Some of the experimental data have been compared with the corresponding modelling results showing good agreement (Fig. 7.5-1). The results have been used primarily to validate the thermal FE models developed and to obtain empirical relationship that could be used to predict the thermal behaviour of the ejector valves for those thermal regimes which could not be simulated directly by FE modelling (e.g. cooling by compressed air, etc.).

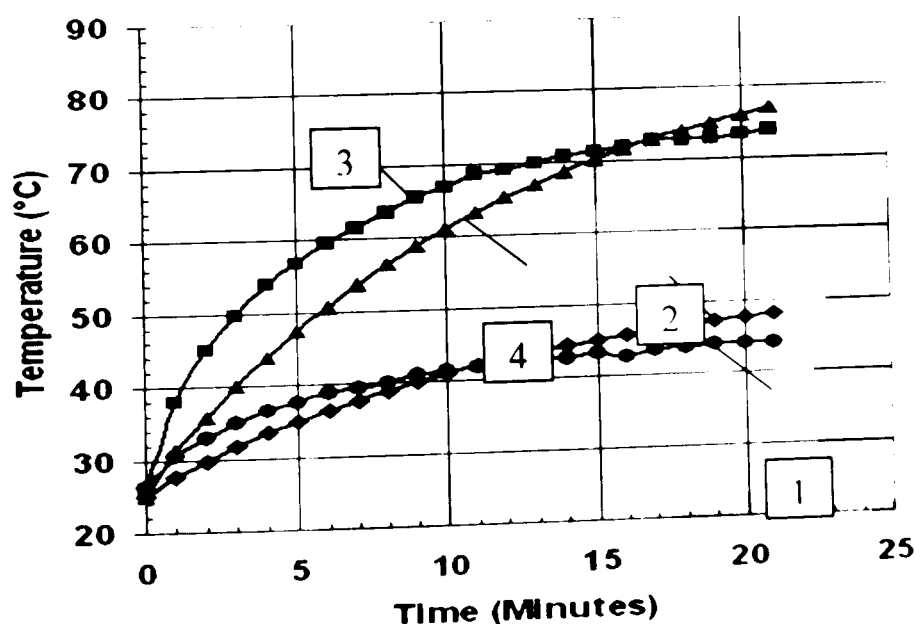


Fig. 7.5-1. Comparison of the thermal modelling results with the corresponding experimental data for the current C-core-I ejector valve (with no air cooling): 1, 2 – current $I=1$ A, 3, 4 – current $I=1.5$ A; 1, 3 – measured, 2, 4 – modelling

The thermal tests carried out on the first batch of prototypes showed that the maximum temperature rise for individual valves over a period of 30 minutes of operation did not exceed 50°C for the 1A current test. The results of specific tests are given in Section 3. These results are in accordance with the modelling results for the maximum power loss in the winding, which have been shown to lie below the specified limit (4 W) for the maximum current level in the winding.

Time, t (minutes)	Temperature, θ (°C)	Comments
Frequency $f=150$ Hz		
0	25.9	Valve excitation is turned on
1	27.5	
2	30.4	
3	32.4	
4	33.2	
5	33.6	
6	33.8	
7	34.0	
8	33.9	
9	34.0	
10	34.0	
Frequency $f=300$ Hz		
11	34.5	Frequency increased to 300 Hz at $t=10$ min.
12	35.5	
13	36.0	
14	36.2	
15	36.0	
16	36.0	
17	35.3	Valve excitation is turned off ($I=0$) at $t=16$ min.
18	35.0	

Table 7.5-1 Experimental data for the thermal test of one of the prototype valves.

C- core-II (Material: Armco), $F=150, 300$ Hz

For the thermal test a K-type thermocouple was attached to the outer casing of the prototype C-core-II (made of Armco ingot iron, first batch) valve. The valve was tested at a winding current $I=1$ A and at a frequency $f=150$ Hz for 10

minutes and the frequency was then raised to 300 Hz for the next 8 minutes. The test data, shown in Table 7.5-1 below are presented in Fig. 7.5-3.

The prototype c-core-II valve was tested at 300 Hz under an excitation $I=1.5$ A. A steady-state temperature of $\theta=48^{\circ}\text{C}$ was reached in about 19 minutes.

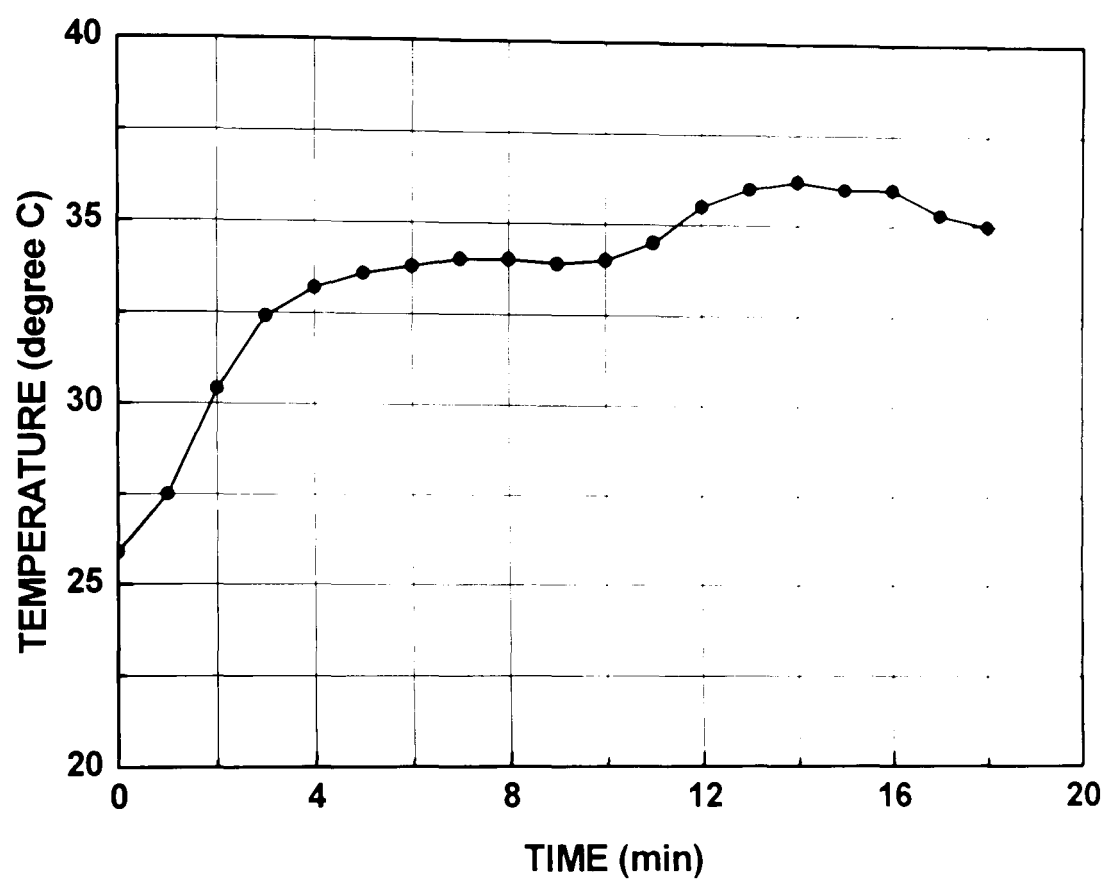


Fig. 7.5-2. Variation of temperature with time corresponding to results of thermal tests shown in Table 7.5-1

7.6 SUMMARY

In this chapter the discussion focused solely on model validation. Initially, the air flow rate was validated against available experimental data from Sortex Ltd. Air flow in the valve that had already been investigated by our project partners Sortex Ltd; the measurements showed that there was quite good quantitative agreement between data from Sortex Ltd and experiment.

Next, the extensive validation of the Opera-2d model inductance values, whose development was pursued immediately afterwards and which was one of the important parameter of the current study, is presented. Initially, obtained results from 2D/3D simulations of C-core-II are presented and compared against

available experimental data; overall, the agreement of the model with the experiment has been found to be quite satisfactory on a qualitative level.

As a result of the computer modelling and design work, a robust design of a solenoid valve actuator were carried out which met the Sortex design specifications. A number of designs were prototyped and tested successfully which showed the robustness of the design and its compliance with design specifications. The results of FE modelling and experimental studies given in this work are meant for references for possible design changes that are recommended to be made only by considering the electrical, magnetic and mechanical processes that underlie the overall performance of the valve designed.

Chapter 8

DEVELOPMENT OF ADVANCED ACTUATORS USING MAGNETIC SHAPE MEMORY MATERIAL

8.1 INTRODUCTION

The MSM materials are a recently discovered new group of materials that can change their shape in a magnetic field. Different types of actuators have been used as input motion and force sources. Hydraulic, pneumatic, and electric actuators are called “conventional” because the majority of robotic and automated mechanical systems use them. Recently, advances in material technology have introduced lightweight and strong substances, making it possible to build structurally strong articulated mechanisms that are compact and weigh very little. Examples of such “smart” materials that can be used to develop novel actuators are magnetic shape memory alloys. Actuators made out of this smart material are often called “non-conventional” to represent the novelty of the actuation concept. They are also called “advanced” to denote that they combine small, compact size with large force or velocity outputs [116-117].

There is a well-demonstrated need for commercial applications of advanced actuators. The present advances in information technology, nanotechnology, and biotechnology will require the development of miniaturized, novel devices and instruments that need to apply substantial forces. The same demand for new actuators occurs in traditional industries such as military, entertainment, medicine, and manufacturing, where there is an increasing need for developing small-size and lightweight devices which are applicable to apply large forces, develop high speeds, achieve large displacements, and are highly energy efficient.

In all these applications, mission requirements are becoming drastically more stringent in terms of mass, dimensions, power, and cost. Improvements in

actuator robustness and reliability associated with power efficiency and compact packaging which can lead to effective devices that are significantly more capable and reliable at a lower cost. Conventional actuators, such as electric motors and hydraulic and pneumatic cylinders, prevent large reductions in the overall weight and complexity of the robotic manipulator [118-124].

8.2 MAGNETIC SHAPE MEMORY MATERIALS

MSM alloys, which change shape under a magnetic field, offer an innovative solution to this problem. With the highest per unit length strain, the MSM alloys cannot be theoretically over-strained, which opens up the prospect of an 'infinite' lifetime. Since the maximum lifetime achieved to date by a few MSM-based devices is only near 300 million cycles, our target of 10 billion cycles will push the boundaries of current MSM technology. This is achievable and will be done by careful design of the magnetic circuit for highly uniform magnetic fields and by growing appropriate MSM alloys that are free from internal defects giving maximum fatigue life to establish a high value actuator manufacturing capability in a materials technology, relatively new to the UK economy.

The materials showing MSM effects have a non-cubic unit cell structure. The shape change effect itself is based on the reorientation of the unit cells in the material. Since the unit cells are not symmetric, the deformation results in a change of macroscopic shape of the material. A special property of MSM material is that the energy needed for deforming the unit cells is small and much smaller than in most materials. In addition, MSM materials have strong magnetic anisotropy, because the anisotropic unit cells can be reoriented with the magnetic field. Another way of generating the shape change is to apply a mechanical stress on the material in an elongated direction [125-127].

The MSM materials are ferromagnetic and anisotropic. Therefore, the magnetization of the material is high. It has a certain saturation value, and depends on the direction of the applied field. The saturation field strength falls within the range 475 kA/m to 500 kA/m.

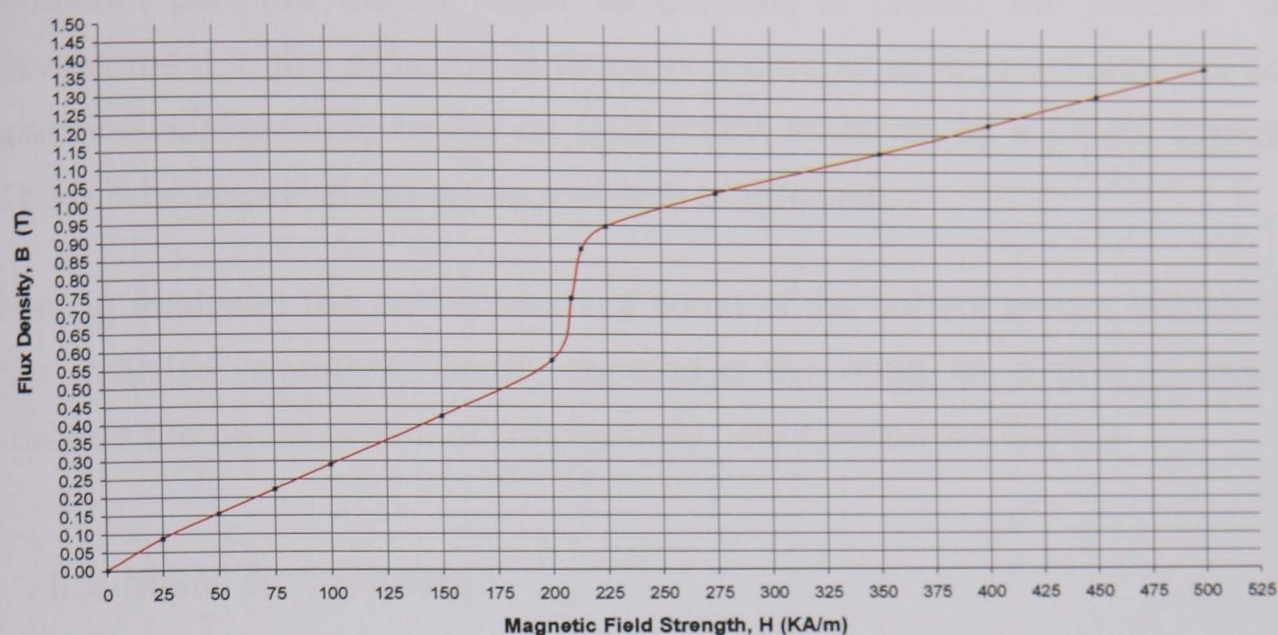


Fig. 8.2-1. MSM material B-H curve

The research had been carried out to explore the possibilities of conceptually new ejector valve designs using the new generation of room temperature smart materials. This mainly took the form of extensive survey of existing literature, and contacting and consulting relevant industries and research groups. Initial contacts have been established with three companies in USA, Finland and China.

The research done so far shows that two groups of smart material might be promising for new ejector technology. These are giant magnetostrictive materials (GMM) and magnetic shape memory (MSM) alloys which change their shape when subjected to magnetic field. The new GMM like TERFENOL-D ($\text{Tb}_x\text{-Dy}_{1-x}\text{-Fe}$) is particularly interesting for this purpose because of their large strain (1600-2400 ppm, 1.6-2.4 mm, 0.1-0.2%), high reliability and apparently longer life. Unlike PZT and conventional solenoid actuators, TERFENOL-D cannot be over-strained. It has been reported that a TERFENOL-D driven projector has operated more than 10^{12} cycles without failure or reduction in performance. Some of the MSM alloys made of Ni-Mn-Ga, Ni-Ti, etc. which are also interesting for ejector application could deliver even higher strain at room temperature [128-132].

Considering the potential of the above materials, it was proposed by the industrial partners that it might be prudent to protect the possible further development in this direction in terms of a product specific actuator (for sorting machine applications) based on GMM/MSM materials by a patent application. This will be explored further as research progresses.

Having analysed the performance of some of the current ejector valves one of the industrial partners, Sortex expressed the need for a shift in emphasis towards the development of conceptually new ejection technology.

8.3 MSM ACTUATORS

MSM actuators are devices that produce the magnetic field for the MSM element, which in turn generates the mechanical motion. An MSM actuator usually consists of an MSM element, a ferromagnetic core and coils [125].

The work output and coupling factor between mechanical and magnetic energies of the MSM materials are important operation parameters. Some simplified equations for calculating the work output have been proposed. The energies related to the MSM actuators are the input magnetic field energy density, W_{mag} output mechanical energy density, W_{mech} , and the loss density, q . The energy conservation principle gives the energy balance as,

$$W_{mag} = q + W_{mech}$$

A schematic view of this type of actuator structure can be seen in Fig. 8.3-1. To minimize the magneto-motive force needed, the magnetic field is usually applied to the MSM element in the transverse direction in relation to the direction of the output mechanical motion. The MSM elements in the actuator consist of two variants; one has the easy magnetization direction along the magnetic field and the other one along the mechanical stress. This maximizes the magnetic field induced (MFI) stress in the material. The overall construction produces a MFI stress to the MSM element to elongate itself in magnetic field.

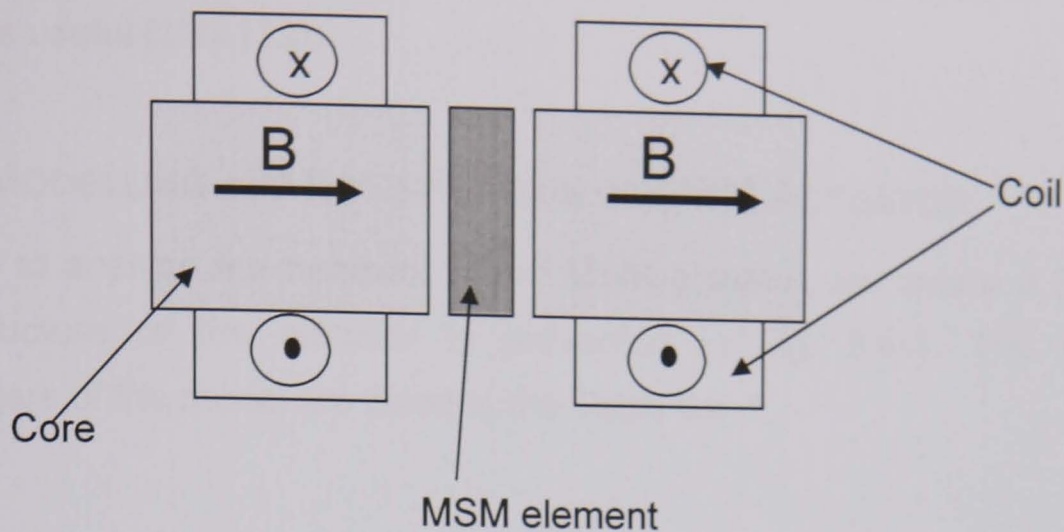


Fig. 8.3-1. Schematic view of the structure of MSM actuator

Fig. 8.3-1 schematic view of the structure of commonly used MSM actuators. The opposite forces against the MSM element are spring force and external force while the MSM element itself generates MFI force F_{mag} .

The twinning stress in the MSM material maintains the strain value, when external forces and magnetic fields are removed. Since the motion of the material is not reversible by itself, opposing load is needed to move the MSM element backward. In pre-stressed actuators, the required opposing loads are realized with springs. It is also possible to use two reverse-coupled MSM actuators to move the elements of each others in opposite direction [122], [127-128].

The hysteresis of MSM material has to be taken into account in the design of specific MSM actuator application. The hysteresis of the material dampens unwanted mechanical vibrations and higher harmonics of current and in that way eases the control of the application. On the other hand some control application can have trouble with the hysteresis. The MSM element is the central part of the MSM actuator. The magnetic field induced force of an element depends on its cross-sectional area. The stroke in turn depends on the length of the MSM element. These affect the measures of the actuator.

Since the MSM shape change is relatively large, the motion can often be used directly without any mechanical amplification. Hence, the structure of the actuator is simple and reliable. An example of this type of application is an MSM

valve. When very large stroke is needed, a mechanical system to amplify motion is useful [129-132].

8.4 MODELLING AND INVESTIGATION OF MSM ACTUATOR

In order to analyse the behavior of the MSM actuator, we create a 2D model. The structure of the actuator is presented in Fig. 8.4-1. The geometric parameters of the model are listed in the Table 8.4-1.

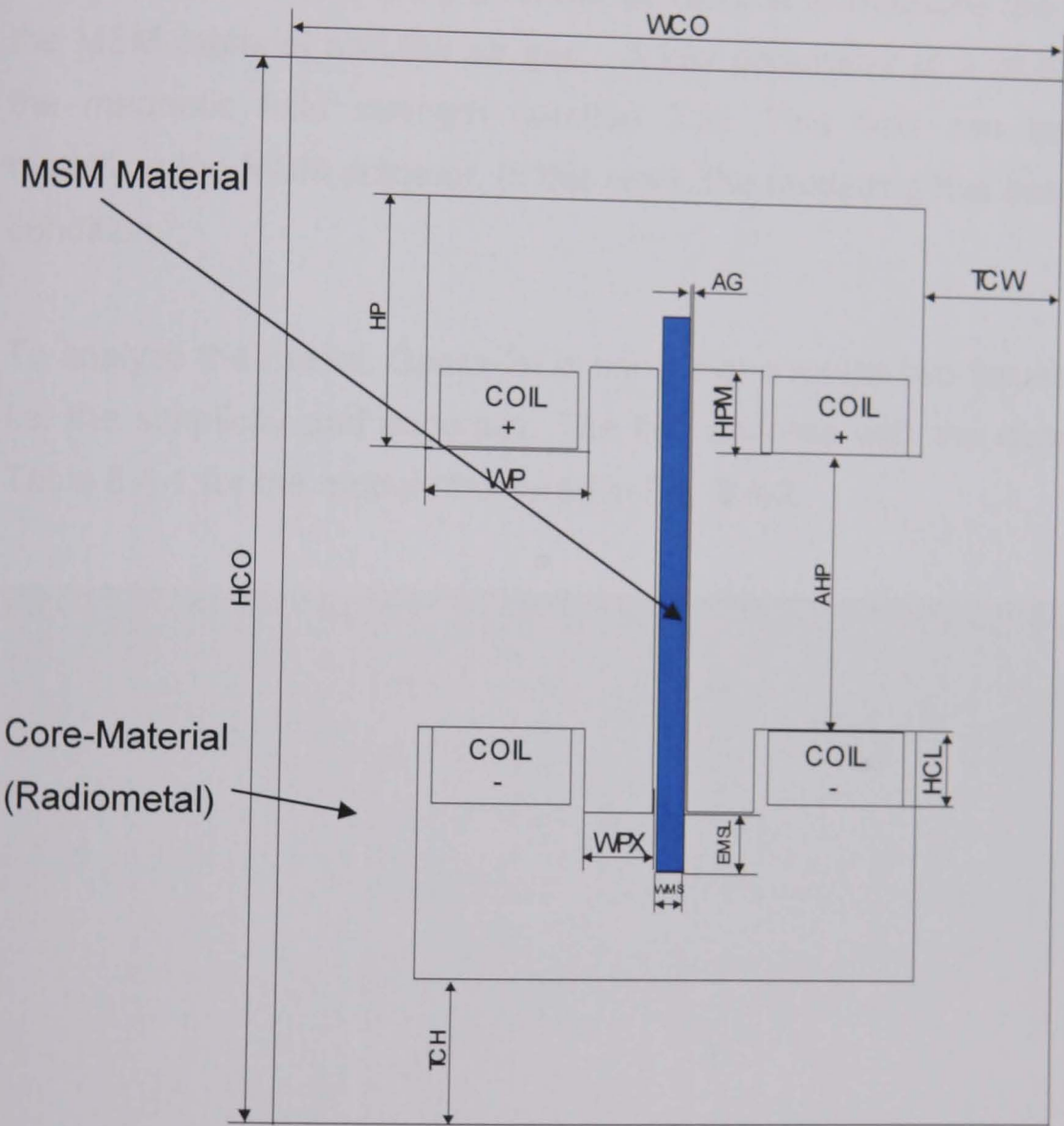


Fig. 8.4-1. MSM actuator model

Dimensions	WCO	TCW	TCH	HCO	HP	WP	HPM	AHP	HCL	EMSL	WMS	WPX	AG
Units	mm	mm	mm	mm	mm	mm	mm	mm	mm	mm	mm	mm	mm
Value	28.20	5.00	5.00	38.00	9.00	6.00	3.00	10.00	2.75	2.00	1.00	2.50	0.10

Table 8.4-1 MSM model -I dimensions

The electromagnetic field analysis package developed by Vector fields is used. The package, based on 2D finite element method, comprises a post processor (Opera). In this piece of work, attention is focused on the model development only. The model was created using *command input file* in Opera-2d. The command input file was written as a program, with all parameters defined at the beginning; followed by a listing of all command procedures in order to generate the whole model.

The main aim in modelling an MSM actuator is to measure the field strength in the MSM material and the air gap. A key parameter of a model is defined by the magnetic field strength (section 2.2). This field can be computed by modelling the MSM actuator. In this work, the modelling has been done in static condition.

To analyze the model, Opera-2d is used. For a model two issues are important, i.e. the simplicity and accuracy. The first analysis with the dimension listed in Table 8.4-1 for the model structured in Fig. 8.4-2.

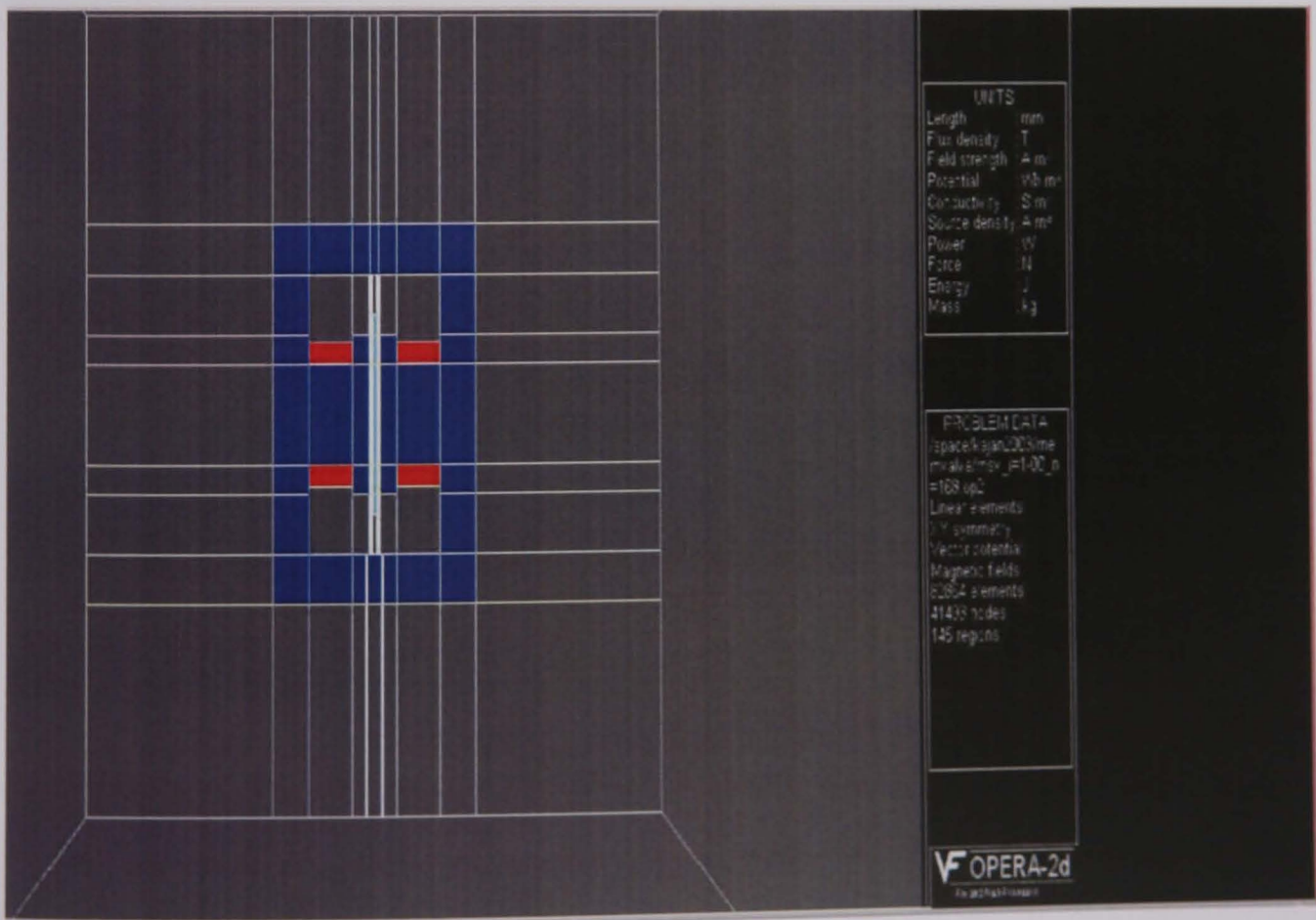


Fig. 8.4-2. MSM actuator Opera-2d model

This is non-linear analysis carried out by Opera-2d. The results from this model analysis are tabulated in Table 8.4-2.

Current, I (A)	Number of Turns, N	MMF, (A)	Flux Density in the Air Gap, B _x (T)	Flux Density in the MSM Material, B _{ms} (T)	Magnetic Field Strength in the MSM Material, H _{mod} (A/m)
1.00	168 x 2	168 x 1 x 2 = 336	0.5681	0.5676	196817
2.00	168x 2	168 x 2 x 2 =672	0.9411	0.9409	226475
1.00	519 x 2	519 x 2 x 1=1038	0.9760	0.9750	240132
2.00	519 x 2	519 x 2 x 2 = 2076	1.0158	1.0143	262125
4.00	519 x 2	519 x 2 x 4 = 4152	1.0907	1.0885	308409
6.00	519 x 2	519 x 2 x 6 = 6228	1.1632	1.1594	355357
8.00	519 x 2	519 x 2 x 8 = 8304	1.2349	1.2315	401986

Table 8.4-2 MSM model- I modelling results

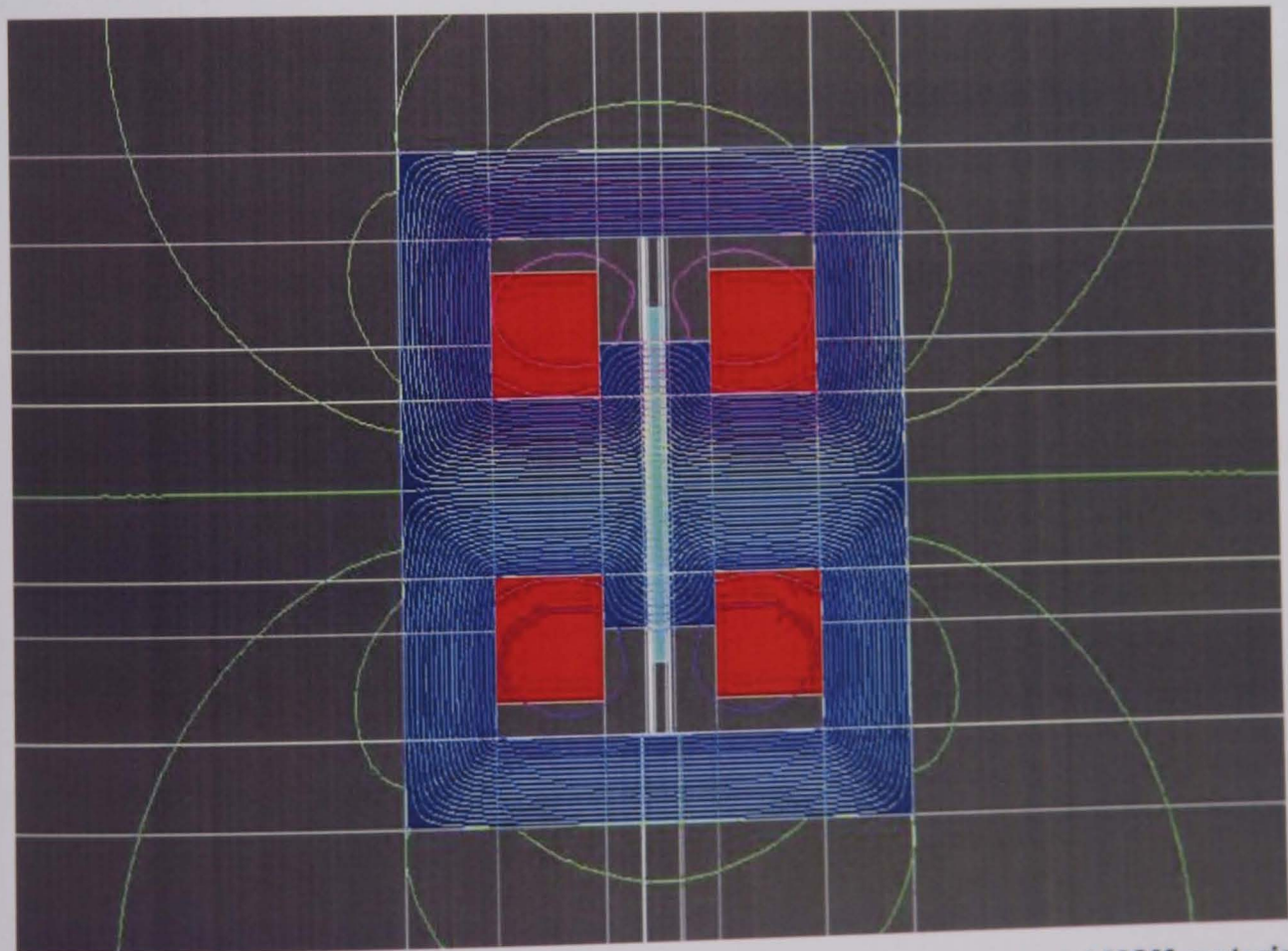


Fig. 8.4-3. Field plot for MMF=8304 A-turn model, with its core and MSM material in the middle

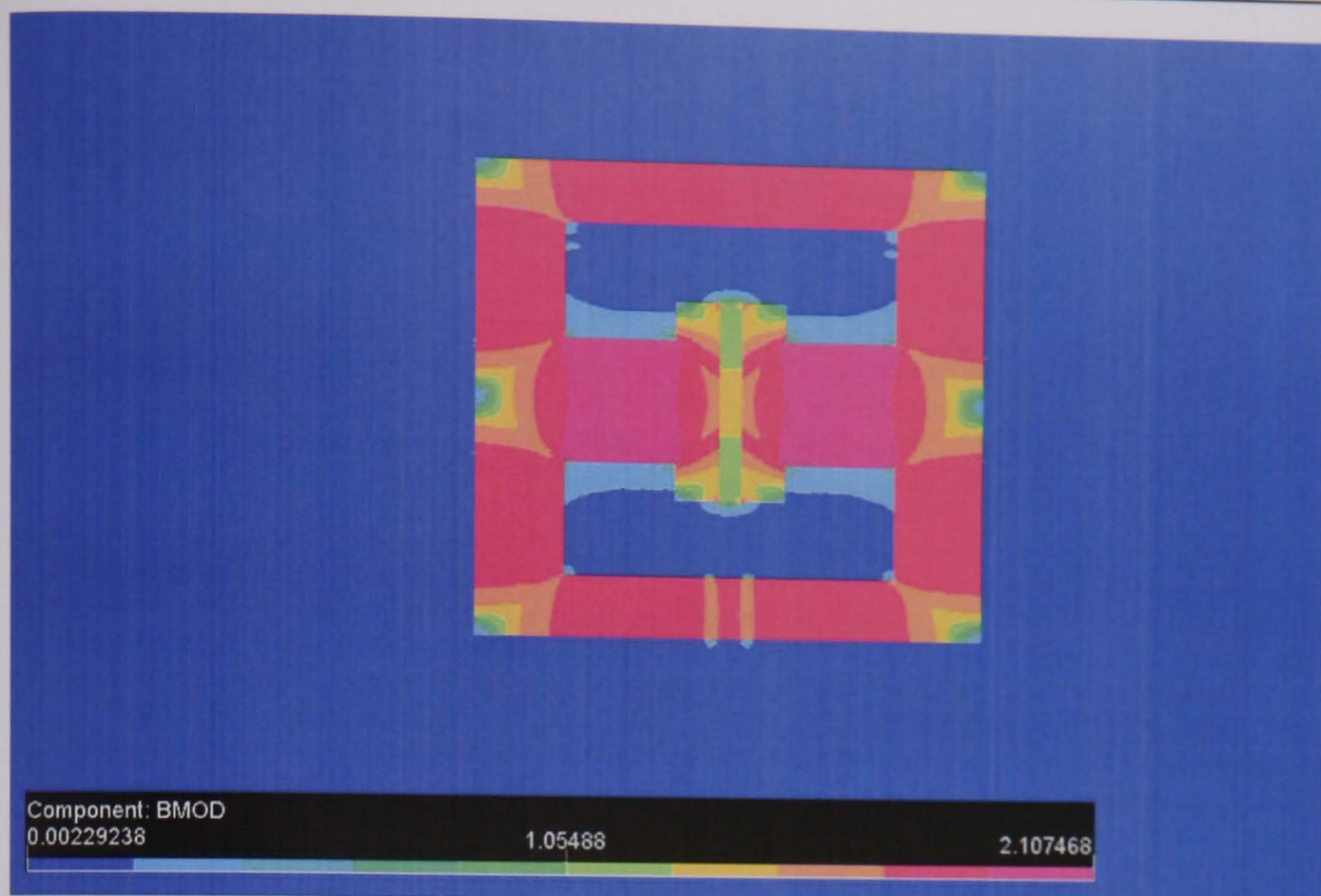


Fig. 8.4-4. Contour plot for MMF=8304 A-turn model, with its core and MSM material in the middle

The field lines and the contour plots of the MSM actuator are shown in Figs. 8.4-3 to 8.4-5. The magnetic field strength and flux density do not have a constant value inside an MSM element and the air gap. Only one field value is used to represent the magnetic state. This is the average value of magnetic field inside the MSM element and the air gap.

Another analysis was carried out using the same structure of the MSM valve with different dimensions, tabulated in Table 8.4-3.

Dimensions	WCO	TCW	TCH	HCO	HP	WP	HPM	AHP	HCL	WMS	WPX	WSR	WAG
Units	mm	mm	mm	mm	mm	mm	mm	mm	mm	mm	mm	mm	mm
Value	34.20	8.00	8.00	66.00	17.00	6.00	3.00	16.00	16.37	1.00	2.50	2.00	0.10

Table 8.4-3 MSM model-II dimensions

Table 8.4-4 shows the results for the new model created according to the dimensions tabulated in the Table 8.4-3.

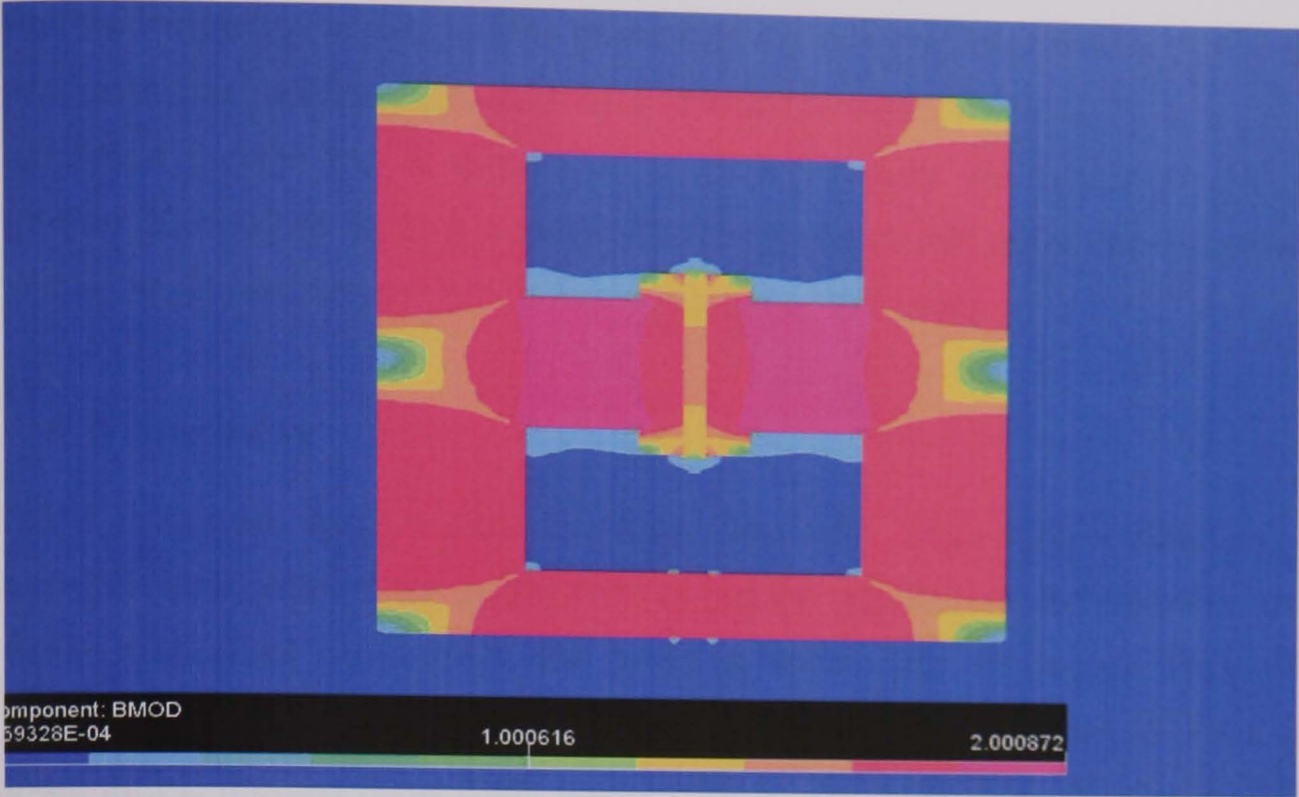


Fig. 8.4-5. Contour plot for MMF=8000 A-turn model , with its core and MSM material In the middle

Our industrial partner Sortex Ltd supplied the preliminary set of specification and design for this modelling work. Finite element modelling using Opera-2d allowed us to determine the typical flux distribution for the MSM actuator. Although the field plot, in itself, cannot be used for and design or analysis purpose. It gives useful information regarding a magnetic circuit, e.g. leakage, flux linkage, shape of flux lines, etc. By using the knowledge of the shape of the flux lines one can use a simpler model with reluctance path type calculation for approximate evaluation of the various quantities of a magnetic circuit (section 2.6).

Current, I (A)	Number of Turns, N	MMF, (A)	Flux Density in the Air Gap, B _x (T)	Flux Density in the MSM Material, B _{ms} (T)	Magnetic Field Strength in the MSM Material, H _{mod} (A/m)
1.00	1000 x 2	1000 x2 x 1	1.1489	1.1458	345143
2.00	1000 x 2	1000 x2 x 2	1.2117	1.2076	386214
3.00	1000 x 2	1000 x2 x 3	1.2727	1.2690	429592
4.00	1000 x 2	1000 x2 x 4	1.3350	1.3300	471762
5.00	1000 x 2	1000 x2 x 5	1.3971	1.3931	514685
6.00	1000 x 2	1000 x2 x 6	1.4594	1.4539	556998

Table 8.4-4 MSM model- II modelling results

Further modelling investigations show that the ejector valve shown in Fig. 8.4-1 produces the required flux density in the MSM material (1.33 T) at a nominal excitation current $I=4$ A. Based on modelling results we asked our industrial partner (Sortex) to build a number of prototypes of this valve for experimental testing and validation for future improvement of this valve.

8.5 SUMMARY

MSM materials form a new material type with interesting properties. The possible applications are in the field of motion generation and sensing. In this work, motion of generation has been studied. The structures of an MSM actuator and the basic reason for operation have been presented. Several MSM material FE models have been made prior to this work. The structures of MSM actuators are similar to each other. These were studied and one of them was selected for the actuator model. The accuracy of the selected model has been found sufficiently good. Based on the results, it is likely that all significant physical phenomena in actuator have been taken into account. The sensitivity of the model has not been studied, but some parameters of the model significantly influence the modelling results. This actuator was designed for an ejector valve.

Chapter 9

CONCLUSIONS

9.1 WORK DONE

The work presented in this report constitutes an important contribution towards the development of modelling and design environment for actuators. The theoretical study summarized in the report shows that a magnetic model for actuators can well describe the dynamic behaviour of the actuators.

Detailed methodologies have been developed for the mathematical modelling of actuators and their realisation using the numerical finite element method. Comparison of the FE (linear solution) modelling results with the corresponding analytical results give us a good agreement. This established confidence in the modelling methodologies and in the 2D/3D FE models that were developed to realise these methodologies for further simulation studies.

Highly accurate and useful models have been developed which are able to solve totally adequately many practical problems of analysis and design. The mathematical models are based on the solution of Maxwell's equations using 'finite element methods' for describing the electromagnetic field distribution in the region of interest. In our study RMS error was kept below 2% for all models.

Finite element modelling methodologies have been developed for the design and investigation of electromagnetic and thermal behaviours of high-speed, large-force and long-lifetime solenoid actuators used as pneumatic ejector valves in optical sorting machines for bulk food sorting.

The E-core and C-core 2D/3D models developed were used to carry out simulation studies to investigate actuators. This comprised, for example, the investigation of the actuator core for various design parameters. With the aid of the highly accurate models, the problem of design can be tackled in a realistic

and efficient way. This work is aimed at the practical production of a specific design. An investigation has been carried out. In such a design procedure the method of modelling analysis (chapter 6 & 7) provides useful information in choosing the most sensitive design variable for the modification of a design. The results of simulation tests performed by means of the model developed comply with the results of experiments carried out using the solenoid actuator what we designed, allow us to state that the actuator model reflects the dynamic properties of the actuator sufficiently well.

The actuator designed so far has been shown to have performed between 3-4 billion cycles under life and field trials and produces 8-19 N of force. It is believed that this design is pushing the limits of performance that can be achieved by actuators based on the EM solenoid principle.

When assessing the goodness of the overall design by means of the performance curves, (Current rise curves in chapter 7) we found the experimental values of the inductance and the modelling prediction to be in close agreement. The prototype shows good flow rate behaviour; of 14.5 litres per minute at 60psi pressure at 150 Hz. The thermal tests carried out on prototypes; the maximum temperature rise for individual valve over a period of 30 minutes of operation without air flow not exceeding 50⁰ C for 1 A current.

The design, development and implementation of a compact, fast, reliable, robust and long-life EM ejector sub-system described in the thesis is very much linked to the enhancement of performance of both the current and the next generation of optical sorting machines. This should further enhance bulk food sorting and lead to an improved food product, quality and safety through the efficient and 'surgical' removal of contaminants. The preservation and growth of the UK food market is fundamental to the future of many food producers and retailers. The presence of contaminants in food products is known to undermine consumer confidence which can be retained by efficient sorting. Retention of brand image is also assured.

The work here presented has provided an important link between Industry and University, from which both parties have greatly benefited. The new C-core-II model has been incorporated in Sortex Ltd product range. It would appear that computer aided methods will find increasing use for practical industrial design as illustrated in this thesis.

9.2 FUTURE WORK

A preliminary study was carried out in the chapter 8 for MSM valves. The modelling methodologies and FE models developed in this work could constitute the basis for further investigation of MSM actuators. It would be possible in future to carry out their detail analysis of MSM valves.

Overall, the work presented in this report constitutes an important contribution in the design and analysis of actuators and other similar electromagnetic devices.

REFERENCES

- [1] K. Yuan and S. Chen, A new algorithm for coupled solutions of electric, magnetic and mechanical systems in dynamic simulation of solenoid actuators, *IEEE Trans. Magn.*, vol. 26, May 1990.
- [2] M. Piron, P. Sangha, G. Reid, T. J. E. Miller, D. M. Lonel and J. R. Coles, Rapid computer-aided design method for fast-acting solenoid actuators, *IEEE Trans. Magn.*, pp. 991-999, Dec 1999.
- [3] G. S. Birth and R. M. Johnson, Detection of mold contamination in corn by optical measurements, *Journ. Assoc. Official Anal. Chem.*, 53 (5), pp. 931–936, 1970.
- [4] T. W. Tyson and R. L. Clark, An investigation of the fluorescent properties of aflatoxin-infected pecans, *Trans. ASAE*, 17 (5), pp. 942–944, 948, 1974.
- [5] J. M. Low, W. S. Maughan, S. C. Bee and M. J. Honeywood, Sorting by colour in the food industry, Chapter 5 in *Instrumentation and Sensors for the Food Industry*, ed. E Kress-Rogers and C. J. B. Brimelow, 2nd edition, Woodhead Publishing Limited, 2001.
- [6] M. C. Pasikatan and F. E. Dowell, Sorting systems based on optical methods for detecting and removing seeds infested internally by insects or fungi: are view, *Applied Spectroscopy Reviews*, 36(4), pp. 399–416, 2001.
- [7] S. Bee, K. T. V. Grattan and S. H. Khan Colour and shape sorting for bulk food processing, In *Sensors and Their Applications XI*, ed., Bristol: Institute of Physics Publishing, pp. 289-295, 2001.

- [8] D. Wang, F. E. Dowell, Y. Lan, M. Pasikatan and E. Maghirang, Determining pecky rice kernels using visible and near-infrared spectroscopy, *International Journal of Food Properties*, vol. 5, No. 3, pp. 629–639, 2002.
- [9] S. C. Bee and M. J. Honeywood, Colour sorting for the bulk food industry, Chapter 6 in *Colour in Food: Improving Quality*, ed. D. B. MacDougall, Woodhead Publishing Limited, 2002.
- [10] A. M. Pawlak and T. W. Nehl, Transient finite element modelling of solenoid actuators, The coupled power electronics, mechanical and magnetic field problem, *IEEE Trans. Magn.*, vol. 24, pp. 270-273, Jan 1988.
- [11] E. P. Furlani and M. O'Brien, Analysis of axial-field actuators, *IEEE Trans. Magn.* 30, pp. 4323-4325, 1994.
- [12] T. Yamaguchi, Y. Kawase, H. Shiimoto and K. Hirata, 3-D Finite element analysis of dynamic characteristics of twin-type electromagnetic relay, *IEEE Trans. Magn.* 38, pp. 361-364, 2002.
- [13] J. M. Low, W. S. Maughan, S. C. Bee and M. J. Honeywood 2001 *Instrumentation and Sensors for the Food Industry*, ed. E Kress-Rogers and C J B Brimelow (Woodhead Publishing Limited) chapter 5.
- [14] A. Rahman, A. A R. Kadan, and M. Jo. J. Vander Deiden, The coupled problem in electromagnetic AC contactors, *IEEE Trans. Magn.*, vol. 33, pp. 1630-1633, Mar 1993.
- [15] B. Lequesne, Dynamic model of solenoids under impact excitation including motion and eddy currents., *IEEE Trans. Magn.*, vol.26, pp. 1107-1116, Mar 1990.
- [16] P. Sangha and D. Rodger, Design and analysis of voltage fed axisymmetric actuators, *IEEE Trans. Magn.*, vol. 30, pt. 2, pp. 3240-3242, Sep 1994.

-
- [17] K. J. Binns, *The Analytical and numerical solution of electric and magnetic fields*, New York, Wiley, 1992.
- [18] M. Piron, The application of magnetic gauge curves to linear motion solenoid actuators and rotary doubly salient reluctance machines, in *Proc. ICEM98*, pp. 1649-1679, Sep 1998.
- [19] D. Shen, G. Meunier J. L. Coulomb and J. C. Sabonnadiere, Solution of magnetic field and electrical circuit combined problem, *IEEE Trans. Magn.*, vol. 21, pp. 2288-2291, 1985.
- [20] J. A. MacBain, A numerical analysis of time-dependent two-dimensional magnetic field, *IEEE Trans. Magn.*, vol. 17, pp. 3259-3261, Nov 1985.
- [21] P. Masse, B. Morel and T. Breville, A finite element prediction-correction scheme for magneto-thermal problem during curie transition, *IEEE Trans. Magn.*, vol. 21, pp. 1871-1873, 1985.
- [22] F. Piriou and A. Razek, A non-linear 3D coupled model for magnetic field and electric equations, *IEEE Trans. Magn.*, vol. 28, pp. 1295-1299, 1992.
- [23] Y. Kawase and Y. Ohdachi, Dynamic analysis of automotive solenoid using finite element method, *IEEE Trans. Magn.*, vol. 27, pp. 3939-3942, 1991.
- [24] Shi-Quen Zheng and Degui Chen, Analysis of transient magnetic fields coupled to mechanical motion in solenoidal electromagnet excited by voltage source, *IEEE Trans. Magn.*, vol. 28, pp. 1315-1317, 1991.
- [25] K. Srairi, M. Feliachi and Z. Ren, Electromagnetic actuator behaviour analysis using finite-element and parametrization methods, *IEEE Trans. Magn.*, vol. 31, pp. 3497-3499, Nov 1995.
- [26] A. Canova, M. Otella, and D. Rodger, A coupled field circuit approach to 3D FEM analysis of electromechanical devices, *In 9th Int Con on Electrical*

- Machines and Drivers*, IEE, Conference Publication 468, pp. 71-75, 1999.
- [27] D. C. White and H. H. Woodson, *Electromechanical Energy Conversion*. New York, Wiley, 1959.
- [28] S. Wang, T. Miyano and M. Hubbard, Electromagnetic field analysis and dynamic simulation of a two-valve solenoid actuator, *IEEE Trans. Magn.*, vol. 29, pp. 1741-1746, Mar 1993.
- [29] D. Rodger, H. C. Lai and P. J. Leonard, Coupled elements for problems involving movements, *IEEE Trans. Magn.*, vol. 26, pp. 548-550, Mar 1990.
- [30] L. A. Nowak, Simulation of dynamics of electromagnetic driving device for come ground penetrator, *IEEE Trans. Magn.*, vol. 30, pp. 3146-3149, Sep 1994.
- [31] M. Kaltenbacher, H. Landes and R. Lerch, An efficient calculation for the numerical simulation coupled magneto mechanical systems, *IEEE Trans. Magn.*, vol. 33, pp. 1646-1649, Sep 1997.
- [32] I. Yatchev, *Mechanics Automatic Control and Robotics*, vol. 3, No 15, 2003.
- [33] A. H. Seilly, Fast acting helical solenoid actuators, *IEEE proc*, vol 127, No 6, Nov 1980.
- [34] Zhang Sheng-Chang, Zhong Ting-xiu and XU Yang-zeng, A new approach for predicting dynamic behaviour of extra-high speed valve, *Journal of Shanghai Jiaotong University.*, vol. E-7, pp. 75-79, 2002.
- [35] S. H. Khan, M. Cai, K. T. V. Grattan, K. Kajan, M. Honeywood and S. Mills. Design and investigation high speed, large fore and long life time electromagnetic actuators by finite element modelling, *Journal of physics:*

- Conference series, Sensors & their application XIII, Institute of Physics*, vol. 15, pp. 300-305, Sep 2005.
- [36] S. H. Khan, M. D. Rotaru and K. T. V. Grattan, Computer Aided Modelling and Design of Solenoid Valves, Sortex Limited, London.
- [37] Z. Ren, and A. Razeq, Modelling of dynamical behaviours of electro-magneto-mechanical coupled system, *CEM*, pp. 20-23, 1994.
- [38] S. H. Le. G. Bisson, P. J. Leonard and D. Rodger, Finite element analysis of transient electromagnetic heating effects three dimensions, *IEEE Trans. Magn.*, vol. 29, pp. 1102-1106, Jan 1993.
- [39] E. Melgoza and D. Rodger, Comparison of table models of electromagnetic actuators. *IEEE Trans. Magn.*, vol. 38, pp. 953-956, Mar 2002.
- [40] S.D. Sudhoff, Magnetic Systems and Magnetic Equivalent Circuits, 2003.
- [41] J. Zieba, Simualtion of a solenoid actuator for a device for investigating dynamic air permeability through flat textile products, *Fibres and Textiles in Eastern Europe*, vol. 11, pp. 85-87, Apr/Jun 2003.
- [42] F. Bouillault and A. Razeq, Dynamic model for eddy current calculation in saturated electric machine, *IEEE Trans. Magn.*, vol. 19, pp. 2639-2642, 1983.
- [43] F. Piriou, and A. Razeq, Coupling of saturated electromagnetic systems to a non-linear power electronic devices, *IEEE Trans. Magn.*, vol. 24 , pp. 274-277, 1988.
- [44] A. Konrad, The numerical solution of steady-state skin effect problems an integrodifferential approach, *IEEE Trans. Magn.*, vol. 17, pp. 1148-1152, 1981.
- [45] H. Iswahjudi and H. H. Gatzert, Proceedings 14th European Simulation Symposium, 2002.

- [46] Vecror Fields, OPERA 2d User Guide, VF-05-03-A3.
- [47] J. K. Watson, Application of Magnetism, 2nd edition as published by author, 1985.
- [48] W. H. Hayt Jr, Engineering Electromagnetic, McGraw-Hill Book Company, 1981.
- [49] D. C. Jiles and D. L. Atherton, Ferromagnetic hysteresis, *IEEE Trans. Magn.*, vol. 19, pp. 2183-2185, Sep 1983.
- [50] K. H. Carpenter and S. Warren, A wide bandwidth, dynamic hysteresis model for magnetization in soft ferrites, *IEEE Trans. Magn.*, vol. 28, pp. 2037-2041, Sep 1992.
- [51] D. Jiles, Introduction to Magnetism and Magnetic Materials, 2nd ed. London: *Chapman & Hall*, 1998.
- [52] B. S. Guru and H. R. Hiziroglu, Electric machinery and transformers, 2nd ed., *Harcourt Brace & Company*, 1995.
- [53] Z. Ren and A. Razek, A strong coupled model for analysing dynamic behaviours of non-linear electromechanical systems" *IEEE Trans. Magn.*, vol. 30, pp. 3252-3255, 1994.
- [54] G. Rizzoni, Laboratory Manual for mechanical engineering 482, *system Dynamics and Electro mechanics*, Ohio State University.
- [55] A. Goldman, Hand Book of Modern ferro-magnetic materials, *Kluwer Academic Publication*, ISBN 0412- 14661-4, 1999.
- [56] D. C. Jiles and C. C. H. Lo, Sensors and actuators, *Elsevier*, A 106 (2003) 3-7, 2003.

- [57] M. E. McHenry, Material science and technology, Published by VCH, ISBN 3-527-28264-5, 1994.
- [58] F. K. Lu and D. S. Jensen Potential viability of a fast-acting micro-solenoid valve for pulsed detonation fuel injection, 41st Aerospace Sciences Meeting, RENO, Nevada, Jan 2003.
- [59] D. H. Smith and D. A. Spinweber, A general model for solenoid fuel injection dynamics, SAE paper 800508, *presented at SAE Congr. Exposition*, Detroit, MI, Feb 1980.
- [60] V. V. Hung and S. E. Ramin, Dynamic systems modelling and analysis, ed. McGraw-Hill Companies, Inc, New York, 1998.
- [61] K. Gniotek, Dynamic permeability of textiles, *Fibres & Textiles in Eastern Europe*, vol. 4, pp. 54-55, Apr/Jun 1996.
- [62] A. H. Seilly, Helonoid actuators A New concept in extremely fast acting solenoids, *SAE Technical Papers Series*, No. 790119, pp. 426-435, Sep 1979.
- [63] A. H. Seilly, Colenoid actuators further developments in extremely fast acting solenoids, *SAE Technical Papers Series*, No. 810462, pp. 1440-1781, 1981.
- [64] T. Kajima, Dynamic model of the plunger type solenoids at deenergizing state, *IEEE Trans. Magn.*, vol. 31, May 1995.
- [65] S. Wang, T. Miyano and, M. Hubbard, Electromagnetic field analysis and dynamic simulation of a two valve solenoid actuator, *IEEE Trans. Magn.*, vol. 29, pp. 1741-1746, Mar 1993.
- [66] W. Muller Comparison of different methods of force calculation, *IEEE*

Trans. Magn., vol. 26, pp. 1058-1061, 1990.

- [67] H. H. Woowdson and J. R. Melcher, *Electro mechanical dynamics-part-1: Discrete systems*, John Wiley, New York, 1968.
- [68] J. L. Coulomb, A methodology for the determination of global electromechanical quantities from a finite element analysis and its application of the evaluation of magnetic forces, torques and stiffness, *IEEE Trans. Magn.*, vol. 19, pp. 2514- 2519, 1983.
- [69] S. R. H. Hoole, *Computer Aided Analysis and Design of Electromagnetic Devices*, Elsevier, Ney York, 1989.
- [70] G. Cannistra, V. Dattoma and M. S. Labini, Analysis of thermal and mechanical stress in the stator of a direct-current motor by the finite element method, *EMD*, pp. 49-54, 1993.
- [71] R. W. Powell, C. Y. Ho and P. G. Klemens, *Thermal conductivity : metallic elements and alloys*, New York, 1970.
- [72] E. R. G. Eckert and R. M. Drake Jr, *Analysis of heat and mass transfer*, McGraw-Hill Book Company, New York, 1972.
- [73] J. D. Lavers, Numerical solution methods for electro-heat problems, *IEEE Trans. Magn.*, vol. 19, pp. 2566-2572, Nov 1983.
- [74] V. Cingoski, A. Namera, K. Kaneda and H. Yamashita, Analysis of magneto-thermal coupled problem involving moving eddy current conductors, *IEEE Trans. Magn.*, vol. 32, pp. 1042-1045, May 1996.
- [75] S. Williamson, and M. R. Lloyd, Cage rotar heating and standstill, *IEE Proceedings*, No. 6, pp. 325-332, Nov 1987.
- [76] C. Chan, L. Yan, P. Chen, Z. Wang and K. Chau, Analysis of electromagnetic

- and thermal field analysis for induction motors, *IEEE Trans. EC*, vol. 9, No 1, Mar 1994.
- [77] J. P. Bastos, M. Cabreira, N. Sadowski and S. R. Arruda, A thermal analysis of induction motors using weak coupled modelling, *IEEE Trans. Magn.*, vol. 33, pp. 1714-1717, Mar 1997.
- [78] D. Jiles, Introduction to magnetism and magnetic materials, 2nd ed, London & New York, *Chapman & hall*, 1998.
- [79] S. Chikazumi, Physics of ferromagnetism., 2nd ed, Oxford, *Clarendon Press*, 1997.
- [80] R. J. Parker, Advanced in permanent magnets., *Wiley*, New York 1990.
- [81] Carpenter Technology Material Data.
- [82] R. O'Handley, Modern magnetic materials, *Wiley-Interscience*, Chapter 10, 1999.
- [83] Metglas, Honeywell, Technical Bulletin.
- [84] F. Piriou and A. Razek, Finite element analysis in electromagnetic systems accounting for electric circuits, *IEEE Trans. Magn.*, vol. 29, pp. 1669-1675, Mar 1993.
- [85] K. J. Binns, P. J. Lawrenson and C. W. Trowbridge, The Analytical and numerical solution of electric and magnetic field, *John Wiley & Sons*, 1992.
- [86] T. W. Nehl, A. M. Pawlak and N. M. Boules, A general purpose finite element package for computer aided design and analysis of electromagnetic devices, *IEEE Trans. Magn.*, vol. 24, pp. 358-361, Jan 1988.

- [87] P. P. Silvester and K. L. Ferrari, Finite elements for electrical engineers, Cambridge, London, 1983.
- [88] K. Takeuchi, M. Shimizu and K. Okazaki, Fast actuator modelling by finite element method, *IEEE Trans. Magn.*, vol. 30, pp. 4284-4286, Nov 1994.
- [89] T. Nakata, N. Takahashi, K. Fujiwara and Y. Shiraki, Comparison of different finite element for 3D eddy current analysis, *IEEE Trans. Magn.*, vol. 26, pp. 434- 437, 1990.
- [90] T. Nakata N. Takahashi, Y. Kawase, H. Funakoshi and S. Ito, Finite element analysis of magnetic circuits composed of axisymmetric and rectangular regions, *IEEE Trans. Magn.*, vol. 21, pp. 2199-2202, 1985.
- [91] J. R. Brauer, J. J. Ruehl, M. A. Juds, M. J. Vanderheiden and A. A. Arkadan, Dynamic stress in magnetic actuator computed by couple structural and electromagnetic finite elements, *IEEE Trans. Magn.*, vol. 32, pp. 1046-1049, May 1996.
- [92] M. Kaspar and J. Franz, Highly accurate computation of field quantities and forces by super convergence in finite elements, *IEEE Trans. Magn.*, May 1995.
- [93] O. C. Zienkiewicz and K. Morgan, Finite elements approximation methods, John Wiley, New York, 1983.
- [94] G. Bedrosian, A new method for coupling finite element field solutions with external circuits with kinematics, *IEEE Trans. Magn.*, vol. 29, pp. 1664-1668, Mar 1993.
- [95] M. V. K. Chari and P. P. Silvester (ed). Finite elements in electrical and magnetic field problems, John Wiley, New York, 1980.
- [96] C. S. Biddlecombe, J. Simkin, A. P. Jay, J. K. Sykulski and S. Lepaul, *IEEE*

Trans. Magn., vol. 34, pp. 3182-3185, Sep 1998.

- [97] J. Vaananen, Theoretical approach to couple two-dimensional finite element models with external circuit equations, *IEEE Trans. Magn.*, vol. 32, pp. 400-409, 1996.
- [98] A. H. Bagegni, G. E. Adams and R. G. Hoft, Tubular linear induction motor for hydraulic capsule pipeline-part I: finite element analysis, *IEEE Trans. Energy Conversion.*, vol. 8, pp. 251-261, Jun 1993.
- [99] N. Sadowski, R. Carlson, A. M. Beckert and J. P.A. Bastos, Dynamic modelling of a newly designed linear actuator using 3D edge element analysis, *IEEE Trans. Magn.*, vol. 32, pp. 1633-1636, May 1996.
- [100] P. I. Koltermann, J. P. A. Bastos and S. R. Arruda, A model of dynamic analysis of AC contactor, *IEEE Trans. Magn.*, vol. 28, pp. 1348-1350, Mar 1992.
- [101] N. Sadowksi, Y. Lefevre, M. Lajoie-Mazenc and J. Cros. Finite element torque calculation in electrical machines while considering the movement, *IEEE Trans. Magn.*, vol. 28, pp. 1410-1413, Mar 1992.
- [102] J. S. Wang and N. Ida, Curvilinear and higher order edge finite elements in electromagnetic field computation, *IEEE Trans. Magn.*, vol. 29, pp. 1491-1494, Mar 1993.
- [103] J. A. McBain, A numerical analysis of time-dependent two-dimensional magnetic fields, *IEEE Trans. Magn.*, vol. 19, pp. 2180-2182, Sep 1983.
- [104] Y. Sang-Baeck, J. In-Soung, K. Ki-Chan and H. Dong-Seok, Dynamic analysis of a reciprocating actuator for gas compression using finite element method, *IEEE Trans. Magn.*, vol. 33, pp. 4113-4115, Sep 1997.
- [105] L. Erping and P. M. McEwan, Analysis of a circuit breaker solenoid

actuator system using the decoupled CAD-FE--integral technique, *IEEE Trans. Magn.*, vol. 28, pp. 1279-1282, Mar 1992.

- [106] P. K. Vong, D. Rodger, P. C. Coles and H. C. Lai, On modelling weakly coupled electromagnetic-thermal problems with prescribed non-linear surface heat transfer. *Power electronics, mechanics and drives*, Conference Publication No 487 pp. 260-265, Apr 2002.
- [107] N. A. Demerdash, T. W. Fouad and O. A. Mohammed, Three dimensional finite element vector potential formulation of magnetic field in electrical apparatus, *IEEE Trans. PAS.*, vol. 100, No 8, 1981.
- [108] J. D. Mayergoz, M. V. K. Chari and J. D'Amdelo, A new scalar potential formulation for three-dimensional magneto static problem, *IEEE Trans. Magn.*, vol. 23, 1987.
- [109] G. Meunier, H. T. Luong and Y. Marechal, Computation of coupled problem of 3D eddy current and electrical using T0-T- Φ formulation, *IEEE Trans. Magn.*, vol. 34, pp. 3074-3077, Sep 1998.
- [110] P. P. Silvester and D. Omeragic, Differentiation of finite element solution of Poisson equation, *IEEE Trans. Magn.*, vol. 29, pp. 1993-1996, Mar 1993.
- [111] Y. Kawasw, S. Tatsuoka and T. Yamaguchi, 3D finite element analysis of operating characteristics of AC electromagnetic contactors, *IEEE Trans. Magn.*, vol. 30, pp. 244-3247, Sep 1994.
- [112] R. E. Clark, D. S. Smith, P.H. Mellor and D. Howe, Design optimization of moving-magnet actuators for reciprocating electro-mechanical systems, *IEEE Trans. Magn.*, vol. 31, pp. 3746-3748, 1995.
- [113] B. Lequesne, Fast-acting, long-stroke solenoids with two springs, *IEEE Trans. Industry Application.*, vol. 26, pp. 848-856, 1990.

-
- [114] D. Ebihara and M. Watada, Development of a single-winding linear oscillatory actuator, *IEEE Trans. Magn.*, vol. 28, pp. 3030-3032, 1992.
- [115] Y. Mitsutake, and K. Hirata, dynamic response analysis of a linear solenoid actuator, *IEEE Trans. Magn.*, vol. 33, pp. 1634-1637, Mar 1997.
- [116] K. Ulakko, Magnetically controlled Shape Memory Alloys: A new class of actuator materials, *Journal of Material Engineering and Performance*, vol. 5, pp. 405-409, 1996.
- [117] R. Tickle, R. D. James, T. Shield, M. Wutting and V. V. Kokorin, Ferromagnetic shape memory in NiMnGa system, *IEEE Trans. Magn.*, vol. 35, pp. 4301-4310, 1999.
- [118] H. Funakubo (ed), Shape memory alloys, *Gordon and Beach*, New York, 1986.
- [119] S. J. Murray, R. C. O'Hamndley, and S. M. Allen, Model of discontinuous actuation of ferromagnetic shape memory alloy, *Journal of Applied Physics*, vol. 89, pp. 1295-1301, 2001.
- [120] R. C. O'Hamndle, Model for strain and magnetization in magnetic shape memory alloys, *Journal of Applied Physics*, vol. 83, pp. 3263-3270, 1998.
- [121] R. C. O'Hamndle, Modern magnetic materials principles and applications, *John Wiley & sons*, New York, 2000.
- [122] M. Pasquale, Mechanical sensors and actuators, *Sensors and Actuators A*, vol. 106, pp. 142-148, 2003.
- [123] W. Stadler, Analytical robotics and mechatronics, *Mc Graw-Hill*, New York, 1995.
- [124] G. Burdea, Force and touch feedback for Virtual Reality, *Wiley*, New York

1996.

- [125] C. Mavroidis, Development of advanced actuators using shape memory alloys and electro rheological fluids, *Res Nondestr Eval*, New York, 2002.
- [126] T. W. Shield Magneto mechanical testing machine for ferromagnetic shape-memory alloys, *Review of Scientific Instruments*, vol. 74, pp. 4077-4088, 2003.
- [127] T. W. Shield and J. Cui , Magneto-mechanical behavior of a ferromagnetic shape memory alloy Fe_3Pd , *Proc.SPIE 2002.*, vol. 4699, pp. 251-262, Jul 2002.
- [128] O. Heczko and K. Ullakko, Effect of temperature on magnetic properties of Ni-Mn-Ga magnetic shape memory alloys, *IEEE Trans. Magn.*, vol. 37, pp. 2672-2674, 2001.
- [129] T. Jokinen, I. Suorsa, and K. Ullakko, Magnetic shape memory materials-new actuator materials for electromechanical devices, *Proc. Speedam 2000 conference*, Shenyang, China, pp. B4-5, B4-12, Jun 2000.
- [130] L. Straka, O. Hetzko, and N. Lanska, Magnetic properties of various martenstic phase in Ni-Mn-Ga alloy, *IEEE Trans. Magn.*, vol. 38, pp. 2835-2837, 2003.
- [131] J. Kajaste, H. Kauranne, I. Suorsa and M. Pietola, Magnetic shape memory (MSM) actuator as linear motor in proportional control valves, *Proc. Of IFK2004 conference*, Germany, Mar 2004.
- [132] A. du Plessis, A. Jessiman, G. Muller and M. van Schoor, Latching valve control using ferromagnetic shape memory ally actuators, *Proc of SPIE 2003.*, vol. 4333, pp. 320-331, Aug 2003.

APPENDICES

APPENDIX A

MAXWELL STRESS TENSOR LAW

A more rigorous of the forces acting on a ferromagnetic body in a magnetic field obtained using Maxwell's stress tensor, which can be derived in the following manner. Assume that the domain currents can be represented as a net current density with some distribution throughout the volume of the material. If the domains are uniformly aligned then, by Ampere's model, the current is entirely concentrated at the periphery of the material. In any case, we can define an effective current density

$$J_M = \nabla \times \mathbf{M}$$

Where \mathbf{M} is the volume differential dipole moment in the material. Further, if there are any free currents in the volume, they lead to a non-zero curl in \mathbf{H} :

$$J_F = \nabla \times \mathbf{H}$$

Given this, the total force acting on the ferromagnetic body is obtained through the volume integral

$$\mathbf{F} = \int (\mathbf{J}_M + \mathbf{J}_F) \times \mathbf{B} \, dv$$

Or

$$\mathbf{F} = \int (\nabla \times \mathbf{H} + \nabla \times \mathbf{M}) \times \mathbf{B} \, dv$$

Since the total magnetic field (due to the imposed field and the domain alignment) is given by $\mathbf{B} = \mu_0 (\mathbf{H} + \mathbf{M})$, this becomes

$$\mathbf{F} = \frac{1}{\mu_0} \int (\nabla \times \mathbf{B}) \times \mathbf{B} \, dv$$

Apply the vector identities

$$\oint (B \cdot B) dS - 2 \oint B (B \cdot dS) = 2 \int B \times (\nabla \times B) dv - 2 \int B (\nabla \cdot B) dv$$

And

$$(\nabla \times B) \times B = -B \times (\nabla \times B)$$

To obtain

$$F = \frac{1}{\mu_0} \oint B (B \cdot dS) - \frac{1}{2\mu_0} \oint (B \cdot B) dS - \frac{1}{\mu_0} \int B (\nabla \cdot B) dv$$

Gauss law states that, for static fields or fields varying at a moderate rate,

$$\nabla \cdot B = 0$$

So that the last term disappears:

$$F = \frac{1}{\mu_0} \oint B (B \cdot dS) - \frac{1}{2\mu_0} \oint (B \cdot B) dS$$

The integration can be represented very compactly using Maxwell's stress tensor, defined in the absence of electric fields ($E=0$) as:

$$T_{ij} = \frac{1}{\mu_0} \left(B_i B_j - \frac{1}{2} \delta_{ij} B^2 \right)$$

Where $\delta_{ij} = 1$ if $i = j$ and $\delta_{ij} = 0$ if $i \neq j$ with this convenient device, the force can be compactly expressed as

$$F = \oint \vec{T} \cdot dS$$

Note that the magnetic field is perpendicular to the surface of the iron everywhere on the surface, and then the force becomes

$$F = \frac{1}{2\mu_0} \oint |B|^2 dS$$

This perpendicularity obtains when the relative permeability of the magnet iron is very high: this is the usual assumption made in computing the force on a ferromagnetic body.

Field governing equations (Maxwell)

$$\nabla \times H = J$$

$$\nabla \cdot B = 0$$

Field Governing equations (Maxwell)

Simplification: Assume that all of the flux lies in a plane and that all of the currents flow perpendicular to that plane:

$$\int_A \nabla \times H \cdot da = \int_A J \cdot da$$

Green's theorem

$$\int_A \nabla \times H \cdot da = \oint H \cdot dl$$

(2d)

$$\oint H \cdot dl = \int_A J \cdot da$$

Lumped Model:

$$\oint H \cdot dl = \int_A J \cdot da$$

Assume:

- Path dl parallel to H
- Path can be broken into n segments where H is constant
- J is confined to electromagnet coils

- J is uniform in n_c coils

Ampere's loop law:

$$\sum_{i=1}^{n_s} H_i l_i = \sum_{i=1}^n N_i I_i \quad (JA = NI)$$

Assume that the permeability is constant in each segment:

$$B_i = \mu_i H_i$$

To get

$$\sum_{i=1}^{n_s} \frac{B_i l_i}{\mu_i} = \sum_{i=1}^{n_c} N_i I_i$$

If the loop is taken in a clockwise direction, then the currents are assumed positive passing into the analysis plane and the fluxes \mathbf{B} are assumed positive in the direction of the integration.

Conservation Flux

$$\nabla \cdot \mathbf{B} = 0$$

In integral form:

$$\iint_s \mathbf{B} \cdot d\mathbf{a} = 0$$

Lumped model: assumed that the perimeter can be broken into n_p discrete patches:

\mathbf{B} is perpendicular to each patch

$$\sum_{i=1}^{n_p} \int_{A_i} \mathbf{B}_i \cdot d\mathbf{a} = 0$$

Further \mathbf{B} is uniform over each perimeter patch

$$\int_{A_i} \mathbf{B}_i \cdot d\mathbf{a} = B_i A_i = \phi_i$$

Finally

$$\sum_{i=1}^{n_p} \phi_i = 0$$

It is assumed that the integral is performed over a solid volume and that da is an outward directed normal to the surface. Therefore, the convection in the summation is that a positive ϕ_i is directed out of the volume.

Lumped Model: Forces

$$f = \frac{1}{2\mu_0} \iint_s B^2 da$$

Assumptions

Surface can be broken into n_a patches

B is constant in each of these patches